3-D Particle Tracking Velocimetry: Development and Applications in Small Scale Flows

Wei-Hsin Tien

A dissertation

submitted in partial fulfillment of the

requirements for the degree of

Doctor of Philosophy

University of Washington

2013

Reading Committee:

Dana Dabiri, Chair

James C. Hermanson

Alberto Aliseda

Program Authorized to Offer Degree:

Aeronautics and Astronautics

University of Washington

Abstract

3-D Particle Tracking Velocimetry: Development and Applications in Small Scale Flows

Wei-Hsin Tien

Chair of the Supervisory Committee:
Professor Dana Dabiri
Aeronautics and Astronautics

This dissertation contains two parts. In part I, a novel volumetric velocimetry technique is developed to measure the 3-D flow field of small-scale flows. The technique utilizes a color-coded pinhole plate with multiple light sources aligned to each pinhole to achieve high particle image density and large measurable depth on a single lens microscope system. A color separation algorithm and an improved particle identification algorithm are developed to identify individual particle images from each pinhole view. Furthermore, a calibration-based technique based on epi-polar line search method is developed to reconstruct the spatial coordinates of the particle, and a new two-frame tracking particle-tracking algorithm is developed to calculate the velocity field. The system was setup to achieve a magnification of 2.69, resulting in an imaging volume of $3.35 \times 2.5 \times 1.5$ mm^3 and showed satisfactory measurement accuracy. The technique was then

further miniaturized to achieve a magnification of 10, resulting in a imaging volume of 600 × 600 × 600 μm^3. The system was applied to a backward-facing step flow to test its ability to reconstruct the unsteady flow field with two-frame tracking. Finally, this technique was applied to a steady streaming flow field in a microfluidic device used to trap particles. The results revealed the three-dimensional flow structure that has not been observed in previous studies, and provided insights to the design of a more efficient trapping device.

In part II, an in-vitro study was carried out to investigate the flow around a prosthetic venous valve. Using 2-D PIV, the dynamics of the valve motion was captured and the velocity fields were measured to investigate the effect of the sinus pocket and the coupling effect of a pair of valves. The PIV and hemodynamic results showed that the sinus pocket around the valve functioned as a flow regulator to smooth the entrained velocity profile and suppress the jet width. For current prosthetic valve design a shorter leaflets is advantageous because it prevents flow stasis and reduce the energy loss. Valve pairing tests showed that an orthogonal configuration of the valve pair result in a complicated 3-D flow around the valve, which can increase the mixing of the blood flow and prevent reversed flow in between the valves. The tests of different valve separation distance showed that the coupling effect of two valves was weakened as the separation distance increased, suggesting the existence of a separation distance between the two valves to maximize the coupling effect and keep the flow structure stable.

Table of Contents

List of Figures

List of Tables

Acknowledgements

First, I would like to thank my adviser, Professor Dana Dabiri, for giving me the chance to work with him, and his patient guidance, enthusiastic encouragement and useful critiques of this work. His energy, creative ideas and determination has always been important inspiration and motivation to me.

I would also like to express my very great appreciation to my supervisory committee members; Professor James C. Hermanson and Professor Alberto Aliseda, for spending their time to read through my dissertation and providing useful critiques to help me improve the contents of the dissertation; Professor Kuen Y. Lin and Professor Jonathan D. Posner, for providing their valuable opinions during the final exam.

I wish to acknowledge the help provided by Professor Daniel T. Schwartz from the UW chemical engineering department for all the support to the hydrodynamic tweezers project, as well as all and suggestions and insightful advices. My special thanks to his student, Valerie Lieu, for building the microfluidic devices, perform the experiments together and share her knowledge and valuable experiences on the hydrodynamic tweezers.

I am particularly grateful to Professor Ghassan Kassab from IUPUI for allowing me to join his exciting venous valve project. It is my privilege to collaborate with his great lab, and I am very grateful to his full support on all the lab facilities for the venous valve project, as well as his wise suggestions and guidance on the project. Thanks to Dr. Henry Y. Chen and Dr. Zachary Berwick for their help on setting up the PIV experiments in IUPUI.

I also want to thank the brilliant people in the Dabiri group that I have been working with. My special thanks to professor Gamal Khalil for his help on making the polystyrene particles and his wise suggestions. Thanks to my past lab colleagues, Joey Duncan, Casper Lei and Micah Paul, for their help in developing the particle tracking code. I really appreciate their creative ideas and hard work.

Lastly, I would like to express my gratitude and love to my parents and my brother, for their unconditional support and patience all these years when I am away. I wish thank my wife, Hui-Ching, for her love and all the support she gave me. She is my constant and guiding light during the toughest time.

Part I Development of Three-Dimensional Micro Particle Tracking Velocimetry

1 Introduction

Flow visualization is a method to study fluid dynamics. By making the flow pattern visible, the property of the flow can be revealed and observed, and qualitative or quantitative information can be extracted. In experimental fluid dynamics, the flow can be visualized in different methods. Ribbons can be attached on the surface of the airfoil in the wind tunnel to show the direction of the flow, or dyes can be injected to the propellers in the water tunnel to reveal the helical flow patterns. If the flow property changes, like supersonic flow with shock waves, optical methods such as Schlieren photography or shadowgraph can be used.

In a lot of cases, the flow can be visualized by adding small tracer particles. Using appropriate optics, the particles can be illuminated by a sheet of light to show a slice of the flow. If the particles are carefully chosen to follow the flow, it is possible to capture the motion of flow by analyzing velocities of those particles. In the last few decades, technology advances in optics and electronics allow us to not only observe the flow qualitatively, but also extract quantitative information with flow visualization techniques. With the help of pulsed laser and digital image recording device such as CCD cameras, the flow can be "frozen" instantly and two sequential snapshots in a very short time interval can recorded. Computational technology advanced so rapidly that large and complex data set can be analyzed in a very short time. The results are the two optical measurement techniques used widely in modern fluid dynamics studies, the particle imaging velocimetry (PIV) and particle tracking velocimetry (PTV). Both are non-intrusive and

capable of measuring the whole flow field simultaneously, while other methods like laser Doppler velocimetry (LDV) or Hot-wire anemometers can only make point measurements.

1.1 **PIV/PTV**

Figure 1-1 Experimental setup of a typical PIV/PTV Experiment (From Raffel *et al.*, 2007) shows the general concept of a PIV/PTV experiment. Tracer particles are added into the flow of interest, and illuminated by a sheet of light made from a light source with a series of optics to shape the beam of light (usually a coherent light source e.g. laser) into a sheet. An imaging recording device is set to capture the images of the tracer particles. Sequential images are recorded with a known time interval, *t'-t*, between the successive image frames. Since the number of tracer particle images in the recording is huge, the image recordings are analyzed by a computer, and complicated algorithms are used to post-processing the images.

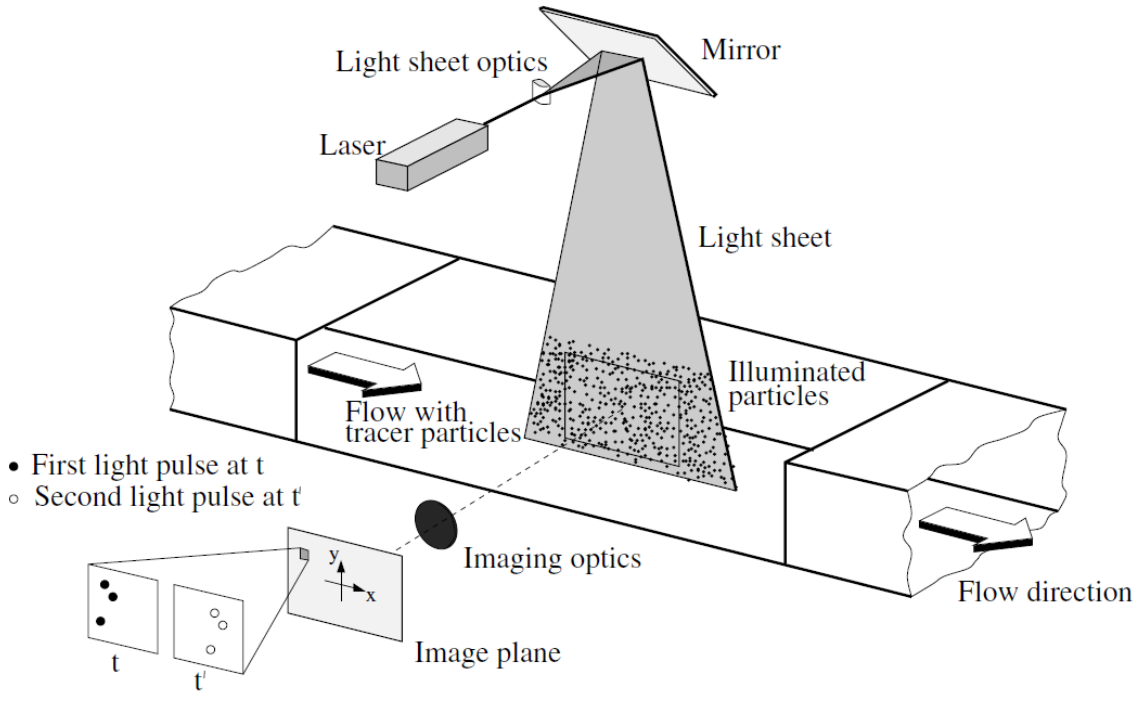

Figure 1-1 Experimental setup of a typical PIV/PTV Experiment (From Raffel *et al.*, 2007)

In both PIV and PTV system, the fluid velocity is approximated by the displacement of the tracer particles in a finite time interval $\Delta t = t" - t'$, i.e.

$$D(X; t', t") = \int_{t'}^{t"} v\,[X)t), t]dt, \tag{1-1}$$

when the error of displacement *D* to the local fluid velocity is within a finite error ε:

$$\|D - u \cdot \Delta t\| < \varepsilon. \tag{1-2}$$

Thus the task of PIV and PTV is to calculate the displacement field from the tracer particle images in successive image recordings and divide it by the time interval to get the approximation of the velocity field.

In PIV, the images are divided into small interrogation windows which are cross-correlated at time *t'* and *t"*. The spatial displacement that produces the maximum cross-correlation statistically approximates the average displacement of the particle images in the interrogation window. Because the interrogation windows are located at regular grid points, the measured velocity vector field is on a uniform grid base. The concept of PIV process is shown in Figure 1-2 (a). This technique has been widely used in fundamental and applied fluid Mechanics research as a diagnostic tool since it was first developed in 1980's. In the last decades, this technique has been improved to meet the requirements of various applications, yet it is still evolving to become a better tool for the researchers to use in many advanced studies. More details of the theoretical basis and applications can be found in Raffel *et al.* (2007), Adrian (2011).

In PTV, each particle image is treated as a separate data sample and the position is identified and tracked from image at time *t* to time *t'*. Since the tracer particles are randomly distributed in the flow, so are the resulting velocity vectors. The velocity vector field is thus on a

non-uniform grid space, and sometimes the data has to be transform back to a uniform grid space for data comparison. The concept of PTV is shown in Figure 1-2 (b). This technique can be traced back to the time of Da Vinci (Gharib, Kremers, Koochesfahani, & Kemp, 2002). However, it is the computational advances in the last several decades that make it possible to automate PTV processes and obtaining quantitative measurements based on streaking motions of tracer particles (Agüí & Jimenez, 1987). Algorithmically, progress was made in the 1990's with the introduction of two-frame (rather than four-frame) particle tracking routines by researchers such as Baek and Lee (1996), whereby particles were matched based on their "Match Probability". This probability was calculated using neighboring particles and some heuristics based on maximum velocities and quasi-rigidity conditions over small areas of the flow. While the approach significantly improved over nearest-neighbor approaches, it was still limited to fairly low gradient flows. Around the same time, super resolution methods were introduced (Keane, Adrian, & Zhang, 1995) based on the autocorrelation of double-pulse PIV images to guide the particle matching routine. This method was augmented with the use of Kalman filter prediction by Takehara *et al.* (2000), which increased the robustness of the super resolution method. Cowen and Monismith (1997) introduced a technique known as hybrid particle tracking, which used the results from two-frame PIV analysis to guide the particle tracking process. Upon initially obtaining PIV results, the algorithm then used these results as a guide to search specific areas in the second image for a single particle, which was then considered the match to the particle from the first frame. It essentially constituted a modified nearest neighbor search, using the added knowledge of approximate displacements from PIV. Further advancements along this line were made by Kim and Lee (2002) by combining the hybrid PIV-PTV idea with the Match Probability concept. Such an approach allowed variations in the maximum velocity along with

variable rigidity conditions depending on the local flow properties, thus expanding the range of the Match Probability Algorithm.

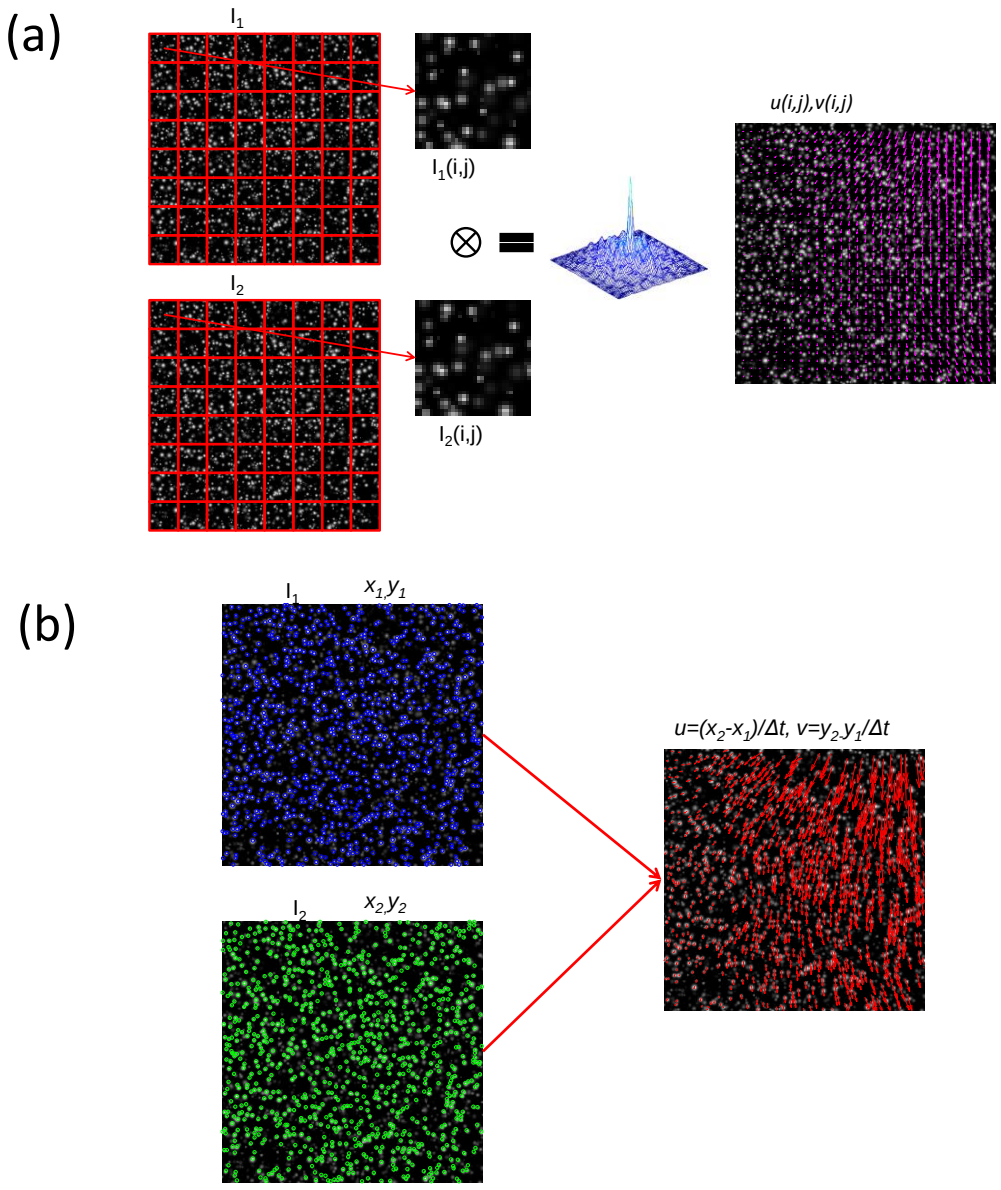

Figure 1-2 Concept of (a) Particle Image Velocimetry (b)Particle Tracking Velocimetry

In recent years, other methods have been developed. One is the deterministic annealing approach (Stellmacher & Obermayer, 2000) which attempts to minimize a cost function relating the particle displacements and an assumed transformation function operating between the two frames. Another is the feature tracking method based on Delaunay Tessellations (Song,

Yamamoto, Iguchi, & Murai, 1999), which matches triangles rather than individual particles, taking advantage of the fact that 2D shapes are identifiable while points are not. Other recently improved algorithms include the variational approach of Runhau *et al.* (2005) which finds the vector field as a whole rather than resolve individual vectors, and thus satisfies a minimization problem while including known smoothness properties of the flow. Mikheev and Zubtsov (2008) modified the original PTV method of Uemura *et al.* (1989) by taking into account the particle size when determining matches, and dubbed the method Enhanced PTV (EPTV). Another method originally developed for three-dimensional flows by Ponchaut and Hornung(2005), involves forming a first guess of the velocity field based on a weighted average between a correlation technique and a simple particle tracking technique. Appropriate weights are assigned to these vectors so that the correlation approach has more influence where it is more accurate (i.e. where the particle image density is high) and the simple particle tracking has more influence where the density is low. Finally, particle tracking uses this hybrid velocity field to create local criteria for the velocity vectors. Brevis *et al.* (2011) proposed an integrated cross-correlation/relaxation algorithm. The combined algorithm first uses a cross-correlation process to obtain an initial solution and further refined the results by the relaxation algorithms in the zones where the cross-correlation scheme shows low reliability. The performance of both of the individual and the integrated algorithms are compared and analyzed using synthetic and experimental images. The results show improved overall performance by the integrated algorithm at high velocity gradient and heterogeneous seeding cases. Panday *et al.* (2011) proposed an ant colony optimization algorithm for matching image pairs of stereo PIV images. Although the tracking algorithm could potentially be used for tracking image pairs over time, it is used to match stereo image pairs from the two camera views instead of temporal tracking.

Shindler *et al.* (2010) proposed a PTV technique based on a modified polar coordinate system similarity method (PCSS) for tracking. The enhanced algorithm shows improved performance for cases that have inhomogeneous seeding density distributions.

One of the advantages PTV has over PIV technique is the sensitivity to high velocity gradient. While PIV has advanced to a very robust and accurate level, there is still the issue of spatial resolution. With advanced weighted iterative techniques, it has been shown that spatial wavelengths as small as twice the grid node distance are detectable (J. Nogueira, Lecuona, & Rodriguez, 2005). In this study, they also found that the velocity error associated with wavelengths of this size approaches 100%. For velocity errors on the order of 10%, the smallest wavelengths detectable are larger by a factor of 4 to 8. On the other hand, PTV is only limited by the mean spacing of particles (which goes as the square root of particle image density, defined as the number of particles per image area in pixels squared). In addition, PIV suffers from an inherent averaging effect over the area of the interrogation windows, which decreases the maximum velocity gradients that can be measured (Scarano, 2003). PTV does not result in this severe averaging effect, since individual particles are tracked. With kriging interpolation (Gunes, Sirisup, & Karniadakis, 2006), it is possible to reconstruct accurate velocity gradients on a uniform grid basis from non-grid PTV results.

Comparing to PIV algorithms which analyze cluster of particle images in each interrogation window, the performance of a particle tracking algorithm depends on their ability to identify particles. In most macro-scale experiments, it has been shown that the optimized particle image size for either PIV or PTV is about 2-4 pixels in diameter. For micro-scale studies, due to the restrictions of volumetric illumination and high magnification, the particle image size can be significantly larger. To fully utilize the high spatial resolution feature of the PTV

approach, the particle density in the imaging area should be as high as possible. Thus overlapping particles becomes an important issue when identifying particle locations. One popular approach to resolving this issue is to start from a local intensity maximum and apply a Gaussian fit to locate the peak with sub-pixel accuracy. Both Gaussian surface fits, and Gaussian line fits (Cowen & Monismith, 1997; Marxen, Sullivan, Loewen, & Jahne, 2000; Ohmi & Li, 2000; Mikheev & Zubtsov, 2008; Brady, Raben, & Vlachos, 2009) have been used. Specifically, Marxen *et al.* (2000) found that Gaussian line fits performed as well as a surface fit with much lower computational time provided the image noise was low. A dynamic threshold binarization method proposed by Ohmi and Li (2000) and modified by Mikheev and Zubtsov (2008) provides a way to overcome the variations due to particle sizes and background noise level, while preserving most of the particle images. In the case of high image noise, the Gaussian surface fit performed better, at the cost of longer computational time. Brady *et al.* (2009) proposed an improved 4-point Gaussian estimator which reduces the error of traditional 3-point Gaussian fit by accounting for pixel discretization effects using integral formulations. Approaches including the use of the CLEAN algorithm (Stellmacher & Obermayer, 2000) and a Gaussian mask correlation (K. Takehara & Etoh, 1999; Saga, Kobayashi, Segawa, & Hu, 2001), apply a "model image" of the particles to the original image to find the maximum of convolution or cross-correlation, thus determining the peak location. The performance of particle mask correlation method (PMCM) tested by Takehara and Etoh (1999) shows that it is possible to use a fixed size of the particle mask for finding a range of particle sizes, and that the normalized critical distance to separately identify two particles is about unity for identical particles but increases when the intensity difference increases. Shindler *et al.* (2010) proposed a new feature-based particle

identification method based on an optical flow equation. Instead of the intensity peak of a particle image, the center-of-mass of a feature is used as the location of the tracer.

The general assumption for most peak finding algorithms is that each particle results in one peak of a particle image and the intensity distribution can be approximated by a 2-D Gaussian function (Adrian & Yao, 1985). Thus a 1-D or 2-D Gaussian fit can be applied to the pixels in the vicinity of a local intensity maximum to locate the particle center. As pointed out by Ponchaut (2005), this assumption no longer holds when the particles severely overlap. Marxen *et al.* (2000) performed simulations of overlapping particles with least-square surface fits and 3-point line fits based on this assumption and the results showed a steep rise in the errors when the particle separation distance approaches the particle diameter. The summation of multiple particle images can result in fewer peaks, where these peaks deviate from the particles' true locations. Even if the peak number is the same as the particle number, the Gaussian fit based on the single particle assumption could lead to greater location errors since the overlap region will add bias error to the peak location towards the nearby particle. The particle mask correlation method (PMCM) can resolve the two overlapping particles up to a minimum critical separation distance, thus providing a way to estimate the presence of nearby particles. However this critical distance is still larger than the particle separation distance that would cause two particles to sufficiently merge so that they would form a single peak and it increases even more when the intensity differences between particles increase. The Cascade Correlation Method (N. C. Angarita-Jaimes, Roca M, Towers, Read, & Towers, 2009) suggests that instead of applying the cross-correlation once with the particle mask image, a cascade of cross-correlation operations make the correlation peak narrower, thus decreasing the critical distance. Their simulation data shows a significant improvement when compared with the PMCM algorithm, reducing the

critical distance to below Rayleigh's resolution limit. The particle location is then determined by performing a 5-point 2-D Gaussian fit to find the peak location in the cross correlation plane. The CCM algorithm provides an efficient way to separate overlapping particles, and is easy to implement. However, the peak locations found from the correlation image plane may suffer additional errors, such as the well-known peak-locking error (J. Nogueira, Lecuona, & Rodriguez, 2001; Liao & Cowen, 2005).

1.2 **Micro-PIV/PTV**

One of the most active areas of the PIV/PTV application in recent years is the Micro PIV/PTV, where the technique is used to imaging flow phenomenon in micro scale. The micro PIV is first developed by Santiago *et al.* (1998) to imaging a Hale-Shaw flow around a 30 micrometer elliptical cylinder, which is a direct implementation from a macro-scale 2D plane PIV system to a micro-scale system. In the study, epifluorescence microscopy is used to image the tracer particles, and a volumetric illumination from a white light source is used. The velocity fields can be measured with spatial resolution down to 6.9 × 6.9 × 1.5 μm. Since then most of the 2D micro PIV systems use a similar experimental setup, with various data processing techniques to reconstruct the flow field. A typical micro-PIV/PTV set up is shown in Figure 1-3. The main components are the same as the macro-scale setup: Imaging the test section of the flow of interest, the illumination source, the image recording device, and the post processing hardware/software. However, because the magnification is very different (macro-scale: ~0.1; micro-scale: ~10) the micro-PIV/PTV have several key features that are worth discussing.

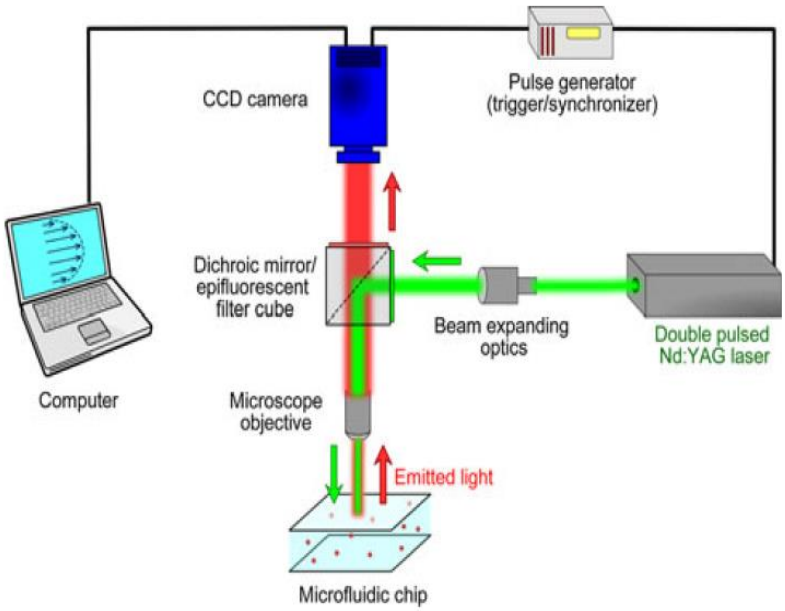

Figure 1-3 Experimental Setup of a typical 2D Micro-PIV/PTV (From Williams *et al.*, 2010)

The first feature of micro-PIV/PTV is volumetric illumination. In micro-PIV/PTV, volumetric illumination is the most common way of illumination instead of using a 2-D light sheet. This is because the imaging size is small in scale and it is practically difficult to create a light sheet in the μm scale. Thus in the 2D micro-PIV/PTV applications, the measurement plane is usually defined by the depth of focus of the optics instead of the thickness of the light sheet. Meinhart *et al.* (2000) derived the theoretical expression of the measurement plane based on the focusing characteristics of the recording optics. The out-of -focus particles that lie outside of the measurement plane contribute to the background noise to decrease the signal to noise ratio of the images. Olsen and Adrian (2000) derived the equations of the cross-correlation function for a micro-PIV system. A weighting function is also used to determine the biasing of the measured velocity due to the motions of the out-of-focus particles. The depth of correlation (DOC), defined as the depth over which particles significantly contribute to the correlation function, is used to define the bound on the interrogation volume in the depth direction.

The second key feature is the small size of the tracer particles. In macro-scale PIV applications for liquid flows, the tracer particle size ranges from 10μm (polystyrene solid particles) to 1000 μm (Oxygen bubbles). In micro-scale applications, the tracer particles used range from 50nm to 10μm because of the imaging size is much smaller for the micro-PIV/PTV. Therefore particles can be much smaller than the light wavelength, and the amount of light scattered by a particle varies as $d_p^{-}6$, as it is in the Rayleigh scattering regime (Born & Wolf, 1999). As a result, imaging the particles can be challenging for micro-PIV/PTV. Epi-fluorescence imaging is a common solution to this problem. Particles dyed with fluorescent dye are used as the tracer, and a long-pass filter is used to remove lights from the light source and background, leave only the light in the emission wavelength of the fluorescent particles. Meinhart *at al.* (1999) applied this technique with 200 nm polystyrene fluorescent particles to imaging a 30 μm by 300 μm wide rectangular channel, and the flow velocity as fast as 10mm/s can be measured.

The third key feature is the effect of the Brownian motion to the tracer particle. Brownian motion is the random moving of particles suspended in a fluid due bombardment by the fast-moving atoms or molecules in the fluid. The relative error ε_b due to the Brownian motion is

$$\varepsilon_{\mathrm{b}} = \frac{1}{u}\sqrt{\frac{2D}{\Delta t}}, \tag{1-3}$$

where u is the local fluid mean velocity during the time interval Δt. D is the diffusivity of the particle,

$$D = \frac{kT}{6\pi\mu d_p}, \tag{1-4}$$

where k is Boltzman's constant, μ viscosity and d_p the tracer particle diameter. From (1-3) and (1-4), if the local fluid velocity is slow and the size of the tracer particle is small, the Brownian motion will contribute to the error in the location measurement due to the uncertainty in the

location of the particle. For micro-PIV, the effect is the broadening of the correlation signal peak. It also increases the depth of correlation and thus increases the bias error (Olsen & Adrian, 2000).

There have been many researches contributing to this field since the first micro-PIV system was introduced in the late 1990s'. Reviews of the recent developments and applications can be found in Williams *et al.* (2010), Lee and Kim (2009) and Lindken *et al.*(2009).

1.3 **3D Methods for Micro-PIV/PTV**

The main limitation of the 2D planar PIV system is that it only measures a slice of the flow with the two co-planar velocity components (2C-2D). To fully resolve a 3-D flow, several 3-D techniques have been developed to overcome this limitation, including confocal laser scanning microscopy, stereoscopy, digital holographic microscopy, wave-front sensing, deconvolution microscopy and defocused techniques.

1.3.1 **Confocal Laser Scanning Microscopy (CLSM)**

If the flow is steady or phase-locked, a volumetric measurement is possible by scanning through the whole volume of interest to get the in-plane velocity field. Park and Kihm (J. S. Park, Choi, & Kihm, 2004; J. S. Park & Kihm, 2006b) use confocal laser scanning microscopy (CLSM) to measure a Couette flow between a rotating and a stationary disk with 180 micrometer apart. They compared the results acquired from CLSM and the conventional wide field microscopy (WFM), and concluded that the CLSM provided far more accurate data with fewer fluctuations. Although the scanning technique is accurate and fast enough for even unsteady flow, the ability to measure the out-of-plane component is still limited. Klein *et al.*(Klein, Moran, Frakes, & Posner, 2012) improved this technique and made it a true 3D-3C method by rapid translation of the high numerical aperture objective using a piezo objective positioner. The flow

is resolved with a 3-D version of super resolution PIV. Flow in a PDMS micro-channel with an expanding section was examined at 3D acquisition rates of 30 Hz, and strong agreement with a computational model was found. The advantage of this technique is the high spatial resolution, because the confocal microscopy eliminates the problem of out-of-focus light. The temporal resolution is still limited by the scanning speed of the objective lens, thus limited the applications to time-resolved flow.

1.3.2 **Stereoscopic Approach**

Stereoscopic technique (Lindken *et al.*, (2006); Bown *et al.* (2006) acquire images from two viewing angles and reconstruct the velocity components from the displacements found in the two image planes. With proper calibration, the system can achieve high accuracy. The technique has been widely used in macro-scale experiments and proved to be very useful for fluid mechanics studies. For micro-scale flow studies, a stereo microscope is usually used. Lindken at al. (2006) used a stereo microscope to measure the mixing region of a T-shaped micromixer, with a spatial resolution of 44 x 44 x 15 μm. Bown *et al.* (2006) improved the spatial resolution to 10 x 10 x 10 μm by using a super-resolution PIV approach, which uses PIV results as a guide to do particle tracking. This approach is used to measure a backward-facing step micro-channel flow. Yu *et al.* (2009) proposed another tracking method for stereo-μPTV, which performs in-plane tracking and then use a stereo approach to calculate the out-of-plane velocity, results in velocities consists of two Lagrangian and one Eulerian components. The disadvantage of the technique for micro application is that the low numerical aperture (NA) required for the stereo microscope objective lens as opposed to traditional high NA objective lens, which limits the spatial resolution of the images. Another limitation is that this technique can only measure out-of-plane

velocity components in a planar region (2D-3C), thus a scanning procedure through the entire volume of interest is required to achieve a volumetric measurement (3D-3C).

1.3.3 **Digital Holographic Microscopy (DHM)**

Digital holographic microscopy (DHM) is digital holography applied to microscopy. Instead of recording images of the object space the image sensor is used to record the scattered light and non-scattered light interference pattern as hologram. With the objective lens to magnify the hologram, the resolution of the current image sensors can replace the traditional photographic film. The locations of the object are then numerically reconstructed from the hologram. Satake *et al.* (2005; 2006) first applied DHM to image a semicircular micro-channel flow. Sheng *et al.* (2006) demonstrated the ability of DHM by imaging and successfully reconstructing 5679 particle locations in a fluid solution of $1.5 \times 1.5 \times 1$ mm^3 volume. Ooms *et al.* (2009) applied the DHM to map a 3-D flow in a T-shape micromixer, and investigated the performance in terms of accuracy, resolution, dynamic spatial range and dynamic velocity range. Choi and Lee (2009) applied this technique to imaging human red blood cell motions in a microtube flow. The technique is proven to be accurate and easy to set up, and the main advantage is the achievable high particle density. The main drawback is that the hologram reconstruction algorithm is very computationally intensive and time consuming.

1.3.4 **Wave-Front Sensing/ Astigmatism Particle Tracking Velocimetry**

The wave-front sensing (WFS) technique (Angarita-Jaimes *et al.* (2006), Towers *et al.*(2006), or wave-front deformation PTV, as used by Kumar *et al.* (2011) is another technique proposed to measure the 3-D flow field in micro scale geometry with a single camera view. An additional cylindrical lens other than a field lens is added to the optics to create an anamorphic

imaging system. The particle images thus deform differently in the x and y direction when the particle is out of focus, so the lengths of the x and y axes of the elliptical particle image relates to the depth location of the particle uniquely. Chen *et al.* (2009) developed the mathematical model and verified the performance of the system and shows that the lateral and depth performance of the sensor can be largely varied independently across a wide range. They also demonstrated the ability to measure the 3-D velocity field of micron-sized fluorescent tracers in a backward-facing step flow within a micro-channel, with an uncertainty of 2.8 μm in the axial direction over a range of 500 μm. Cierpka *et al.* (2010) independently derived similar theoretical analysis and developed a processing algorithm based on continuous wavelet analysis and autocorrelation to estimate the particle positions. The system is named as Astigmatism Particle Tracking Velocimetry (APTV). In their recent study (Cierpka *et al.*(2011), an intrinsic calibration procedure based on the imaging function of the particles is proposed to extend the size of measurement volume and to account for the image aberrations. Kumar *et al.* (2011) recently applied this technique to study the 3-D transport in a electrothermal microvortex (EMV), providing 3-D time-resolved particle trajectories with Lagrangian velocity and acceleration. Compare with other methods, the main advantage of this technique is the ease of changing the size of the measuring depth range by either changing the different focal length of the cylindrical lens or the distance between the cylindrical lens and the spherical lens.

1.3.5 **Defocusing Methods - Diffraction Ring Approach**

There are two categories of defocused techniques has been used to measure the 3-D micro flow field. The first category of techniques is based on the diffraction effect of the defocused particle image. When a particle is out of focus of the imaging system, the diffraction causes the defocused particle image to form concentric ring structure and varies with the depth

distance. Therefore it is possible to relate the depth location with the diffraction pattern to calculate the particle position. One way to calculate the particle position is to fit the particle intensity profile to theoretical values predicted by scattering theories or to an experimental image of known depth location. Ovryn (2000) applied classical Lorenz-Mie scattering theory to model the scattering intensity profile of 7μm particles, and successfully resolved the parabolic velocity profile of a micro-channel of 315μm depth. Moreno *et al.* (2000) and Guerrero *et al.* (2000) used generalized Lorenz-Mie theory (GLMT) to model the defocused particle image of a particle on the order of 20μm diameter at different depth location, and quantitatively compared the results with experimental images. Instead of matching to theoretical values, Zhang and Meng (2008) match the diffraction pattern to a calibrated experimental data by converting the 2-D intensity images to a 1-D radial vector through radial projection. This way, the error coming from the theoretical component is removed and the measurement accuracy is improved. The matching process of the intensity profile is computationally intensive, so the alternative method is to measure the outermost diffraction ring size as a function of the depth location, which can be either determined through experiment or through a regression analysis of theoretical values. Speidel *et al.* (2003) shows that the outer-most diffraction ring size of the defocused particle image has a linear relationship to the depth location and sub-nanometer precision of a single particle of size 216 nm can be achieved. Wu *et al.* (2005) analyzed a fluorescent particle imaged by a optical system and compared them with numerical results. They concluded that the outer-most ring is caused by the spherical aberration. Park and Kihm (2006a) used a calibration curve of the ring size to depth location to measure the confined flow around a microsphere. They also developed an image processing algorithm to extract the radii of the diffraction ring. Peterson *et al.* (2008) used a similar method to measure a fully developed duct flow of 50μm depth. Luo *et*

al. (2006) used scalar diffraction model proposed by Gibson and Lanni (1991) to calculate the depth location of the defocused particle image. They combined both the first dark and bright fringe diameters to determine the depth location. Later on Luo and Sun (2011) improved the accuracy of depth calculation by matching to a radial diffraction pattern instead of merely matching the outer most bright/dark ring size to the model. The main advantages of these methods are the high accuracy of depth location, and no additional optics is required to perform the measurement. However, due to the complex diffraction ring structure to calculate the depth location, the particle image density needs to be kept low in order to accurately identify the individual particle.

1.3.6 **Defocusing Technique - DDPIV Approach**

The second category of the defocused technique uses multiple pinholes to create multiple exposures of the same particle on the image plane to create a certain patterns. The particle location can be calculated by relating the pattern size variation related to the depth location. This concept was first proposed by Willert and Gharib (1992), in which a three-pinhole aperture mask is inserted between the image sensor and the measuring volume. Any particle away from the focal plane forms triple image exposures on the imaging plane, and the distances between each exposure increases as the actual distance of the particle to the focal plane increases. Thus the depth location can be calculated based on the size of the triangle pattern formed from the three exposures. The technique is successfully applied to the macro-scale flows (Pereira *et al.* (2000); Pereira *et al.* (2002). Park and Kihm (2006) first applied the method to a micro backward-facing step flow, and derived a mathematical model to account for effect of the pinhole plate location. A calibration based method is proposed later by Pereira *et al.* (2007) as an equivalent optical model of the complicated multi-element microscope system to simplify the calculation. Lu *et al.* (2008)

applied this approach to measure the blood flow inside zebrafish embryos. Other pinhole shape, such as an annular ring is proposed by Lin *et al.* (2008) to provide higher optical efficiency and ability to deal with ambiguities due to overlapped particle image patterns. The main advantage of this technique is the potential to have a better balance between computational cost and particle density. Since depth calculation is purely based on geometric optics, the requirement for computation power is less than those methods based on diffraction patterns or DHM. The particle image density can also be potentially higher than other method except DHM technique, since the defocused particle image size is smaller. The major disadvantage is the lower optical efficiency due to the use of small pinholes which significantly reduce the light allowed to go to the image sensor.

1.4 **Goal**

From the literatures discussed in the previous sections, it can be shown that the current 3-D micro-PIV/PTV system is still developing and evolving. Various methods have been proposed and they all have their advantages and disadvantages. However there are two common problems encountered by these systems. First problem is the particle overlapping. To resolve the depth location of the tracer particles in space with a 2-D image, it is inevitable to have particle images overlap to each other if a higher particle imaging density is desired. The particle image quality has to be good enough to assure it can be used to resolve the particle's depth location in space. Therefore the particle overlapping has to be resolved to increase the particle image density. The second problem is the measureable imaging depth. In a large aperture optical system, the imaging depth is shallow and only particles close to the focal plane have sharp images. The image quality degrades quickly as the particles are out of focus. Most of the 3-D micro PIV/PTV systems therefore limit their measurable depth to ensure the measurement accuracy.

Theoretically DHM system is the answer to these problems since all the depth information is recorded in the hologram and the particle locations are reconstructed all together. However the computational power required is extensive and the accuracy in the depth location still need to be improved.

The main goal of this work is to develop a 3-D velocimetry system that is suitable for imaging micro-scale flows and to provide a practical answer to these two problems. The DDPIV approach introduced in the previous section has several advantages that has potentials to provide solutions to these problems. The author therefore proposed a microscopic particle tracking system based on the DDPIV approach. A mini-scale system is first built to image a small scale flows, and then the system is miniaturized to measure the micro-scale flows. The system is built based on infinity-corrected microscope optics, and a new lighting method is proposed for better performance. The system has the potential of measuring micro-scale flows by two frame tracking. A new calibration-based method is proposed to calculate the depth location based on an epi-polar line search method, and integrated processing software with novel image processing algorithms to separate overlapping particle images is developed to identify, locate, and track the Lagrangian motions of the tracer particles, and reconstruct the flow field. To demonstrate the ability of the system, the method is applied to measure an accelerating backward-facing step micro-channel flow. Finally, the technique is used to image a novel micro-channel flow application that can be used to trap single cell and particles.

1.5 **Organization of Part I**

In the following chapters, the 3-D μPTV system and its applications are described in detail. In Chapter 2, the principle of the 3-D μPTV system is described, including the system concept, the illumination methods, particle identification, 3-D location reconstruction and

particle tracking algorithms are described. Chapter 3 describes the hardware experimental setup. In Chapter 4, the post-processing procedures of raw images and outlier detection are described. In Chapter 5, the experimental results are presented for the micro-scale backward-facing step flow and hydrodynamic tweezers. Finally, in Chapter 6, the conclusions draw form the current study and recommendations to the future work are provided.

2 Principle

2.1 System Concept

2.1.1 DDPIV Original Concept

The concept of the single camera DDPIV system is best described by a three-dimensional representation of the imaging system in Figure 2-1 (F. Pereira *et al*., 2000; Kajitani & Dabiri, 2005). The light, reflecting from particles between the plane of focus and the lens plane (the defocused region), passes through the pinholes and forms triple exposures (triplets) on the CCD plane. The size of the triplets depends on the location of the particle within the defocused region. Hence it is possible to reconstruct the location of a particle based on the triplet exposure images of the particle. Theoretically, a dual pinhole system is enough to determine the distance based on the exposure image separation. Practically, due to the difficulty of uniquely matching particle image pairs in densely seeded flows, the dual pinhole system generates too many ambiguous data. Adding a third pinhole to the system generates the triplet patterns that are easily identifiable. This concept is first proposed by Willert and Gharib (1992), and it is applied to trace

the flow field of a vortex ring impinging on a wall. A 25mm lens was used with a pinhole mask with three 1mm diameter pinholes to form a equilateral triangle of 6mm sides. The resulting imaging depth is 50mm. The in-plane resolution was found to be roughly 40 times better than the out-of-plane resolution. The concept is simple and elegant, and a three-dimensional particle location can be reconstructed with only one camera without cumbersome optical alignment procedures encountered in the multiple-view photogrammetric systems. However, it is difficult to use in practice when the imaged particle density becomes sufficiently large. They are difficult to identify, separate, and use towards particle identification. This is because the overlapped triplet exposures cause ambiguously identified triplets, since the exposures formed by one pinhole cannot be distinguished from the ones formed by another pinholes. Furthermore, the necessity of the pinholes has the unfortunate consequence of severely reducing the amount of light that exposes the CCD.

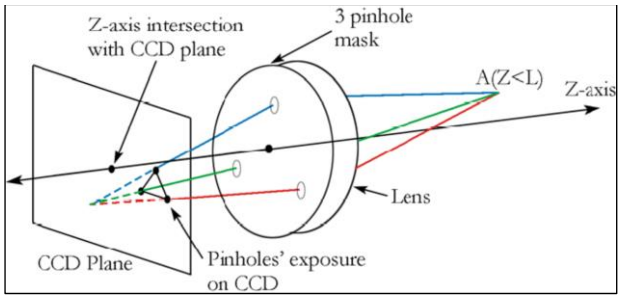

Figure 2-1 The single lens DDPIV system concept (Pereira *et al.*, 2000; Kajitani and Dabiri, 2005)

2.1.2 **Multiple Camera Approach**

One way to solve the particle image overcrowding problem using the single camera lens is replace the single camera with three single camera and lens (Pereira *et al.*, 2000). The pinholes are replaced by the three lenses, and the images formed through each lens are projected onto separate CCD sensors. Figure 2-2 shows the schematic of the concept from Pereira *et al.* (2000).

This configuration also increase the resolution in the out-of-plane measurement, because allowing to use separate lenses provides a larger separation distance from each lens, which has been proved to be proportional to the sensitivity in the out-of-plane measurement (Pereira and Gharib 2002). In the following studies (Kajitani and Dabiri 2005; Grothe and Dabiri 2008) the system is fully characterized and the equations are modified to increase the observable volume. It is found that the volume imaged by the three CCDs is a truncated pyramid shape, and a geometric uncertainty analysis is performed to study how the measurement error correlates to the optical parameters.

Ponchaut *et al.* (2005) developed a different optical setup for the three camera concept. In their system, the lenses are not parallel to the imaging planes of the CCDs and each lens-CCD system has its own focal length, which is different to Pereira's system. The benefit of this setup is that the lens aberration due to the large off-axis angle of the lens can be avoided. Since each lens-CCD system has a different focal length, the system is essentially a multi-view photogrammetric system. The equations derived from the DDPIV system no longer holds, and a set of more generalized equations is used to determine the particle locations in space.

These multi-view configurations are best suited for macro-scale applications, since the utilization of multiple cameras and lenses requires precise alignment for the optical system and enough space to setup. The latter is very critical, since it becomes a problem for the small scale applications. For small scale applications the magnification is usually larger than 1, and the working distance (the distance between the object plane to the lens) is short. The off-axis aberrations due to large magnification also make these configurations hard to be utilized for small scale measurements. This is because a lens can remove the off-axis aberrations require

multiple lens elements and three of these lenses can be difficult to position to imaging the small volume of interest.

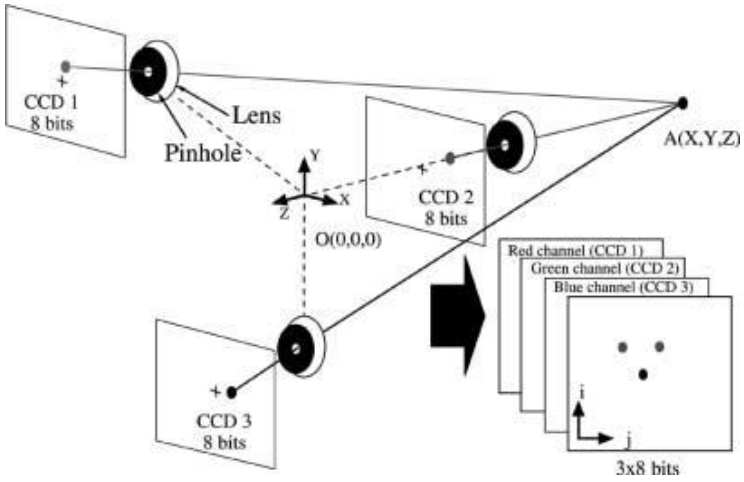

Figure 2-2 The three camera DDPIV setup schematic from Pereira *et al.* (2000).

2.1.3 **Color-Coded Pinhole System**

Another approach to solve the ambiguity problem in the original DDPIV system is make the exposures go through each pinhole distinguishable from another. This can be done by utilizing a color camera sensors and project the exposure images to each of the R, G and B color planes. For this purpose, different color filters (red, green and blue) are overlaid onto each of the pinhole apertures, as shown in Figure 2-3. Since the color-coded pinholes will result in colored images, a 3-CCD color camera is used for image acquisition. With this modification, the projected triplet image on the CCD plane is such that each pinhole's image will have a unique color, thus allowing for its identification. Furthermore, if the pinhole exposures overlap, the resulting color is also unique, still allowing for identification of each of the overlapped particles. In this manner, it is now possible to image high particle densities while eliminating the need for the more complex three-camera/lens system. Figure 2-4 (a) shows the resulting triplet if no color

filters are used; Figure 2-4 (b) shows the resulting triplet if red, green, and blue color filters are used. The formation of the red, green and blue triplet colors is addressed below.

Figure 2-3 The three color-filtered pinholes on the aperture mask

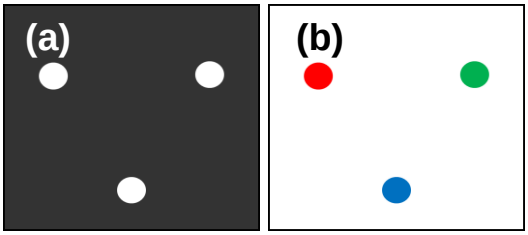

Figure 2-4 The triplet image formed on a 3-CCD color camera: (a) without color filters (b) with color filters

The main advantage of this configuration is its simplicity in hardware setup of the original Willert and Gharib's system is preserved. The system requires only a single lens and imaging sensor, and hence the optical alignment issue can be avoided. The space taken by the system is also smaller, making it more flexible to setup for imaging different types of applications.

2.1.4 **Mini-Scale System**

To demonstrate the feasibility of this proposed concept, an experiment is setup to imaging small scale buoyancy-driven flow. The seeding and illumination methods of the test

section are also modified. In the previous DDPIV configuration, light illuminates each seeding particle and the CCD camera images the light reflected from the particles. Since the DDPIV system is imaging a volume, significantly more light is needed compared to planar PIV systems. The presence of the pinhole apertures further limits the amount of light reaching the CCD camera. Usually a laser system is needed to provide sufficient reflected light. A similar method used by Estevadeordal and Goss (2005) is proposed to overcome this difficulty. Initially, the test section is seeded with black, non-reflective particles. The aforementioned color filters over each pinhole preclude the use of a single wavelength laser illumination source, thereby necessitating the use of a white light source. This light source is set to intentionally illuminate towards the camera (forward scattering setup), resulting in an image with a white background and different colored triplet images. Figure 2-5 (a) shows the resulting triplet if no color filters are used; Figure 2-5 (b) shows the resulting triplet if red, green, and blue color filters are used. The formation of the cyan, yellow and magenta triplet colors is addressed below.

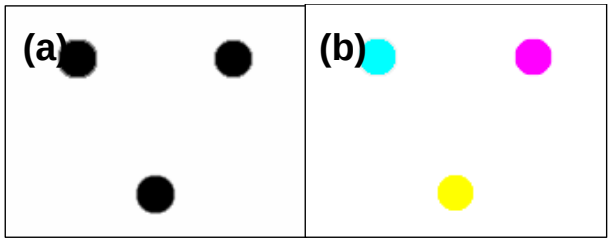

Figure 2-5 The shadow triplet image formed on a 3-CCD color camera: (a) without color filters (b) with color filters

Figure 2-6 shows how the defocused particle image (triplet) on the CCD plane is superimposed from the three pinhole apertures. Since black particles are imaged, these particles will block the light and form particle shadows on the images emerging from each of the red, green and blue filtered pinhole apertures. When the red and the green planes are superimposed, the image will result in a yellow background (red + green), but with green/red particle images where the black particle has blocked light in the red/green planes, respectively. Similarly, the

other two combinations of the color planes (green + blue, red + blue) also form the cyan and magenta regions, respectively, with blue/green particle images and blue/red particle images, respectively (see Figure 2-6). Finally, when all three planes are superimposed as shown in the central region of the CCD plane, the image will result in a white (red + green + blue) background, but with cyan (green + blue)/yellow(red + green)/magenta(blue + red) particle images. This modification also provides good contrast between the background and the particle images, which is useful for particle identification.

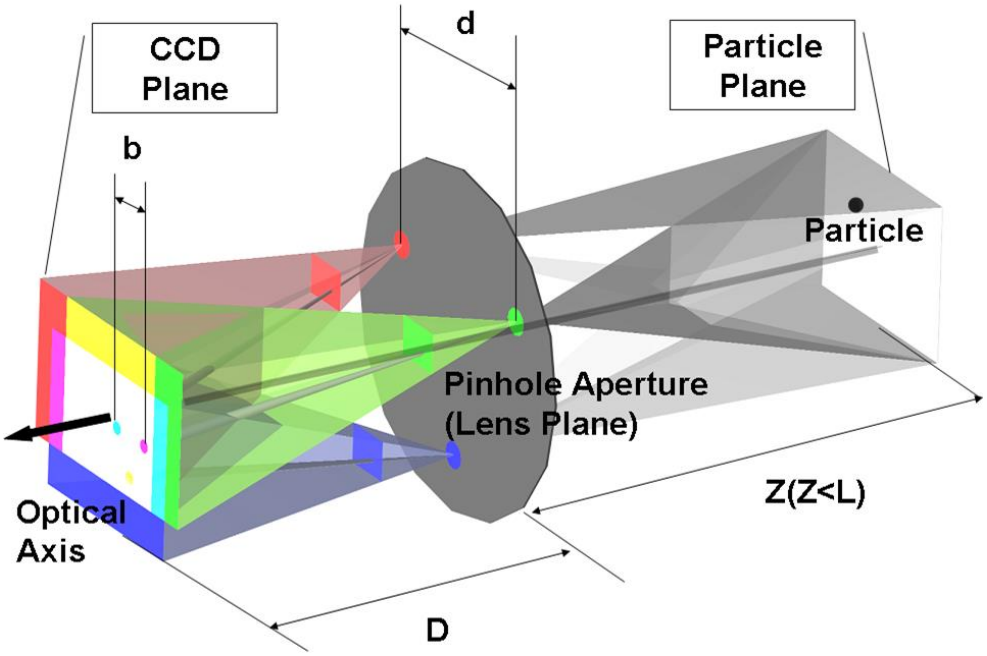

Figure 2-6 Defocused images obtained from a black particle illuminated with backlighting from a white light source through three color filters. Also seen are the superimposed images from each of the two color plane overlays and the superposition of the three color planes.

Figure 2-7 shows the experimental setup of the system used for the mini-scale system. This system consists of a Xenon flash lamp (Perkin Elmer FX-4400), a Nikon AF Micro 105mm camera lens, a pinhole mask with 2.74mm diameter pinholes that is located at the vertices of an equilateral triangle with side lengths of 15mm, Roscolux color filters (CalColor 90 Red #4690,

CalColor 90 Green 4490 and Calcolor 90 Blue #4290), a 640×480 pixels Sony XC-007 3-CCD chip camera, and a translation stage. The three-pinhole mask with color filters is placed inside the lens. The lens is attached to the camera via a bellows tube at a distance such that the measured magnification factor is 2.69. The resulting imaging volume is 3.35 × 2.5 × 1.5 mm^3. The light source is pulsed at 15 Hz and located sufficiently far from the lens so the resulting white background is uniform. Twenty micrometer diameter polystyrene particles manufactured by Polysciences Inc. are dyed black to absorb incident light, and are used to seed the flow within the test section.

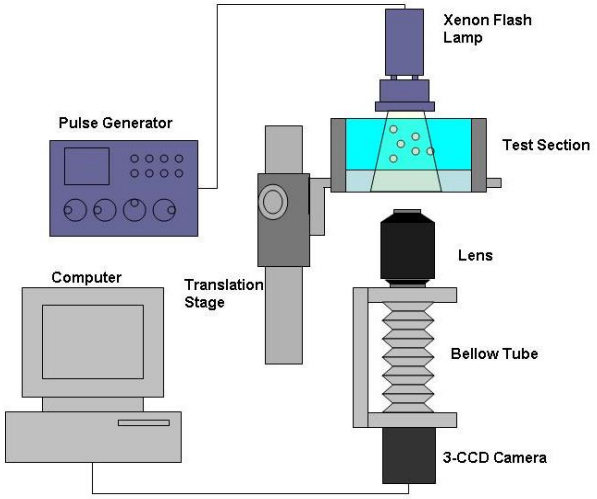

Figure 2-7 Experimental Setup of the Mini system

To demonstrate the feasibility of this system, an experiment is performed, where the test section is filled with a 30% glycerol-water solution, and is densely seeded with polystyrene particles. The top and bottom of the test section are heated to 60℃ and 80℃, respectively, thereby generating buoyancy-driven flow. The imaged volume is 3.35×2.5×1.5 mm. Figure 2-8 shows the comparison of the original image, the pre-processed image, the resulting image after inversion and color separation, and the image showing identified triplets. Comparison of Figure

2-8 (a) and (b) shows the improvement due to preprocessing the background. The effect of the inversion and color separation is shown by comparing Figure 2-8 (b) and (c), where the cyan, yellow and magenta colors are converted to red, green, and blue colors. The identified triplets are shown in Figure 2-8 (d), where the number of particles found in the frame shown is 347 particles. The identification of the triplets is performed using the original DDPIV method, which is discussed in detail in section 2.5.2.2. The reconstructed particle field is obtained by processing 2 successive particle fields, as detailed in section 2.5.3.1 . Figure 2-9 (a) shows the particle pairs reconstructed from two successive image frames.

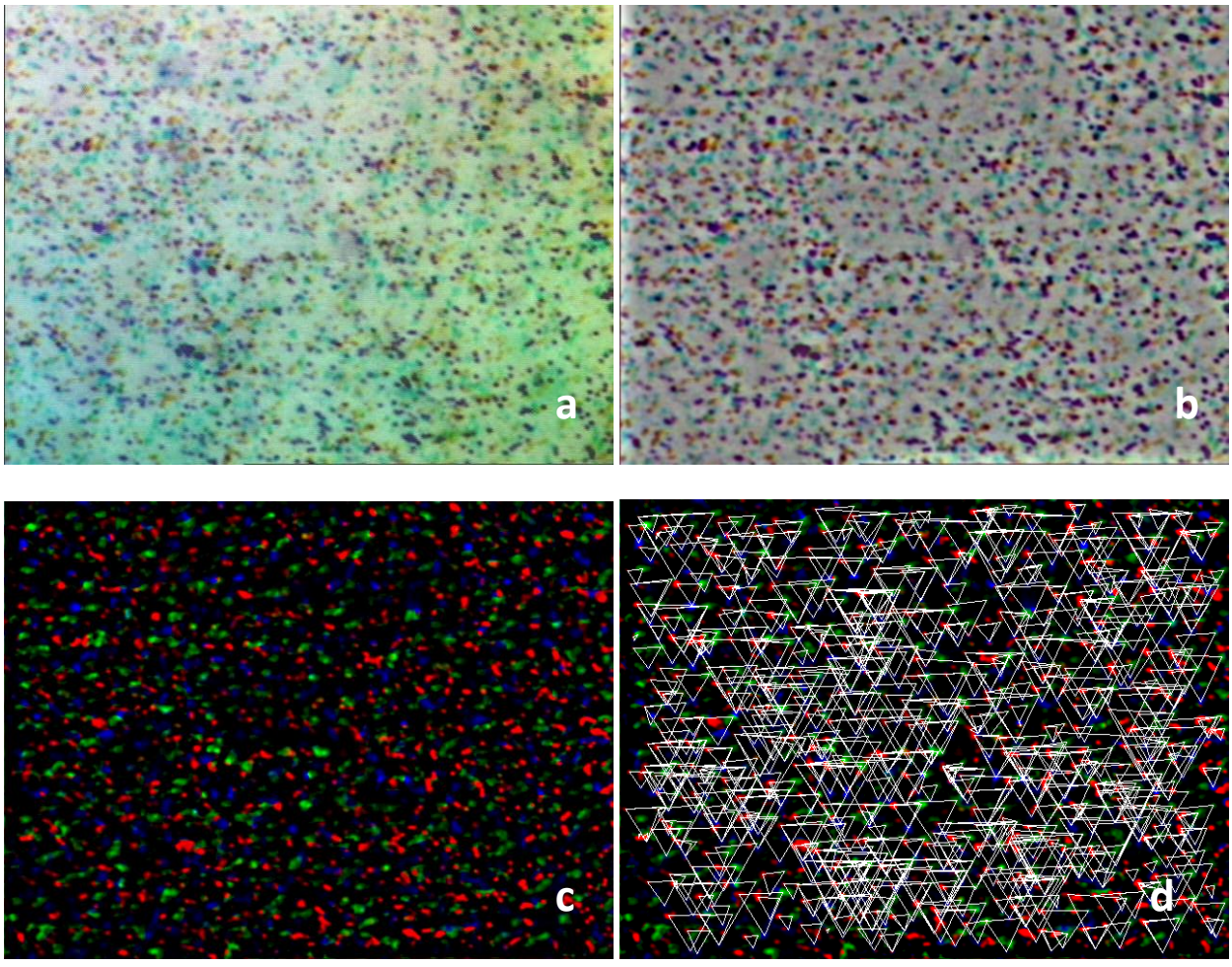

Figure 2-8 (a) Original image (b) pre-processed image (c) color separation (d) triplets found by DDPIV equations

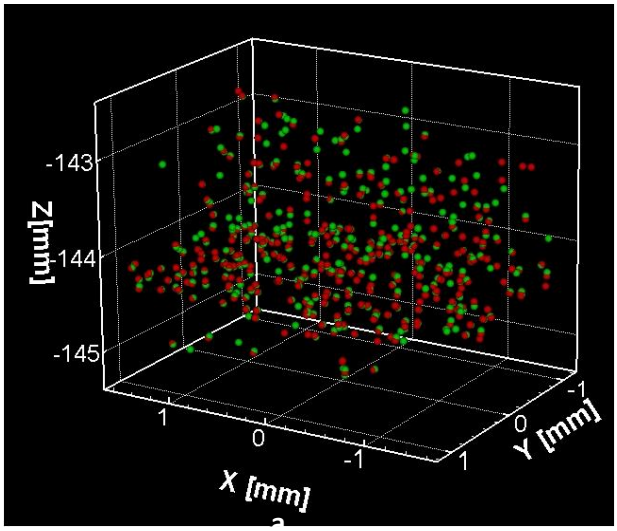

Figure 2-9 Particle pair image shown particles reconstructed in 3-D space. The particles found in the1st frame shows in red and 2nd frame in green.

2.1.5 **Color Coded 3-Pinhole System - Micro version**

With the success of the mini-scale system, the first attempt was to apply the method directly to a microscopic system. To achieve our purpose of imaging micro-scale fluid flow, it is found that several components of the mini system have to be modified again. The biggest change is to increase the modification of the optical system. In the mini system, a 105mm photographic lens for single lens reflex camera (SLR) is used with a bellow tube to increase the magnification to 2.69. In the current system, a microscope system is used and the minimum magnification is 10. The huge difference in magnification increases the aberration of the optics, especially the chromatic aberration. The chromatic aberration causes different wavelengths of light to have different focal lengths (Figure 2-10), and it affects the DDPIV system in several ways. Thus modifications are made to adapt the DDPIV system suitable for microscopic applications, and the name is also changed from DDPIV to 3-D μPTV system. These modifications are discussed in the following sections.

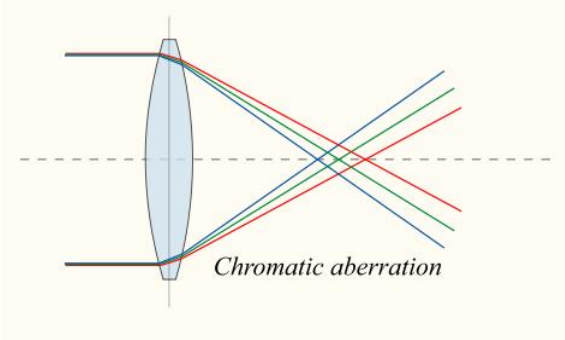

Figure 2-10 Chromatic aberration after a lens. The focus points of different wavelengths of light deviates due to dispersion of the lens.

2.2 Illumination Methods

2.2.1 Formation of Particle Images – Shadow / Scattering

The intensity profile of a particle under coherent illumination produced by a diffraction-limited imaging system can be best described by the Airy function (Adrian & Westerweel, 2011),

$$|h(r)|^2 = \left(\frac{\pi D_a^2}{4\lambda Z_0}\right)^2 \left[2\frac{J_1(\pi D_a r/\lambda Z_0)}{\pi D_a r/\lambda Z_0}\right],^2 \tag{2-1}$$

Where $h(r)$ is the intensity point spread function to the spot radius r, $J1(r)$ is the first-order Bessel function of the first kind, Z_0 is the object distance, D_a is the diameter of the aberration free lens aperture and λ is the wavelength of light. The first zero occurs for $r \approx 1.22\lambda Z_0/D_a$ is used to define the diffraction-limited spot diameter d_s, which is defined as the particle image diameter. The peak location represents where the particle is projected on the imaging plane, hence in PIV/PTV applications it is important to calculate the peak locations. To simplify the calculation, in practice the Airy function can be approximated by a Gaussian distribution (Adrian & Yao, 1985),

$$|h(s)| \cong (h(0))\exp(-4\beta^2 \frac{s}{d_s^2}^2), \tag{2-2}$$

where β^2 = 3.67 and the peak location is therefore easily calculated by fitting the Gaussian profile to the particle intensity profile (see Figure 2-11).

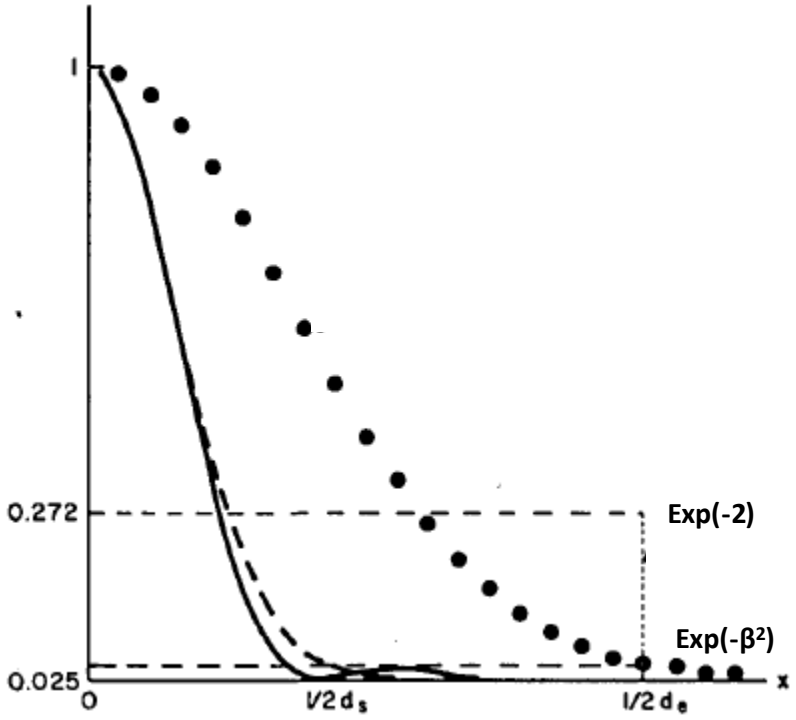

Figure 2-11 The point spread intensity function given by Airy function (continuous line), approximated by Gaussian function (dashed line) and example of a Gaussian image distribution (black solid circle). From Adrian and Yao (1985, Figure 2).

Instead of utilizing scattering approach to image the tracer particles, it is also possible to utilize geometrical imaging methods. Estevadeordal and Goss (2005) proposed a particle-shadow-velocimetry (PSV) technique that employs light sources with significantly lower power than lasers as a variant of PIV. In this case images that resemble a "negative" or "inverse"of the standard PIV scattering mode are produced by casting particle shadows on a bright background. Using an in-line zero degree forward scattering illumination setup, the particle shadow cast on a bright background is recorded. The particle shadow of a certain area given by the light-extinction characteristics (Bohren & Huffman, 1983) can be considerably greater or smaller than the

geometrical shadow of the particle. Adjusting the contrast yields particle-shadow-diameter variations and permits the diameter to be adjusted by varying the intensity of the incident light. A brighter light produces a smaller particle shadow images. The same method is applied to the mini-scale system and validates the feasibility (see section 2.1.4). In the shadow imaging method, the profile of the particle shadow image has not been determined and depends on the aforementioned light-particle interaction characteristics. However it is found that in practice with careful adjustment of the lighting, the profile can be approximate by the Gaussian shape curve after image intensity inversion. Hence it is possible to calculate the particle image location by fitting the Gaussian profile to the inversed intensity profile of the particle shadow image. The benefit of this imaging method is that the amount of light reaching the image plane and the contrast of the seeding particles are significantly increased while requiring significantly lower power than scattering approaches.

It is an interesting question to consider which imaging method should be used for the 3-D μPTV system. The particle shadow approach is attractive since the amount of light reaching the imaging plane is higher with significantly lower power required for the light source. However, because the resolution of the optical system is limited, as the particle size decreases the particle image/shadow image become more blurred. It affects both imaging methods, but the influences can be different. On the other hand, as particle density increases more light is occluded by the particles, resulting in a darker background and lower signal to noise ratio for the particle shadow imaging method. For the scattering imaging method, the particle image intensity increases with increasing density because more light from the neighboring particles will be scattered to the particle, making the spot image brighter.

To determine which imaging method is more suitable for the 3-D μPTV system, a comparison is made to test the signal strength of the particle shadow image and the diffraction limited particle image and the intensity plots are shown in Figure 2-12. 3 μm and 6 μm dots were imaged using both methods with 10X magnification for comparison. The signal strength is defined as the intensity difference between the image peaks to the averaged background noise level. It is found that the signal strength is about an order of magnitude difference for the same particle size (19 of the particle shadow image in Figure 2-12 (a) and 201 of the scattering image in Figure 2-12 (b). For the particle shadow imaging method, the results of the 6um dot (63 in Figure 2-12 (c) is about 3 times of the 3μm dots. This results show that for the tracer particle is under 3 μm the scattering method is a more appropriate choice. For typical micro-scale flow applications, 3 μm is the roughly the upper limit of the tracer particles can be used. For a larger scale application, 6 μm or larger particle can be used and the particle shadow imaging technique can be an option since the contrast is significantly improved and the advantage of low power requirement can be beneficial to the system.

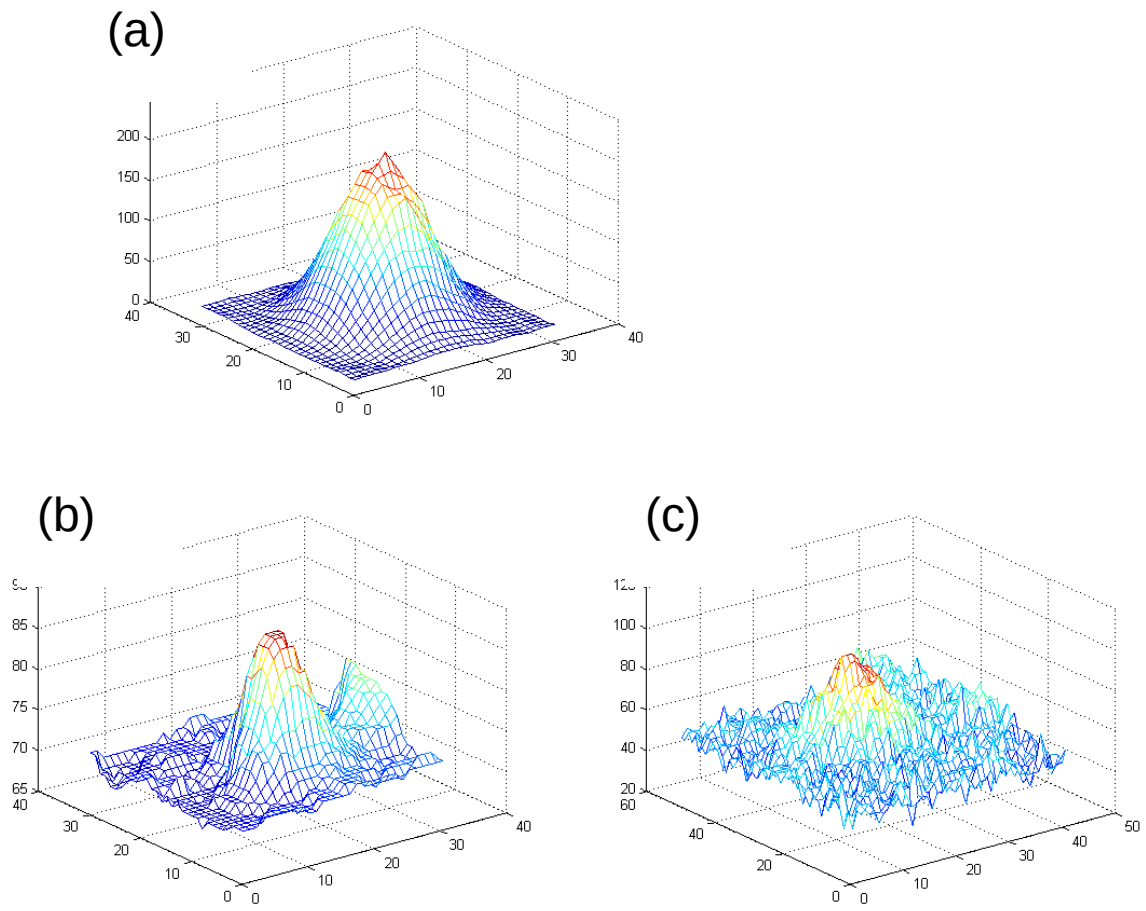

Figure 2-12 Intensity profiles of (a) 3 μm particles using scattering imaging method (b)3um particles using particle shadow imaging method (c)6um particles using particle shadow imaging method

2.2.2 **Illumination: Single / Multiple Light Source Approach**

In the mini-scale system discussed in section 2.1.4, illumination was provided by a single white light source in-line to the optical axis of the camera and lens. The purpose of this is to provide the maximum amount of light to be received by the image sensor. For the 3-D μPTV system, the magnification is increased from 2.69 to 10 and a microscopic objective lens is used to replace the SLR lens. Because of the high magnification and different lens design, the color aberration (shown in Figure 2-10) is more severe. The major effect of color aberration is that it shifts the peak locations of the particle images. A typical spectral response of the pinhole color

filters, shown in Figure 2-13, is not a narrow band-pass filter because it is desirable to collect as much light as possible from an incoherent light source. Therefore spectral response of white light signal passing through a filter is still an integral contains all wavelengths of light, just with weighting function that suppress wavelengths other than the dominant wavelength of the filter.

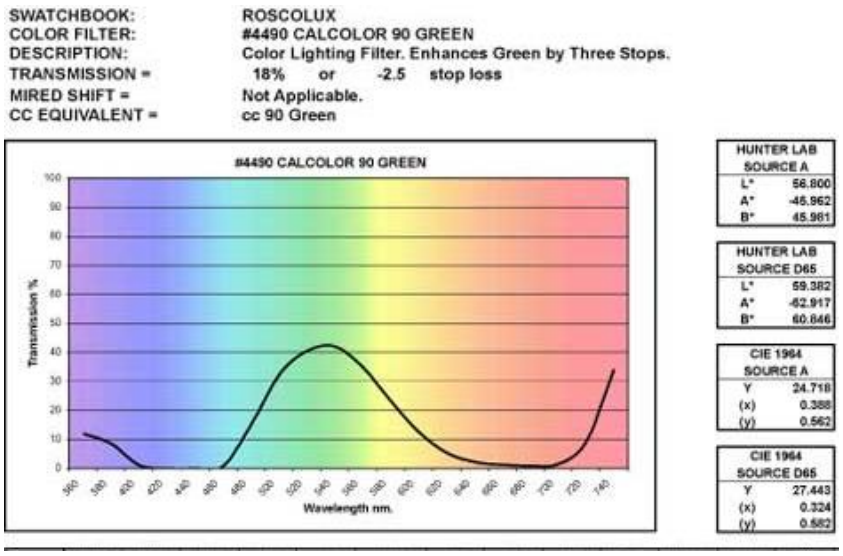

Figure 2-13 Typical spectral response of a color filter

The image formed by the light going through one pinhole is the convolution of the image formed by all wavelengths of light except those filtered out by the pinhole color filter. For a perfect optical system with no color aberration, the peak location is the same for all wavelengths of light because the focal length is the same for all wavelengths. Hence the peak calculated from the particle image profile based on the Gaussian shape assumption is accurate. However, with color aberration the peak locations for different wavelengths deviate from each other, as shown in Figure 2-14 (a). Thus the calculated peak location shifts from the true peak locations and contribute to the measurement error of the system (Figure 2-14 (b)). The amount of shift is a function of the particle physical location, therefore cannot be corrected without knowing the particle location first.

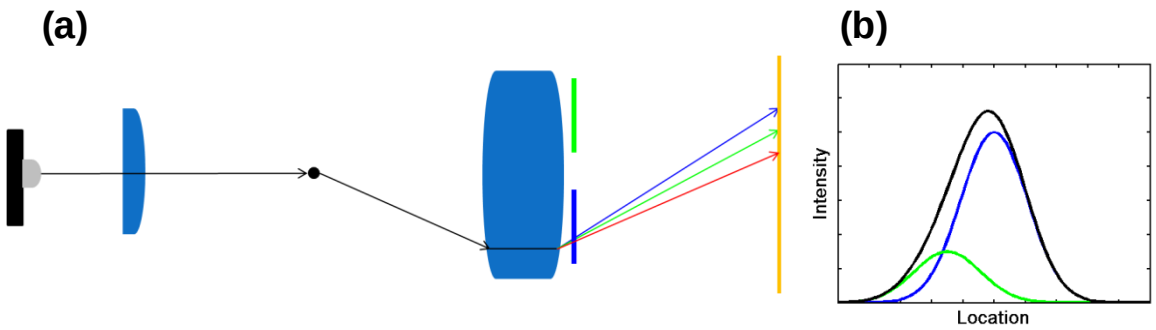

Figure 2-14 Particle image peak shifts due to color aberration: (a) color aberration due to white light illumination, (b) The skewed Gaussian distribution due to the peak shifts. Profile in black is the combination of green and blue Gaussian distributions with different intensity.

To resolve this issue without using the narrow-band filter and reduce the light intensity, a new configuration of lighting is used for the 3-D μPTV system. As show in Figure 2-15, each pinhole is now aligned with an individual light source with corresponding color to match the spectral response of the color filter on each pinhole. Because the light is from an inclined angle aligned with the corresponding pinhole, the scattering angle of the light to the other two pinholes are significantly away from the optimized scattering angle (≈ 0°). Therefore only the wavelength of light coming from the matched light source results in the particle image exposure for the corresponding pinhole, and the peak shift due to color aberration can be minimized.

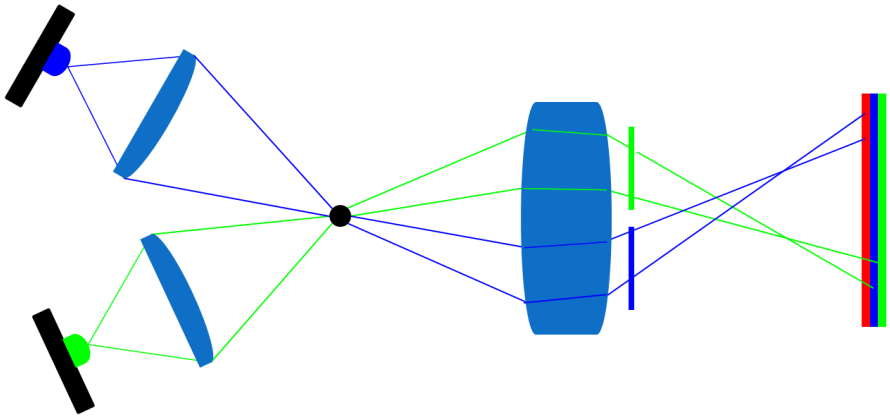

Figure 2-15 modified illumination configuration

2.3 Color Separation

2.3.1 Separation by HSV transform

Since a color camera is used to record the color-coded exposure images formed from all three pinholes, a method for separating the three colors is necessary before the peak finding procedure can proceed. In theory, this can be easily done if the spectrums of each of the red, green, and blue color filters perfectly match the spectrum of each of the red, green, and blue CCDs, respectively, since light emerging from each of the color filtered pinholes would expose only their respective CCDs. In reality, the spectrum of the color filters and the CCDs do not match, thereby causing multiple pinhole exposures on each of the CCDs shown in Figure 2-16 (a). In the mini-scale system discussed in section 2.1.4, a transformation algorithm defined by Pratt (1991) is therefore adopted to correct this problem.

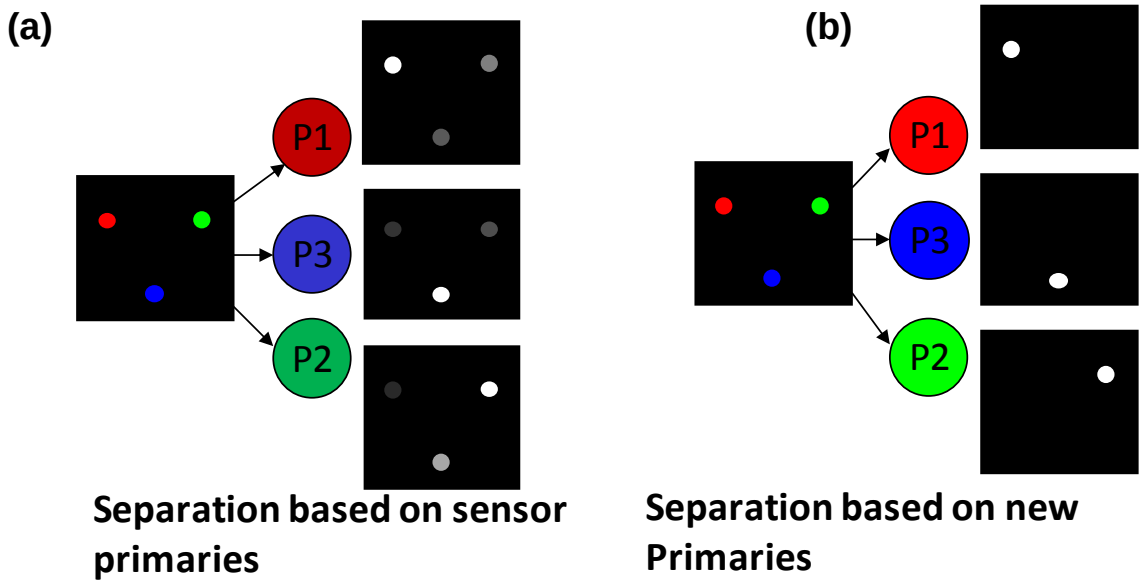

Figure 2-16 (a) multiple exposures caused by signal bleed-through on the sensor color channels (b) completely separate exposures on each new color channels created by color separation procedure

The main concept of the transformation algorithm is to transform colors defined within an original set of primaries, [P_1], [P_2], and [P_3], into another color space defined by a new set of primary colors [P_1'], [P_2'] and [P_3']. With this new set of primary colors, an arbitrary color, C, can be expressed by a new set of tristimulus values, $\boldsymbol{T'}(C)$, that are based on the new set of primaries,

$$\boldsymbol{T'}(C) = \begin{bmatrix} T_1'(C) \\ T_2'(C) \\ T_3'(C) \end{bmatrix}, \tag{2-3}$$

while the arbitrary color can also be expressed by the tristimulus values defined with the original primaries, $\boldsymbol{T}(C)$,

$$\boldsymbol{T}(C) = \begin{bmatrix} T_1(C) \\ T_2(C) \\ T_3(C) \end{bmatrix}. \tag{2-4}$$

Using the linear transformation of the primary colors' tristimulus values derived by Pratt (1991), the color matched by the original set of primaries (Red/Green/Blue or *RGB*), $\boldsymbol{T}(C)$, can be transformed into the new set of primaries (Cyan/Magenta/Yellow or *CMY*), $\boldsymbol{T'}(C)$, by the following equation:

$$\begin{bmatrix} T_1'(C) \\ T_2'(C) \\ T_3'(C) \end{bmatrix} = \begin{bmatrix} \begin{vmatrix} T_1(C) & T_1(P_2') & T_1(P_3') \\ T_2(C) & T_2(P_2') & T_2(P_3') \\ T_3(C) & T_3(P_2') & T_3(P_3') \end{vmatrix} / \begin{vmatrix} T_1(W) & T_1(P_2') & T_1(P_3') \\ T_2(W) & T_2(P_2') & T_2(P_3') \\ T_3(W) & T_3(P_2') & T_3(P_3') \end{vmatrix} \\ \begin{vmatrix} T_1(P_1') & T_1(C) & T_1(P_3') \\ T_2(P_1') & T_2(C) & T_2(P_3') \\ T_3(P_1') & T_3(C) & T_3(P_3') \end{vmatrix} / \begin{vmatrix} T_1(P_1') & T_1(W) & T_1(P_3') \\ T_2(P_1') & T_2(W) & T_2(P_3') \\ T_3(P_1') & T_3(W) & T_3(P_3') \end{vmatrix} \\ \begin{vmatrix} T_1(P_1') & T_1(P_2') & T_1(C) \\ T_2(P_1') & T_2(P_2') & T_2(C) \\ T_3(P_1') & T_3(P_2') & T_3(C) \end{vmatrix} / \begin{vmatrix} T_1(P_1') & T_1(P_2') & T_1(W) \\ T_2(P_1') & T_2(P_2') & T_2(W) \\ T_3(P_1') & T_3(P_2') & T_3(W) \end{vmatrix} \end{bmatrix}, \tag{2-5}$$

where *W* represents the reference white color.

To find the new set of primaries, a black dot patterned transparency is put within the defocusing region, thereby generating triplets with cyan, magenta, and yellow dots, and imaged with the modified DDPIV camera system. To identify cyan, magenta, and yellow in terms of the original *RGB* primaries, the background is separated from the particles by using its low saturation as a thresholding criterion. For the remaining pixels, the *RGB* color space is converted into *HSV* color space in Matlab. The HSV color space describes the color of a pixel by three components: hue (in degrees), saturation and value (brightness). The reason to do this transformation is that the hue value inside a particle region does not change, so it can be used to find the new set of primaries. Figure 2-17 shows a typical distribution of the hue after its conversion to degrees, where its *CMY* peaks, (185.23, 297.48, 50.52), are slightly different than the standard *CMY* values, (180, 300, 60). It should be noted that this slight difference necessitates this procedure and precludes the use of the standard *RGB*-to-*CMY* transformation. Once the *CMY* peaks are identified, they are re-transformed to the *RGB* domain, so that they can be used within equation (2-5) to identify colors defined by the new *CMY* primaries for all pixels within the image that do not have low saturation values.

Application of this procedure easily allows for splitting the three *CMY* channels, where each channel represents the intensity image from each pinhole. Figure 2-18 is a comparison of the original image containing a triplet of a defocused particle, its inversed intensity and the successfully separated pinhole images after the application of the color separation described above. The result of overlapped triplets from different defocused particles is shown in Figure 2-19. While its intensity clearly cannot provide useful information to identify each exposure, the color separation procedure clearly identifies overlapped particles.

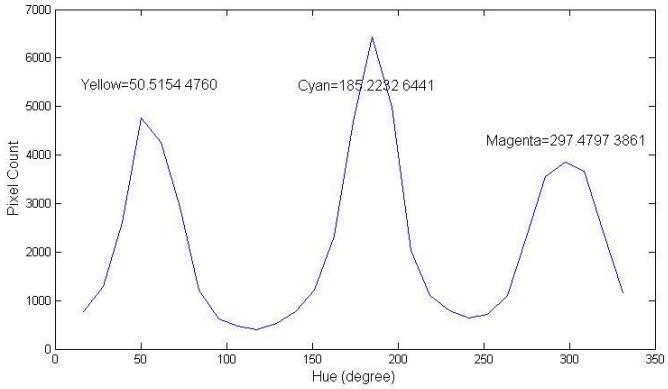

Figure 2-17 Typical color-filtered pinhole hue histogram of a DDPIV image.

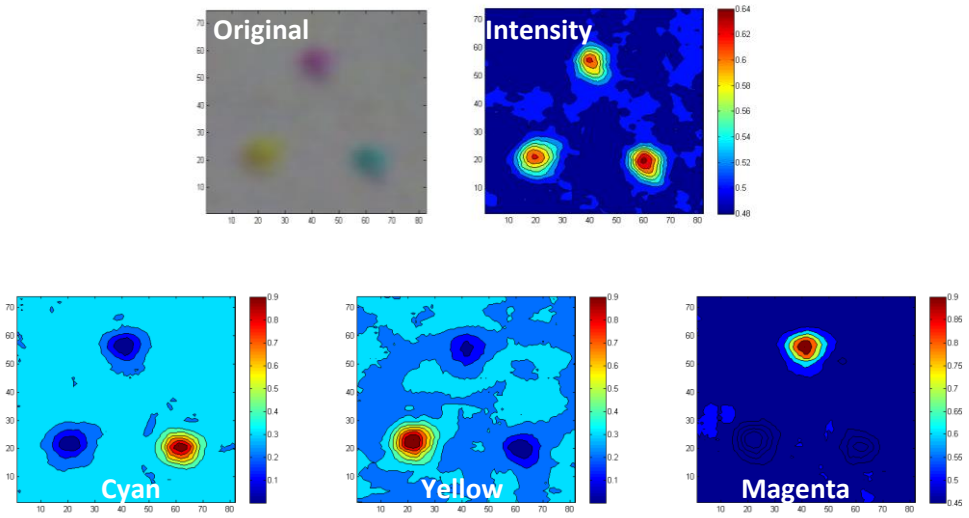

Figure 2-18 Identification and separation of particle exposures within a single triplet using the color separation algorithm.

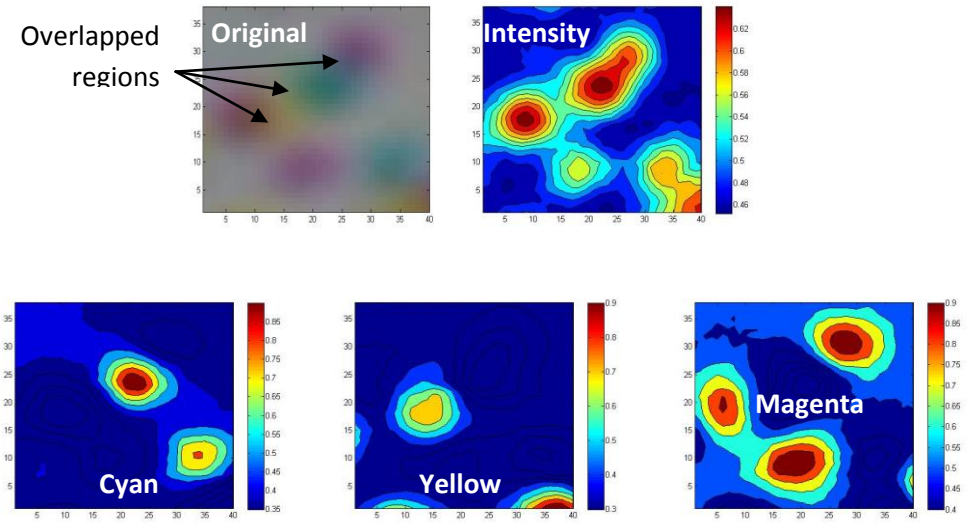

Figure 2-19 Identification and separation of particle exposures within overlapped triplets using the color separation algorithm.

2.3.2 **Generalized Separation by Principal Component Transformation**

With the use of the separated light source discussed in section 2.2.2, it seems that the color separation is no longer necessary since the wavelength of light for each pinhole is matched. However, it is found that due to the signal crosstalk between the color channels of the image sensor, multiple exposures still happens even a single wavelength light passing through a pinhole. As shown in Figure 2-20 (a), the typical spectral response of the color filters used in a CCD camera shows overlap region between color channels. Wavelength of light falls in these regions creates signal bleed-through to both color channels, thus causing multiple exposure images at the same location through each pinhole with the corresponding single color light source, as shown in Figure 2-20 (b). The effect is that at each of the color channel (the sensor primary color plane) multiple exposures are recorded (Figure 2-16 (a)). The purpose of the color separation is

therefore to transform the original color channels to new color channels with a new set of primary colors (Figure 2-16 (b)).

In the process it is found that the correlation between green and blue color is strong and individual peaks for green and blue in the HSV plane are harder to identify. Therefore the only separating the light source is not efficient to separate green and blue exposures. As a result, a new algorithm to separate the color is developed to resolve this issue.

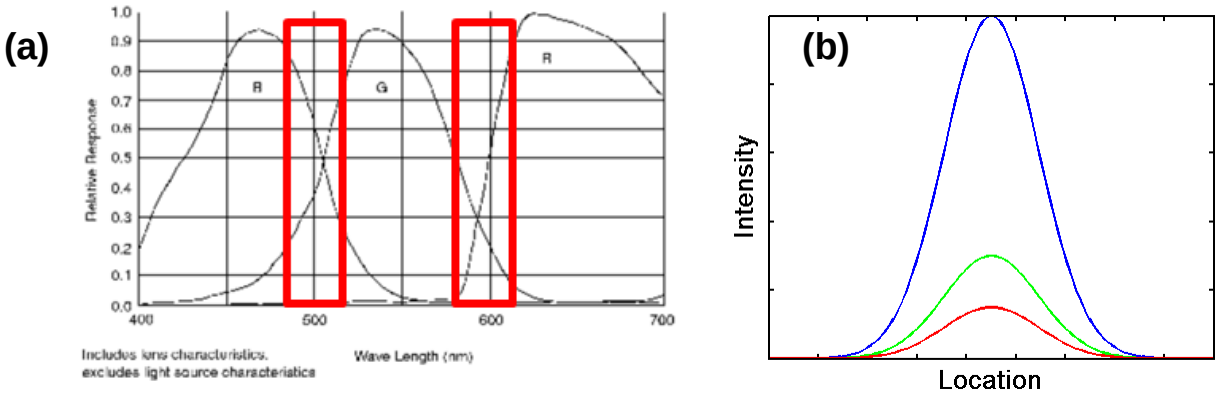

Figure 2-20 multiple exposures caused by signal bleed-through: (a) spectral response of a CCD sensor, (b) multiple exposures from the same wavelength of light to different color channels

Eliminating the crosstalk between color channels is equivalent to decorrelating the image data from the color channels. Using principal component transformation (Richards and Jia, 1999), the image data based on the correlated R, G and B primaries can be decorrelated to form a new image based on three independent new primaries. For each pixel of the image, the color can be expressed as

Equation 2-6

$$\mathbf{C}_{ij} = \begin{bmatrix} R_{ij} \\ G_{ij} \\ B_{ij} \end{bmatrix}, \tag{2-7}$$

where R, G, B are values in term of the original primaries. It can also be expressed as

$$\mathbf{C}_{ij}' = \begin{bmatrix} R_{ij}' \\ G_{ij}' \\ B_{ij}' \end{bmatrix} \tag{2-8}$$

where R'$_{ij}$, G'$_{ij}$ and B'$_{ij}$ are values in term of the new uncorrelated primaries. Thus $\mathbf{C}'_{ij}$ is related to $\mathbf{C}_{ij}$ by a transformation matrix $\mathbf{T}$

$$\mathbf{C}_{ij}' = \mathbf{T}\mathbf{C}_{ij} \tag{2-9}$$

The covariance of the pixel data $\Sigma_{\mathbf{C}'_{ij}}$ is defined as

$$\Sigma_{\mathbf{C}'} = \frac{1}{I \cdot J}\sum_{i=1}^{I}\sum_{j=1}^{J}(\mathbf{C}_{ij}' - \mathbf{m}_{C_{ij}'})(\mathbf{C}_{ij}' - \mathbf{m}_{C_{ij}'})^t = \varepsilon\left\{(\mathbf{C}_{ij}' - \mathbf{m}_{C_{ij}'})(\mathbf{C}_{ij}' - \mathbf{m}_{C_{ij}'})^t\right\} \tag{2-10}$$

where $\mathbf{m}_{\mathbf{C}_{ij}}$ is the mean vector of the image data in terms of the new primaries,

$$\mathbf{m}_{\mathbf{C}_{ij}} = \frac{1}{I \cdot J}\sum_{i=1}^{I}\sum_{j=1}^{J} C_{ij}\,. \tag{2-11}$$

Since

$$\mathbf{m}_{\mathbf{C}'_{ij}} = \varepsilon\left\{\mathbf{C}'_{ij}\right\} = \varepsilon\left\{\mathbf{T}\mathbf{C}_{ij}'\right\} = \mathbf{T}\varepsilon\left\{\mathbf{C}_{ij}\right\} = \mathbf{T}m_{\mathbf{C}_{ij}}\,. \tag{2-12}$$

Therefore

$$\sum\nolimits_{\mathbf{C}_{ij}'} = \varepsilon\left\{(\mathbf{C}_{ij}' - \mathbf{m}_{\mathbf{C}_{ij}'})(\mathbf{C}_{ij}' - \mathbf{m}_{\mathbf{C}_{ij}'})^t\right\} = \varepsilon\left\{(\mathbf{T}\mathbf{C}_{ij} - \mathbf{T}\mathbf{m}\mathbf{C}_{ij})(\mathbf{T}\mathbf{C}_{ij} - \mathbf{T}\mathbf{m}\mathbf{C}_{ij})^t\right\}$$
$$= \mathbf{T}\varepsilon\left\{(\mathbf{C}_{ij} - \mathbf{m}\mathbf{C}_{ij})(\mathbf{C}_{ij} - \mathbf{m}\mathbf{C}_{ij})^t\right\}\mathbf{T}^t$$

i. e.

$$\sum\nolimits_{\mathbf{C}_{ij}'} = \mathbf{T}\sum\nolimits_{\mathbf{C}_{ij}}\mathbf{T}^t \tag{2-13}$$

Since the new primaries are uncorrelated, $\Sigma_{\mathbf{C}'_{ij}}$ is diagonal. Thus **T** is the transposed matrix of eigenvectors and **T** is an orthogonal matrix. Elements in $\Sigma_{\mathbf{C}'_{ij}}$ is the eigenvalues of $\Sigma_{\mathbf{C}_{ij}}$.

The advantage of this method, compared to the HSV transform method described in 2.3.1, is that no parameter is required throughout the process, and the results are more robust to the variations of lighting. Figure 2-21 shows the result of color separation using the proposed algorithm. In the circled region, two green particles can be seen from both the green and blue channels before color separation, but after the color separation only the new green channel keeps the two particle images.

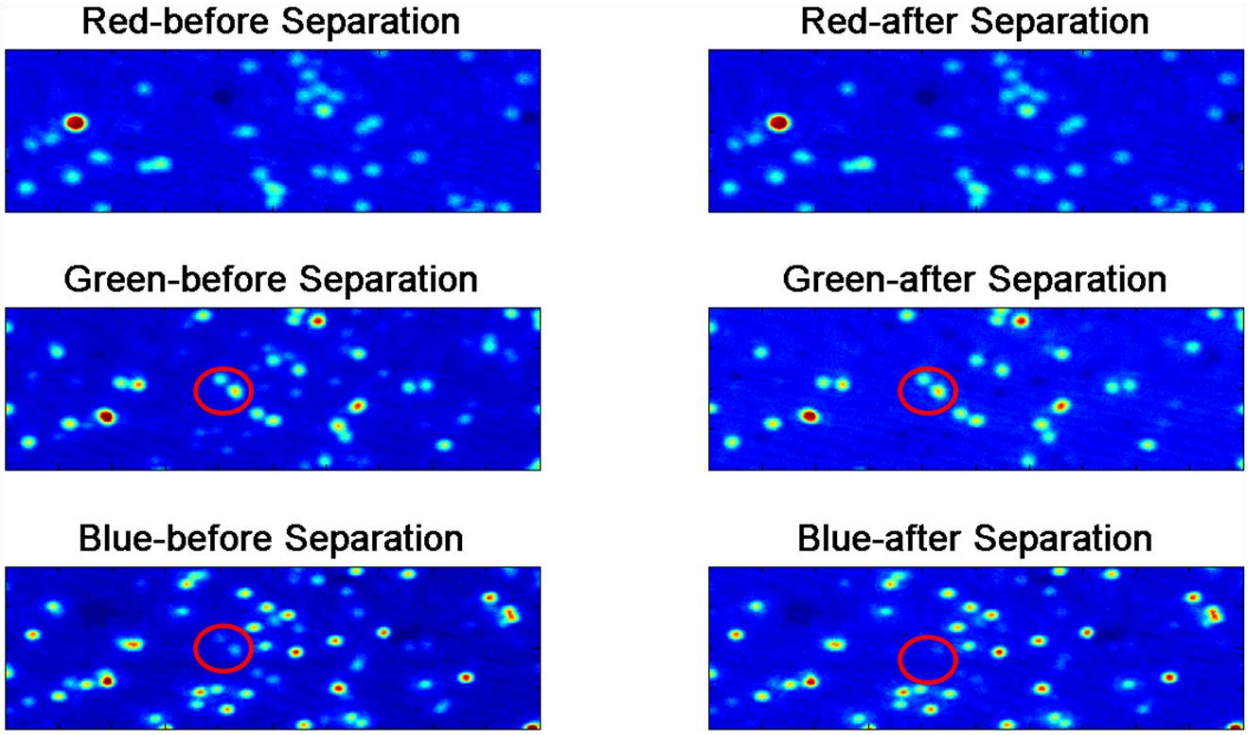

Figure 2-21 Results of color separation algorithm

2.4 **Particle Identification**

Once the exposure images are separated, the next step is to identify the locations of each exposure so that they can be used for later process to calculate the exact particle locations in space. The main challenge of the particle identification of the the 3-D μPTV system is to identify individual peak locations from overlapped particle images. This is because the high magnification of the microscope optics with the pinhole configuration also changed the particle image size significantly. The aberration-free particle image diameter d_τ can be approximated by (Adrian & Westerweel, 2011)

$$d_\tau = c\left(M^2 d_p^2 + d_s^2\right)^{1/2}, \tag{2-14}$$

where

$$d_s = 2.44(1+M^2)\, f^{\#}\lambda \tag{2-15}$$

is the diffraction limited spot diameter, $f^{\#}$ the f-number of the lens, D_a the diameter of the pinhole aperture, λ the wavelength of light, d_p the diameter of the actual particle size, and c is a constant. c =1 if d_τ is defined as half of the diffraction limited spot diameter d_s, and c=0.74 if d_τ is defined as the e^{-2} diameter of the particle image intensity distribution. It is worth noting that the f-number of an infinity-corrected optical system is given by Meinhart and Wereley (2003)

$$f_\infty^{\#} = \frac{1}{2}\left[\left(\frac{n_0}{NA}\right)^2 - 1\right]^{1/2}, \tag{2-16}$$

since the current microscope configuration is infinity-corrected, where n_0 is the refraction index of the immersion medium between the object and the objective, and NA is the numerical aperture defined by $NA=n_0 sin\Theta$, Θ is the half-angle of the cone of light collected by the pinhole. Due to the high magnification (M>10) and small NA because of the small pinhole diameter, d_τ is

dominated by d_s. A typical particle image size from a 3-D μPTV image is around 25 pixels, since we are imaging a depth that extends beyond the focal plane; this is much larger than the 2-4 pixel diameter usually encountered in traditional 2-D PIV/PTV applications. As a result, the chance of a particle image overlap with another one increases drastically. Severe particle overlap would cause location errors of the peak and are critical to velocity measurement error. To identify the particle image peak location more accurately, a particle identification algorithm, modified CCM Algorithm, from the previous work (Lei *et al*., 2012) is used to improve the ability to identify overlap particle images. For completeness of the work, the detail of this algorithm is presented in the following sections.

2.4.1 **Peak Finding by Least Square Estimation**

There are two major categories of peak finding methods for PIV/PTV applications: centroid estimation and least squares estimation (Adrian & Westerweel, 2011). Centroid estimation is nonparametric and can be implemented with fast algorithms. However its accuracy is sensitive to intensity saturation and image noise and it is subject to peak locking effects for particles with small diameters. Compared to centroid estimation, least squares estimation is more accurate and has less peak locking effect (1991) and thus widely used in PIV/PTV applications.

The general assumption for most least squares type peak-finding algorithms is that each particle results in one peak of a particle image and the intensity distribution can be approximated by a 2-D Gaussian function (Adrian and Yao, 1985). Then a parameter set that can be estimated by minimizing the sum of squared difference χ^2 between the recorded image intensities and suitable model with respect to the parameter set. For faster implementation a three point or four point Gaussian fit schemes can be used without the least squares estimation.

As pointed out by Ponchaut (2005) this assumption no longer holds when the particles overlap severely. Marxen *et al.* (2000) performed simulations of overlapping particles with least-square surface fits and 3-point line fits based on this assumption and the results showed a steep rise in the errors when the particle separation distance approaches the particle diameter. The summation of multiple particle images can result in fewer peaks, where these peaks deviate from the particles' true locations. Figure 2-22 shows an example of two severely overlapped particle images and their intensity profile. Even if the peak number is the same as the particle number, the Gaussian fit based on the single particle assumption could lead to greater location errors since the overlap region will add bias error to the peak location towards the nearby particle.

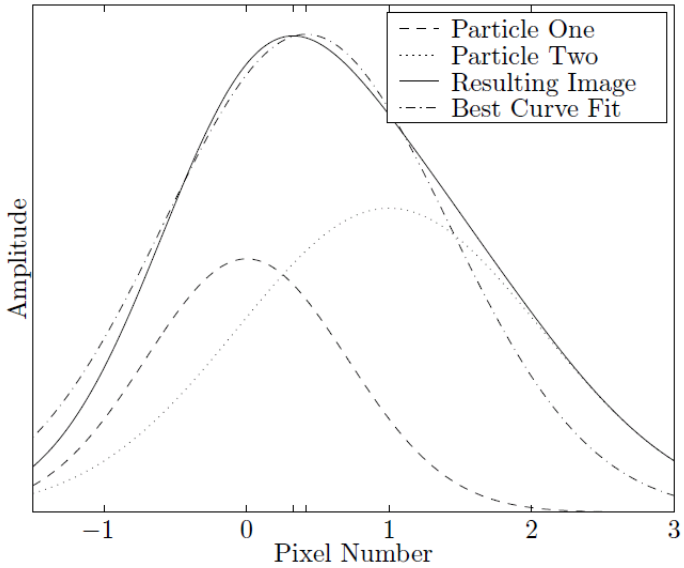

Figure 2-22 Severely overlapped two Particles image

2.4.2 **PMCM algorithm**

Since the particle image profile is approximated by a Gaussian profile, it is possible to use a model particle image as a template for pattern matching. Takehara and Etoh (1999)

proposed a method with using the concept. The Particle Mask Correlation Method (PMCM) calculates the cross-correlation coefficient of the between the model particle mask image and a certain interrogation area of the particle image plane. The particle image area can then be found from the correlation image with a threshold value. The particle size and peak location is then calculate with the centroid method.

There are several advantages of this method. First, the peak brightness of a particle image is replaced by a cross-correlation coefficient which is normalized between -1 to 1. Therefore the method is robust to brightness change, which is often encountered in 3-D applications because of the depth of field and volumetric imaging. Second, the unwanted solid boundaries or edges in the raw image are automatically eliminated because they have low correlation coefficient. The third advantage is that it can resolve two overlapping particles up to a minimum critical separation distance, thus providing a way to estimate the presence of nearby particles. However this critical distance is still not enough to resolve the overlapping particle images that have merged intensity peaks, and it increases even more when the intensity differences between particles increase. This is because the particle location is still determined by the centroid estimation and the particle mask is only used to identify the particle image area. Therefore this method still share the same issue with the centroid estimation, which less accurate and sensitive to peak-locking effect.

2.4.3 **CCM algorithm**

Although the PMCM method is not able to resolve the overlapping particle images, it certainly provides a direction to the solution. Angarita-Jaimes *et al.* (2009) proposed a modified approach called the Cascade Correlation Method (CCM) that instead of applying the cross-correlation once with the particle mask image, a cascade of cross-correlation operations is applied to make the correlation peak narrower, thus decreasing the critical distance. The

correlation peak location is found by a simple three-point Gaussian fit method instead of centroid estimation. Their simulation data shows a significant improvement when compared with the PMCM algorithm, reducing the critical distance to below Rayleigh's resolution limit $\Delta l \approx 2.44\lambda \cdot f^{\#}$. The CCM algorithm provides an efficient way to separate overlapping particles, and is easy to implement. It is also robust to intensity variations so that even two particle images with large intensity difference can be resolved by this method. However, the peak locations found from the correlation image plane may suffer additional errors. The peaks in the correlation image, for example, can be distorted due to noise, and the subpixel peak-fitting algorithms may introduce bias errors towards integer values due to discretization of the particle images. A well-known example is the peak-locking error encountered in typical PIV applications (Nogueira *et al.*, 2001; Liao & Cowen, 2005).

2.4.4 **Resolve Overlapped Particles by Surface fitting**

The least squares estimation is not limited by the single particle assumption discussed in section 2.4.1. In theory it is possible to use the least squares method to solve for overlapping particle problem. However with the number of particles in the area of interest unknown, the solution is not unique. Hence it is the key to estimate the number of particles in the area of interest so that the surface fitting can be applied. Ponchaut (2005) proposed a peak search scheme that can resolve the overlapping particle problem using the surface Gaussian fit. In their method, the raw image is first split into smaller blobs that contain unknown number of particles. In each blob, the algorithm starts with an initial guess of particle number N_b equal to the number of local maximum in the blob. The fitting procedure proceeds with an increment of one for N_b if the error is larger than a threshold. This method provides a way to use the surface fitting method

to resolve the overlapping particle problem. The key issue still remains since this method does not attempt to estimate the number of peaks in the blob.

2.4.5 **Modified CCM algorithm**

From the previous sections, the two methods trying to resolve the overlapping particle problem both have their advantages and disadvantages. The interesting question is whether these two approach can be combined together to provide a better solution. An improved algorithm based on the two approaches is therefore proposed to try to answer this question.

Each PTV image can be considered as a summation of an unknown number *N* of particle images, each having a different location, intensity and radius assuming a Gaussian shape distribution, plus the noise signal mainly due to thermal noise of the CCD sensor. Thus the intensity *I(j, k)* at pixel *(j, k)* is

$$\boldsymbol{I(j,k)} = \sum_{\boldsymbol{i=1}}^{\boldsymbol{N}} (\boldsymbol{I_0})_{\boldsymbol{i}} \cdot \boldsymbol{e}^{-\frac{\boldsymbol{X_i(j,k)^2}}{\boldsymbol{2{r_i}^2}}}, \tag{2-17}$$

where $(I_0)_i$ is the peak intensity of the i^{th} particle image, X_i(j,k) is the distance from the pixel to the particle center (x_{ci}, y_{ci}), and r_i is the representative radius of the particle image. The particle identification process finds a solution

$$\boldsymbol{I'(j,k)} = \sum_{\boldsymbol{i=1}}^{\boldsymbol{N}} (\boldsymbol{I_0'})_{\boldsymbol{i}} \cdot \boldsymbol{e}^{-\frac{\boldsymbol{X'_i(j,k)^2}}{\boldsymbol{2{r_i'}^2}}}, \tag{2-18}$$

so that the difference between *I(j, k)* and *I'(j, k)* for all pixels in the image is minimized in a least square sense. Note that the number of particles, *N*, in traditional particle identification algorithms is assumed to be equal to the number of peaks in the image, and *I(j, k)* is independent for each

particle *i* under the assumption that the particle image density is sufficiently low. Thus for each particle *i*, the equation can be reduced to

$$\boldsymbol{I_i(j,k) = I_i e^{-\frac{X'_i(j,k)^2}{2r_i'^2}}} \tag{2-19}$$

in order to make the 3-point or 5-point Gaussian fit work. Therefore with overlapping particles, the key is to estimate *N* as accurately as possible. Since the CCM algorithm provides a way to separate the overlapping particle peaks, *N* can be estimated by counting the number of peaks in the last cross-correlation image from the CCM algorithm. The CCM algorithm first calculates the cross-correlation image R_1 between the original particle image *I* and the model particle mask image I_M,

$$\boldsymbol{R_1(u,v)} = \frac{\sum_{i=u-m/2}^{u+m/2}\sum_{j=v-n/2}^{v+n/2}(\boldsymbol{I(i,j)-\bar{I}})(\boldsymbol{I_M(i,j)-\overline{I_M}})}{\sqrt{\sum_{i=u-m/2}^{u+m/2}\sum_{j=v-n/2}^{v+n/2}(\boldsymbol{I(i,j)-\bar{I}})^2}\sqrt{\sum_{i=u-m/2}^{u+m/2}\sum_{j=v-n/2}^{v+n/2}(\boldsymbol{\overline{I_M}(i,j)-\overline{I_M}})^2}}, \tag{2-20}$$

where the model particle mask image is defined as an intensity image of size $m \times n$ containing a particle image with a Gaussian shaped intensity profile which follows equation (2-19). The operation is then repeated to generate a cascade correlation image R_2 by replacing *I* in equation (2-19) with correlation image R_1 and reducing the particle mask image radius *r* by 1 pixel. In the original CCM algorithm, the peak locations in the R_2 plane are used to indicate the particle locations. In the present method the number of peaks, *N*, is counted instead. With the *N* in equation (2-17) known, the least-square fitting can be performed to find the best estimate of the particle locations in the original image.

In practice, the computational cost of this method for a typical PTV image containing thousands of particles is high. The intensity of each particle considered only extends to ±4 r_i due to the e^{-2} intensity level drop of the Gaussian curve. This indicates that the image can be broken into small sections to reduce the computational cost without sacrificing accuracy. The raw image is broken down into small blob images, each containing an unknown number of particles. A blob is defined as a set of connected pixels. As an example, in **Error! Not a valid bookmark self-reference.** the binary image contains three blobs. The blob identification process starts here with Otsu's method (Otsu, 1979), which segments the foreground (blobs) and background image (noise) by finding the threshold to minimize the variance between the two classes of pixels. The connected foreground pixels are then sorted into blobs. Each of the blobs is then considered as an independent image containing an unknown number of particles described by equation (2-17). The number of particles in each blob is then determined by the improved CCM algorithm described in the paragraph below.

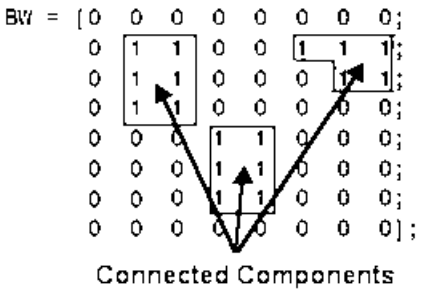

Figure 2-23 Example of connected pixels forming blobs in a binary image.

Expanding the original idea of the CCM method, the cross-correlation operation in equation (2-20) is now performed *k* times, with a gradually decreasing particle mask size. Each time a cross-correlation is performed, the model particle mask image radius (the representative radius *r*) shrinks by 1 pixel until it reaches a user determined minimum radius. The choice of the radius is usually the lower limit of the particle image radius observed in the experiment. This modification

has two purposes; one is to reduce the critical separation distance between particles even further since the correlation is narrower. The other goal is to increase the ability to detect a wider range of particles, since the results from Takehara and Etoh (1999) show that the correlation coefficients drop much more quickly when the particle size is smaller. Thus a sweep of radius from large to small provides more chances to detect the heavily overlapped small particles. The number of peaks N is calculated by counting the local maxima in the last correlation plane R_k which are greater than a threshold value. Once the number of particles N is estimated, a nonlinear least-square fit is performed by minimizing χ^2:

$$\chi^2 = \sum_{j=1,j=1}^{j=m,k=n} \left[I(j,k) - \sum_{\mathrm{i}=1}^{\mathrm{N}} (\mathrm{I}_0)_{\mathrm{i}} \cdot e^{-\frac{X_i(\mathrm{j,k})^2}{2{r_i}'^2}} \right]^2 . \tag{2-21}$$

By solving the least square fit problem, the location (x_i, y_i), intensity $(I_0)_i$ and radius r_i of each of the particles in the blob can be found. This process is repeated for all the blobs and the final result is the summation of all the blob results. The block diagram for the whole procedure is shown in Figure 2-24.

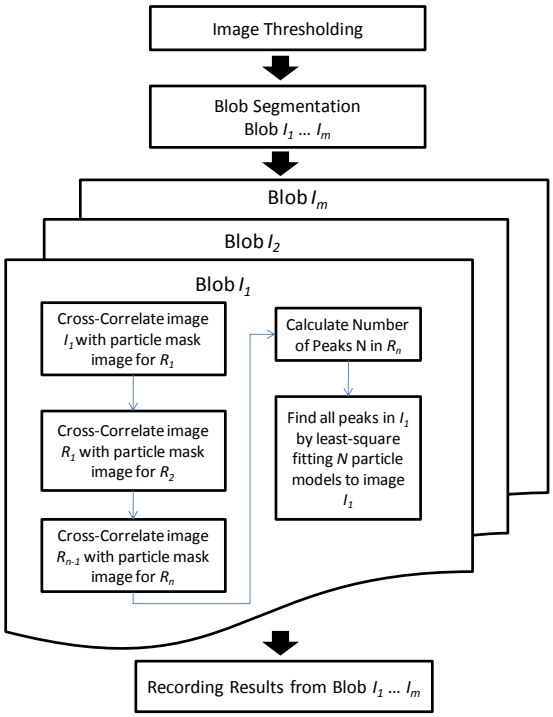

Figure 2-24 Process flow of the proposed particle identification algorithm

To verify the performance and robustness of the new method, simulation tests are carried out on images of two identical overlapped particles, which are together varied in size, normalized separation distance, and noise types. Each of the simulated particle images is generated using the Gaussian intensity profile defined by equation (2-19), with fixed I, x_c, y_c and r. The simulated particle diameter, D, varies from 4 pixels to 20 pixels, is defined as the e^{-2} intensity level of the Gaussian. D is equal to $4r_P$, which is the representative radius of the particle image. The particle overlap ratio is defined as $(D-L)/D$, where L is the separation distance between the overlapped particles and D is the particle diameter. The particle overlap ratio in the present tests varies from -150% to 50%. The pixel intensities are then the sum of the two particle images discretized by sampling the Gaussian intensity profile. Two types of noise are tested: the Poisson noise and Gaussian noise. The Poisson noise is used to simulate photon noise, which is the dominant noise source of fluorescence microscopy encountered in micro-PIV applications. The noise of each

pixel follows a Poisson distribution with a mean that is equal to the intensity value *I (i, j)* of the pixel *(i, j)*. Since the noise increases as $\sqrt{I(i,j)}$, the signal to noise ratio (SNR) can be calculated as $SNR = I_c/\sqrt{I_c} = \sqrt{I_c}$, where I_c is the intensity value at the particle image center. The Poisson noise is added so that the signal-to-noise ratio varies from 10 to 25. The Gaussian noise is used to simulate the thermal noise of an image sensor, which is a major noise source in general PIV applications. The Gaussian noise tested in this study is added with a standard deviation of 2.5% and 5% of the dynamic range of the model sensor, which is set to 8 bits (0-255). The test for each case is repeated 1000 times and the averaged results are reported.

Figure 2-25 shows the relationship between the separation distances of two identical particles at different noise levels, processed by the proposed method with D=20 (r_P=5). Figure 2-25 (a) shows the results of the Poisson noise level variation from no noise (SNR=infinity) to SNR=10, and these results are compared to the results of the original CCM algorithm (Angarita-Jaimes *et al.*, 2009). All the averaged errors of the current method are below 0.2 pixels, with an increasing trend when the overlap ratio increases beyond 0%. Compared with the original CCM algorithm, the error increases to 0.154 pixels when the particle overlap ratio reaches 50% for the case of SNR=10, whereas the original CCM method's error increases beyond 0.5 pixels. Figure 2-25 (b) shows the results of different Gaussian noise level. They show similar trends as the Poisson noise tests. For a 50% particle overlap ratio, the errors are within 0.25 pixels, and errors are within 0.09 pixels for all overlap ratios under 40%.

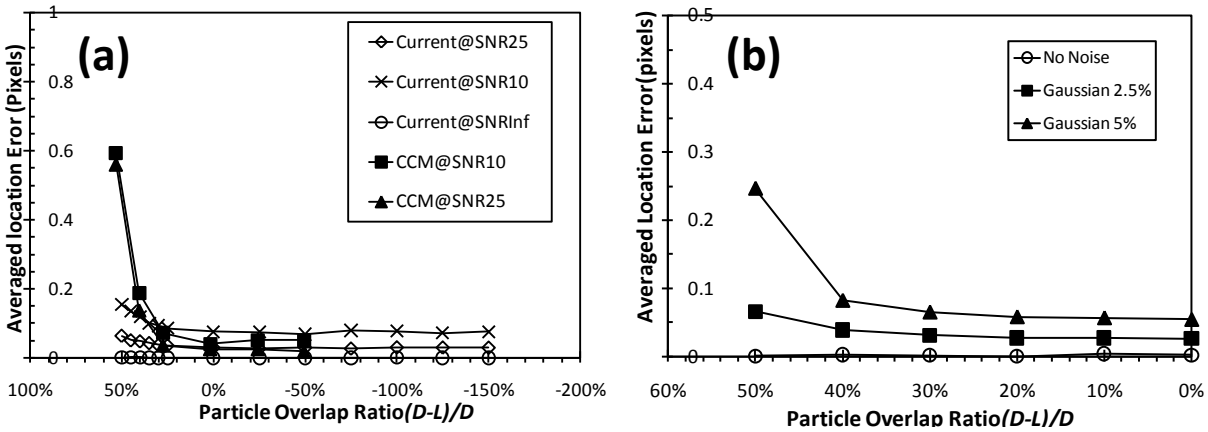

Figure 2-25 Averaged particle location error versus particle overlap ratio between two particles for (a) different Poisson noise levels (b) different Gaussian noise levels

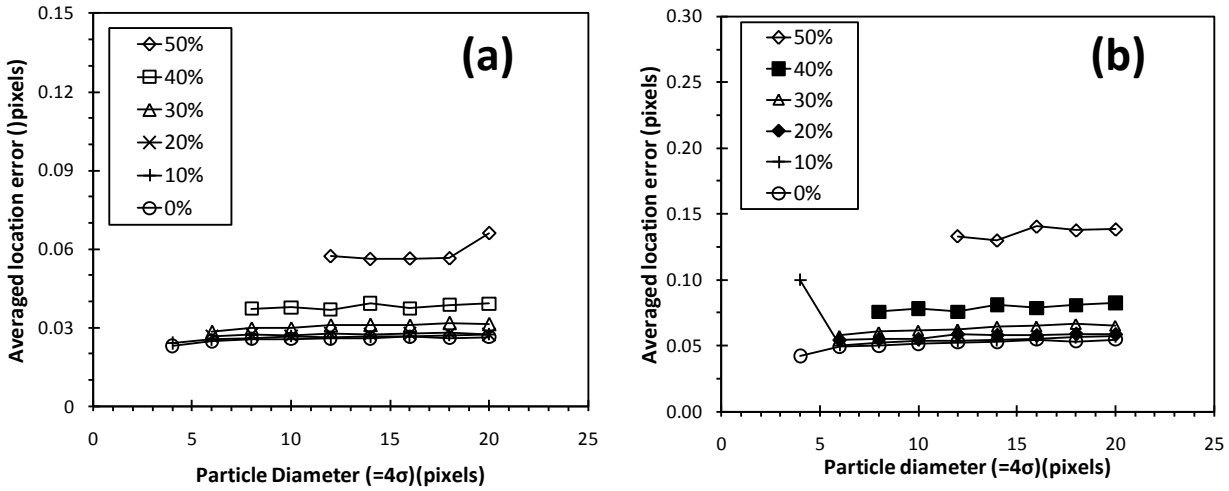

Figure 2-26 Averaged particle location error versus particle diameter for different overlap ratios (a) 2.5% Gaussian noise (b) 5% Gaussian noise

Figure 2-26 shows the effects of particle size and Gaussian noise level on the particle location errors. The particle sizes vary from D=4 to D=20, and different particle overlap ratios varying from 0% to 50% are shown in different curves. In Figure 2-26 (a) the Gaussian noise level is 2.5%, and at high overlap ratios the current algorithm fails to resolve the overlapping particles when D<10, thus causing the loss of data points at each curve. As particle size increases, the maximum resolvable overlap ratio increases up to 50%. This result is expected, since the

CCM method requires enough particle image spatial resolution to form the individual correlation peaks. In Figure 2-26 (b) the noise level is 5%. For larger particle sizes (D>6), the proposed method is able to separate the overlapping particles with pixel errors below 0.1 for overlap ratios of up to 40%. For 50% overlap, the resolvable particle size range is the same, and the errors go up to 0.15 pixels due to the increase of noise level. For small particles, the error comes from the background pixels. Since the particle size is smaller, more pixels containing only noise contribute to the total error of the least-square fitting.

In practice, the size of seeding particles varies if polydisperse particles are used. Even if the seeding particles are uniform in size, the particle image diameters can still vary due to the out-of-focus effect of the optical system. Figure 2-27 shows the performance of the proposed method with two particles of different sizes overlapping at different Gaussian noise levels. The sizes of two particles are controlled by the particle diameter ratio, *DiaR*. In this test, the smaller particle is fixed to 4 pixels in diameter, while *DiaR* varies from 1 to 5. The particle diameter, *D*, used here is the average of the two particles. The detectable overlap ratio limit rises to 60% when *DiaR* is 4 or 5. This is due to the fact that the proposed method separates overlap particles better with larger particle diameter ratios. For *DiaR* smaller than 4 at 60% overlap, the algorithm cannot resolve the overlap, thus no data points are shown. The errors are under 0.1 pixels with overlap ratios of up to 60%, and for overlap ratios under 50% the errors are lower than 0.07 pixels. The error increases slightly for larger overlap ratios but insensitive to *DiaR* changes. It is clear that the error increases as the Gaussian noise level increases, and the algorithm begins to fail to resolve both particles at all overlap ratios above 50% at a 5% Gaussian noise level. The error for *DiaR* equals to 4 at 60% overlap is slightly larger than *DiaR* equals to 5. This is again

due to the fact the distance between the peaks for the smaller particle is actually larger for the same overlap ratio as the *DiaR* increases.

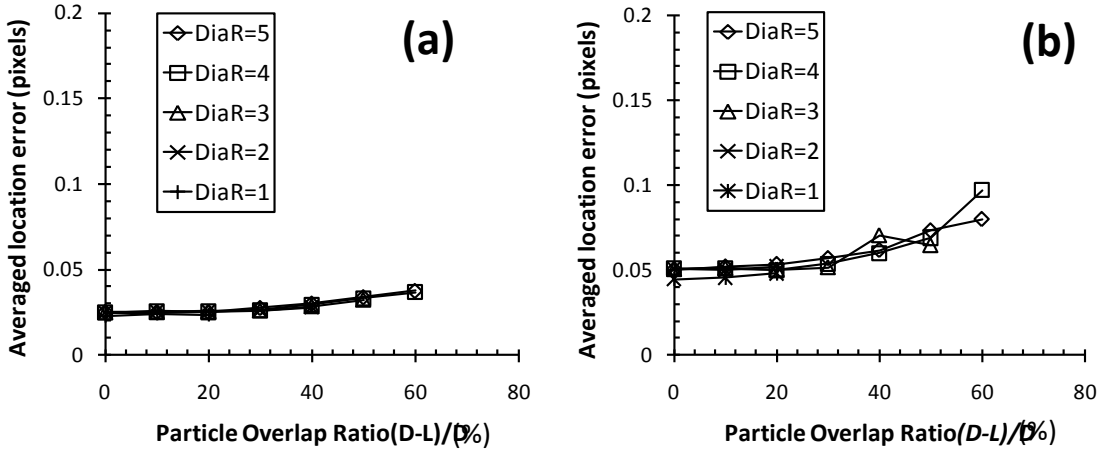

Figure 2-27 Averaged particle location error with various particle diameter ratios and noise levels: (a) 2.5% Gaussian noise versus particle overlap ratio (b) 5% Gaussian noise versus particle overlap ratio

2.5 **Reconstruct Particle Location**

Using the color separation method introduced in section 2.3.2, the color separation procedure has separated the exposure images formed by each pinhole into three individual images. The particle peak locations at each color plane can then be determined using the modified CCM algorithms discussed in the previous section. With these results, the actual particle location in space can be reconstructed. The procedure contains two stages: Triplet Finding and Locating Particles. In this section these procedures to reconstruct the particle location are discussed.

2.5.1 **Limitation of DDPIV Approach**

For the original DDPIV system, the optics is approximated by a pinhole model, the three pinholes are aligned to an equilateral triangle pattern and all the imaging sensors are co-planar. These arrangements simplify the equations and the matching algorithms (F. Pereira & Gharib, 2002). However, because of the high magnification of the optics and the larger depth of field due to the pinholes, the accuracy of simple pinhole model is not enough for the micro-scale system in the current study. Moreover, the chromatic aberration also causes the equilateral triangle pattern seriously skewed and the pattern deforms with depth locations. Figure 2-28 shows the skewed triangle pattern of the exposures from a dot pattern target imaging by the 3-D μPTV system. With this degree of distorted pattern, the simplified equations derived for the DDPIV systems are no longer applicable. The reason is shown in Figure 2-29. To make the DDPIV equation work, the triplet exposure images projected from particles at the same *X* and *Y* but different *Z* locations have to be approximate by equilateral triangles. The centroids of these triangle patterns are assumed to overlap to a point *G*, which is the projection point when the particle Z location is at focal plane, as shown on the left side of the figure. In 3-D μPTV system, the actual triplet image formed is shown as the right side of the figure. The triangular patterns are not only non-equilateral but also do not share the same centroid. As a result, the X and Y coordinates cannot be determined by the reference point *G* using the DDPIV equations, but has to be considered independently from the three reference points $G_{rg,}$ G_{gb} *and* G_{br}. This affects both the triplet matching and the later particle locating procedures, since both procedures rely on the DDPIV characteristic equations. In order to resolve this problem, a calibration-based method is developed to first match the triplet particle images of a particle from each color channel, and then the particle location in physical space is calculated based on the calibration results. This

approach is discussed in more detail in section 2.5.3.2. For the mini-scale system, the distortion is not as severe, and a modified DDPIV approach is used to correct the refraction indices of the fluid and model wall and described in section 2.5.3.1.

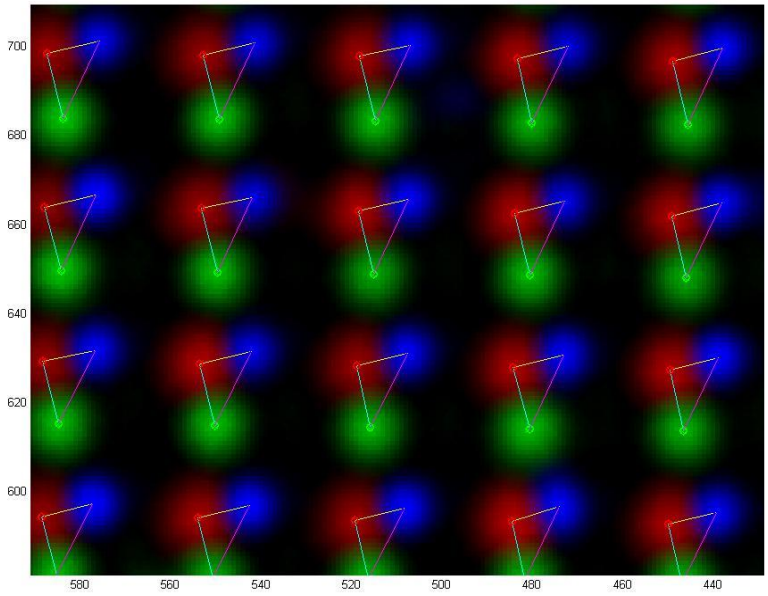

Figure 2-28 skewed triangle pattern of the triplet exposures due to chromatic aberration

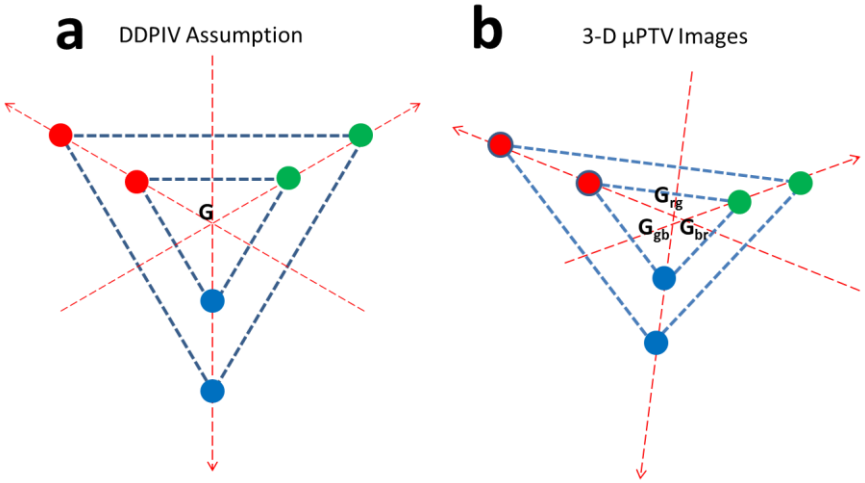

Figure 2-29 Comparison of the triplet pattern formed (a) based on DDPIV Assumption (b) based on actual images taken by 3-D µPTV system

2.5.2 **Triplet Finding**

The first stage to reconstruct the particle locations is to match the triplet exposures of each particle. After color-separation and peak finding procedure, the peak location for every exposure at each color plane is known. However, for each triangular pattern formed by which triplet exposures are yet to be matched. The matching process depends on how the triangular pattern is formed and is hence related to the optical model that describes the system.

2.5.2.1 Epipolar Geometry

Figure 2-30 shows an example of epipolar line on a two camera view system. O_L and O_R represent the centers of projection of the left and right camera, respectively. The line O_LP_3 is the line of project of particle P_3 to the left camera, and O_RP_3 is the line of projection of the same particle P_3 to the right camera. The left camera observes line O_LP_3 as one point x_{L1} on the left image plane, as the right camera observes them as a line $e_{L\text{-}R}$ on the right image plane. Thus particle P_1, P_2 and P_3 on the projection line O_LP_3 projected to the same point x_{L1} on the left camera are projected to different points x_{R1}, x_{R2} and x_{R3} on the right camera. Line $e_{L\text{-}R}$ is called an epipolar line from left image plane to right image plane. It is worth noting that any projection point on $e_{L\text{-}R}$ can be incorrectly matched with x_{L1} to produce a false particle in space. Therefore a two camera view system inherently produces ambiguous results. However, the epipolar geometry also shows that a projection point from left camera image plane must form an epipolar line on right camera image plane, and the projection of the same particle must lie on the epipolar line. The ambiguity can be eliminated by adding a third camera view to the system. The following procedure shows how to match the three projection point on each camera view to the correct particle in space. This is the method proposed by Maas *et al.* (1993).

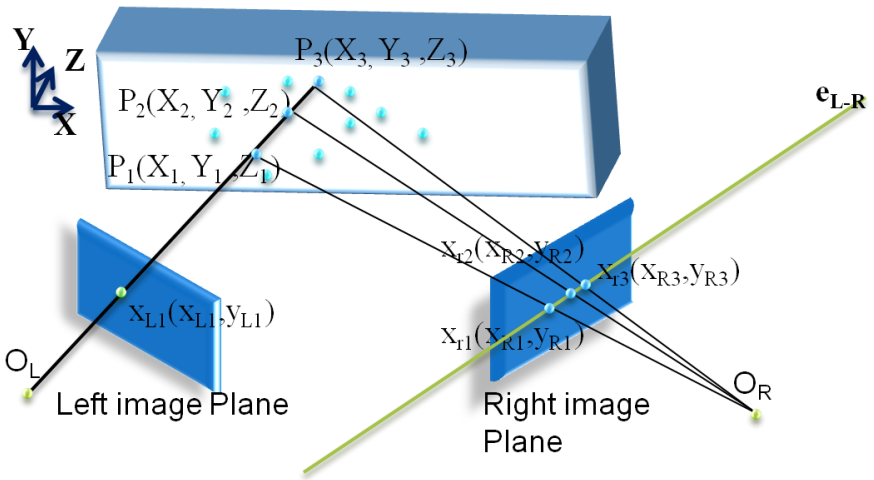

Figure 2-30 epipolar geometry

2.5.2.2 Triplet finding – Epipolar Line Search Method

Start from a point (P_1) in plane 1(Figure 2-31 (a)), find the epi-polar line $e_{1\text{-}2}$ at plane 2 and locate possible candidate points P_1, P_2 and P_3, as shown in Figure 2-31 (b). Theoretically, the candidate points should intersect with the epipolar line perfectly. In practice, due to lens distortion, image noise and error of peak finding algorithm, it is common to use a search area ε around the epipolar line to find the candidates. Repeat this step to all candidates (P_1, P_2 and P_3) in plane 2 to find corresponding candidates in plane 3, and epipolar lines $e_{2\text{-}3}$ $e_{2\text{-}3}$' and $e_{2\text{-}3}$" can be found and candidates are those points within the retctangular area of the epipolar lines (Figure 2-31 (c)). Finally, find epipolar line $e_{1\text{-}3}$ of P_1 from plane 1 to plane 3 and locate the candidates (Figure 2-31 (d)). The intersection of the candidate set found from $e_{1\text{-}3}$ and those from $e_{2\text{-}3}$, $e_{2\text{-}3}$' and $e_{2\text{-}3}$" are the most possible triplet(s) as shown in Figure 2-31 (e).

Since the 3-D μPTV system can be considered as a system with three pinhole camera view, the epipolar line search method can be applied to the 3-D μPTV system to find the triplet match. The epipolar line has to be generated from any image point in the image plane from a specific image point in another image plane. This can be done by finding the line of projection of

the point of interest and then project it to the plane where the epipolar line is to be found in. For instance, in Figure 2-30 the line of projection $O_L P_1$ can be calculated from x_{L1} in the left image plane and the epipolar line $e_{L\text{-}R}$ can be found by projecting P_1 and P_3 to x_{r1} and x_{r3} in the right image plane. The calculation of line of projections requires a full optical model of the system. The optical system is usually approximated by a pinhole camera model, and the camera parameters are found through a calibration procedure (Maas *et al.*, 1993).

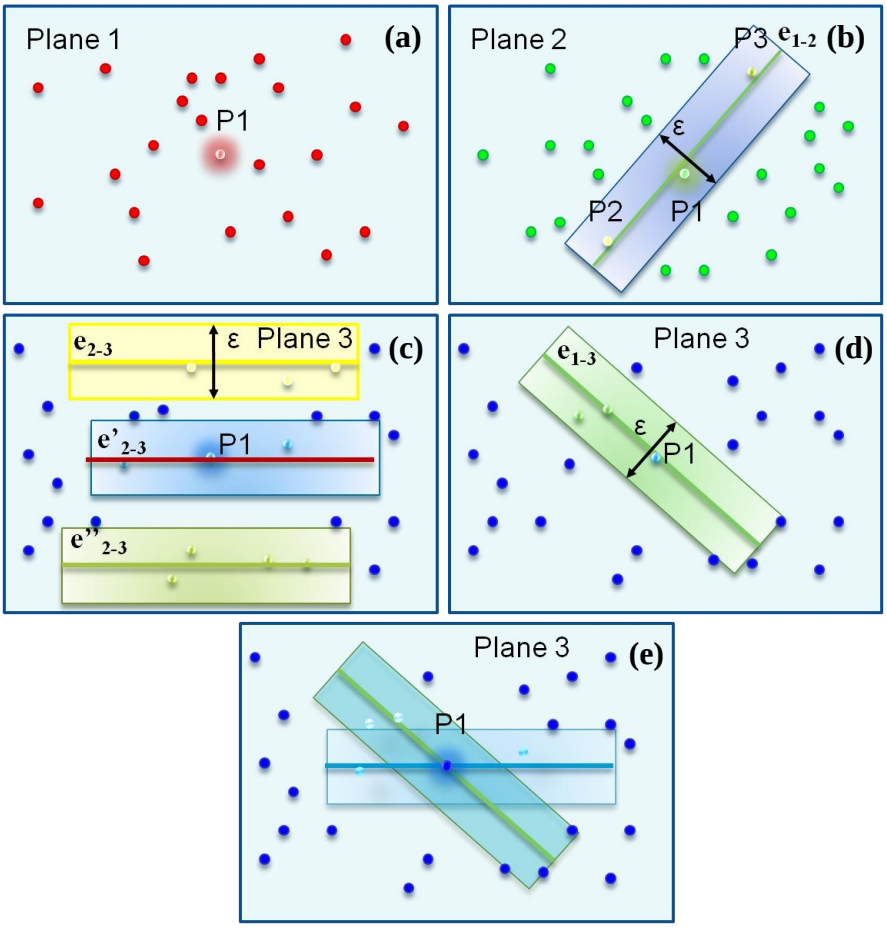

Figure 2-31 epipolar line search procedure

2.5.3 **Particle Location Calculation**

The second stage of reconstructing the particle locations is calculating spatial coordinates of particles using the matched triplet images found as described in the previous sections. In the mini-scale system discussed in section 2.1.4, a modified DDPIV approach was used and achieved satisfactory results. For reasons explained in the previous section, the 3-D μPTV system utilized a calibration-based approach to calculate the particle locations and the epipolar line projections. Both the modified DDPIV and 3D μPTV approaches for finding particle spatial coordinates are explained in detail in the rest of the sections.

2.5.3.1 Modified DDPIV Approach

Based on the original concept discussed in section 2.1.1, the three-dimensional mapping relation between the spatial coordinates (*X,Y,Z*) and image coordinates (*x, y*) of each pinhole exposure image has been derived previously (Grothe & Dabiri, 2008). The spatial coordinates, *X* and *Y*, are functions of the average image coordinates, x_0 and y_0, magnification of the optical system, *M*, distance from the lens plane to the reference plane, *L*, and spatial coordinate, *Z*:

$$X = \frac{-x_0 Z}{ML},\ Y = \frac{-y_0 Z}{ML}. \tag{2-22}$$

The spatial coordinate, *Z*, is also shown to be

$$Z = \left(\frac{1}{L} + \frac{b}{MdL}\right)^{-1}, \tag{2-23}$$

where *b* is the image separation and *d* is the distance between the pinhole apertures, as shown in Figure 2-32.

Since these derivations assumed that the system was comprised of a single-element lens, *d* has been a known parameter. However, since the present lens contains multiple elements, and since the pinhole mask is placed within the lens, an "effective" pinhole separation, *d'*, should be used rather than the actual pinhole separation, *d*, in the above equations. This inconsistency is a source of error in the displacement measurements and will also reduce the precision of the velocity measurements. In addition, since the lens is multi-element, *L* is not readily known either. To solve these problems, a calibration procedure is developed to determine the "effective" pinhole separation, *d,'* as well as compensate for the unknown distance, *L*.

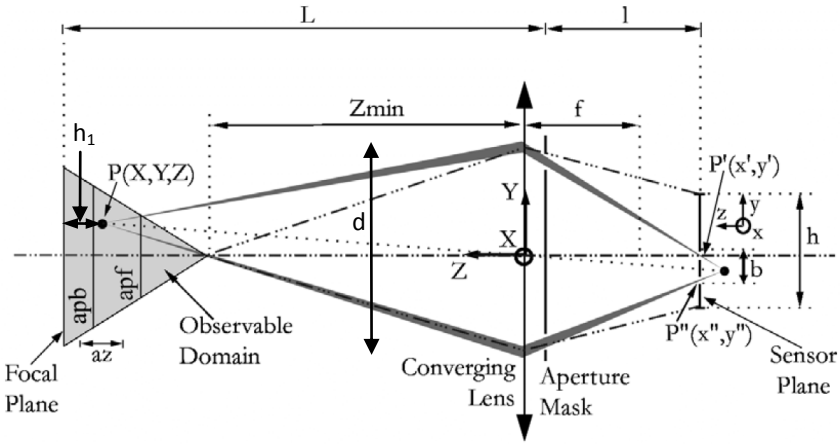

Figure 2-32 2D projection of the 3D defocusing model (Kajitani & Dabiri, 2005)

Particles placed on the bottom surface of the test section are first imaged at the focal plane, resulting in only single particle exposures. The test section is then moved towards the lens system by a distance *h1* (shown inFigure 2-32), causing defocused triple particle exposures with a separation distance b_1. The *Z* location of a particle on the bottom surface of the test section is then calculated using equation (2-23), where *d* is replaced by the "effective" pinhole separation *d'*:

$$Z = (\frac{1}{L} + \frac{b}{Md'L})^{-1}. \tag{2-24}$$

Using the approach taken by Pereira *et al.* (2007), Z can be represented by the displacement h_1 and L

$$L - Z = h_1 \Rightarrow Z = L - h_1, \tag{2-25}$$

where L can be determined by the nominal magnification M and focal length of the lens f from the lens equation:

$$M = \frac{f}{L - f} \Rightarrow L = \frac{f(1+M)}{M}. \tag{2-26}$$

Combining equations (2-24)-(2-26), the effective spacing of the pinhole apertures, d', can be calculated from the image separation b_1, magnification M, focal length of the camera f, and the displacement h_1:

$$d' = \frac{b_1}{M}(\frac{f(1+M)}{Mh_1} - 1). \tag{2-27}$$

Rewriting equation (2-27), and assuming $f >> h_1$, the relation of b_1 and h_1 can be written as:

$$b_1 = \frac{d'M^2h_1}{f(1+M) - Mh_1} \approx \frac{d'M^2h_1}{f(1+M)}, \tag{2-28}$$

Repeating the procedure for different distances, h_2, h_3,…, a set of image separations, b_2, b_3,…, can be measured. Equation (2-28) suggests that the relation between the separation b and distance h should be approximated by a straight line. Using a least square curve fit, the slope of the line can be found and d' can be determined given the focus length of the lens, f, and the

magnification, *M*. The focus length *f* is a known parameter of the lens, and the magnification *M* is obtained by directly measuring an exact known length in physical space in the image. In this way, the system of equations used to describe DDPIV systems with a single-element lens can be used to describe DDPIV systems with a multi-element lens, thereby allowing for its methodology to determine three-dimensional velocities.

In practice, light passes through the fluid, the transparent container wall, and the air before entering the lens system. As shown in Figure 2-32, the multiple refractions will change the path of the incident ray and make the measured *Z* location appear smaller than its actual location, *Z'*, for the case without fluid in the test section. For the case with fluid in the test section, the fluid index of refraction is different from that of the glass plate, thus resulting in an actual location *Z"*, different than *Z'*. *Z"* is usually larger than *Z'*, because the fluid index of refraction (water, *n"*=1.333) is smaller than the glass plate's index of refraction (*n'*=1.5). The correction for the *Z* location due to such refractions is derived in Pereira and Gharib (2002) as follow:

$$Z" = D + t + [Z - D - \frac{t}{\Omega(n\prime)}] \times \Omega(n"),$$

$$\text{with } \Omega(v) = \sqrt{\frac{R^2}{Z^2}\left[\left(\frac{v}{n}\right)^2 - 1\right] + \left(\frac{v}{n}\right)} \approx \sqrt{\left(\frac{v}{n}\right)^2} = \frac{v}{n} \quad (2\text{-}29)$$

$$\text{for } R^2 = X^2 + Y^2 \text{ and } R \approx Z \text{ ,}$$

where *D* is the distance from the lens plane to the bottom surface of the test section, *t* is the thickness of the bottom surface of the test section, and *n*, *n'* and *n"* are the indices of refraction of air, glass and fluid, respectively. The simplification shown in equation (2-29) is valid since in the present configuration $R < 5$ mm and $Z > 140$ mm. Since the actual *Z* location is now *Z"*, the

depth, *h*, used in section 5.1 needs to be adjusted due to refractive effects through multiple surfaces to obtain a more accurate *d'*. For the case without fluid, the actual particle location *Z'*, is calculated using the same equation (2-29), with *n''* = 1, indicating the fluid is air.

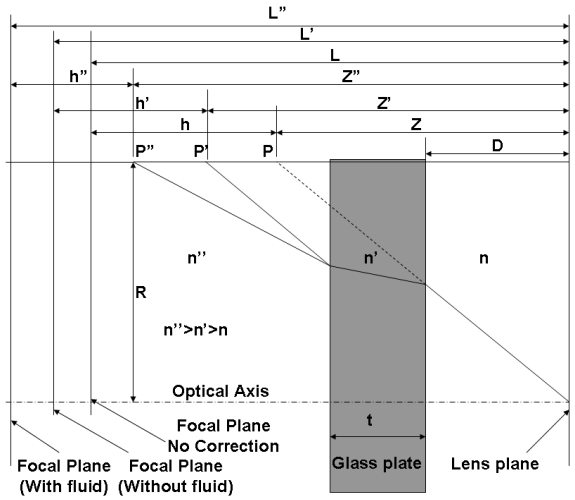

Figure 2-33 Parameters associated with correcting for multi-surface refractions (adapted from Pereira and Gharib, 2002)

To correct for *d'*, *L* from equation (2-26) is substituted in equation (2-24), resulting in

$$Z = \frac{f^2(1+M)d}{bf+dMf}, \tag{2-30}$$

In equation (2-25), *L* and *Z* are replaced by their effective values, *L''* and *Z''*, respectively, where $L" = Z"\big|_{b=0}$. *h* is also be replaced by its effective value, *h''*

$$h" = \frac{h}{\Omega(n")} = L - Z, \tag{2-31}$$

resulting in the corrected effective *d', d''*,

$$d" = \frac{b_1}{M}\left(\frac{f(1+M)}{Mh"} - 1\right)., \tag{2-32}$$

Similarly, assuming f>>h_1, the relation of b_1 and h_1 can be written as:

$$b_1 = \frac{d"M^2 h_1^"}{f(1+M)-Mh_1^"} \approx \frac{d"M^2 h_1^"}{f(1+M)}, \tag{2-33}$$

Equation (2-33) is similar to equation (2-28); however, the effective *d'* is replaced by *d"*, which has a refraction correction effect due to the index refraction of the fluid, *n"*. It is interesting that equation (2-33) shows that *d"* is not affected by the glass plate's index of refraction, and that the depth of the fluid does not affect *Z"* or *d"*.

The increase in the length of the effective pinhole separation and the multi-surface refraction correction, also affect the sensitivity of the system. For a system without fluid, Willert and Gharib (1992) defined this sensitivity as the change of the triplet image size to the change of depth

$$\frac{\partial b}{\partial Z} = -\frac{MdL}{Z^2}, \tag{2-34}$$

where

$$Z = \left(\frac{1}{L} + \frac{b}{MdL}\right). \tag{2-35}$$

Using *d"* instead of *d'* in equation (2-24), and using it to replace *Z* in equation (2-29), it can be shown that with multi-surface refraction corrections, the system sensitivity is

$$\frac{\partial b}{\partial Z} = -\frac{Md"L}{Z^2}\frac{n}{n"}. \tag{2-36}$$

It can be immediately seen that an increased effective pinhole separation increases the system sensitivity, while the index of refraction ratio will most often decrease the sensitivity,

since in most applications, n corresponds to the refraction index of air, while n'' corresponds to the refraction index of the fluid.

Figure 2-34 shows the calibration results for the image separation, b, versus the depth, h, for the cases with and without fluid present in the test section, where the linear fit equation is forced through the origin, since the separation distance, b, must be zero when the depth, h, is zero. This equation is $b = 34.58h$, with a correlation coefficient of 0.9998. The high correlation coefficient to the linear fit indicates that the approximations made in equations (2-28) and (2-33) are accurate and that the effective separation, d', can be accurately extracted from the slope. Using equation (2-28) and the slope of the linear fit, d' is found to be 25.47 mm, which is then used to determine the Z' location of the particles in the flow field using Equations (2-24) and (2-29). In an alternative approach, the variation of the calculated d' values are plotted against the depth, h, as shown in Figure 2-35. The averaged value of d' using this approach is 25.31 mm, shown by the straight line in Figure 2-35. Both approaches therefore provide nearly identical results, as the former is within 0.6% of the latter. The corresponding effective radial distance from the optical axis to the pinhole center γ', using these two approaches is 14.71mm and 14.61mm, respectively.

Figure 2-34 also shows the resulting particle image separation versus depth with fluid in the test section, which is clearly different than the case without fluid in the test section. In re-performing the calibration procedure outlined in Section 5.1 and 5.2, the test section is filled with water (n''=1.333), allowing the heavier particles to stay on the bottom surface of the test section. The linear fit equation is forced through the origin resulting in $b = 39.15h$, with a correlation coefficient of 0.99985. Interestingly, the linear fit without forcing the curve through the origin is $b = 39.10h + 0.05719$, with a correlation coefficient of R=0.99985. This further suggests that

since the *y*-intercept of this equation, which is the biased separation distance, *b*, in pixel, is nearly zero, that the procedure for determining an effective *d'* is accurate and valid. Extracting *d"* from the slope of the calibration curve shown in Figure 2-34 results in a value of 38.46 mm. Averaging the *d"* values for different depth locations (see Figure 2-35) results in a value of 38.27 mm, which is within 0.1% of the former value. The corresponding radial distance from the optical axis to the pinhole center, *γ"*, is 22.20mm and 22.09mm, respectively.

Regarding the sensitivity of the system (see equation (2-36)), the larger pinhole separation increases the sensitivity by a factor of 2.55, while the refractive index ratio decreases the sensitivity by a factor of 1.333, resulting in a total increase in system sensitivity by a factor of 1.91.

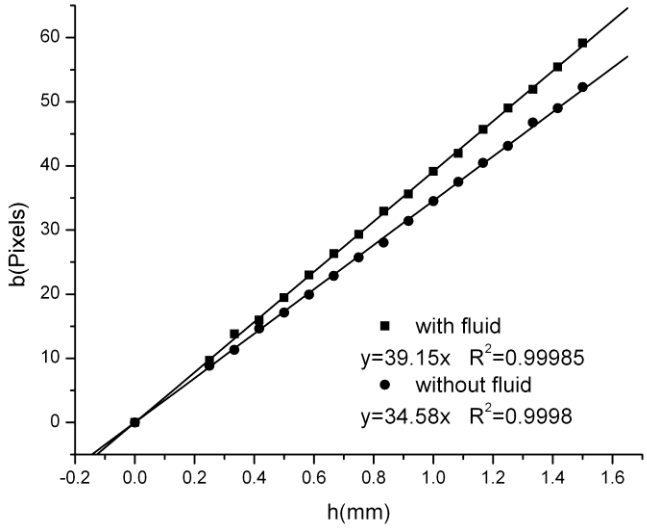

Figure 2-34 Particle image separation, b, versus depth, h. The shown curve fits are forced through zero.

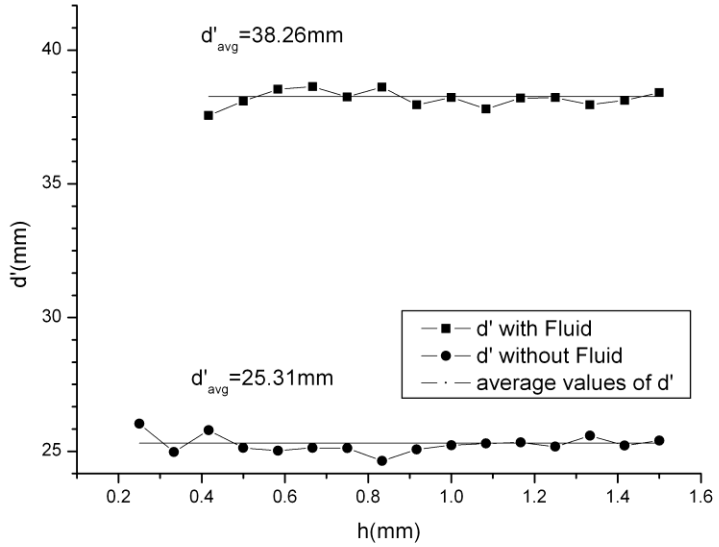

Figure 2-35 Variation of effective d' versus depth h

2.5.3.2 3-D μPTV – A 3-D Interpolation Model

2.5.3.2.1 Calibration

The calculation of the particle spatial location P(X,Y,Z) in the 3-D μPTV is a calibration-based approach. A set of calibration images is taken to form the database and the particle location is then determined by a 3-D interpolation of the database. The calibration procedure is explained by Figure 2-36. A target plate with an array of dots is set move to different positions. At each position, the calibration images are taken with the left and right cameras. Each calibration image is processed through the peak-finding algorithm introduced in section 2.4.5 to find the projected peak locations. The projected peak locations from each image plane and the true physical positions of the calibration dots can be related by mapping functions.

$$\begin{aligned} x_R &= f_{x,L\Rightarrow R}(x_L, y_L, Z) \qquad y_R = f_{y,L\Rightarrow R}(x_L, y_L, Z) \\ x_L &= f_{x,R\Rightarrow L}(x_R, y_R, Z) \qquad y_L = f_{y,R\Rightarrow L}(x_R, y_R, Z) \end{aligned} \tag{2-37}$$

$$X = F_{X,L\Rightarrow XYZ}(x_L, y_L, Z) \quad Y = F_{Y,L\Rightarrow XYZ}(x_L, y_L, Z)$$
$$X = F_{X,R\Rightarrow XYZ}(x_R, y_R, Z) \quad Y = F_{Y,R\Rightarrow XYZ}(x_R, y_R, Z) \tag{2-38}$$

where (X, Y, Z) are the physical coordinates of the dot, (x_L, y_L) are the image coordinates of the projected peak location in the left image plane and (x_R, y_R) are the image coordinates of the projected peak location in the right image plane. The functions are approximated with radial base functions (RBF) by MATLAB routine (Chirokov 2006), and same procedure is performed for each pinhole pair (red to green, green to blue and blue to red). Once these functions are built, epipolar line can be created for any point in the image plane with equation (2-37). For triplet matching procedure, equation (2-38) is used for calculating the particle locations in experiments.

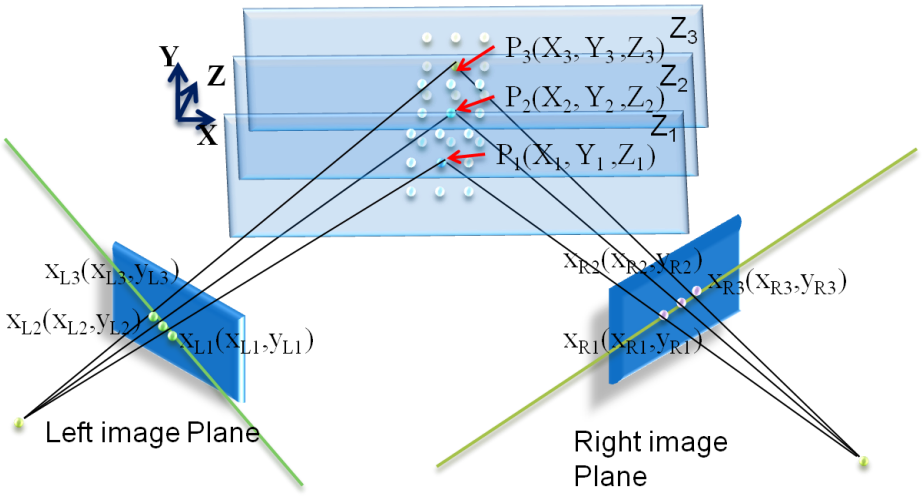

Figure 2-36 Calibration

2.5.3.2.2 Calculate particle physical position

In the actual experiment, once the image triplets of a particle are matched by the epipolar line search method, the next step is to calculate the physical coordinates of the particle location (X_p, Y_p, Z_p) based on the peak image coordinates(x_r, y_r),(x_g,y_g) and (x_b.y_b) of red, green and blue pinhole respectively. The Z coordinate is first to be found from equation (2-37). It is calculated iteratively by a minimum search routine based on a derivative-free method (MATLAB). Once the

Z coordinate is found, equation (2-38) is used to calculate the X and Y coordinates of the particle location. Only two of the peak locations are necessary, but all three pinhole pairs (red to green, green to blue and blue to red) are used to get the coordinates, and the average values are used to improve the accuracy.

2.6 **Particle Tracking**

After particle locations from two time frames are found, the last processing stage of 3-D μPTV system is to find the velocity field. In the current work the particle tracking algorithm is an adaptation of the previous work (Lei *et al*., 2012), but expand it from 2-D to 3-D. For completeness the concept is presented in the rest of the section.

2.6.1 **Vision-Based Matching - Scott and Longuet-Higgins' Method**

A long- standing problem in the field of computer vision has traditionally been the ability to correlate features in images, such as sequential images in time, to discern motion. In many situations, the features in the images can be very distinct, making the problem fairly easy to solve. In some situations however, the corresponding features may be too similar in appearance (such as particle images) to allow simple matching. In the field of computer vision, the attempt to match many similar features has led to two principles known as the "Principle of Proximity," and the "Principle of Exclusion" (Scott and Longuet-Higgins, 1991). The proximity principle states that a shorter-distance feature match is more likely than a long-distance match. This reduces to the nearest neighbor approach taken early on in the evolution of particle tracking algorithms. The exclusion principle eliminates the possibility of several features in one frame corresponding to a single feature in another frame. Together, these principles make up much of what determines a match to human vision. While some have proposed to explicitly require the

exclusion principle to apply (Ullman, 1979), Scott and Longuet-Higgins determined that conditions placed on the problem statement can enforce this principle without explicitly programming for it. The approach of Scott and Longuet-Higgins was to first develop the proximity matrix, *G*,

$$G_{ij} = e^{-r_{ij}^2/2\sigma^2} \tag{2-39}$$

where r_{ij} represents the distance between features I_i and J_j, where the *I* and *J* refer to the first and second images, respectively, and the subscripts *i* and *j* are the feature indices. In the exponential denominator, σ is a characteristic distance.

Given the above proximity matrix, the next task is to determine a pairing matrix, *P*, that maximizes the inner product, $P: G = trace(P^T G)$. The method taken by Scott and Longuet-Higgins is to find the singular value decomposition (SVD) of *G*, such that,

$$G = TDU \tag{2-40}$$

By the nature of the SVD, *T* and *U* are orthogonal matrices. The entries of the *D* matrix (which is purely diagonal) can be replaced with ones, resulting in the identity matrix, *I*. Substituting this for the *D* matrix results in the pairing matrix *P*,

$$P = TIU. \tag{2-41}$$

This can be shown to be the matrix with the maximum inner product with the proximity matrix, having rows which are mutually orthogonal. An element of P_{ij} can be thought of as the measure of correspondence between features I_i and J_j. A large value of P_{ij} indicates a large element of G_{ij}, which is a Gaussian weighted distance, and therefore P_{ij} provides an overall least squared distance mapping between features I_i and J_j. This provides the principle of proximity. The orthogonality of *P* means there can be only one maximum element per row or per column and

thus insures one-to-one mapping between particles in different images. This provides the principle of exclusion. Therefore if an entry of the pairing matrix, P_{ij}, is the maximum value of both the row i and the column j, then features I_i and J_j are considered matches. Further mathematical details can be found in Scott and Longuet-Higgins (1991) and Schonemann (1966).

Scott and Longuet-Higgins' method clearly has applications in the field of particle tracking where both the principle of proximity and the principle of exclusion play major roles. Also, the method is very simple to implement once the particle locations are known as it only requires a SVD, matrix multiplication, and a maximum value search. However, there are some problems associated with this technique when considering its use for particle tracking. The major problem is that the algorithm requires, as an input, a single characteristic length on which to base the proximity matrix. In the original Scott and Longuet-Higgins method, the choice of σ is arbitrary, but is suggested to reflect the average displacement of the features. Based on the experimental results, Pilu (1997) suggests that σ should roughly match the actual displacement. For implementation to PTV, it is a natural choice to use PIV results as a guide. Since PIV results are still a regional average over a certain interrogation window size, data interpolation is used to provide more accurate estimate of the local σ value.

Another known problem of the Scott and Longuet-Higgins method is the inability to match particles which travel through a large rotation between frames. This clearly has implications in the field of PTV, especially in studying vortical flows. However, as noted in Luo and Hancock (2002), the critical angle is on the order of 20 degrees. While this is a limiting factor in some applications, PTV rotation levels should never be as high as 20 degrees if the experiment is properly performed.

2.6.2 **Modified Vision- Based Matching in 2-D PTV**

A modified tracking algorithm is proposed based on the original Scott and Longuet-Higgins (1991) method. The implementation of the method is hybridized with PIV results, and an iterative scheme with outlier detection (Duncan, Dabiri, Hove, & Gharib, 2010) is used to increase the robustness and accuracy of the method.

To account for the different characteristic displacements present in the flow, twice the displacement magnitude at each particle location (found by interpolating the PIV results) is used as the characteristic displacement, σ, as it performs better when the characteristic length is an overestimate of the expected displacement (see section 5 of Scott and Longuet-Higgins (1991). This displacement is then used to construct the proximity matrix discussed above, which is then processed via singular value decomposition to determine a pairing matrix. Each entry, which is the maximum of its row and column, is considered a match and is subject to validation.

In order to make the feature matching technique described in section 2.6.1 more robust, two iterative approaches are taken. The outer iteration, termed the particle removal loop, focuses on removing already matched particles from the possible matches list. In this manner, straightforward matches are made early on in the process, making the remaining particle list easier to match later on. This iteration is in accordance with the exclusion principle, since any particle found to be a match in an early iteration can clearly not be a match with another particle in future iterations. The second iterative loop, termed the validation loop, takes place inside the particle removal loop listed above. For each particle list, the P matrix is created (by way of the singular value decomposition of the proximity matrix G mentioned in section 2.6.1) and maxima of both rows and columns are sought. When such a maximum is found, an outlier detection step is performed using the modified universal outlier detection method (Duncan *et al.* 2010). If the

entry in the *P* matrix is considered an outlier, then it is set to zero. Upon the next iteration of the validation loop, another entry in the *P* matrix may become the maximum of its row and column since the previous maximum may have been removed. This loop ends when the *P* matrix no longer changes, at which point the particle removal loop moves on to the next iteration until completion. The process flow of the iterative matching algorithm is shown in Figure 2-37.

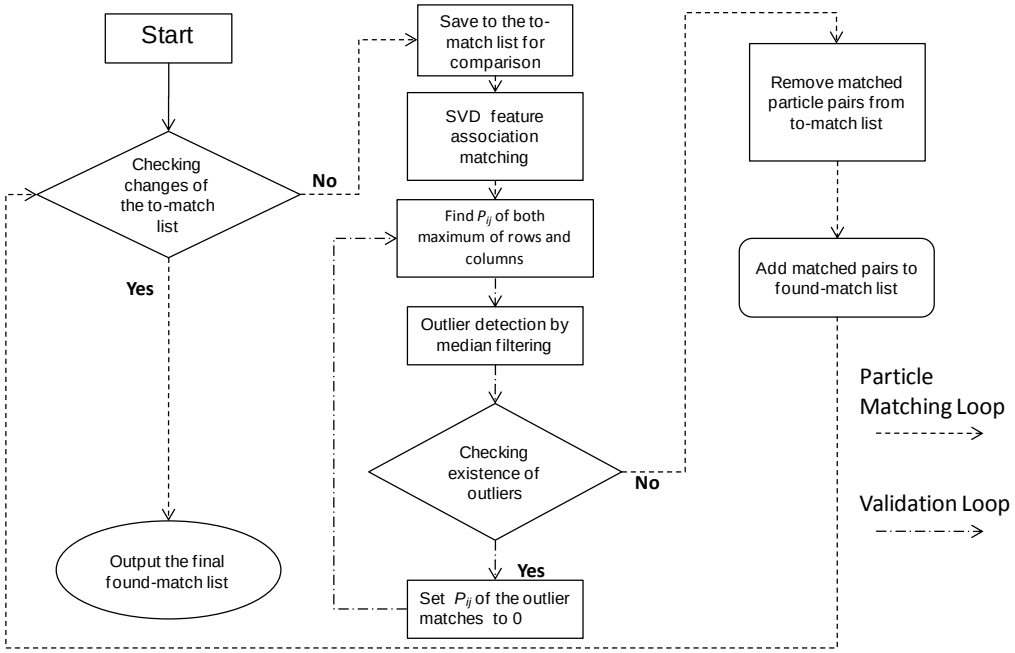

Figure 2-37 Process Flow of the proposed tracking Algorithm

2.6.3 **3-D Adaptation**

The process flow discussed in section 2.6.2 is extended to 3-D for the 3-D μPTV. The guiding 3-D PIV field is obtained using a 3-D cross-correlation method developed by (F. Pereira & Gharib, 2002). The main difference between the 2-D and 3-D cross-correlation function is that in 3-D cross-correlation scheme the process performs a 3D spatial cross-correlation of particle locations, i.e. in the physical space of the particle field and not in the discrete pixel image space as in the 2-D PIV.

The 3-D tracking algorithm is validated with two set of flow fields of analytical solutions. Random particle locations are generated in a volume of interest of side length L, and the particles locations in the next time frame after the time interval Δt is generated based on the velocity of a chosen analytical solution. The analytical solutions used for the tests are Hill's spherical vortex and Burgers vortex. The performance of the tracking algorithm is tested by varying the time interval Δt and particle density ρ.

For Burgers vortex, the velocity field is

$$\begin{aligned} v_r &= -ar \\ v_z &= 2az \\ v_\theta &= \left(\frac{\Gamma}{2\pi r} \left[1 - e^{\left(\frac{-ar^2}{2\nu} \right)} \right] \right) \end{aligned} \tag{2-42}$$

In the present work a = 0.1, T = 500 and ν = 0.1. Figure 2-38 shows the tracking results of the Burgers vortex. The velocity field of a Hill's spherical vortex is given in cylindrical coordinates,

$$\begin{aligned} v_r &= U \cdot \frac{r}{R}\left(\frac{z}{R} \right) \\ v_\theta &= 0 \\ v_z &= U\left[1 - \left(\frac{z}{R} \right)^2 - 2\left(\frac{z}{R} \right)^2 \right] \end{aligned} \tag{2-43}$$

In the present work U = 1 and R is set to 75% of the side length of the volume of interest. Figure 2-39 shows the tracking results of the Hill's spherical vortex. The volume of interest is defined as a 512 × 512 × 512 voxel. The particle density is defined as number of particle per voxel.

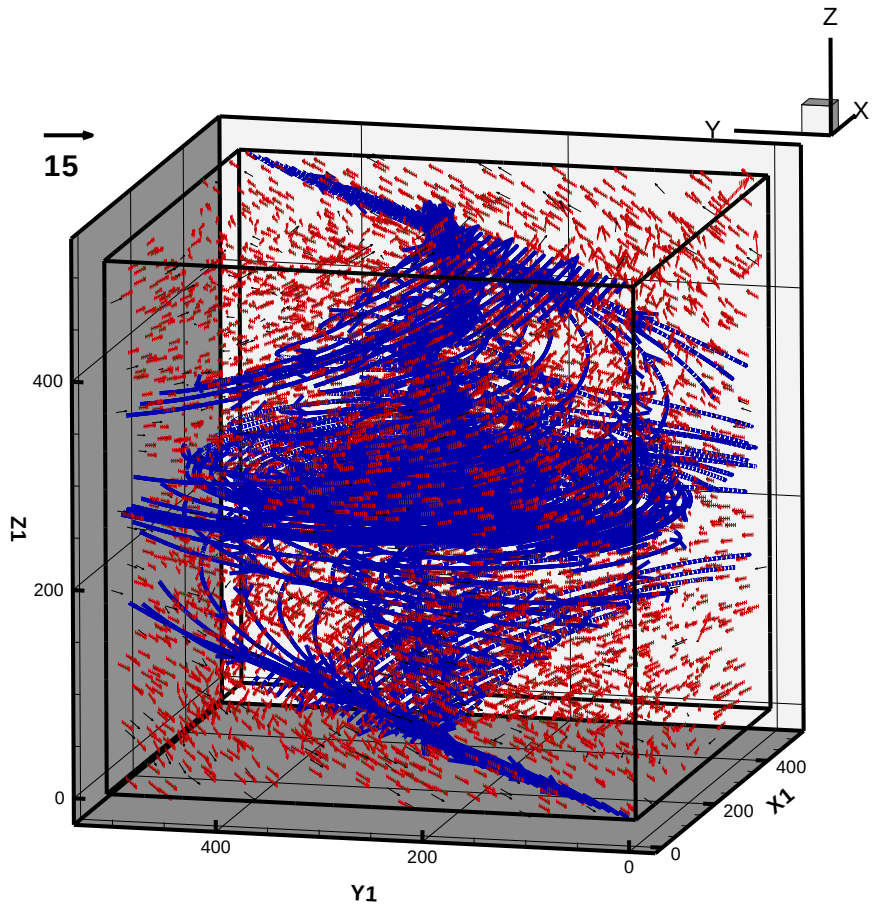

Figure 2-38 Tracking results of the Burgers Vortex. Red vectors represent the tracking results, black vectors is the true answer, and blue lines are the streamtraces. Animated version can be found at http://www.aa.washington.edu/research/fluidDynamic/fdrf/images/BurgersZAxisRotation.gif

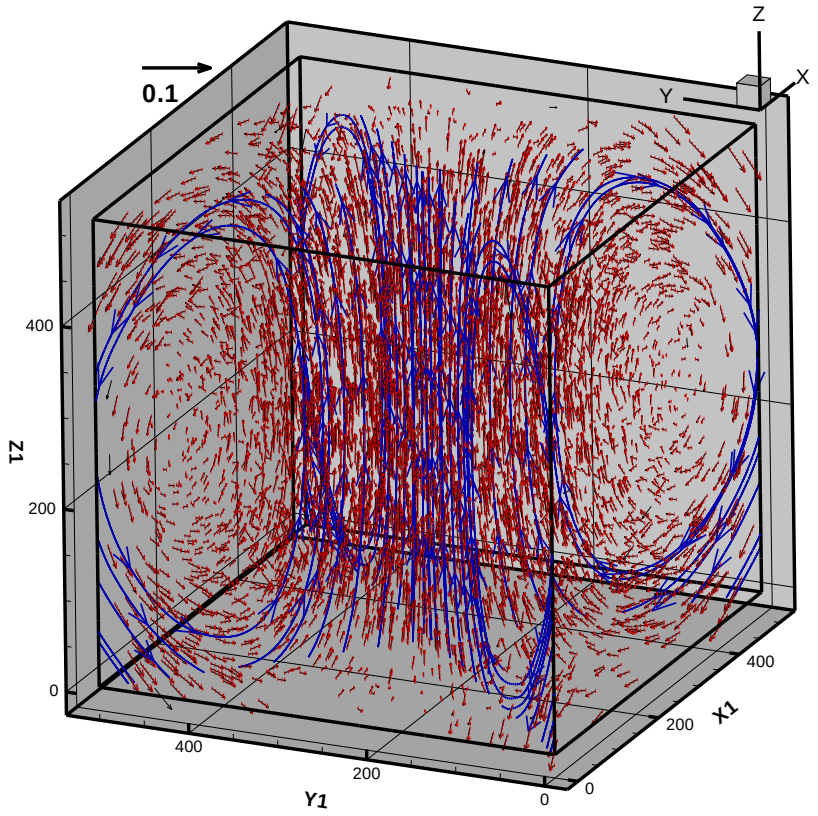

Figure 2-39 Tracking results of the Hill's spherical Vortex. Red vectors represent the tracking results, black vectors is the true answer, and blue lines are the streamtraces. Animated version can be found at http://www.aa.washington.edu/research/fluidDynamic/fdrf/images/HillSphericalZAxisRotation.gif

In the present work, two particle densities (3.73×10^{-5} and 7.45×10^{-6} particle/voxel) are tested, corresponding to total number of 5000 and 1000 particles in the volume of interest. Time interval t is varied from 0.1 to 20 to test the performance of the tracking algorithm. Figure 2-40 (a) shows the results of the Hill's spherical vortex, and Figure 2-40 (b) is the results of Burgers Vortex for the case of 5000 particles. The particle yield is defined as the ratio between numbers of correct vector found and total number of vector in the field; match reliability is the ratio between numbers of correct vectors found and total number of vectors found. Particle yield can be interpreted as the "throughput" of the tracking algorithm, and match reliability is the "yield" of the tracking algorithm. The mean displacement and mean particle spacing are all normalized by the side length L of the volume of interest. In both cases the particle yield drops when the

mean displacement increases, but the reliability remains higher than 90%. This is due to the fact that the field is rotational, thus the large displacement due to longer time interval would cause a larger velocity gradient in the rectangular volume of tracking and reduce the performance of the algorithm. These results show that the current tracking algorithm is able to capture a rotational motion with high accuracy up to the displacement around 1.5% of the size of the measurement volume.

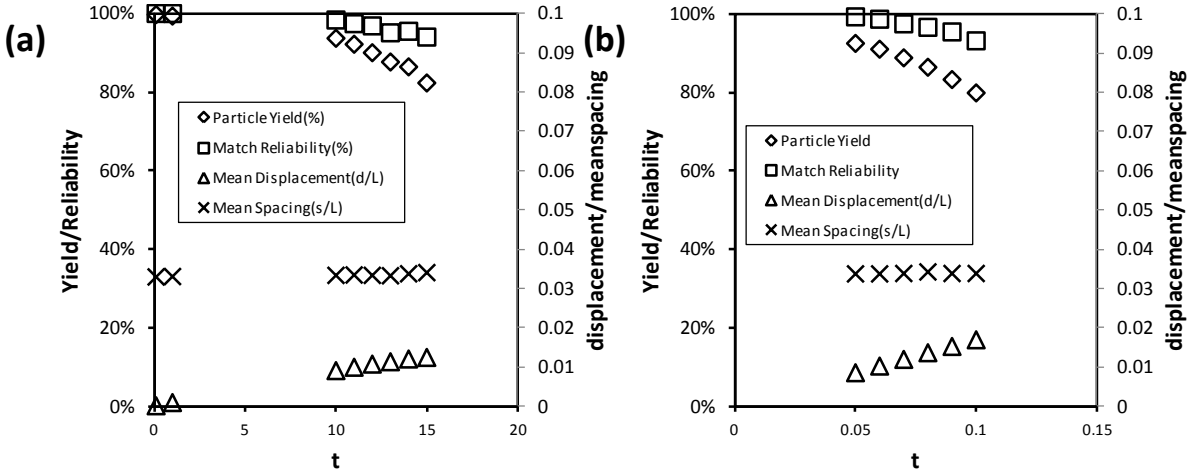

Figure 2-40 Tracking Performance of the synthetic flow fields: (a) Hill's spherical Vortex (b) Burgers Vortex

3 Post-Processing of Data

After acquisition of sequences of images taken during the experiment, the images has to go through a post-processing stage to remove unwanted background objects and image noise. During the post-processing stage, the color images are also “separated” by the decorrelation method discussed in chapter 2 to transfer the image data to the new color primary planes. In section 3.1 the raw image post-processing procedures to remove background, denoise and color separation are described.

The other post-processing stage is performed after the particle tracking is performed and the displacement data is converted to velocity data. The velocity vectors are then validated and outliers are removed. The procedure and algorithms are discussed in Section 3.2.

3.1 Raw Image Processing

Under ideal experimental conditions, the images recorded consist of only particle images and no noise is present, and the background is dark and free of reflections. In practice, this is usually not the case. Background intensity may vary due to uneven illumination source, and thermal and the photon noise from image sensors cause the intensity fluctuations. Reflections due to the geometry of the test section are also common. These factors are the error source to the measurement and sometimes degrade to results severely. In order to minimize the impact of these factors, image processing techniques are often applied to the raw images to improve the image qualities. There are many image processing techniques applicable to perform these tasks and are depending on the experimental conditions to decide which techniques are more suitable to use. In the current work, the main issues on the raw images have to be resolved is the reflections from the test section geometry, uneven illumination and thermal noise from the image sensor.

3.1.1 **Background Removal**

The reflections from the test section geometry create an intensity shift to the affected image area, and therefore have to be removed before the peak finding can proceed. Since it is caused by a stationary object in the field of view, it is possible to time-average the image sequence to get the mean image. This image can then be used as a representation of the background object and be subtracted out from each of the raw images. In the current work, the time-averaged mean image is replaced by the minimum image of the image sequence. In other words, the minimum of each pixel in a recorded image sequence is used instead of the time-averaged mean of each pixel to form the background image. It gives improved results because at regions have slow flow or stagnation points, tracer particle stay at the same area for a long period of time and the time-averaged mean is biased. Using the minimum value in the time-series for each pixel provides a better estimate of the pixel intensity value free of tracer particles. The only concern is that if the intensity variation of the light source is not negligible, the minimum value always underestimates the reflections and therefore cannot efficiently remove them. In the current work, since the LED illumination source used in the current work provides a stable continuous illumination, the pulse variation is not an issue. Figure 3-1 shows the effect of the background subtraction method.

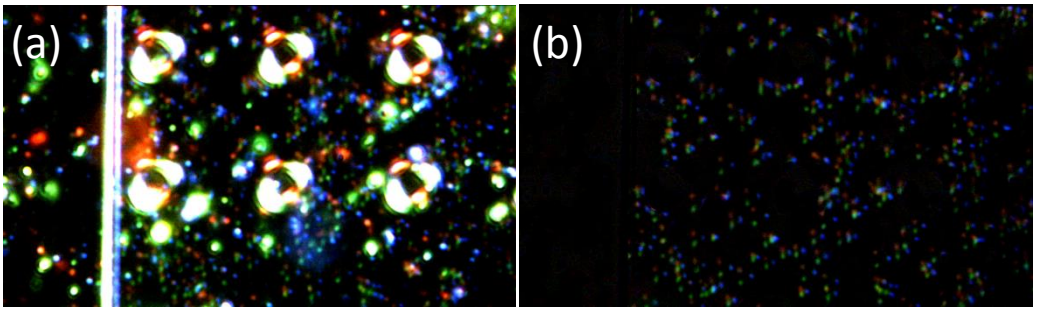

Figure 3-1 Result of background removal process: (a) raw image (b) after background removal

3.1.2 **Pre-Stage Filtering: Denoise with Band-pass Filtering**

The background removal procedure described in section 3.1.1 can remove the reflections from fixed objects, but it is not useful in removing the spatial variation of the illumination. The LED illumination method used in the current work is not a coherent light source, and spatial intensity variation is inevitable. It is preferred to take out the background variation so that the particle image intensity peak does not saturate the image sensor to increase the location error.

The other issue that cannot be dealt with by the background subtraction procedure is the image noise. As discussed in section 2.4.5, either the thermal noise or the shot noise add uncertainties to the peak finding algorithm and thus should be minimized. Because of the random nature of the noise, subtraction by the mean does not remove the noise efficiently.

To resolve these two issues, filtering techniques in the spatial-frequency domain are applied to provide a fast and more efficient way. It performs low pass (gaussian blurring) and high pass filtering to reduce both the image noise (high frequency signal) and background variation due to any non-uniform lighting (low frequency signal). The frequency parameter can be set manually to match different image qualities. This procedure is performed for each color channel, so the procedure has to be done after the color separation to avoid correlation from the filtering process.

3.1.3 **Post-Stage Filtering: Image Contrast Normalization**

After the background removal and band-pass filtering, the image is smoothed out and the contrast is usually lower than the raw image. More importantly these processing procedures are done to each image frame, and the histogram of each image frame can be different. Since the following peak finding algorithm requires a global threshold to filter the noise in the correlation

image plane in order to count reliable peaks, it is desirable to normalize the image contrast for each image frame. To achieve these goals, the images are processed by a contrast-stretching procedure. It maps the intensity values in the old image into a new image such that only values between a input range in the old image is mapped to the new image. Values outside the range are clipped; that is, values outside the range limit are set to the range limit values. The range limit is adaptively set based on the image histogram, therefore the ratio of clipping for each image frame is the same and the image contrast is stretched equally. Figure 3-2 shows the results of the post-stage filtering.

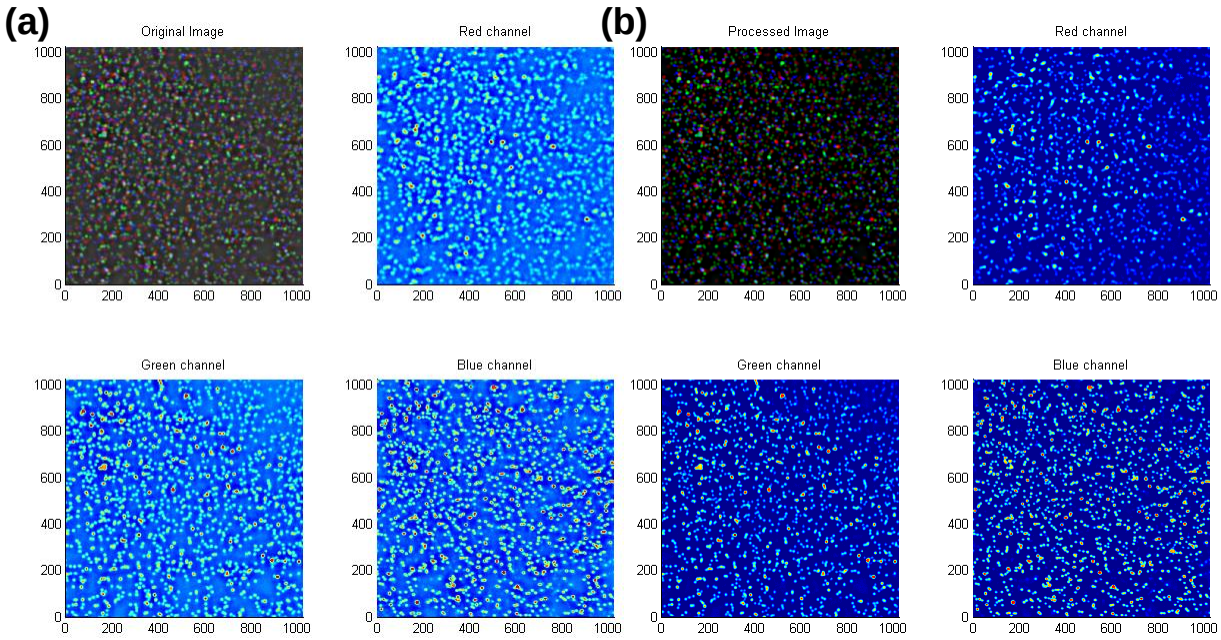

Figure 3-2 Results of the contrast normalization: (a) Before normalization (b)after normalization

3.1.4 **Color Separation**

The decorrelation results described in section 2.3.2 can be poor if a large portion of the sample pixels are highly correlated, which means they are part of the image consists of particle images from three different color planes. These pixels should be taken out from the samples to increase the accuracy of the transformation matrix. To solve this issue, a pre-selection procedure

is performed to find those three-color overlapped pixels. The pixel is first transform from RGB color space to HSI color space. A histogram of the saturation value is calculated, and the low clipping limit is found by setting a threshold to the histogram. Figure 3-3 shows the histogram of saturation value of a raw image. The saturation value lower than the threshold (0.56) indicates that the pixel is either too dim (low intensity values for all three color planes) or overexposed by all three color planes (low saturation values) and should be taken out. The rest of the sample pixels should provide more accurate estimate of the transformation matrix T to calculate the color separation. Figure 3-4 shows the result of applying the threshold to the raw image.

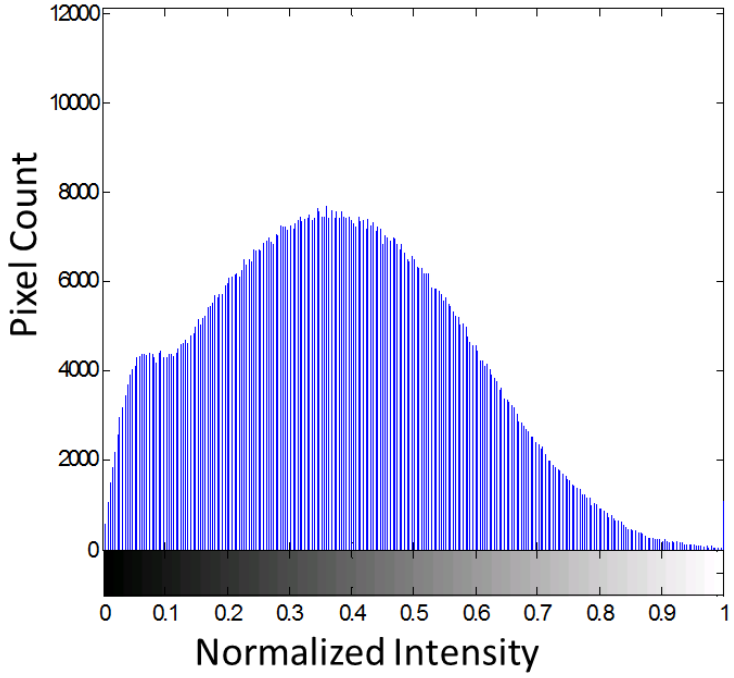

Figure 3-3 Histogram of the saturation value of an image

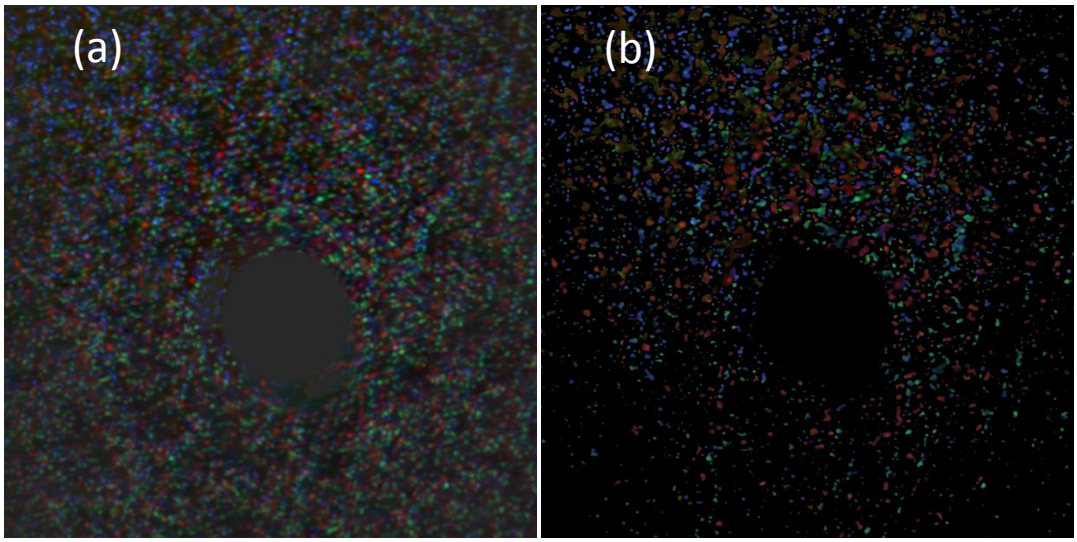

Figure 3-4 Result of the saturation selection (a) the raw image (b) selected pixels based on the saturation threshold Note that the more "colorful" pixels are selected.

3.1.5 **Blob Finding**

The particle identification method described in section 2.4.5 works on an image of any size contains unknown number of particles. In practice the least squares method may require substantial computation power if the whole image is treated as one problem. The solution is to break the image into small blobs and treat each blob as an individual image to identify the particles in each blob. A blob can be identified by finding the threshold value between the blob pixels to the background pixels. This operation is known as image segmentation. The key to the image segmentation is to determine the optimal threshold value that isolates the blob pixels from the background pixels. Because of the high number of particle images, an automated algorithm is required to sort the pixels and identify the blobs.

In the current work, Otsu's method (OTSU, 1979) is used to find the optimal threshold value. It assumes that the image has a bi-modal histogram, e.g. there are two classes of pixels, the "blob" and "background". The optimum threshold is then calculated to separate those two

classes so that their combined spread (within-class variance) is minimal. The within-class variance is defined as a weighted sum of variances of the two classes:

$$\sigma_w^2(t) = \omega_1(t)\sigma_1^2(t) + \omega_2(t)\sigma_2^2(t) \tag{3-1}$$

where the weights

$$\omega_1(t) = \sum_{i=1}^{t} P(i) \tag{3-2}$$

$$\omega_2(t) = \sum_{i=t+1}^{I} P(i) \tag{3-3}$$

are the probabilities of the two classes separated by a threshold t . The covariances σ_1^2, σ_2^2 of these classes are defined by

$$\sigma_1^2(t) = \sum_{i=1}^{t} [i - \mu_1(t)]^2 \frac{P(i)}{\omega_1(t)} \tag{3-4}$$

$$\sigma_2^2(t) = \sum_{i=t+1}^{I} [i - \mu_2(t)]^2 \frac{P(i)}{\omega_2(t)}, \tag{3-5}$$

where

$$\mu_1(t) = \sum_{i=1}^{t} \frac{iP(i)}{\omega_1(t)} \tag{3-6}$$

$$\mu_2(t) = \sum_{i=t+1}^{I} \frac{iP(i)}{\omega_2(t)} \tag{3-7}$$

are the class means, i is the center value of the i^{th} histogram bin. Otsu proves that because the total variance does not depend on the threshold value t, minimizing (3-1) is equal to maximizing between class variance σ_b^2:

$$\sigma_b^2 = \sigma^2(t) - \sigma_w^2(t) = \omega_1(t)[1-\omega_1(t)][\mu_1(t)-\mu_2(t)]^2 . \quad (3\text{-}8)$$

Since ω_1 and ω_2 are computed from the histogram as the threshold value t, equation (3-8) can be computed iteratively, yield a faster algorithm to calculate within-class covariance (the minimum of (3-1)). Figure 3-5 (a) and (b) shows the result of this procedure on a raw image.

After the image is segmented, a binary mask image is created and a morphological operation is performed to sort the classified blob pixels to each blob. The basic steps in finding the connected components are:

a. Search for the next unsorted pixel, p.

b. Use a flood-fill algorithm to label all the pixels in the connected component containing p, and label it with a integer.

c. Repeat steps 1 and 2 until all the blob pixels are sorted out.

Figure 3-5 (c) shows the sorted results. The label image can then be used to create small blob images and processed by the peak finding algorithm.

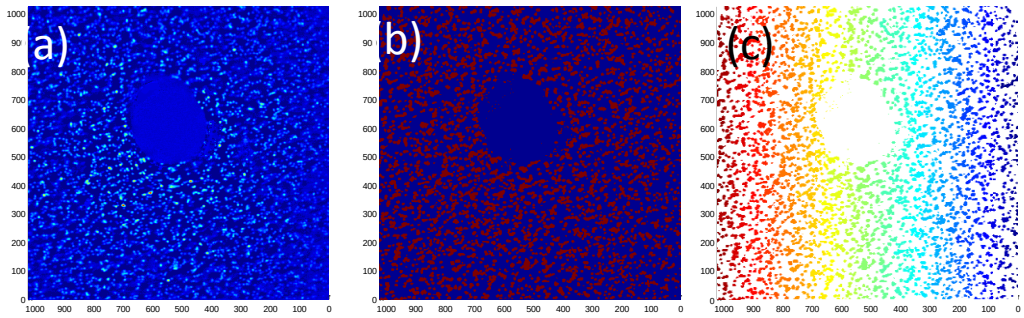

Figure 3-5 Result of blob finding: (a) The raw image from one color channel (b) Binarized image by Otsu's method(c) found blobs colored by R,G and B.

3.2 Post-processing for Velocity

3.2.1 Outlier detection

The raw output of a PIV/PTV velocity field usually contains a certain number of vectors that stands out from the neighboring vectors. They are identifiable because either the direction or the magnitude is different from the rest of the neighboring vectors (sometimes both). In PIV, it is mostly because the correlation peak of the true displacement does not exceed the random noise peaks. In PTV, the cause of these spurious vectors is usually a matching error. Figure 3-6 shows a typical 2-D PIV raw output.

It is usually inevitable to have these spurious vectors, and due to the huge amount of vectors, PIV/PTV can produce with multiple frames, it is cumbersome to take out these vectors manually. Many methods had been applied to automate this process, such as the variable threshold method (Shinneeb, Bugg, & Balachandar, 2004) and model-based validation method (Young, Johnson, & Weckman, 2004). In the current work, an extended universal outlier detection method proposed by Duncan *et al.*(2010) is used for the PTV data post processing. It is an extension from the universal outlier detection method (Westerweel & Scarano, 2005). More details of this method will be described in the following sections.

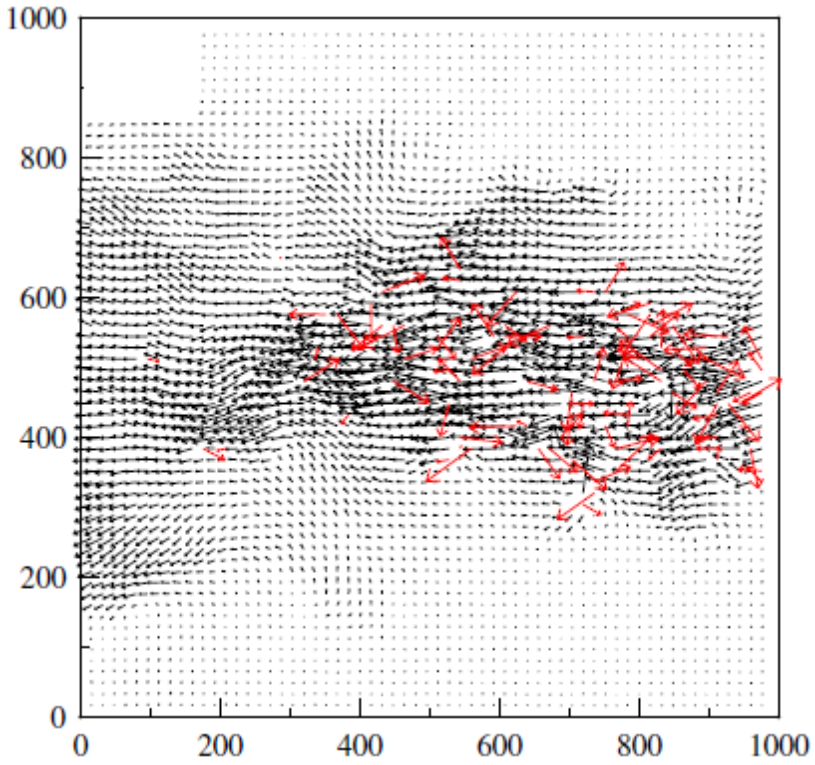

Figure 3-6 Outliers in a PIV measured turbulent jet. Vectors in red represent the outliers. From Westerweel & Scarano (2005)

3.2.2 **Universal outlier detection on uniform grid**

Usually a local approach that compares each vector with its neighboring vectors is used to detect the outlier vectors. Comparing with local mean value is the straightforward approach, but it is strongly biased by the spurious vector itself. Using a vector median can avoid this problem since it is insensitive to the spurious vector and otherwise has similar statistical properties as the local mean. The universal outlier detection method (Westerweel & Scarano, 2005) improved the vector median approach for PIV data by adding an adaptive normalization factor. The deviation of each vector is defined as

$$r = \frac{|U_0 - med(U_i)|}{\sigma_s}, \tag{3-9}$$

where $med(U_i)$ is the median displacement of the data in the neighborhood of the vector U_0 and σ_s is the normalization factor. The normalization factor should be robust to local flow conditions, so the median of the absolute deviations of neighborhood points plus an offset, σ_ε, is used to improve the performance:

$$r_0^* = \frac{|U_0 - med(U_i)|}{med\big(U_i - med(U_i)\big) + \varepsilon}, \tag{3-10}$$

This outlier test provides a "universal" probability density function for the residual and that a single threshold value can be applied to effectively detect outlier vectors (Westerweel & Scarano, 2005). Because of its simplicity and efficiency, this method has become widely used for PIV data post-processing .

3.2.3 **Extension to non-uniform grid**

Equation (3-10) is efficient and robust and is widely used for the post-processing for PIV data, which is on a uniform grid space. However, the PTV raw data is on a non-uniform grid space and the method cannot be applied directly. The main issue to apply the method to an unstructured data is to define the neighbors for the vector to be evaluated. Duncan *et al.* (2010) proposed a modified method for the unstructured PTV data using Delaunay tessellation. Delaunay tessellation is a mathematical method to divide a surface or plane polygon into a set of triangles. It is widely used in mesh generation for the computational modeling and interpolation problems for computer graphics. The main feature of the method is the ability to connect every scattered point efficiently to form triangles/triangular pyramids in 2-D/3-D space. Figure 3-7 shows the resulting Delaunay tessellation from 300 random points. A circle circumscribing any Delaunay triangle does not contain any other input points in its interior (Stoyan, 1994). With the tessellation established, the neighboring points of each data point in the plane can be defined.

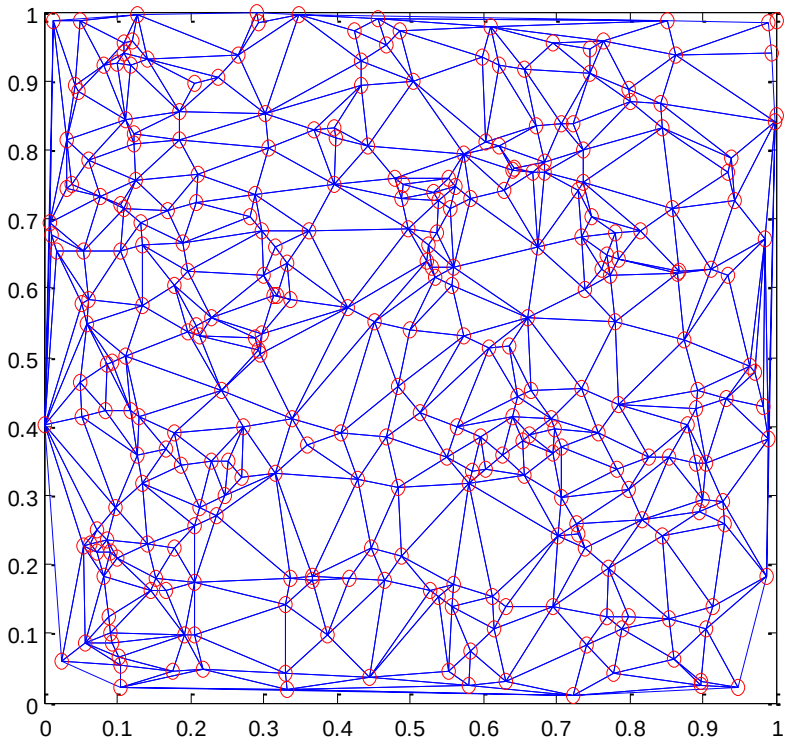

Figure 3-7 Delaunay tessellation of 300 random points in a plane

As shown in Figure 3-7, the random spacing of the PTV data points indicates that the distance of each neighboring point are different. This is a major difference to the uniformly spaced PIV data. The velocity variation of a neighboring point that is further away should be larger than the one that is closer, hence a weighting is necessary. Duncan *et al.* (2010) used the inverse-distance weighting plus a distance tolerance and proposed a modified form of equation (3-11):

$$r_0^* = \frac{\left|\frac{U_0}{med(d_i)+\varepsilon_a} - med(\frac{U_i}{d_i+\varepsilon_a})\right|}{med\left(\left|\frac{U_i}{d_i+\varepsilon_a} - med\left(\frac{U_i}{d_i+\varepsilon_a}\right)\right|\right)+\varepsilon_a}. \tag{3-11}$$

The modified method was tested on flows varying from impinging jets to turbulent boundary layers and wakes to wingtip vortices, and residuals for these flows also show universality in their probability density functions.

In the current work, this method is extended from the 2-D plane to the 3-D space for the 3-D PTV data. The Delaunay tessellation is similar to the 2-D case, only the Delaunay triangles become triangular pyramids.

4 Experiment Hardware Setup

The 3-D μPTV system is developed and tested based on the principles introduced in the previous chapter. Figure 4-1 shows a schematic of the current 3-D μPTV system setup. To demonstrate the capability of the system, a micro-scale backward-facing step flow is set up and the flow field is resolved by the 3-D μPTV system. The experimental apparatus consists of four major components: the infinity-corrected inverted microscope system, calibration system, data processing software and test section. Each of the components is presented in the following sections.

4.1 Inverted Microscope system

Since the 3-D μPTV system is designed to measure fluid flow in micron scale, the requirement for magnification (usually >10) makes microscope system a critical component of the system. In order to have more flexibility to test different optical configuration, a customized inverted microscope system is designed and assembled. As shown in Figure 4-1, the lights are set on top and the objective lens is put underneath the flow model. The main reason to choose the inverted configuration is for the ease of testing different lighting configurations, and it also provides an easy access for aligning the calibration target and micro-channel model, since in this configuration more space is available to setup the light source.

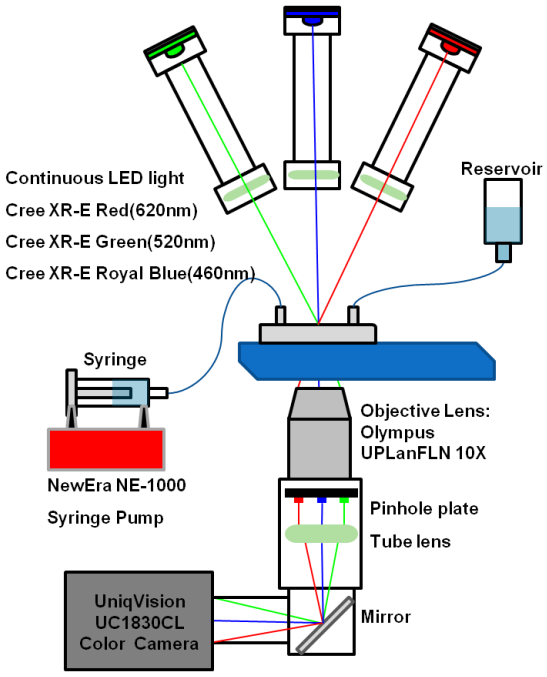

Figure 4-1 Schematic of 3-D µPTV experimental setup

4.1.1 **Infinity Optical System**

The schematic of optical path of the 3-D µPTV system is shown in Figure 4-2. The image from the objective lens is first focused to infinity, and then refocused to the image plane by the tube lens. The space in between the objective lens and the tube lens is called infinity space and provides a path of parallel rays. The optical configuration is called infinity-corrected optical system, which is widely adopted by the major manufacturers of research-grade biomedical and industrial microscopes (Optical Microscopy Primer). Since the objective lens and the tube lens together form a compound objective lens system, the magnification of the system becomes the ratio of the reference focal length L to the objective focal length f:

$$M = L / f. \tag{4-1}$$

One of the major advantages this configuration has over the traditional (finite) configuration without the tube lens is the infinity space. Additional optical components can be

placed into the system in the infinity space without the introduction of spherical aberration or modification of the objective working distance. It is very important to the 3-D μPTV system, because the best position to put the pinhole plate in the optical path is at the aperture plane of the optical system. This is the assumption of the original DDPIV system. With the finite configuration, the pinhole plate is always shifted from the aperture plane, as pointed out in the study by Yoon and Kim (2006). Figure 4-3 shows the ray tracing schematic in their study. $\delta_A$is the distance between the aperture plane and the location of the pinhole plate.

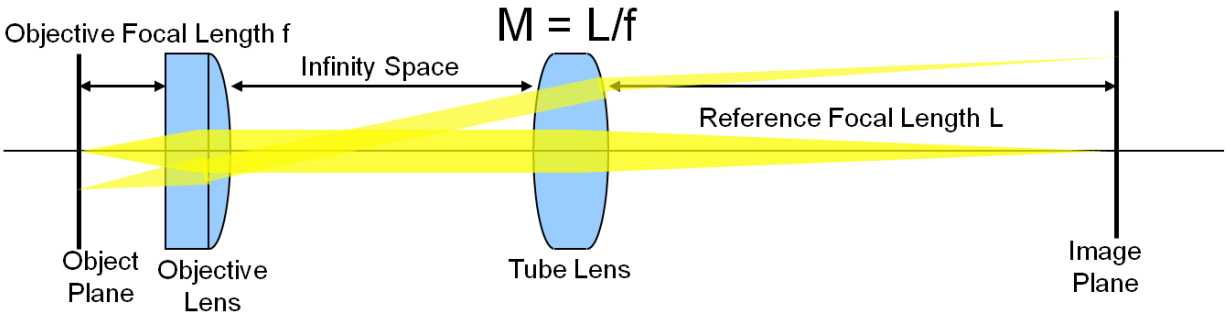

Figure 4-2 Infinity corrected optical system

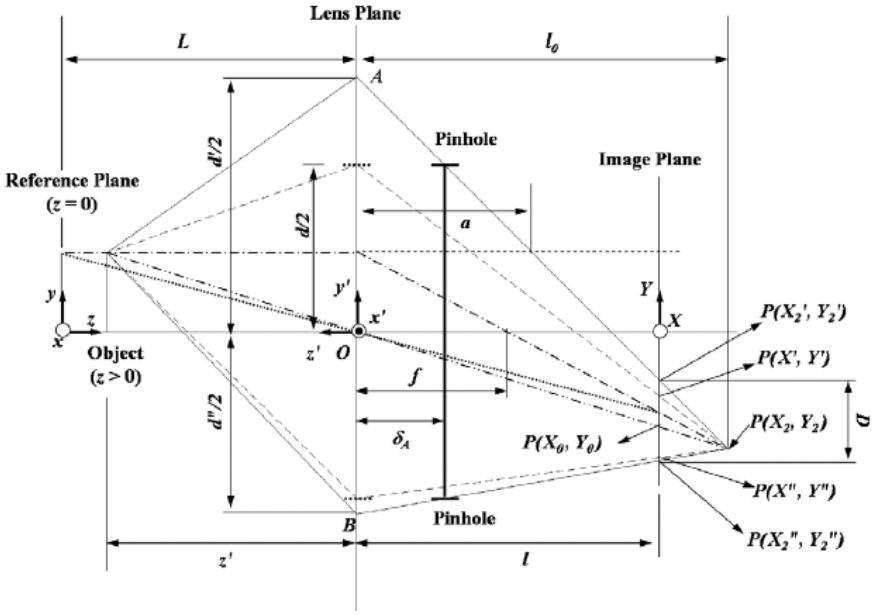

Figure 4-3 Ray tracing diagram of the case when the pinhole plate is not at the aperture plane (Lens plane) of the optical system. From Yoon and Kim (2006)

It was found that the *Z* locations calculated from the standard DDPIV equations shifted significantly from the actual locations. Solutions to this issue on the finite optical system are to either calculate the shift and compensate for it (Yoon & Kim, 2006), or utilize the concept of an effective optical system to compensate the shift (J. Lu *et al*., 2008; F. Pereira *et al*., 2007). In the current 3-D μPTV system this is not as important, since the calibration-based method described in chapter 2 can also account for this issue as well.

The other issue with the shift of the pinhole plate is it creates spherical aberration from the pinhole. This is because the ray passing through the pinhole is not parallel when the pinhole is shifted from the aperture plane, and the spherical aberration on the edge of the lens system is more significant than that in the center. This is harder to compensate for, since the microscope objective lens is a multi-element system and the detailed information of the lenses is not always available. With the infinity configuration, the pinhole plate is placed at the infinity space, which means that the pinhole is always at the aperture plane. Therefore the aberration issue is minimized.

In the current setup, both the objective lens (Olympus UPLanFLN 10X) and the tube lens (U-TLU) are made by Olympus to insure the optical performances are matched. Due to the additional length of the adapter ring for the camera mounting, the actual magnification measured from the image of a target plate is 10.965 instead of 10.

4.1.2 **Pinhole Plate**

The 3-pinhole plate is placed in the objective lens right after the lens elements, as shown in Figure 4-4 (a). The pinhole plate pattern is shown in Figure 4-4 (b). The diameter of each pinhole is *d* 1.5 mm, and the distance *R* (from the pattern center to each pinhole center) is 3 mm, results in a pinhole separation distance of 5.196mm. This configuration is chosen from a set of 16

different pinhole configurations of d = 2 ~ 4.2mm and R = 0.75~2mm, based on the depth of field and particle image intensities measured from the images of a target plate at different depth locations. As discussed in Lu (2008), the choice of d and R is a tradeoff between depths of field to particle image intensity. Larger d allows more light into the system thus increase the particle image intensity but also reduces the depth of field. R is preferred to be large for better depth resolution but limited by the aperture size of the objective lens and pinhole diameter, because the edge of the pinhole cannot exceeds the aperture edge. An appropriate choice of R and d should provide a depth of field larger than the volume of interest so that the particle images are in focus in the volume of interest, while keeping the particle image intensity and the depth resolution as high as possible. The current configuration results in a measurable image volume of 600 x 600 x 600 μm^3.

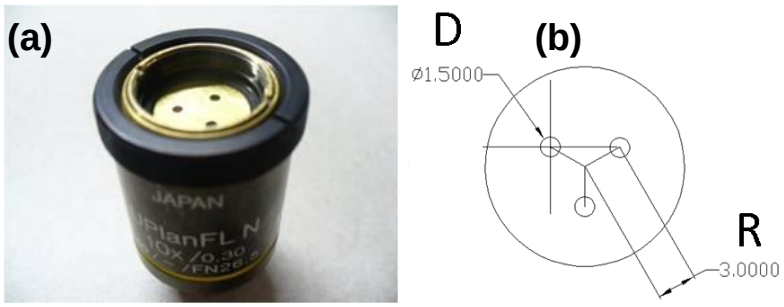

Figure 4-4 Objective lens modified for 3-D µPTV system: (a) Objective lens with pinhole plate (b) dimension of pinhole plate

4.1.3 **Light Source**

High power LEDs (light-emitting diode) are used as the light source for the system. Compared to other incoherent light sources, the main advantage of LEDs are the narrow spectral width. As shown in Figure 4-5, the spectral width (full width at half maximum, FWHW) of a typical quasi-monochromatic LED varies from 20~ 40 nanometers, which is ideal to match the spectral response of those pinhole color filters. Lasers are ideal for the same reason and have

been the main light sources for most of the PIV applications, whereas the high cost of lasers with three different wavelengths, especially the blue laser, make them not acceptable. The downside is that the total radiant output is still low compare to pulsed laser, so the exposure time of the camera has to be long enough to get high image quality. In the current system, three Cree XR-E series LEDs with Red (620 nm), Green (520nm) and Royal Blue (460 nm) are used to provide a continuous light source system. Critical illumination configuration is used where each LED is aligned with a lens doublet to focus the light to the object plane. This configuration requires a highly uniform emitting surface, because the image of the light source is directly focus onto the object plane. Since the LED provides enough uniformity, this configuration is used in order to provide more photon per unit area to the camera image plane. Figure 4-6 shows the setup of the three LED light sources and the corresponding focusing optics.

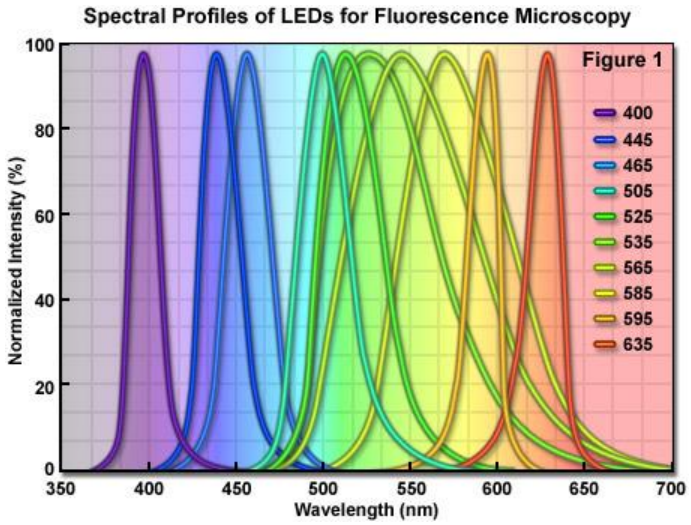

Figure 4-5 Typical Spectral response of single wavelength LEDs (from Optical Microscopy Primer)

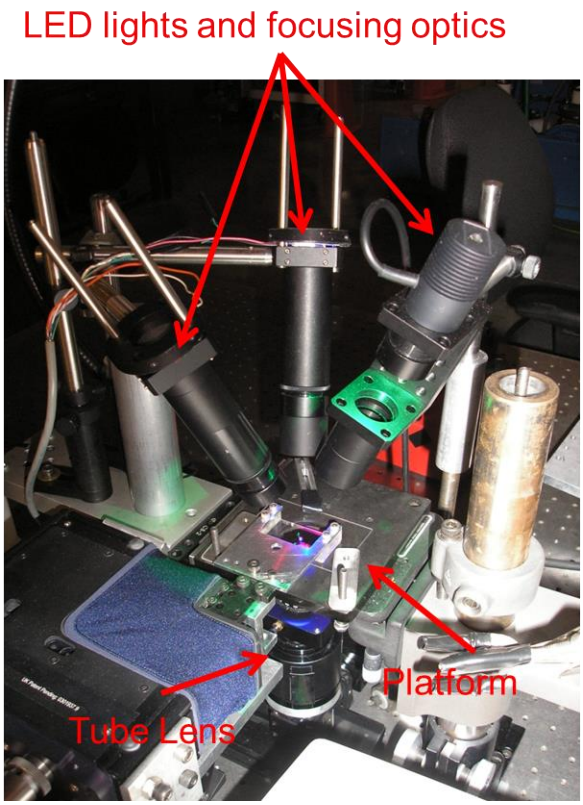

Figure 4-6 LED Light Source at work

4.1.4 Image Sensor

A 1024 x 1024 pixel^2 resolution color CCD camera (uniqvision UC-1830CL) of a frame rate of 30 frame per second is used to capture the images. The image depth is 8-bit for each color channel. The typical exposure time is set to 4.167 ms (1/240 s). For particle density high enough to perform two frame tracking, the data rate is 29 Hz. Images are captured and recorded by software (Video Savant® 4, IO Industries Inc.) through a frame grabber board (Road Runner R3 CL, Bitflow Inc.) into a PC.

4.2 Calibration system

A calibration apparatus is constructed to perform the calibration procedure presented in chapter 2. As shown in Figure 4-7 (a), the calibration target is a 50 mm x 25 mm x 1.52 mm glass

plate with grid arrays of blue chrome dots. The size of each dot is 3 μm with a grid spacing of 20 μm (Figure 4-7 (b)). The target plate is connected to a 6-axis translation stage (APT 600, Thorlabs). The stage is used to align the calibration target with the optical axis of the microscope system to provide the accurate Z-axis position of the target for each calibration plane. A glass slide of the same thickness to the bottom glass plate used to make the micro-channel flow model is put in between the objective lens and the calibration target, and water is put to fill the gap between the glass slide and the target plate. The refraction index of water and glass slide is then matched during calibration. A total of 14 planes data are taken, with 25 μm spacing in the Z-axis. The focal plane is set to the mid-plane of the 14 calibration planes and centered around the step so that the measurable volume covers the whole micro-channel. Figure 4-7 (c) shows a typical calibration image taken during the calibration test. Figure 4-8 shows the calibration system setup mounted on the 3-D μPTV system.

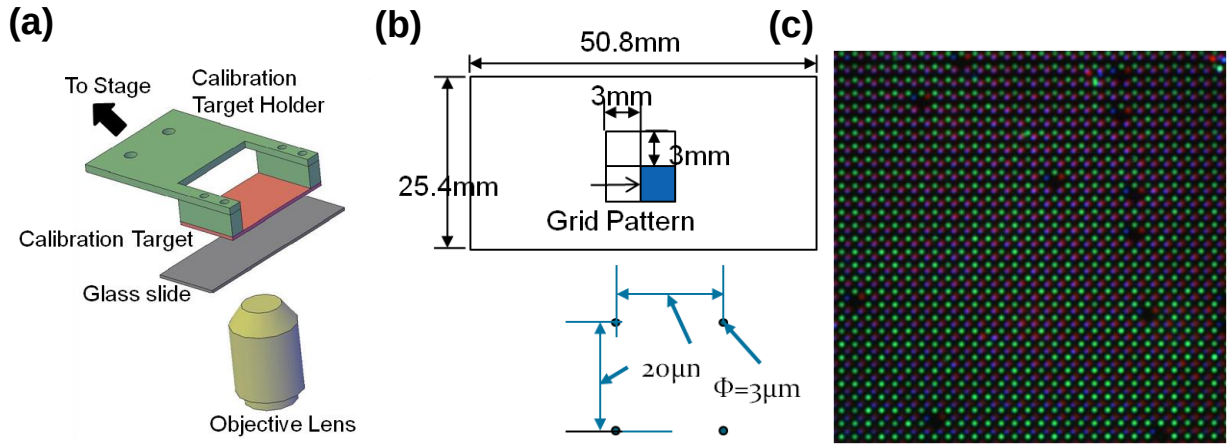

Figure 4-7 System Calibration: (a) Experimental Setup (b) Target plate pattern (c) Example of a calibration image

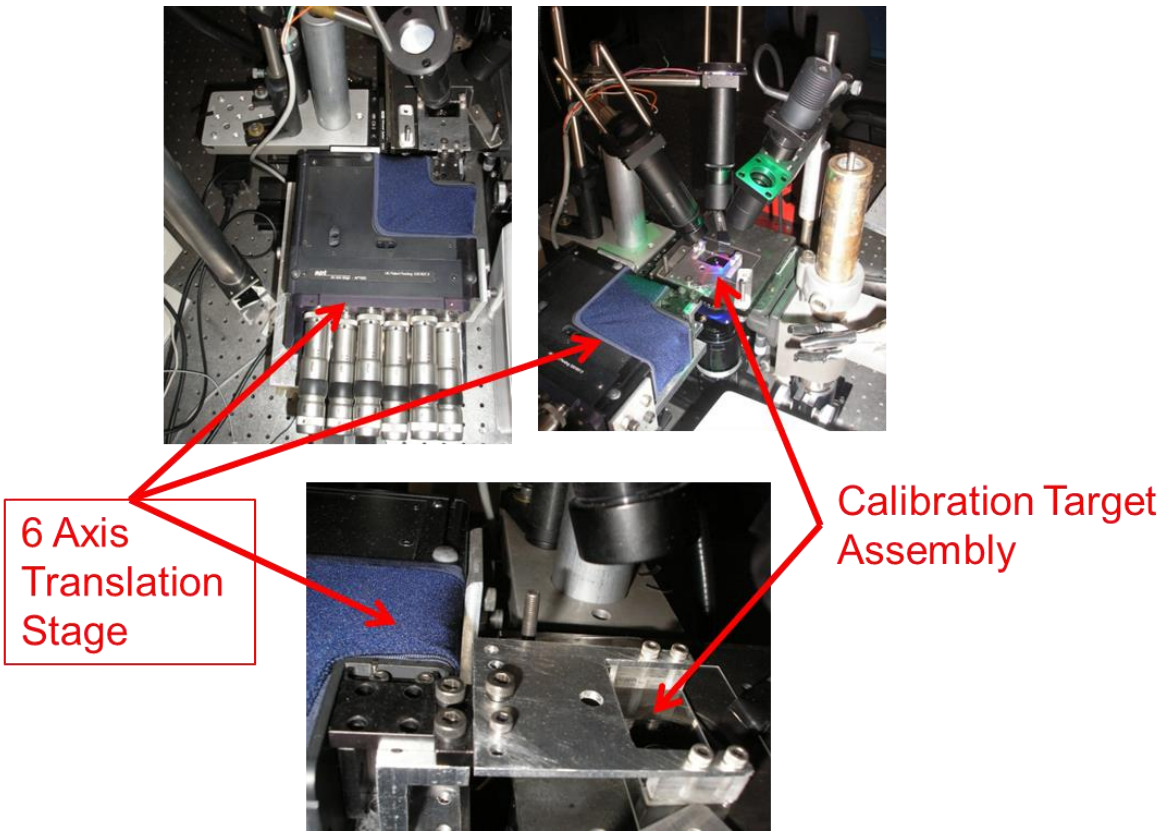

Figure 4-8 Calibration system setup

4.3 **Data Processing System**

The data processing is performed on a Dell Precision T7400 computer with a 2.00 GHz Intel ® Xeon® E5405 CPU. All the algorithms are developed in the MATLAB environment. A GUI interface is developed to perform all the processing procedure described in chapter 2 and 3.

5 Results and Discussions

5.1 Uncertainty Analysis

5.1.1 Validation Experiment Setup

To test the accuracy of the 3-D μPTV system, an experiment is conducted using the calibration apparatus described in section 4.2. The calibration target is moved by the translation stage by a known amount, and images are taken before and after the movement. Then the images of the dots are processed as if they are the actual particles, and tracking is performed to find out the displacement of each dot. Since the locations of the dots on the target are known, the accuracy of the system can be estimated. The advantage of this approach is the ability to estimate the accuracy of the system closest to the actual experimental condition, because all measurement errors other than that introduced by the flow system are reflected to the results. Since the present work is using the photogrammetric imaging approach, the velocity is calculated from the displacement of each tracer particle between two frames, the location error directly contributes to the final velocity error. Thus the location error is estimated from each image and the displacement error is calculated using the image pairs.

5.1.2 Location Error

The location errors are estimated in two ways: the mean error and the standard deviation. The errors are also sorted to two different groups: the in-plane error and out-of-plane error. The in-plane error represents errors in the X and *Y* directions, which is parallel to the image plane, and out-of-plane errors represent the error in the *Z* direction, which is along the optical axis. The calibration target is moved in the *Z* direction by increments of 25 μm as the procedure as

described in the calibration section, except the dots are shifted away from the calibration locations. The image is taken and processed with the processing discussed in the previous chapters. The mean error is estimated by comparing to the *Z* readings of the translation stage. Figure 5-1 (a) shows the mean error with normalization throughout the calibration range ($Z = 0 \sim 325$ µm). It is shown that the mean error is lower than 1.5% of the full calibration range, which corresponds to a variation from 0.09µm to 3.96µm.

The in-plane RMS (root mean square) error is estimated by comparing the calculated dot positions at different *Z* locations to those on a model plane. Figure 5-1 (b) shows both the normalized in-plane (*X* and *Y*) and out-of-plane errors. The in-plane variations are both less than 0.05%, while the out-of-plane error is around 0.25%, which correspond to 0.16 and 0.81 µm, respectively.

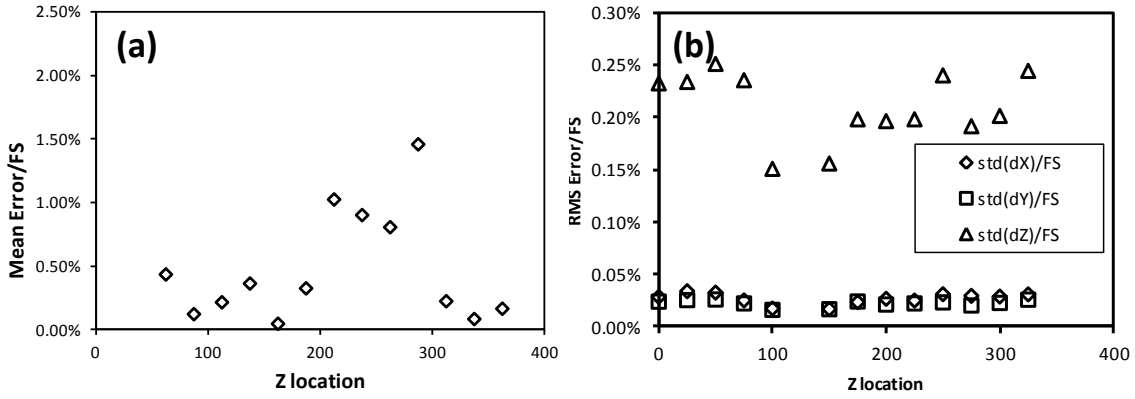

Figure 5-1 Location Error Test Results: (a) Mean Error (b) RMS Error

5.1.3 **Displacement Error**

To test for the displacement error, the target is moving by the translation stage in all three axes with a increments of 10 µm for the in-plane and out-of-plane tests. The mean and standard deviation of the error of displacement are calculated and shown as Figure 5-2. Both the mean and standard deviation of the errors are lower than 1% of the full measurement range, which are on

the same level with the location error. This result indicates the accuracy of the 3-D μ PTV system is high and uniform throughout the field of view, since with large displacement up to 50 μm (8% of the length of view) the error is still low.

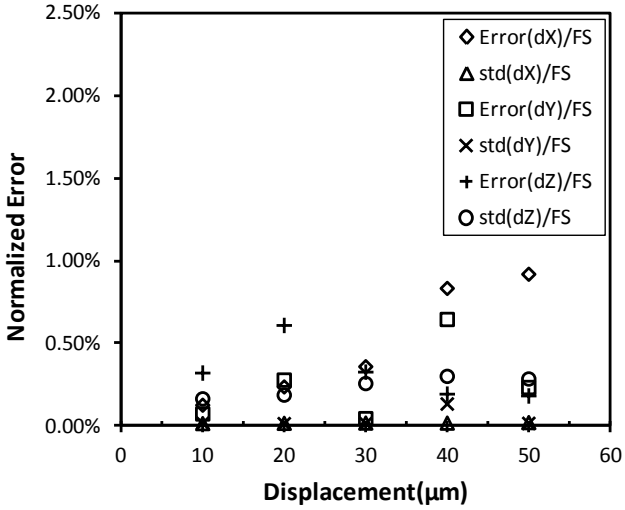

Figure 5-2 Displacement Error

5.2 **Backward-Facing Step Micro Channel Flow**

The true test of the performance of 3-D μPTV system is of course to resolve a real flow case. The backward facing step flow micro-channel is used for this purpose. The main advantage of the 3-D μPTV system based on the color-coded pinhole system is the possibility to increase the particle density. Most of the current 3-D techniques are limited to low particle density; as a result, they have to rely on time-averaging to get enough data to resolve the whole flow field and the consequence is that the flow field has to be steady. Thus it is important to test if the proposed new technique can be used to break this limitation.

To achieve this goal, a backward-facing step flow is constructed in micro-scale to test the capability of the 3-D μPTV system. Figure 5-3 shows concept of a backward-facing step flow. Flow across the step encountered a sudden expansion in geometry and cause flow separations

near the step. The size of the recirculation zone is related to the Reynolds number of the flow. Backward-facing step flow is chosen to demonstrate the flow visualization technique because of its simplicity in geometry. It is also convenient to measure the out-of -plane velocities (the downward flow across the step) from top view and allowing optical access from the bottom for illumination.

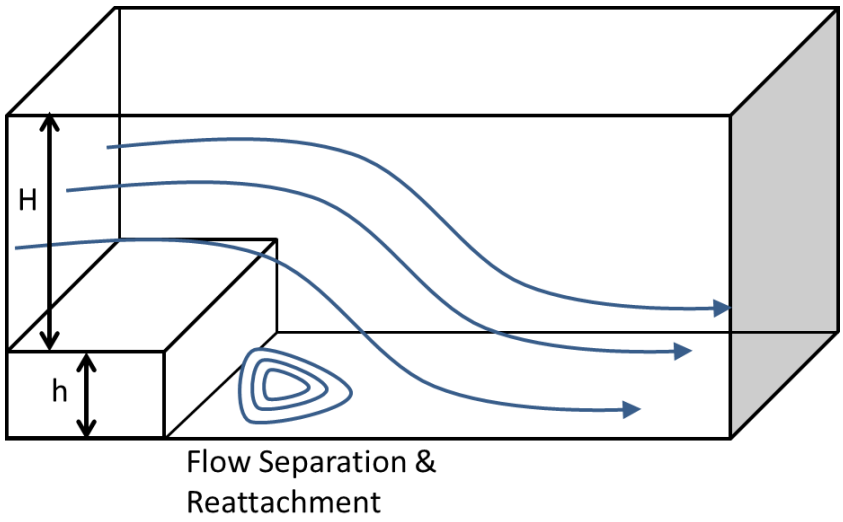

Figure 5-3 Schematic of a backlward-facing step flow

5.2.1 **Experimental Setup**

A backward-facing step flow micro-channel is constructed to test the performance of the 3-D μPTV system (Figure 5-4). A piece of 22 mm x 6 mm x 0.2 mm thin glass plate cut from a cover glass is glued to a 75 mm x 25 mm glass slide to form the step of the flow channel. The top wall is a transparent plexiglas plate cut to the same size as the bottom glass slide and glued together by double-sided PMMA (Poly (methyl methacrylate)) tape and a thin layer of epoxy glue. These tape and glue are also served as the side walls of the micro-channel. Both the top and bottom walls are transparent to ensure clear optical access for lighting the imaging. The resulting

channel dimension is 22 mm x 6 mm x 0.35 mm before the step and 15 mm x 6mm x 0.6 mm after the step. The laminar flow is driven by a syringe pump (NewEra NE-1000), and deionized (DI) water is used as the working fluid. 2 µm polystyrene particles (Polybead® Microspheres, Polysciences Inc.) are used as the tracer particles.

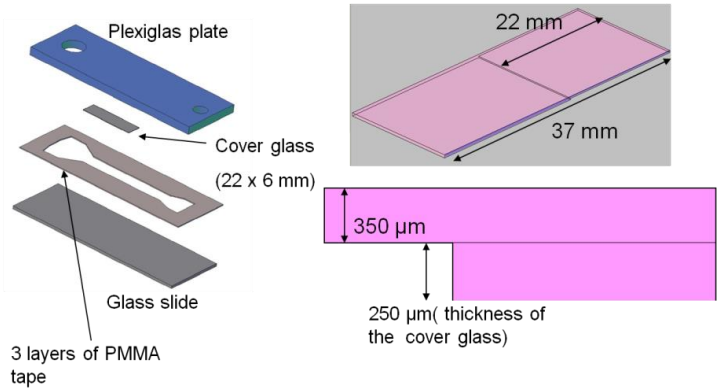

Figure 5-4 Backward-facing step Micro-channel

5.2.2 **Results**

5.2.2.1 Steady Flow

The first experiment is to verify the system performance with a steady flow. Using the set up presented in section, the flow is maintained at 40 µl/min which correspond to a Reynolds number Re =0.22. The field of view is located right after the backward-facing step. 156 image pairs are processed and the results are overlapped to one field, as shown in Figure 5-5. (red vectors). A total of 20592 vectors are identified, indicating an average of 132 vectors per image pair. The PTV result is interpolated to a uniform grid spacing on the size of 10 µm x 10 µm x 10 µm, as shown in fig. (Black vectors, only showing the representative planes).

The flow field result clearly shows the flow structure after the step with high spatial resolution. Due to the low Reynolds number, the flow is laminar and recirculation zone is small. The recirculation zone extends about 200 µm after the step, and the velocity vectors are more

random. This is likely because of the Brownian motion of particles under extremely low flow speed to cause the increasing measurement uncertainty.

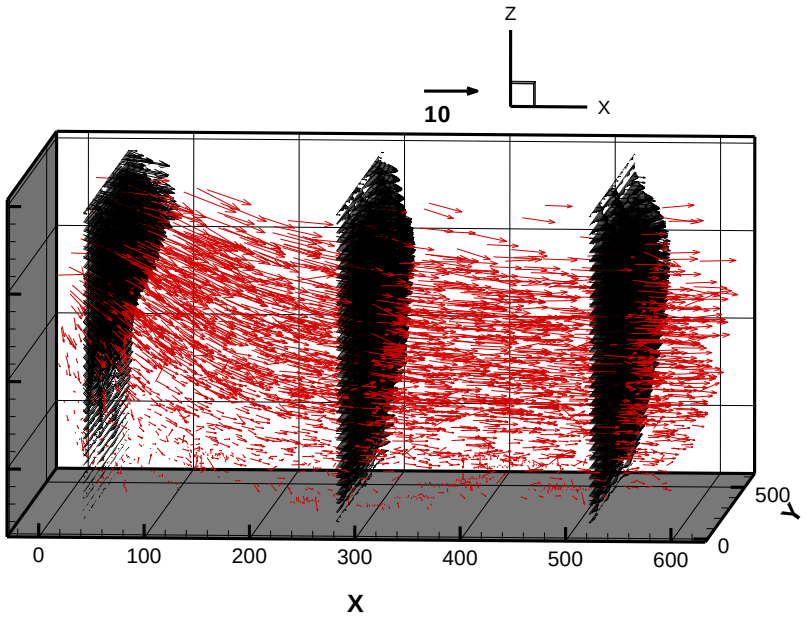

Figure 5-5 Resolved Backward-facing step flow field: Steady Flow Case. The Step is located at the origin.

5.2.2.2 Accelerating Flow

The second experiment is to explore the possibility to use only one image pair to resolve the flow field with reasonable spatial resolution for a unsteady flow. The unsteady backward-facing step flow is created by decelerating the constant flow rate at 150 µl/min by 12 step decrements at 12 µl/min, resulting a Reynolds number changing from 0.825 to 0.033. The syringe and the tubing provide a damping effect, so the flow is decelerating smoothly without step change. Figure 5-6 shows the vector filed of particle tracking results from the starting frame pair (Q = 150 µl/min). A total of 392 vectors are identified in an image pair, shown in the red vectors, and the corresponding interpolated vector field (black vectors) on a uniform grid of size of 40 µm x 40 µm x 30 µm. The spatial resolution is lower than the time-averaged case, but the flow features are still captured reasonably well. Figure 5-7 shows the vector field of particle

tracking results from the ending frame pair (Q = 6 µl/min). A total of 444 vectors are identified in a image pair, shown in the red vectors, and the corresponding interpolated vector field (black vectors) on a uniform grid of size of 40 µm x 40 µm x 30 µm.

These results indicate that the unsteady flow can be resolved with our 3-D µPTV technique. The velocity change is captured between frame pairs, as shown in Figure 5-6 and Figure 5-7 of the starting frame pair and the ending frame pair, respectively.

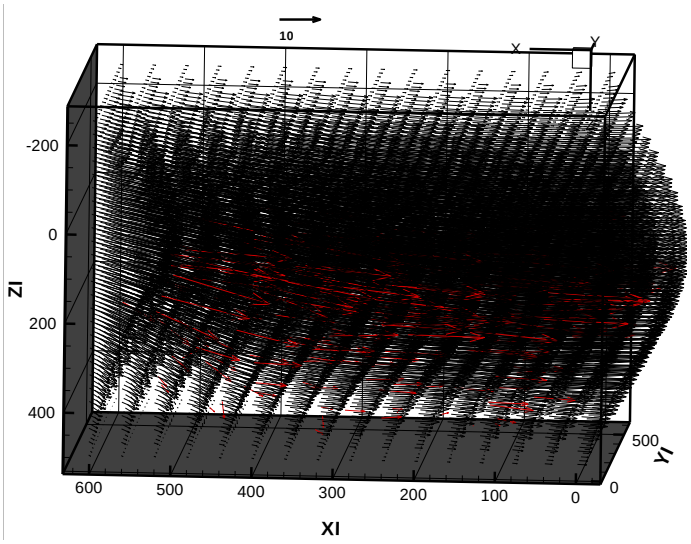

Figure 5-6 Resolved Backward-facing step flow field: Decelerating Flow at the start

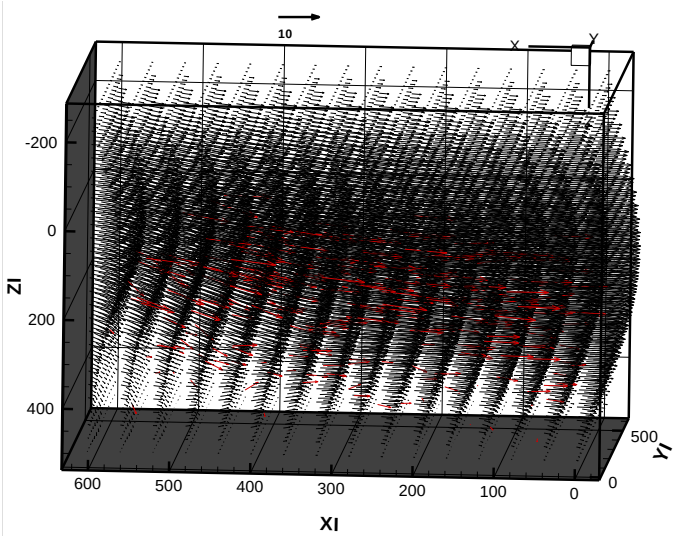

Figure 5-7 Resolved Backward-facing step flow field: Decelerating Flow at the end

5.3 **Flow around a Hydrodynamic Tweezers**

5.3.1 **Background**

Hydrodynamic tweezers, proposed by Lutz *et al.* (B. R. Lutz, Chen, & Schwartz, 2006), is a noncontact method that utilizes the secondary flow to trap and suspend single cells. Generated by audible-frequency fluid oscillation in a micro-channel, the micro-eddies around an obstacle can capture single cells and suspend them at predictable locations. Steady streaming refers to time averaging the Navier-Stokes equations produces average stresses that drive a steady secondary flow around obstructions. Adjacent to the circular cylinder inside the micro-channel, four steady eddies can be formed symmetrically, as shown in Figure 5-8. By choosing appropriate frequencies to oscillate the flow, object of certain size can be trapped inside these eddies due to the balance of time-averaged Lagrangian drift force to the Stokes drag force. Compare to other nonintrusive methods like optical tweezers, dielectrophoretic traps or acoustical tweezers, this technique can output comparable magnitude of trapping force without the need of additional eternal field and operates at conditions within the physiological range for typical cells. This technique is well suited for cell separation, filtering and single cell analysis. To demonstrate the feasibility of the concept, a motile phytoplankton (Prorocentrum micans cell) is put to the micro-channel filled with sea water, and the cell is successfully trapped and released by changing the oscillation amplitude and frequency, as shown in Figure 5-9. Experimental results show that trapping forces up to 30pN are generated while exerting moderate shear stresses ($\leq$1.5N/m^2) on the trapped cell.

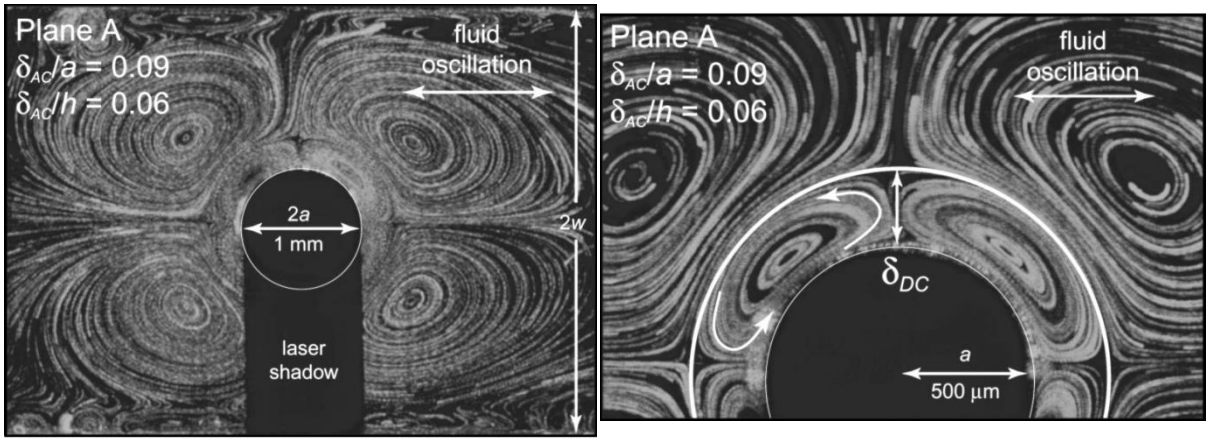

Figure 5-8 Flow Visualization Results of the steady streaming particle path line (a) Extended View of full channel width (b) close-up view around the cylinder. From Lutz *et al.* (2005)

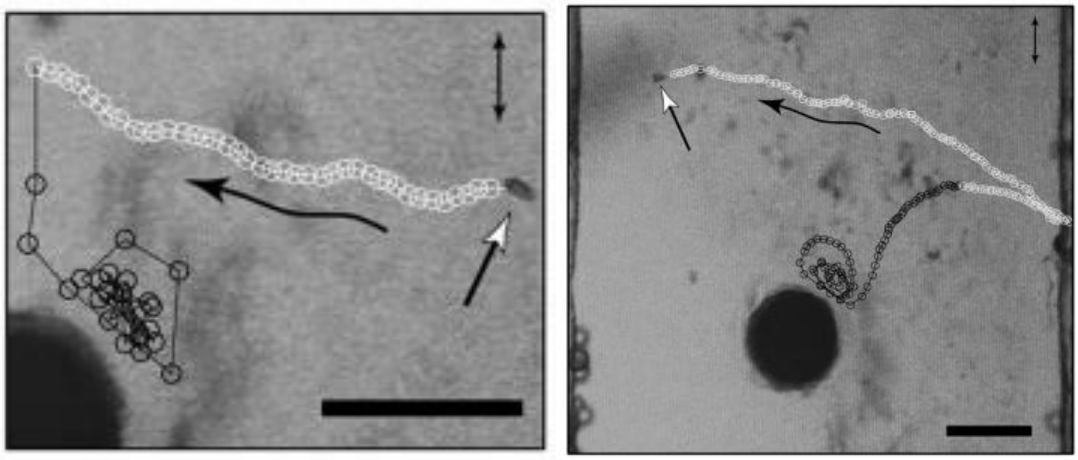

Figure 5-9 Trapping of P. micans cell: (a) Cell trapped to the cylinder after flow oscillation (b) cell escaping from the cylinder by step decrement of oscillation amplitude. From Lutz *et al.* (2006)

Although the technique has been proved to be highly feasible, the physics behind it is still not fully understood. Lutz *et al.* (2005) performed a flow visualization experiment with a scale-up model to image the steady streaming behavior near a single cylinder in an oscillating flow inside a rectangular channel. The flow behavior is characterized by several parameters: the channel height h, diameter of the cylinder a, the Stokes layer thickness δ_{AC}, which is related to the oscillating flow, and the boundary layer thickness δ_{DC}, which is related to the near-cylinder eddy size. They found that when δ_{AC}/h is small, the flow in the core region of the channel is not affected by the wall effect and the flow behavior can be simulated by 2D steady streaming

around a cylinder in an unbounded flow. However, outside the core region the flow is 3-D and strongly affected by the wall. Lieu *et al.* (2011) tested this technique with arrays of cylinders in the micro-channel and found that steady streaming form a cellular pattern in the channel and agree with the 2-D simulation results in the core region. Wall protrusion and cavity were also proved to be able to trap particles or cells, but the latter with much weaker trapping force.

Due to the limitation of the visualization technique, these previous studies are focused on the flow patterns observed by a 2-D slice of the flow, or the streak lines formed by long exposures of the particle images. As shown in the 2-D flow visualization results in Lutz *et al.* (2005) the flow is three-dimensional but only confined in a thin layer, but it is a scaled-up model and is made of rigid material. The question is whether the flow shows the same characteristics under the small scale model made of compliant material. To answer this question, the 3-D μPTV technique is applied to measure the flow around the hydrodynamic tweezers to investigate the flow phenomenon.

5.3.2 **Micro-channel Setup**

In the current study, the micro-channel used was made of PDMS (Polydimethylsiloxane) using softlitography method (Anderson, Chiu, Wu, Schueller, & Whitesides, 2000; Duffy, McDonald, Schueller, & Whitesides, 1998). The PDMS channel was molded from a master of epoxy-based negative photoresist (SU-8) and plasma bounded to a drilled coverslip on one side and a glass slide on the other side, as shown in Figure 5-10 (a). The SU-8 master was made by contact lithography and the details can be found in Lieu *et al.* (2011). The drilled coverslip provides access to load the fluid and tracer particles. Two single layer piezoelectric disks were attached on top of the coverslip, right above the cavities in the micro-channel, as shown in Figure 5-10 (c). The piezoelectric disks were connected to an audio amplifier and a function generator.

The function generator generated a sinusoidal voltage signal at audio frequency (1KHz – 20KHz), amplified by the audio amplifier and drove the piezoelectric disk to vibrates at a displacement amplitudes of 1-3 µm. The vibration was transferred into the cavities in the micro-channel and created the oscillating flow required to produce the steady streaming flow.

The micro-channel is 150µm high and 1000µm wide, and a length of 30mm. The cylinder posts were in the middle of the channel and formed an array pattern. The post size and pattern varies for each testing case. Two sizes of cylinder post were tested: 50 or 150µm in diameter. For the array cases and the single post case, respectively (Please refer to Figure 5-10 (b)). There are two patterns of array design investigated in the current work: In-line array or staggered array. For the in-line array the spacing between the posts is 120 µm. For stagger array, the spacing between the posts in the same row is 200 µm, and the spacing between the adjacent rows is 100 µm.

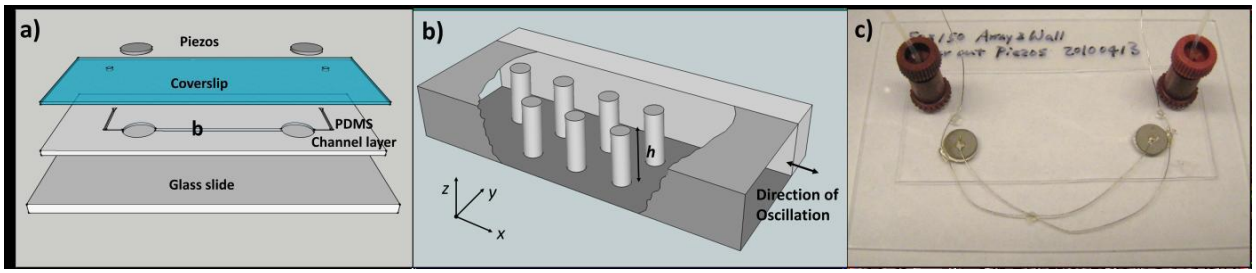

Figure 5-10 Setup of the trapping micro-channel with micro cylinder array. From Lieu *et al.* (2011)

5.3.3 **3-D µPTV System Setup**

The magnification of the current imaging system are suitable to the dimensions of the microfluidic device of the hydrodynamic tweezers, thus the modification needed is minimal. The pinhole diameter adapted is 2.53mm, results in a measurable image depth of 240 µm to cover 150µm full height of the channel. The measurable imaging volume therefore is 600 ×600×240

μm. The exposure time of the CCD camera was set to 4.2 ms and 700 frames of image were taken for each testing case to ensure good image qualities.

A glass slide spin-coated with a PDMS layer of the same thickness to the device was used for calibration to match the index of refraction. 1μm polystyrene particles (Fluoresbrite® Multifluorescent Microspheres) were used as tracer particles (ρ_p = 1.05 g/cm3) in water for the current study. The Stokes number defined as

$$St = 2{d_p}^2 \rho_p \omega / 9\mu, \quad (5\text{-}1)$$

where ω is the frequency of the oscillation, μ is the fluid dynamic viscosity. The calculated Stokes number is 0.00012 ~ 0.0023 at the audio frequency range and is negligible.

5.3.4 **Results**

The raw images were processed with the method described in chapter 3 and 4 to reconstruct the 3-D flow field. To visualize and flow better and compute derivative properties such as vorticity, the velocity field resolved by particle tracking was interpolated to uniform grid using an inverse-distance interpolation scheme, which weights the neighboring points proportional to the inverse of distance to the point to calculate. The interpolated grid size is 10 ×10 × 10 μm. In all results shown the oscillation is on the *X* direction.

5.3.4.1 Single Post

Figure 5-11 shows the reconstructed 3-D flow field of a single post configuration at oscillation frequency of 1260Hz, with 3-D velocity vectors shown at selected planes. The 4 eddies formed near the corner of the cylinder post can be observed from the *X*-*Y* plane vectors (in blue). The vectors on the *Y*-*Z* plane (in red) and *X*-*Z* plane (in green) shows that flow direction

was towards the post in *X* direction (the oscillation direction) and away from the post in *Y* direction.

Figure 5-12 shows the 2-D velocity field at different *Y*-*Z* planes of the single post configuration. The velocity vectors shown are the *Y* and *Z* components. *X*=300 (Figure 5-12 (c)) is the cross-section pass through the center of the post. Near the top of the cylinder, the corner formed by the top surface of the channel and the cylinder post created the corner flow pattern. The main flow was moving out on the middle section ($Z \approx 100\sim150$) and flow decelerated around 1D location (distance normalized by the post diameter D). At *X*=400 (Figure 5-12 (b)), flow was mainly up and towards post near the post region, and relatively slow in the outer region. At *X*=500 (Figure 5-12 (a)), the trend of flow was similar to *X*=400. Flow moved towards the post region but the magnitude was smaller.

Figure 5-13 shows the 2-D velocity field at different *X*-*Z* planes of the single post configuration. At the center plane of the post (*Y*=300, Figure 5-13 (a)), flow was towards the post but no corner flow pattern as observed in the *Y*-*Z* plane. Strong rotational flow was observed at *Y*=200 (Figure 5-13 (b)), forming the flow away from the post in the middle section of the channel. At *Y*=100 (Figure 5-13 (c)), flow was further reduced and no particular pattern can be observed.

Figure 5-14 to Figure 5-16 shows the 2-D velocity field at different *X*-*Y* planes of the single post configuration, overlaid with the *Z* component of the vorticity contour. In this view the four eddies can be easily observed, with strong vorticity present at the eddy region. The eddies were weaker at the top region (*Z*=177.5, Figure 5-16) and bottom region (*Z*=92.5, Figure 5-14). The vorticity map shows roughly the eddy size which extends to 1.3D. The velocities at the

dividing stream line, which is aligned with the center of the post, decreased to ambient level around 2.7D.

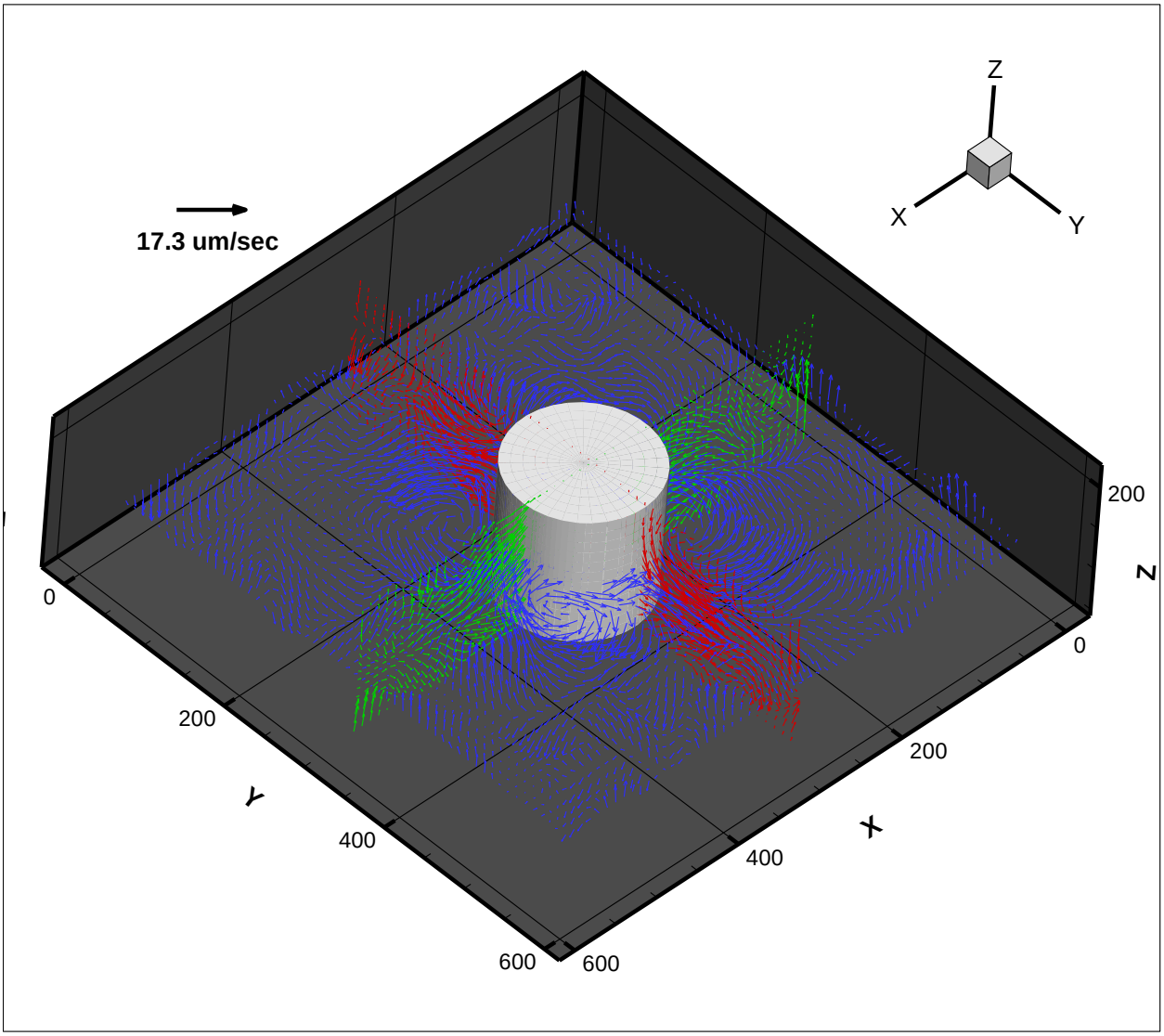

Figure 5-11 reconstructed 3-D Flow field of single post configuration at 1260Hz. Only a slice of vector field for each X-Y, Y-Z and X-Z plane is shown

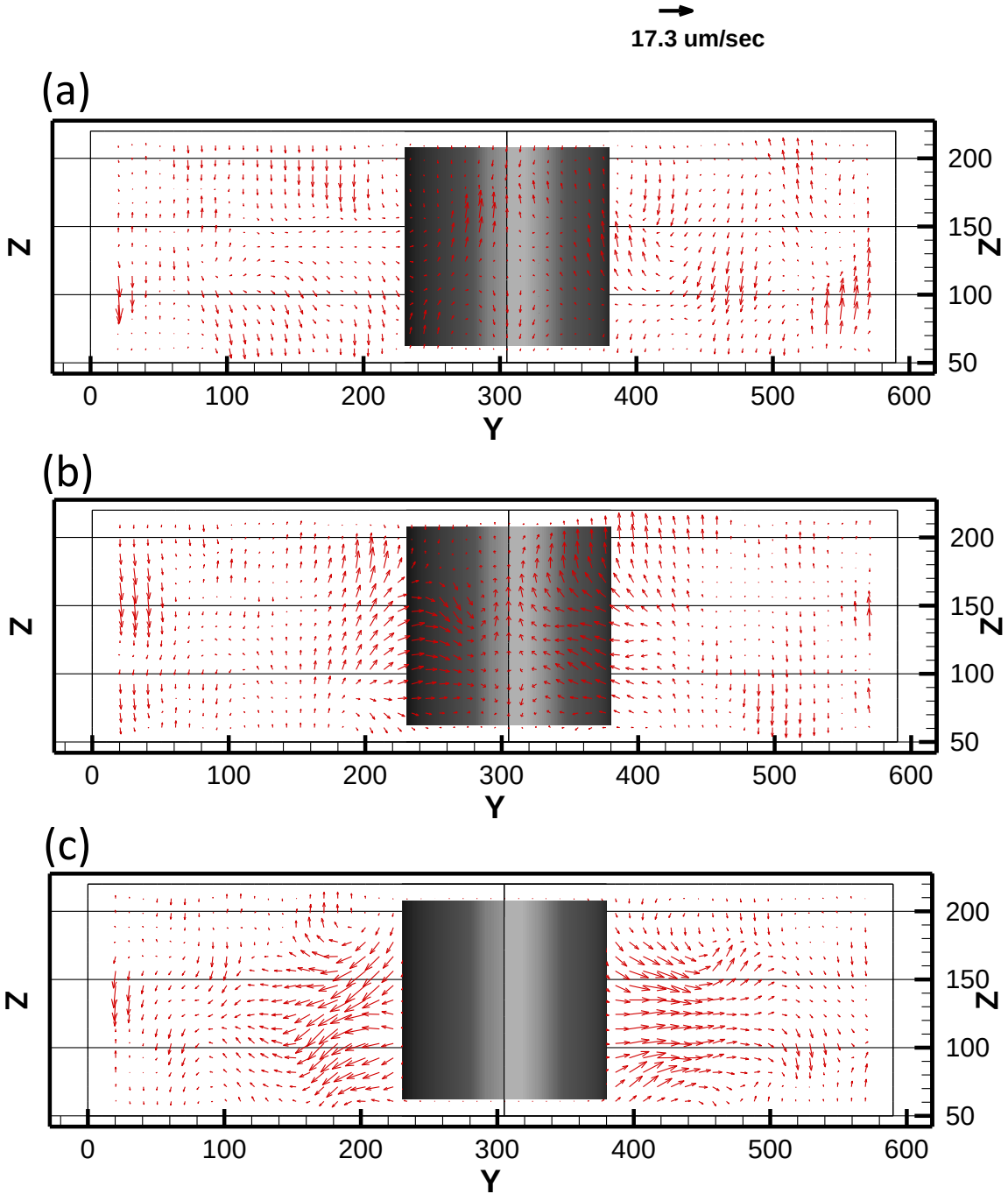

Figure 5-12 Velocity Profile at different Y-Z planes of the single large post configuration: (a) X=500(b) X=400 (c) X=300.

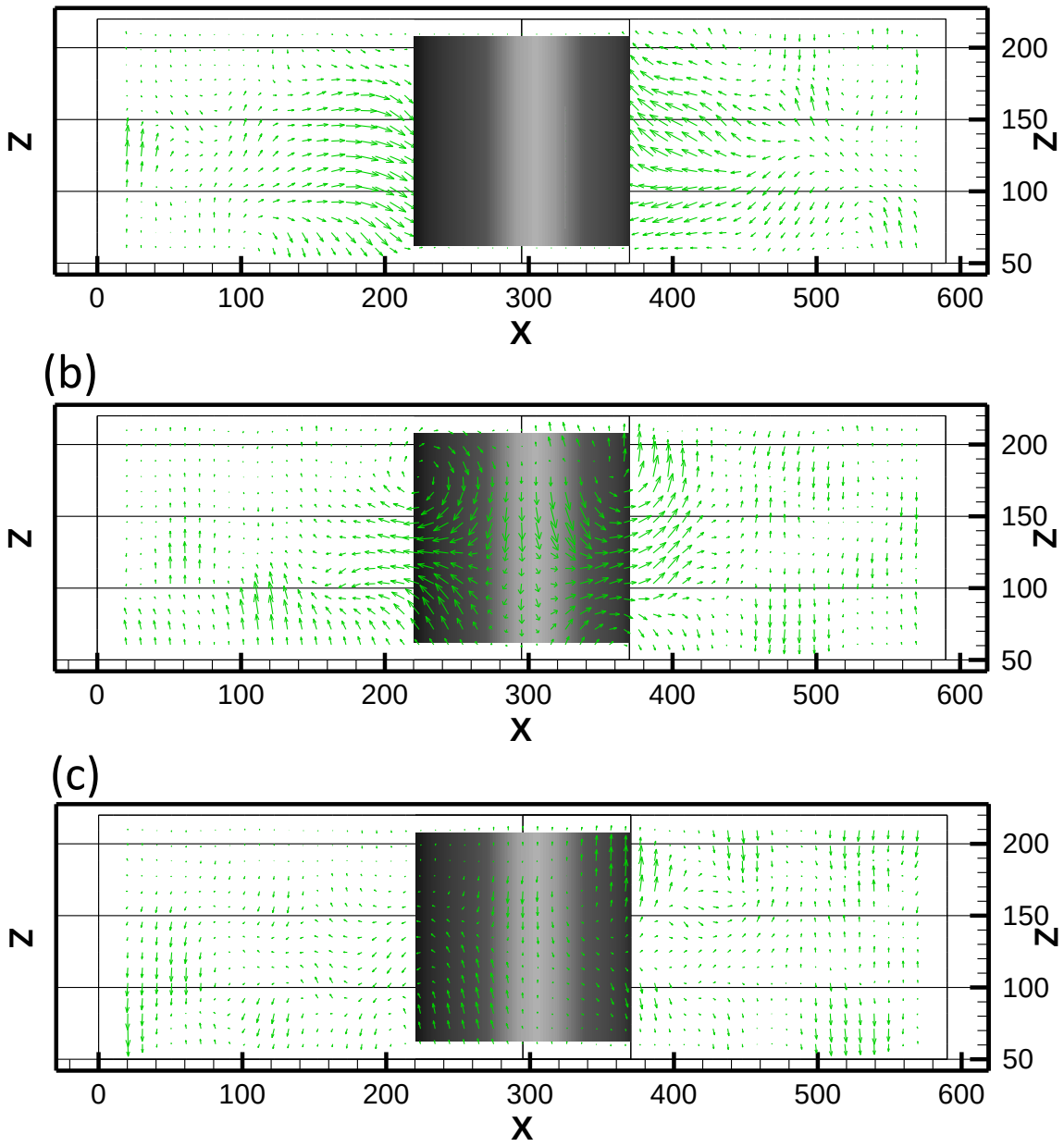

Figure 5-13 Velocity Profile at different X-Z planes of the single large post configuration: (a) Y=300(b) Y=200 (c) Y=100.

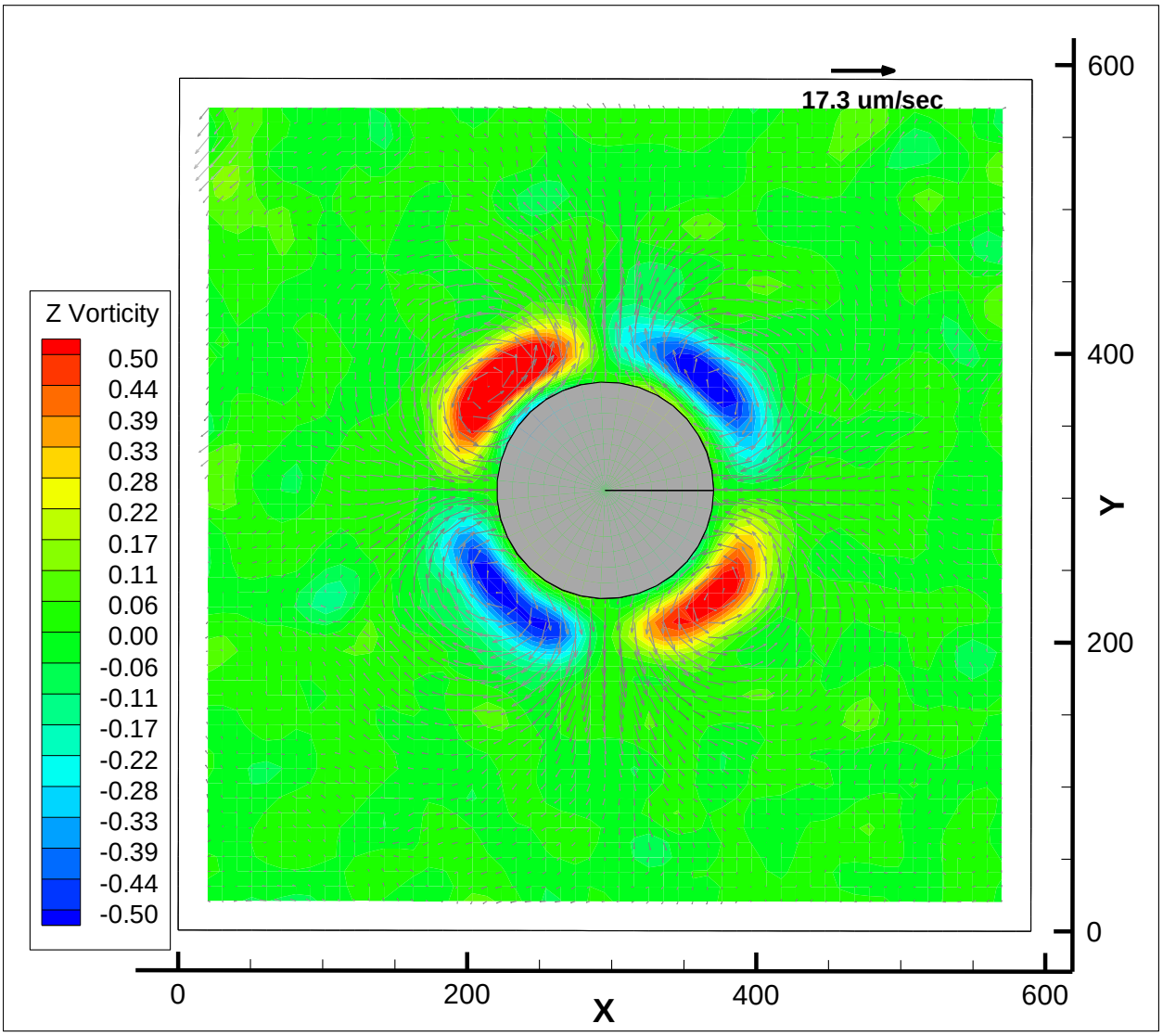

Figure 5-14 Velocity Profile at X-Y plane of the single large post configuration at Z= 92.5. The W component is shown in gray scale on the vector and the Z vorticity is shown as contour plot on the back ground.

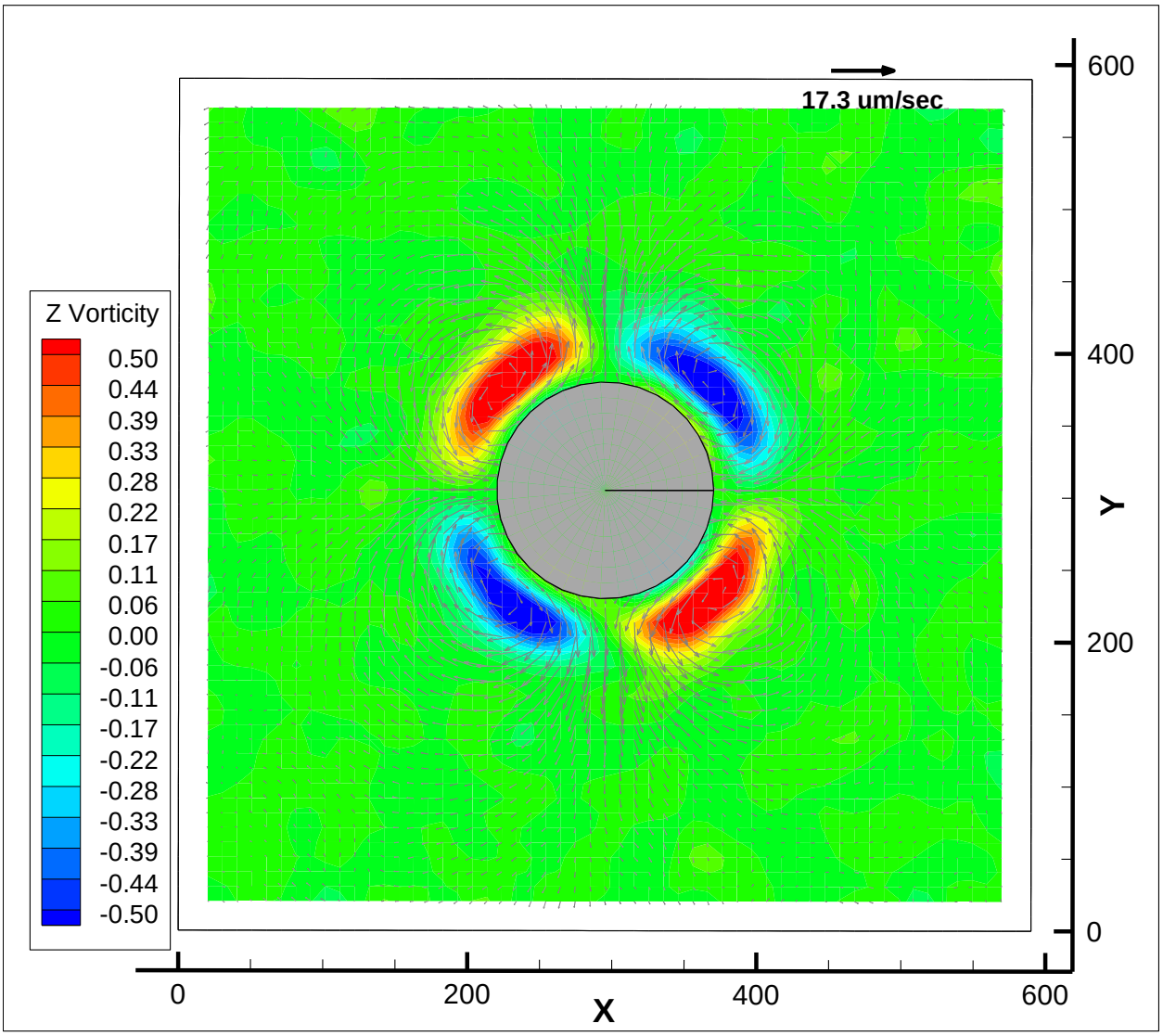

Figure 5-15 Velocity Profile at X-Y plane of the single large post configuration at Z= 135. The W component is shown in gray scale on the vector and the Z vorticity is shown as contour plot on the back ground.

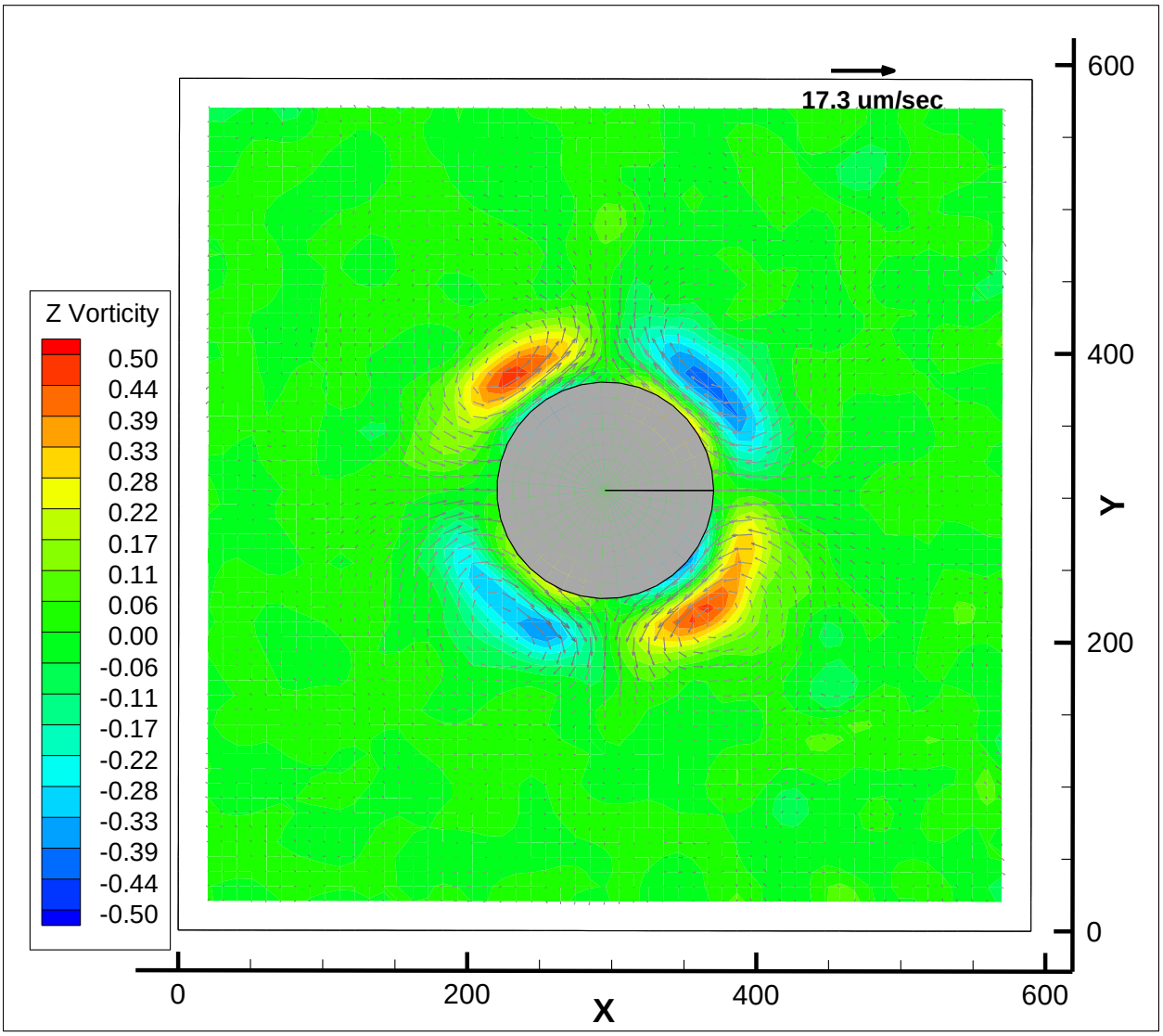

Figure 5-16 Velocity Profile at X-Y plane of the single large post configuration at Z= 177.5. The W component is shown in gray scale on the vector and the Z vorticity is shown as contour plot on the back ground.

5.3.4.2 Array Posts

5.3.4.2.1 In-line array

Figure 5-17 shows the reconstructed 3-D flow field of an in-line array post configuration at oscillation frequency of 2840Hz. The main feature observed is that the flow formed a cell-like structure around each post. Because of the tight spacing, the eddies were confined to the cell and

dividing stream lines are formed in between each cell. The flow patterns were also more three dimensional.

Slices of the flow field at *Y-Z* plane of the in-line array post configuration are shown in Figure 5-18 to Figure 5-22. The *X* locations of the cross-section are chosen to show the variation of the flow field around a single post in the array. The *X* vorticity map is also shown in each figure, and the out-of-plane velocity vector (the *X* component) is shown in grayscale to help to demonstrate the 3-D flow pattern. The flow at the post center cross-section (*X*=50, Figure 5-18) shows that the flow was symmetric across the *Z* direction, and the flow direction was away from the post. The flows from the adjacent post meet together and formed a dividing streamline in the middle of the two posts. The vorticity map shows 4 major vorticity concentrated regions and they were located at the four corners in between the two adjacent posts. As *X* increases, the flow direction turned around between *X*=70 (Figure 5-19) and *X*=90(Figure 5-20). This turning also resulted in a change sign of the *X* vorticity and formed an inversed vorticity pattern. Although without the posts, at *X*=110 and 130 (Figure 5-21 and Figure 5-22), the flow pattern was still aligned well with the post, forming the dividing stream plane aligned with the center of the post.

Slices of the flow field at *X-Z* plane of the in-line array post configuration are shown in Figure 5-23 to Figure 5-27. Similar to the *Y-Z* planes, the *X-Z* planes are selected to show the flow variations inside the cell and vorticity map is overlaid with the vector plot. At *Y*=210(Figure 5-23), Flow direction was towards the post from the dividing stream plane in the middle of the two post (the 2nd post is not shown in the scale up picture). As *Y* decreased, the flow turned around between *Y* =195(Figure 5-24) and *Y*=180 (Figure 5-25). At *Y*=165 (Figure 5-26) and *Y*=150 (Figure 5-27), four vorticity concentrated regions were formed and the dividing stream plane was formed at the *X* location of the post.

Figure 5-28 to Figure 5-30 shows the 2-D velocity field at different *X*-*Y* planes of the in-line array post configuration, overlaid with the *Z* component of the vorticity contour and the W component of velocity is shown in gray scale together with the velocity vectors of U and V components. Closer to the bottom of the channel (*Z*=122.5, Figure 5-28), the *Z* vorticity was lower than those at the middle and top section of the channel (*Z*=160, Figure 5-29 and *Z*=197.5, Figure 5-30). The cell structure was at its strongest at *Z*=160 (Figure 5-29), and the cell structure is easily observed on the velocity vector plot. The vorticity was concentrated and almost filled the entire cell. The flow maintained the same level of velocity magnitude at the dividing stream planes and formed clear dividing stream planes.

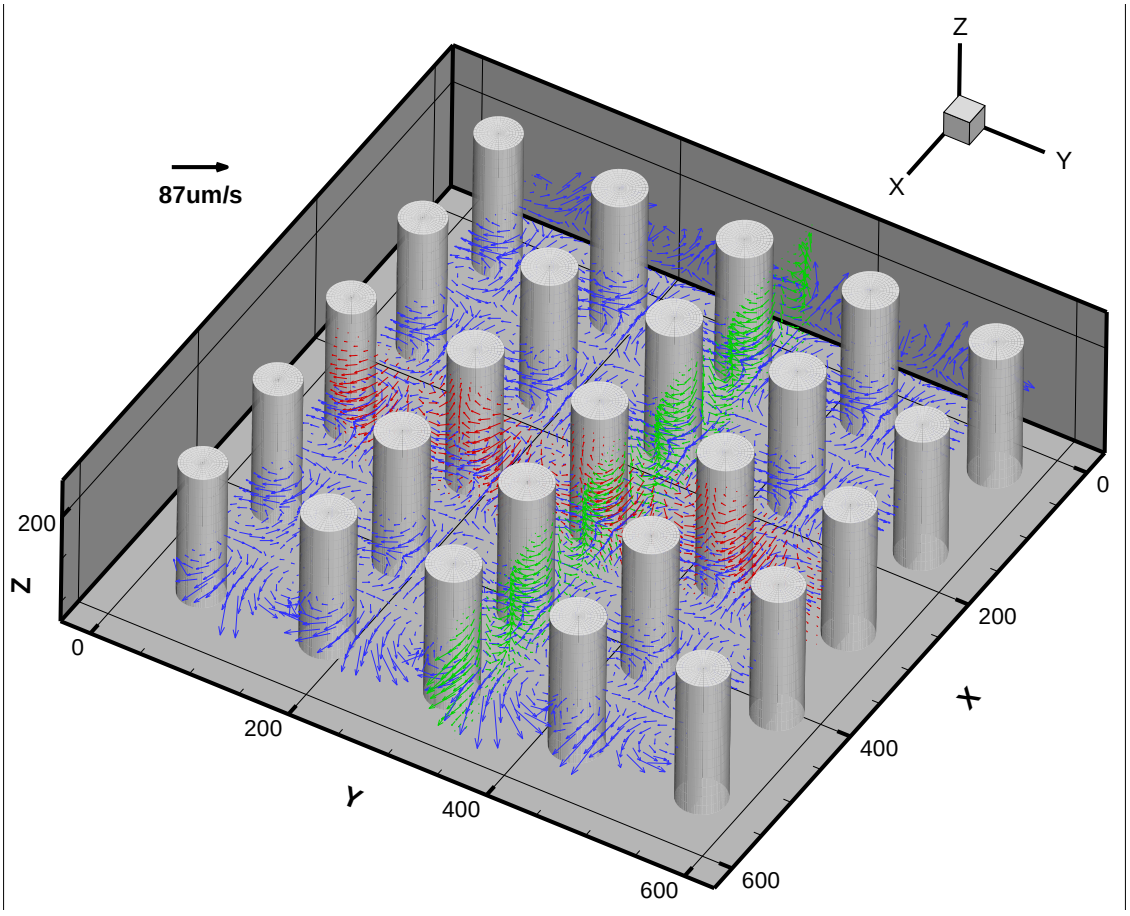

Figure 5-17 reconstructed 3-D Flow field of in-line array configuration at 2840Hz. Only a slice of vector field for each X-Y, Y-Z and X-Z plane is shown

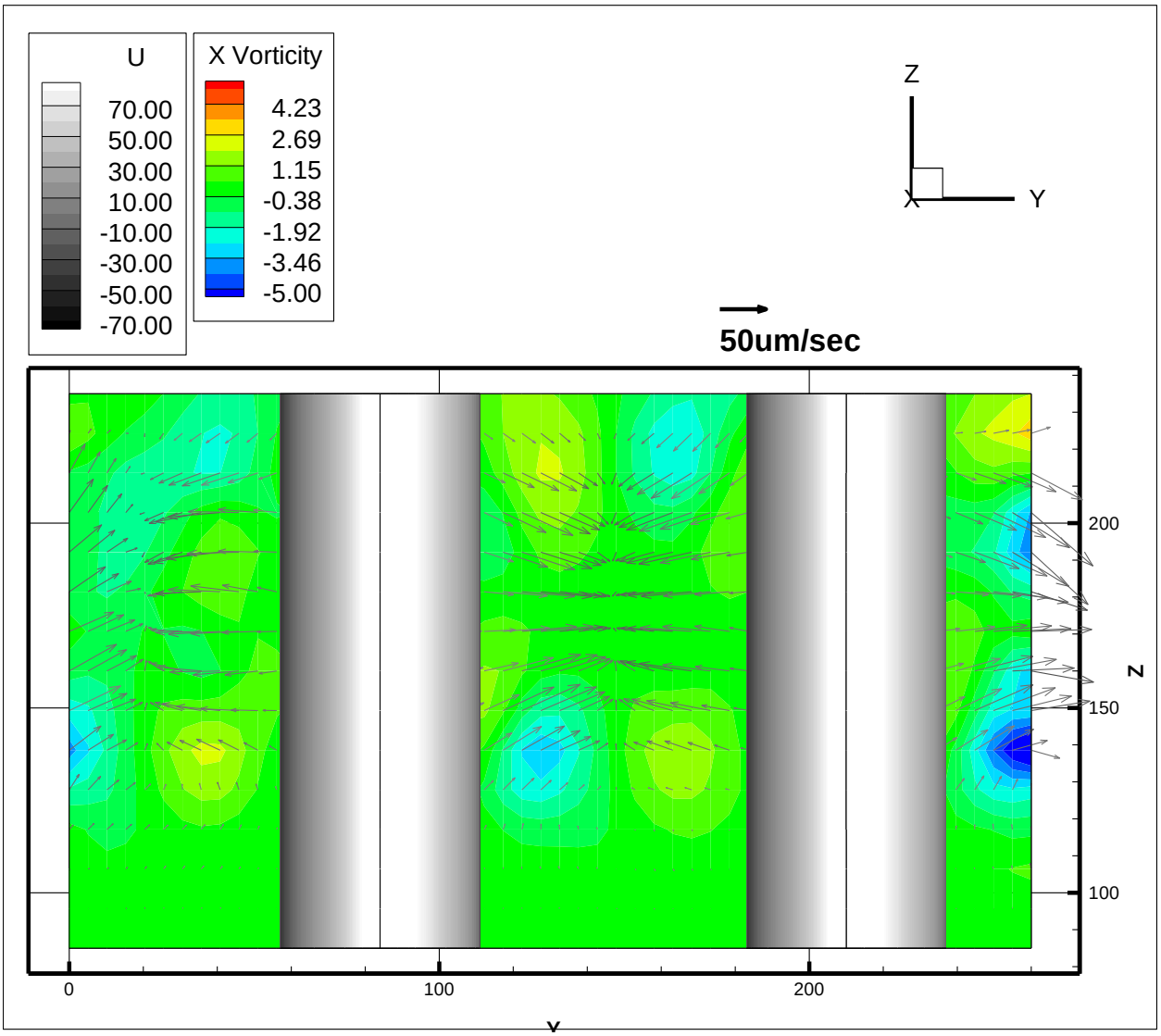

Figure 5-18 Partial Velocity Profile at Y-Z plane of the in-line array post configuration at X= 50. U component is shown by the gray scale and the X vorticity is shown by contour plot on the background

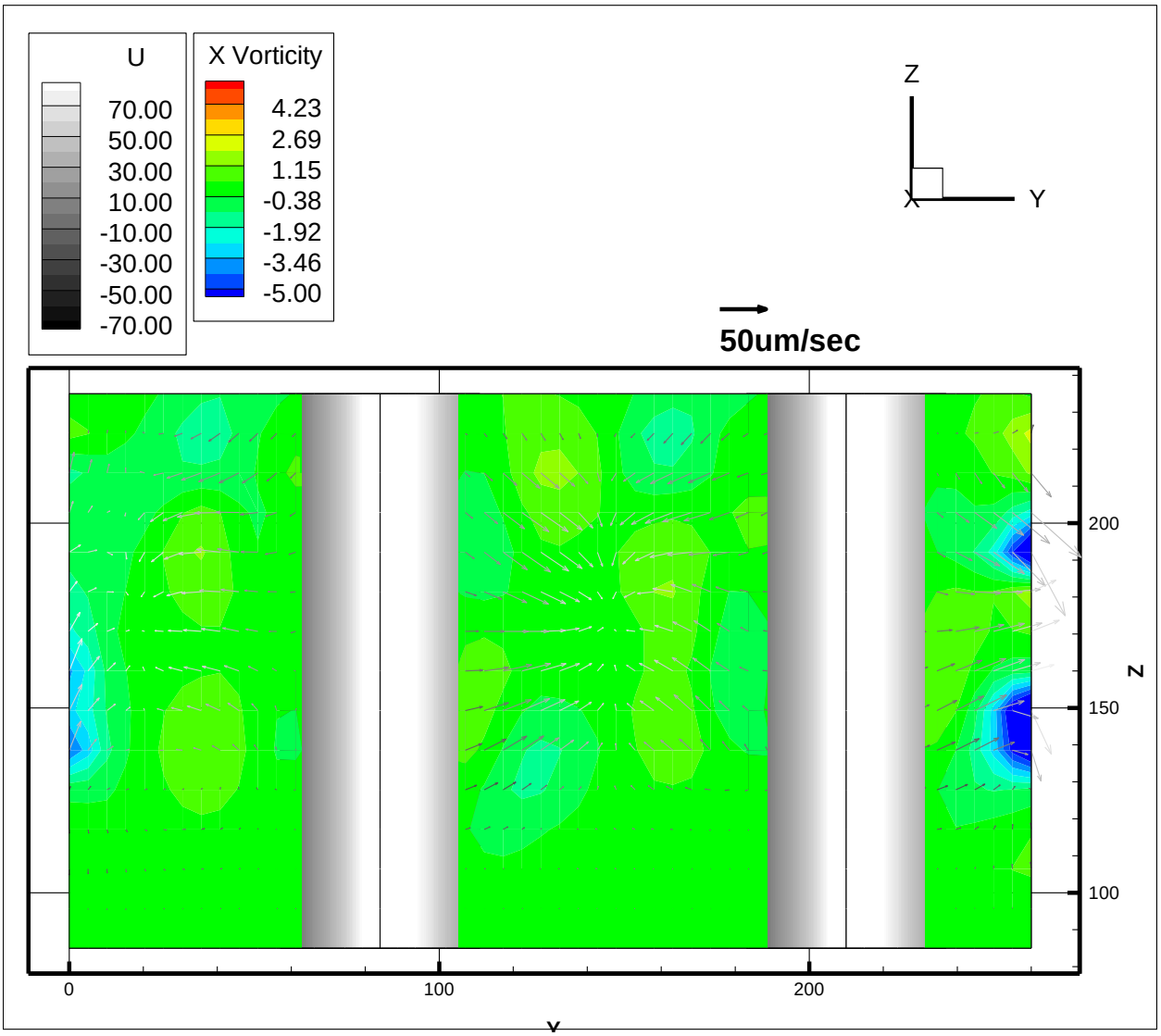

Figure 5-19 Partial Velocity Profile at Y-Z plane of the in-line array post configuration at X= 70. U component is shown by the gray scale and the X vorticity is shown by contour plot on the background

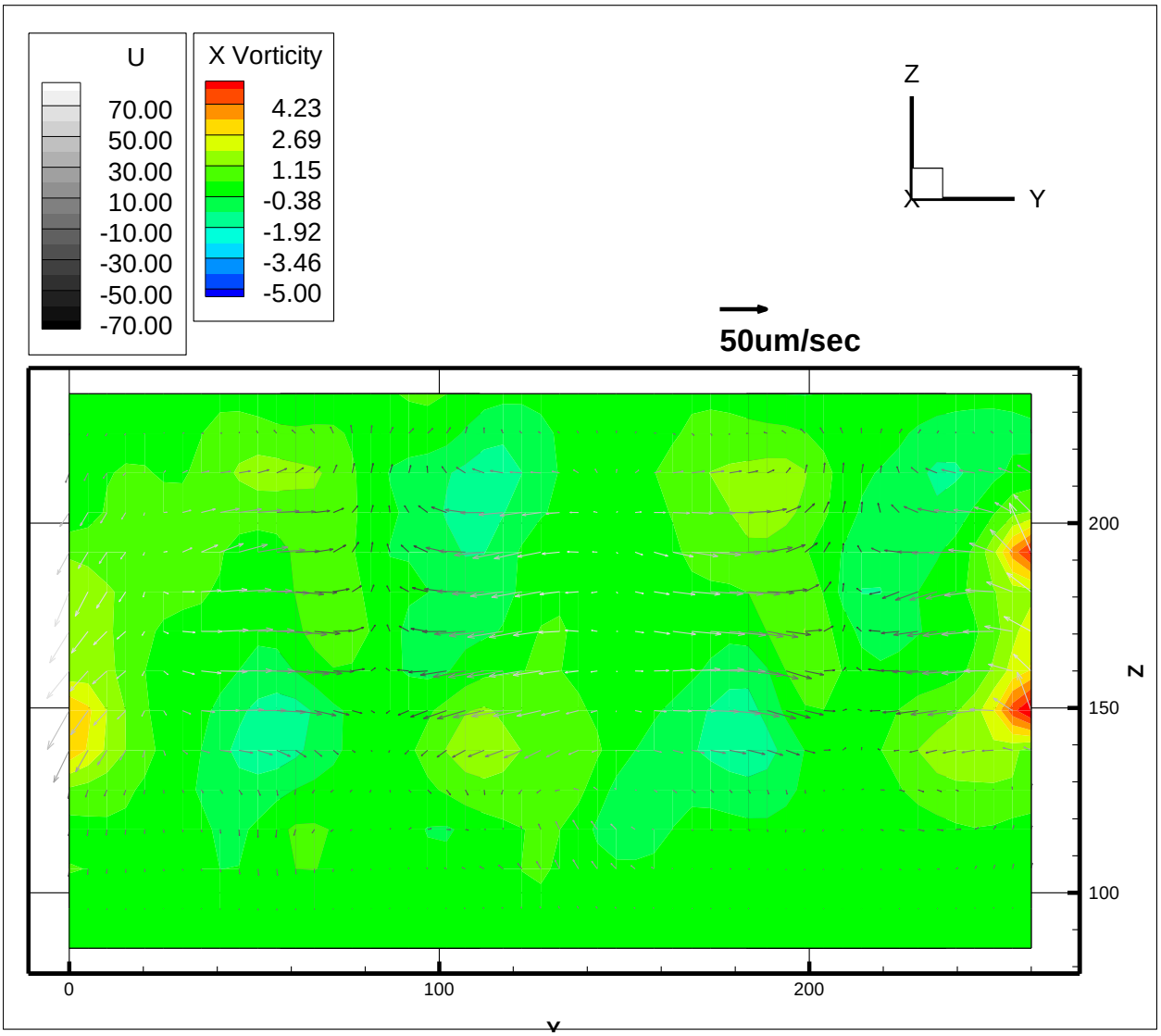

Figure 5-20 Partial Velocity Profile at Y-Z plane of the in-line array post configuration at X= 90. U component is shown by the gray scale and the X vorticity is shown by contour plot on the background

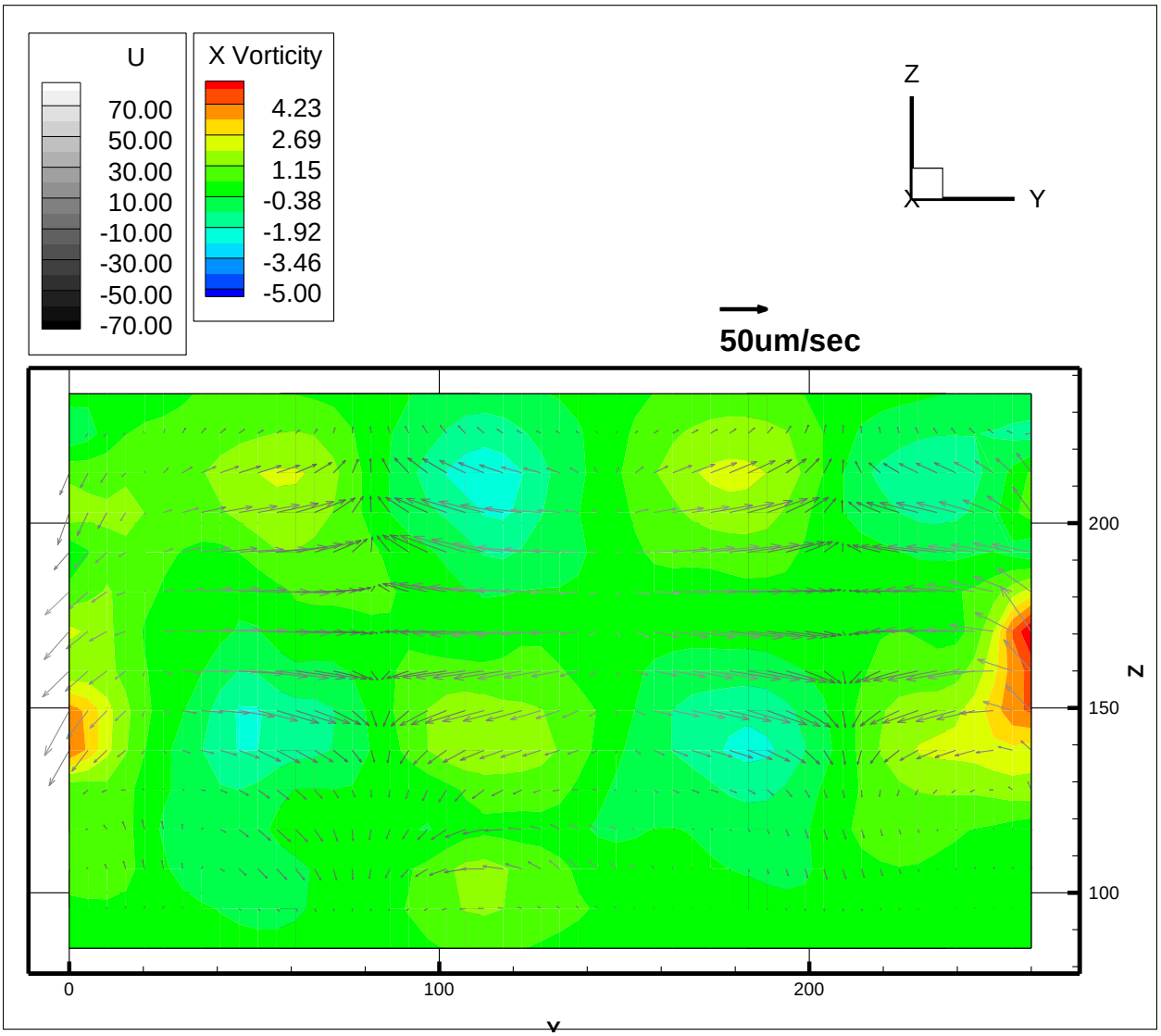

Figure 5-21 Partial Velocity Profile at Y-Z plane of the in-line array post configuration at X= 110. U component is shown by the gray scale and the X vorticity is shown by contour plot on the background

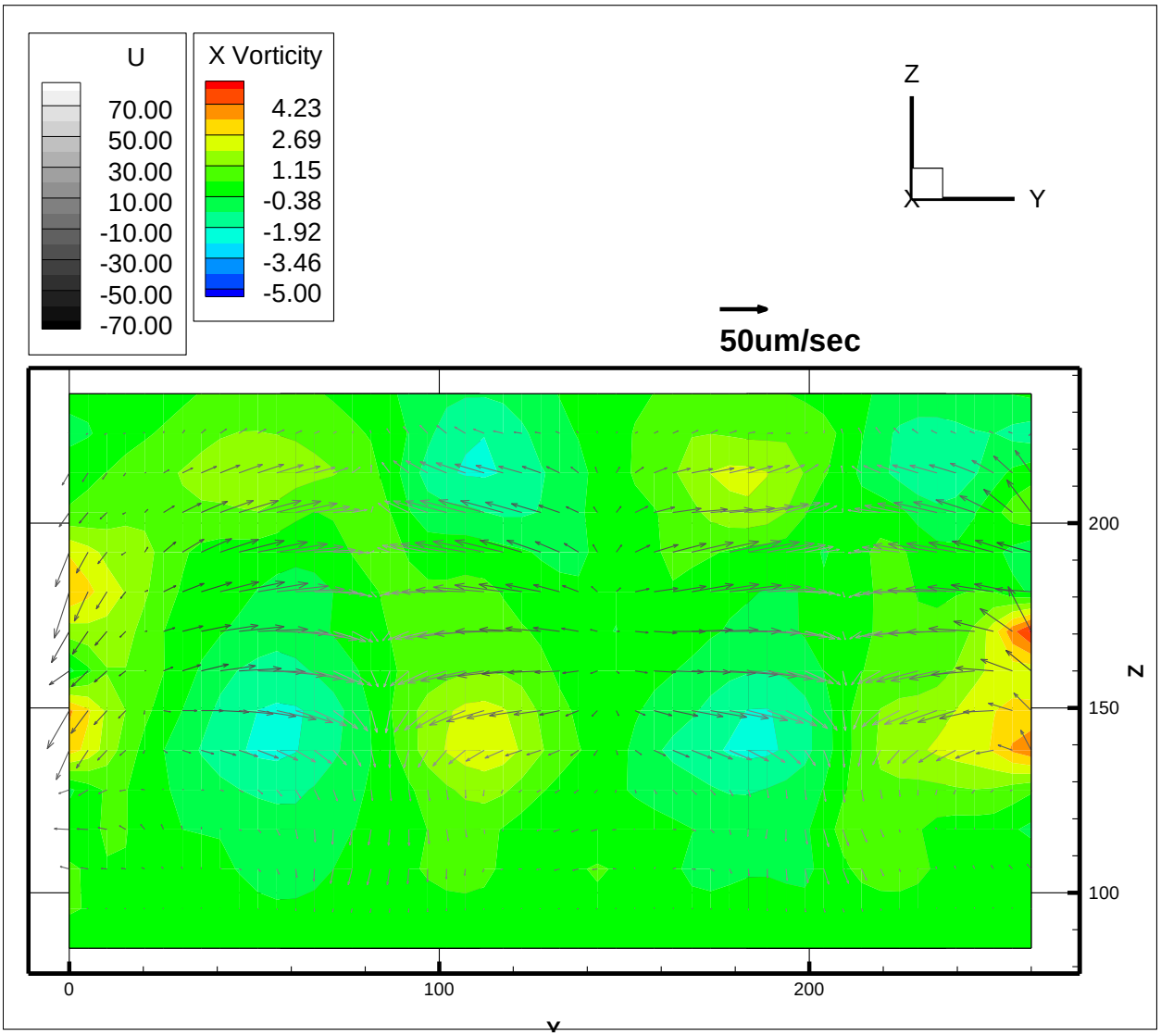

Figure 5-22 Partial Velocity Profile at Y-Z plane of the in-line array post configuration at X= 130. U component is shown by the gray scale and the X vorticity is shown by contour plot on the background

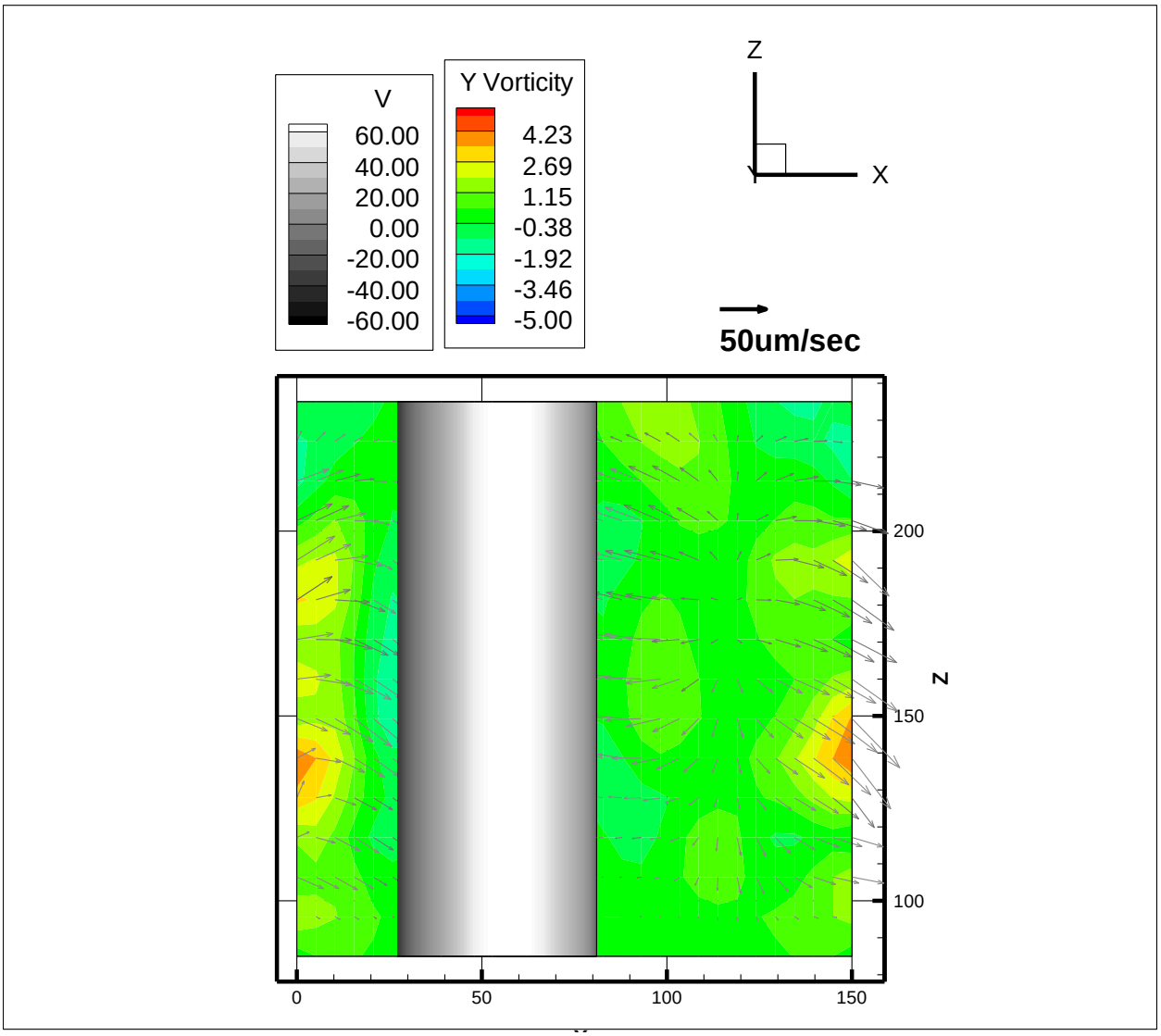

Figure 5-23 Partial Velocity Profile at X-Z plane of the in-line array post configuration at Y= 210. V component is shown by the gray scale and the Y vorticity is shown by contour plot on the background

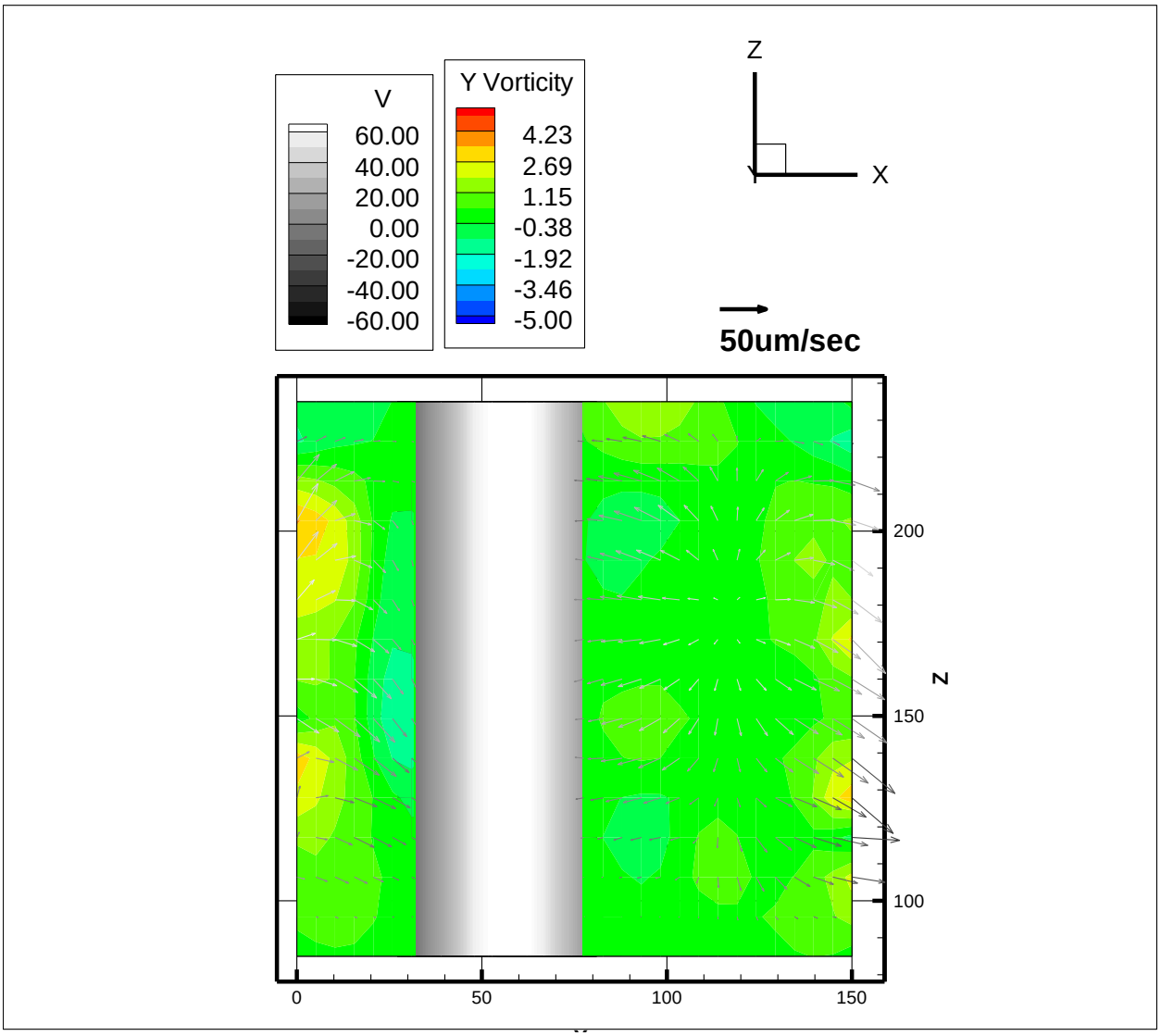

Figure 5-24 Partial Velocity Profile at X-Z plane of the in-line array post configuration at Y= 195. V component is shown by the gray scale and the Y vorticity is shown by contour plot on the background

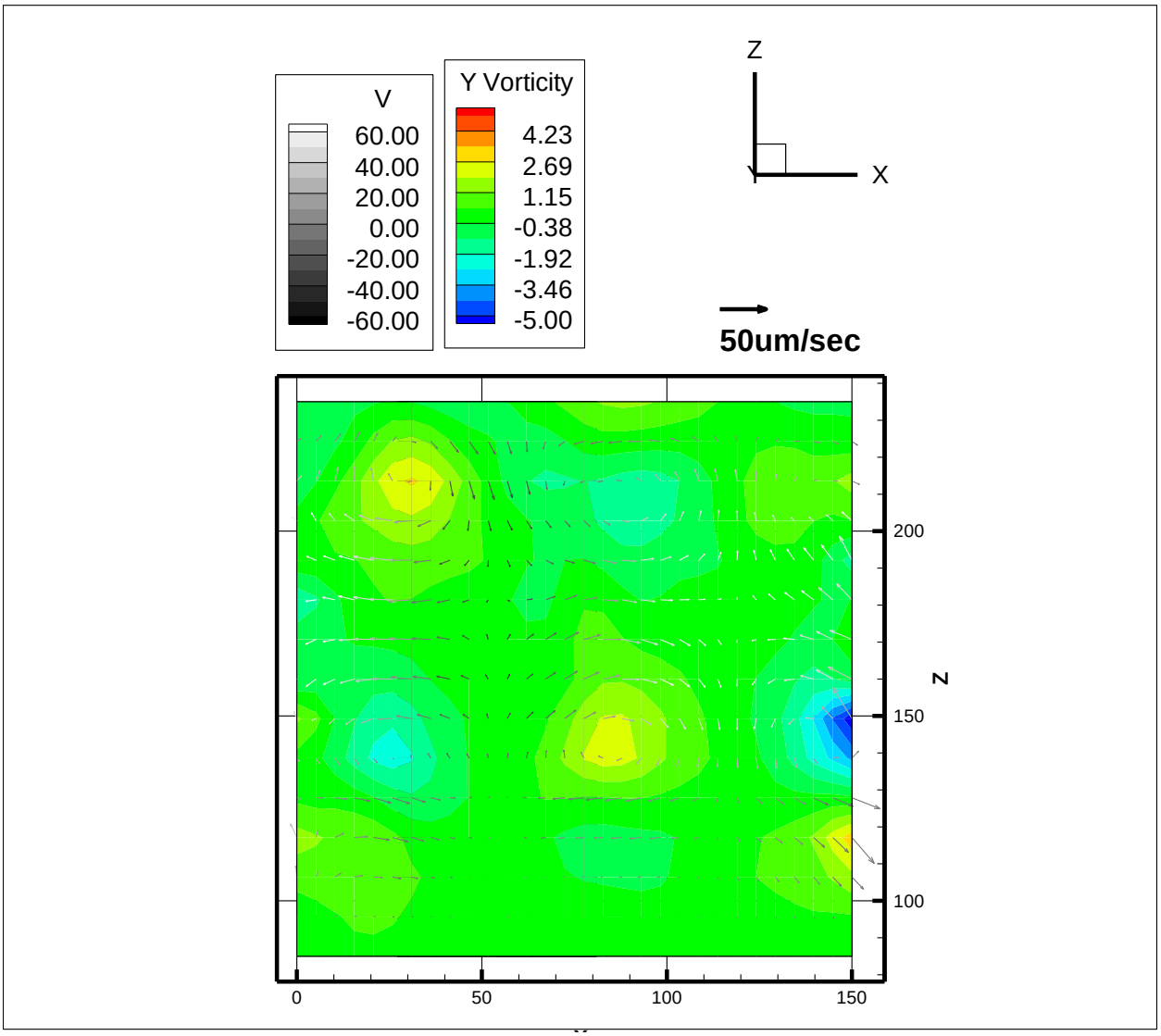

Figure 5-25 Partial Velocity Profile at X-Z plane of the in-line array post configuration at Y= 180. V component is shown by the gray scale and the Y vorticity is shown by contour plot on the background

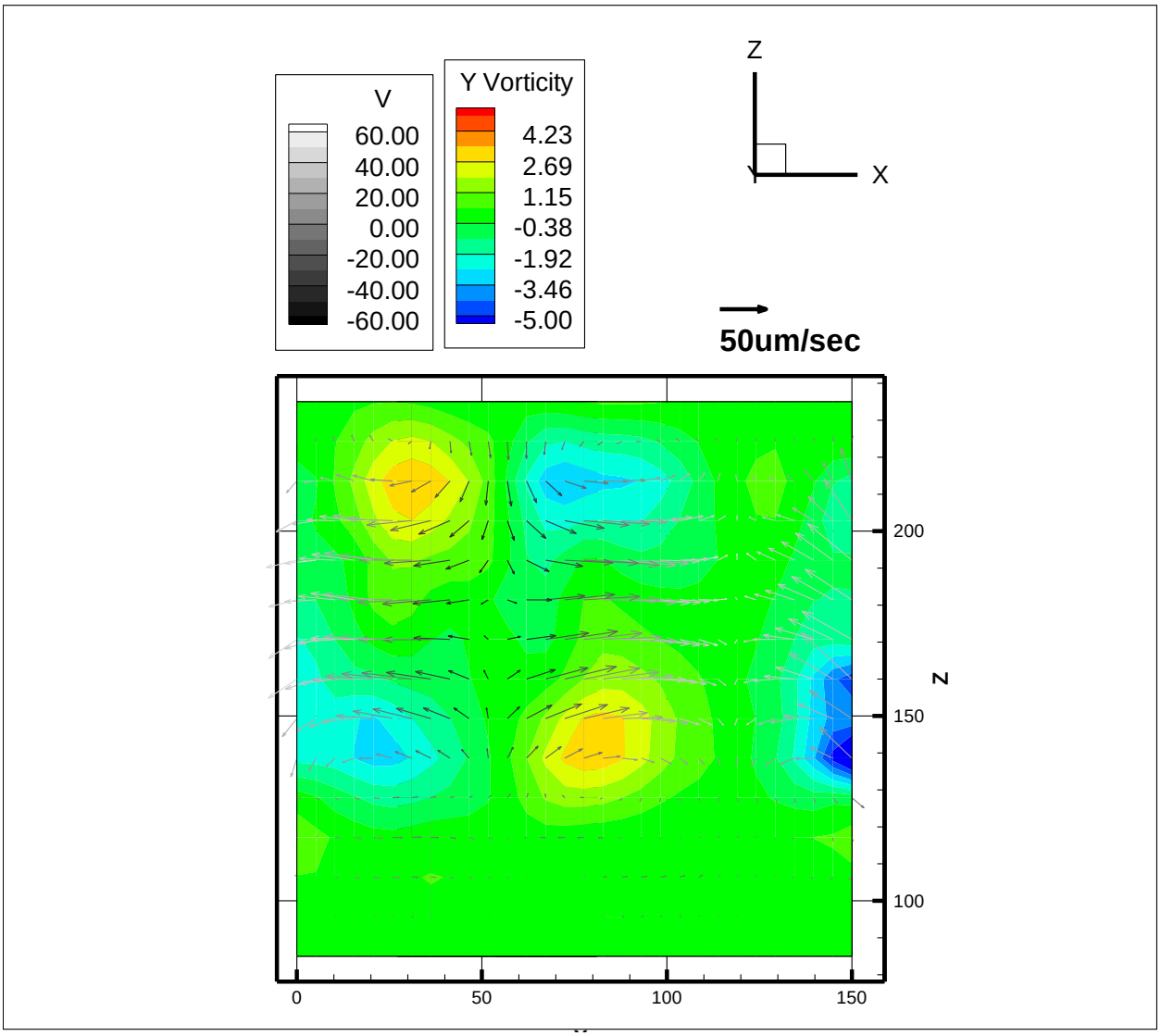

Figure 5-26 Partial Velocity Profile at X-Z plane of the in-line array post configuration at Y= 165. V component is shown by the gray scale and the Y vorticity is shown by contour plot on the background

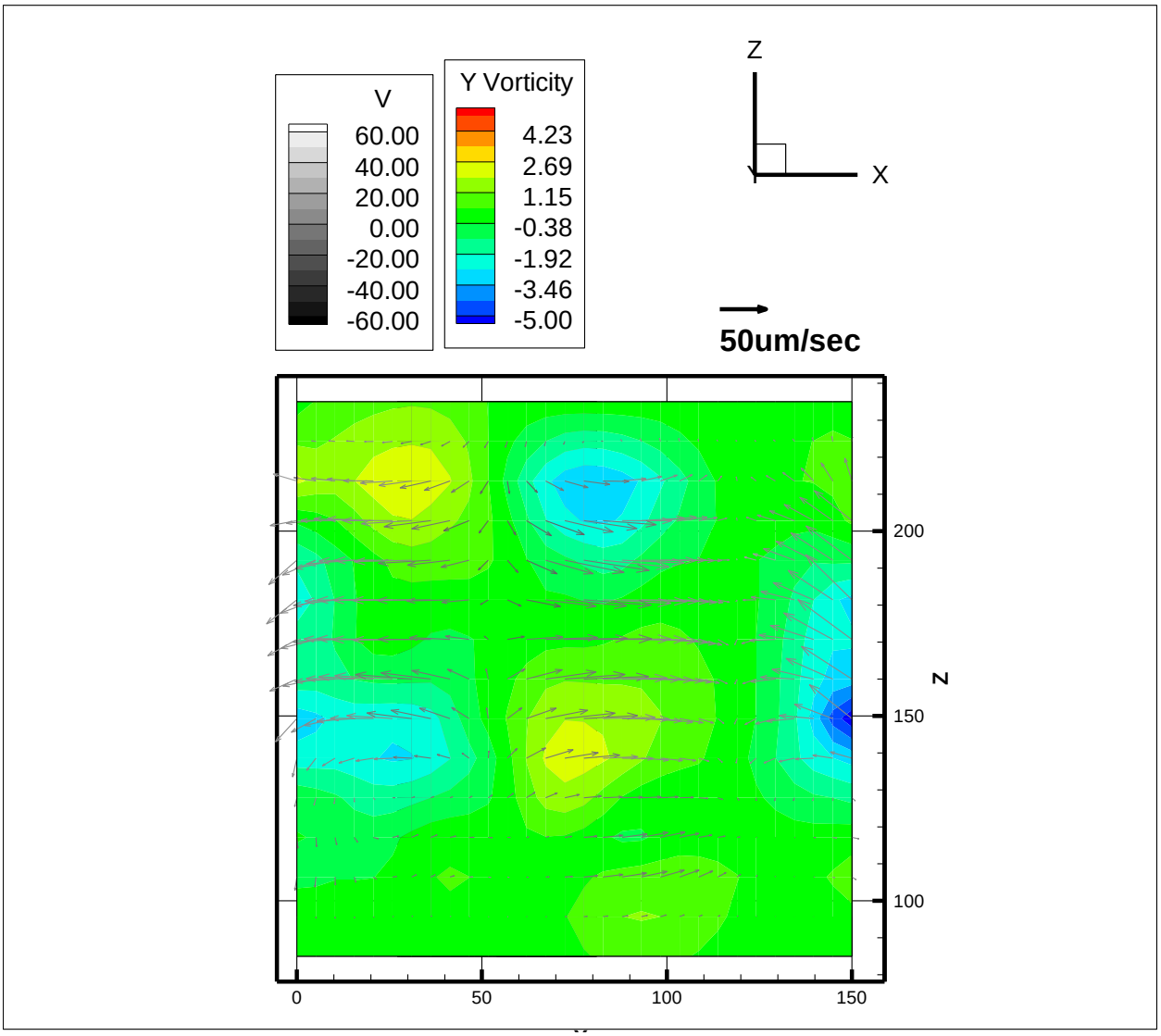

Figure 5-27 Partial Velocity Profile at X-Z plane of the in-line array post configuration at Y= 150. V component is shown by the gray scale and the Y vorticity is shown by contour plot on the background

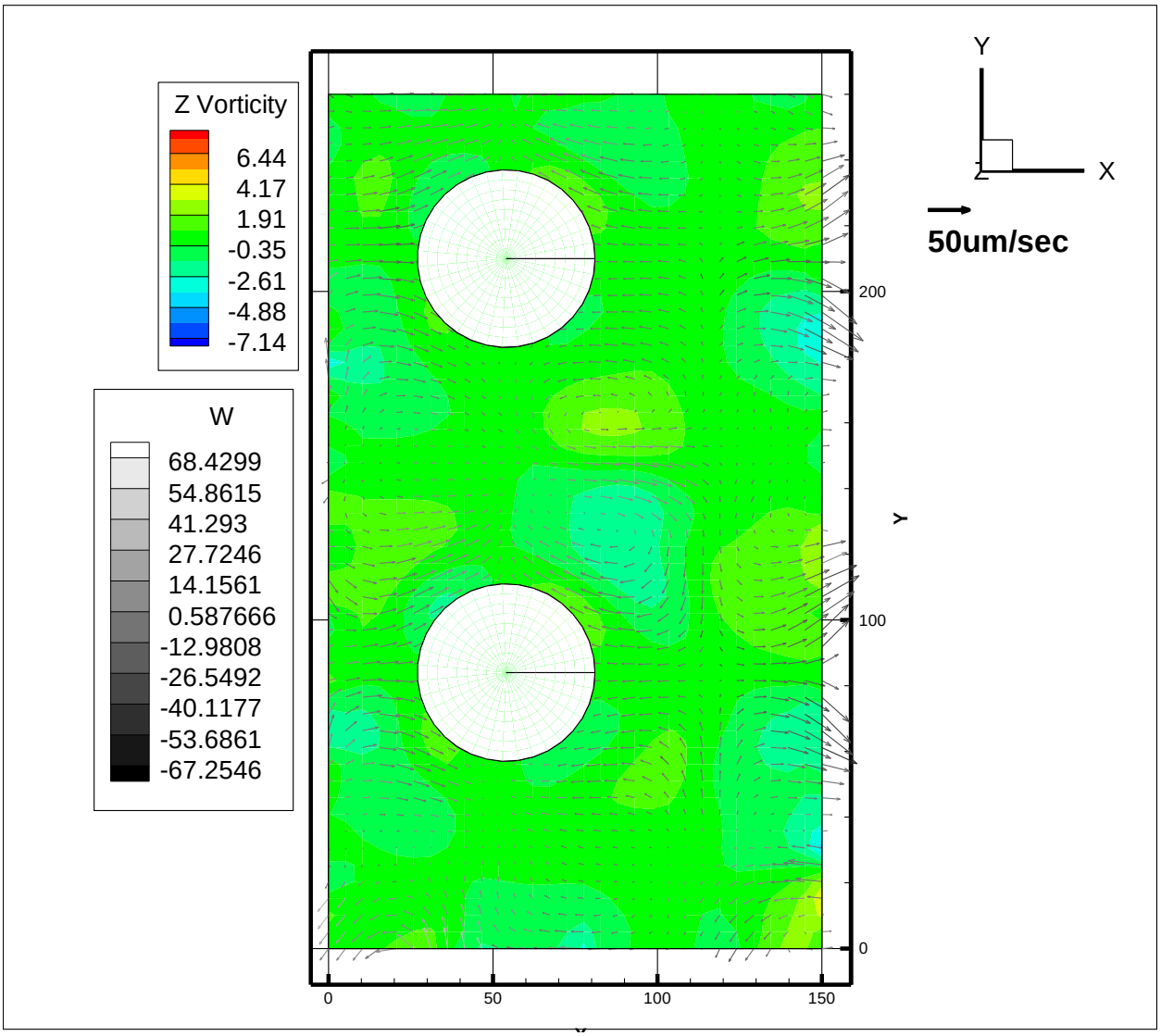

Figure 5-28 Partial Velocity Profile at X-Y plane of the in-line array post configuration at Z= 122.5. W component is shown by the gray scale and the Z vorticity is shown by contour plot on the background

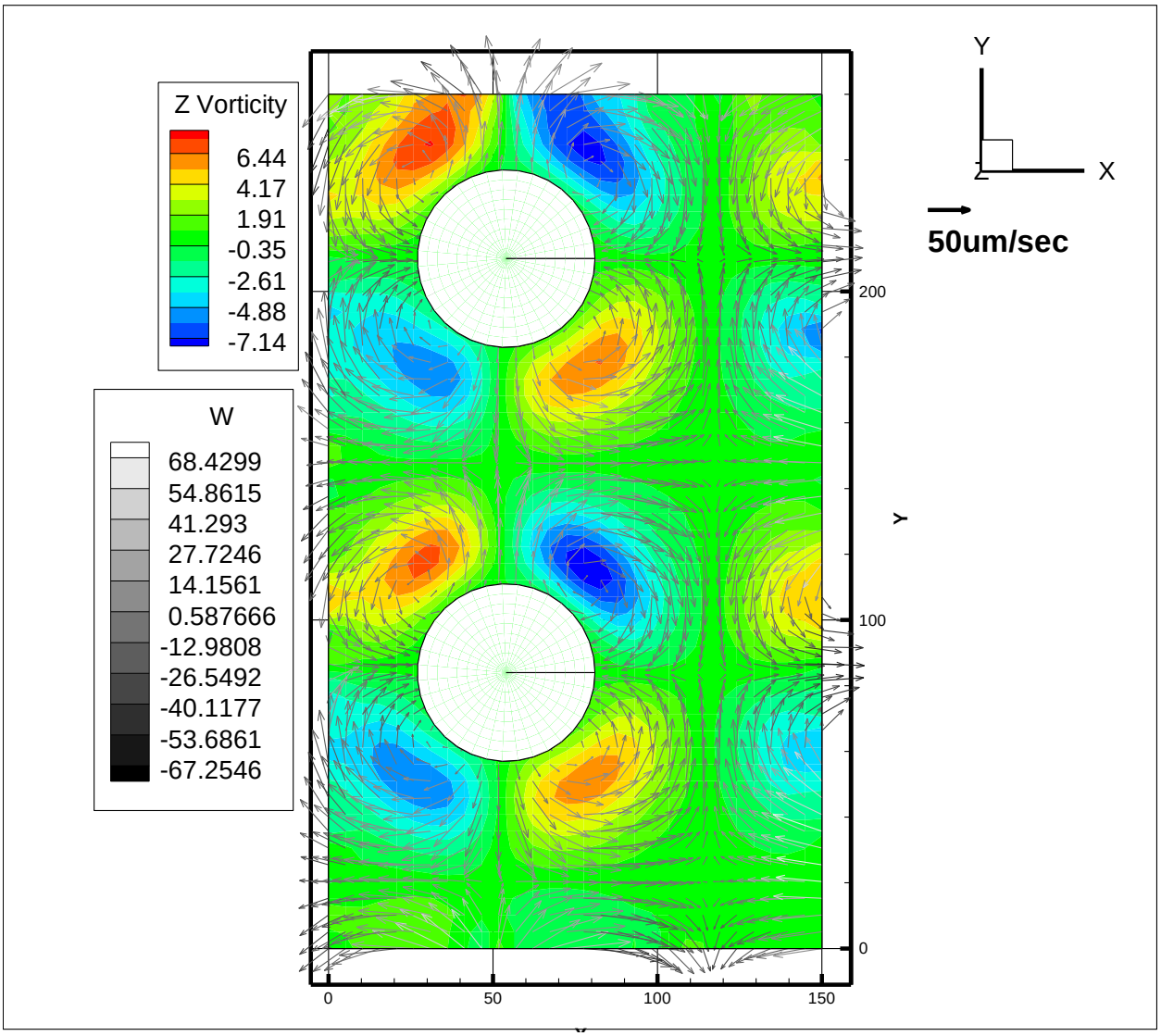

Figure 5-29 Partial Velocity Profile at X-Y plane of the in-line array post configuration at Z= 160. W component is shown by the gray scale and the Z vorticity is shown by contour plot on the background

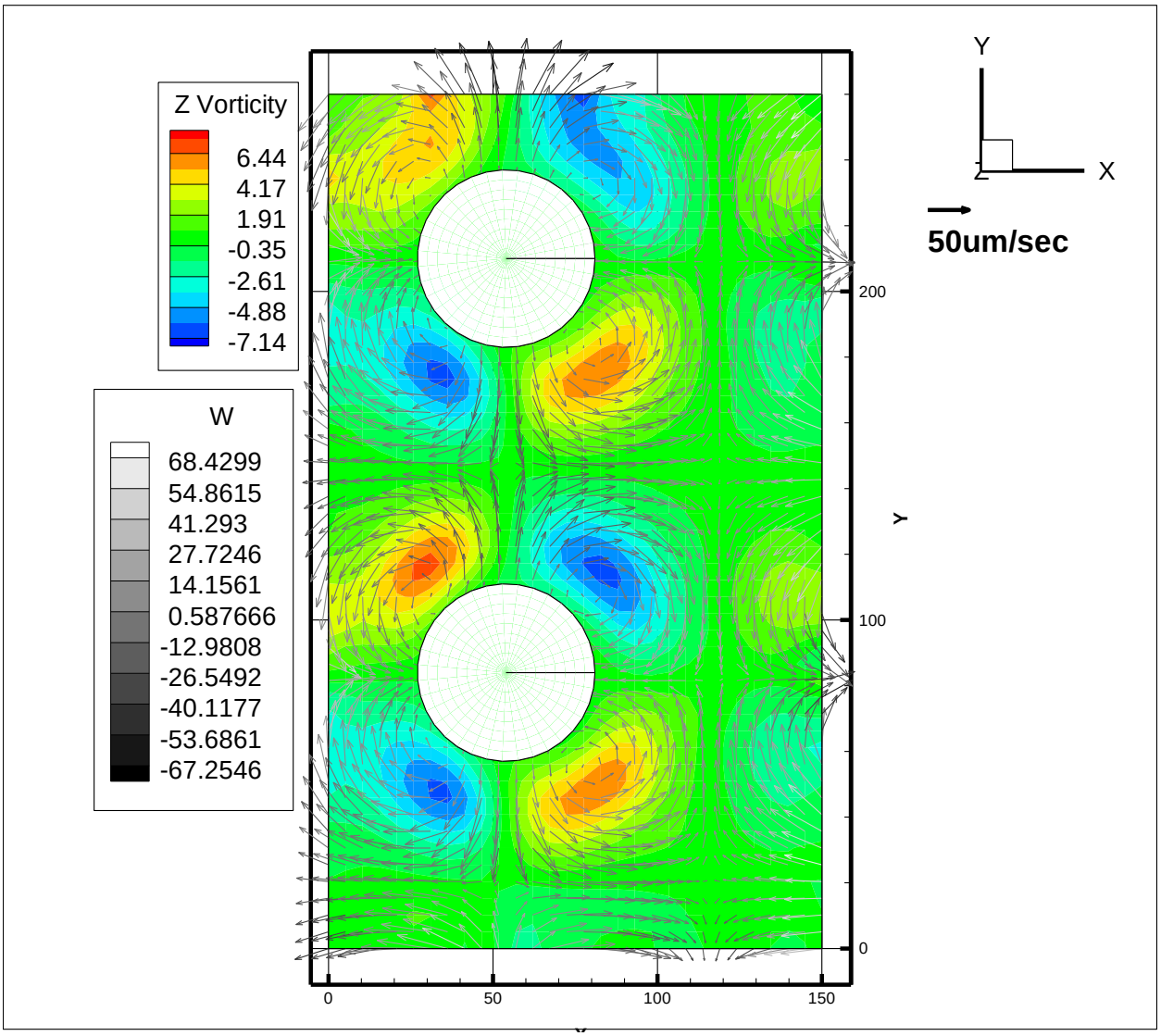

Figure 5-30 Partial Velocity Profile at X-Y plane of the in-line array post configuration at Z= 197.5. W component is shown by the gray scale and the Z vorticity is shown by contour plot on the background

5.3.4.2.2 Staggered array

The third case investigated is the stagger array post configuration. Figure 5-31 shows the reconstructed 3-D flow field of a stagger array post configuration at oscillation frequency of 3500Hz. Similar to the case of in-line array configuration, the cell-like flow structure was nicely

formed between the cylinder posts. The size of each cell was larger and the flow was more complex, and the flow structure lost the self-symmetry observed in the single and in-line array post configuration.

Slices of the flow field at *Y*-*Z* plane of the stagger array post configuration are shown in Figure 5-32 to Figure 5-37. The velocity vector is shown together with the *X* vorticity component. At the centerline cross-section of the post (*X*=135, Figure 5-32), the downward flow from the top left corner of the post was stronger than the other corner on the top right side, went away from the post. At the middle section of the post, the flow on the left side turned upwards at the dividing stream plane. At the bottom left side of the post, the flow also turned up and skewed the flow in the middle section went upward. At the right side of the post the flow turning was not as sharp as the left side, and flow structure was more symmetrical to the *Z* direction. The flow maintained the same trend at *X*=155 (Figure 5-33), but the vorticity map shows it is in general weaker. The flow direction turned completely in between *X*=155 and *X*=175(Figure 5-34) so that the flow at the *Y* location of the post went towards the post. The flow was more symmetric at the middle section of the channel at *X*=195 and *X*=215 (Figure 5-35, Figure 5-36), but turned to asymmetric at *X*=235(Figure 5-37) again. The flow from the top-right side of the post produced strong downward flow but turned slightly upward quickly. The left side of the flow was mostly horizontal, but a downward flow can be seen at the bottom left side of the post.

Slices of the flow field at *X*-*Z* plane of the in-line array post configuration are shown in Figure 5-38 to Figure 5-43. The velocity vector is shown together with the *Y* vorticity component. Similar turning of flow direction can be found between *Y*=155 (Figure 5-39) and *Y*=135 (Figure 5-40). At *Y*=155, the flows were asymmetric and two vorticity concentrated region can be found at the bottom-left and top-right side of the post. The flows were relatively

more symmetric to the *Z* direction at *Y*=115 (Figure 5-41) and *Y*=95 (Figure 5-42), and finally became asymmetric again at *Z*=75 (Figure 5-43).

Figure 5-44 to Figure 5-46 shows the 2-D velocity field at different *X*-*Y* planes of the stagger array post configuration, overlaid with the *Z* component of the vorticity contour and the W component of velocity is shown in gray scale together with the velocity vectors of U and V components. Because the post interacted with another post in the diagonal direction, the flow cell structure became asymmetric also in the *X* and *Y* direction. The steady streaming eddies on the four corners of a post had different vorticity levels and the eddy shapes were also different. These eddies interacted with their diagonal eddy pair of another adjacent post, and formed a strong-weak eddy pair. An eddy with stronger vorticity was always paired with the weaker eddy, and for each post the relative position of these eddies were fixed. As shown in Figure 5-45, The eddy on the top left and top-right corner of a post were the weaker eddy of the eddy pair, and the other two were the stronger ones. The flows at the top and bottom of the channel were weaker than the middle section of the channel, as shown in the vorticity maps at the different *Z* locations.

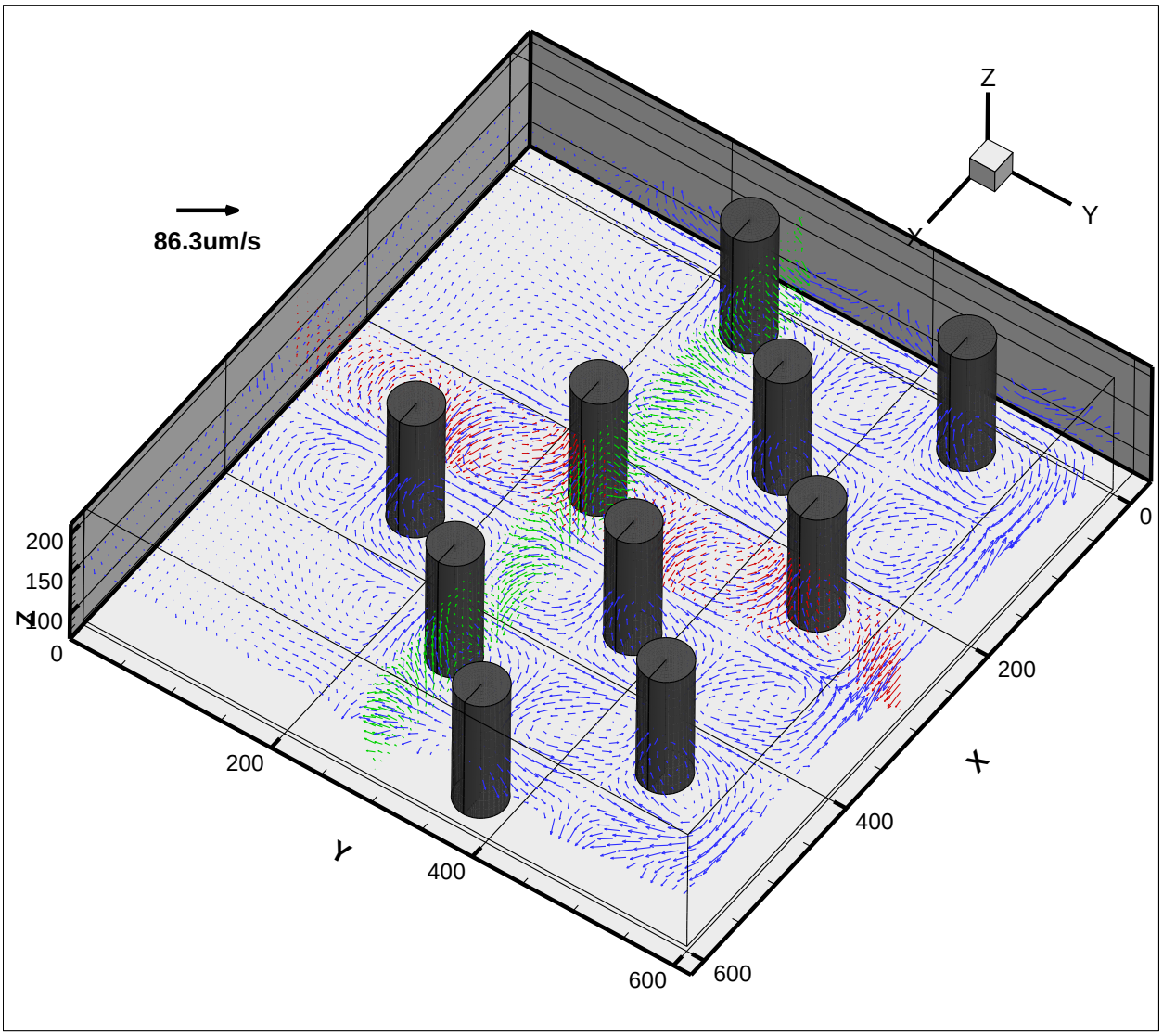

Figure 5-31 reconstructed 3-D Flow field of stagger array configuration at 3500Hz. Only a slice of vector field for each X-Y, Y-Z and X-Z plane is shown

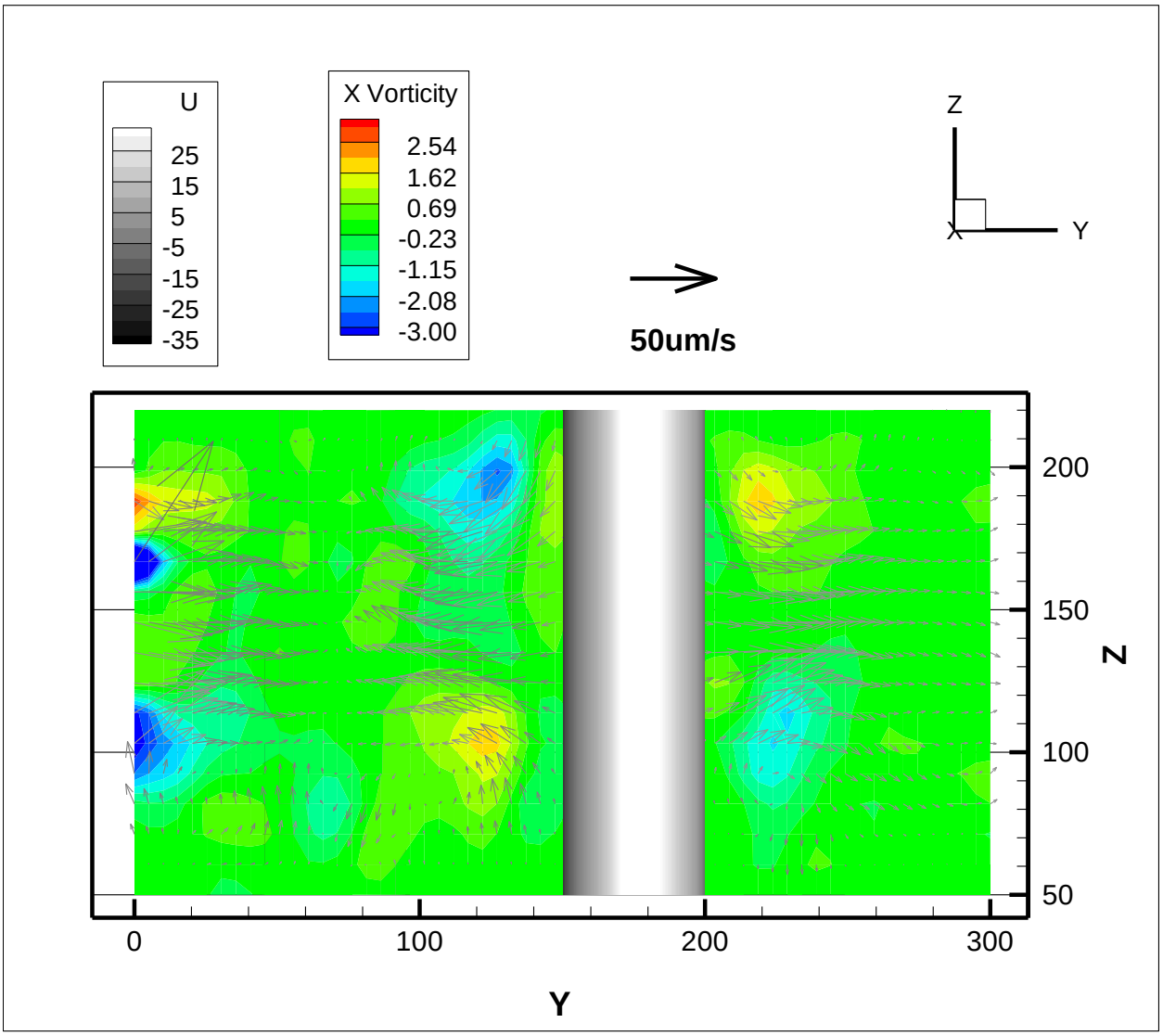

Figure 5-32 Partial Velocity Profile at Y-Z plane of the stagger array post configuration at X= 135. U component is shown by the gray scale and the X vorticity is shown by contour plot on the background

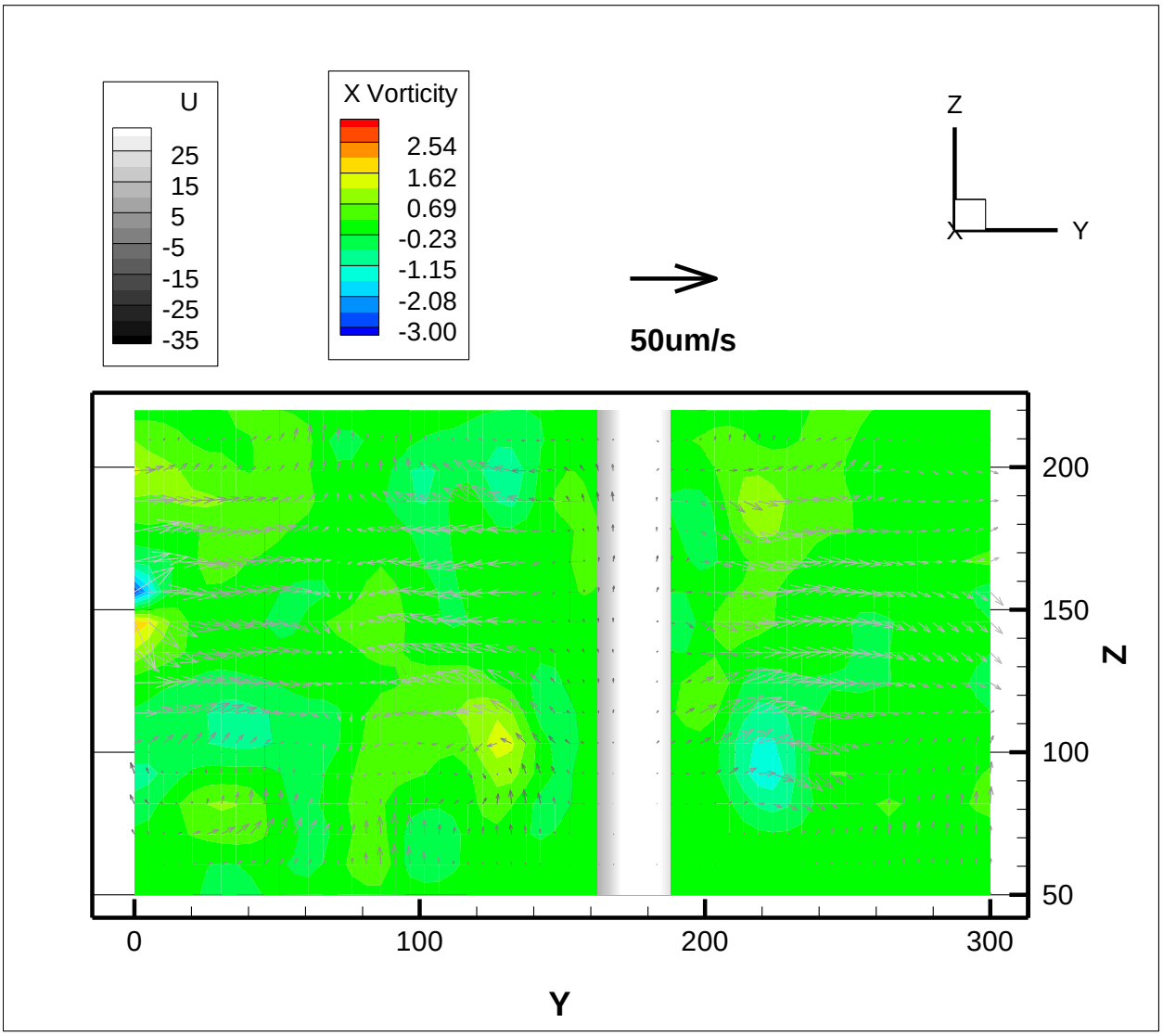

Figure 5-33 Partial Velocity Profile at Y-Z plane of the stagger array post configuration at X= 155. U component is shown by the gray scale and the X vorticity is shown by contour plot on the background

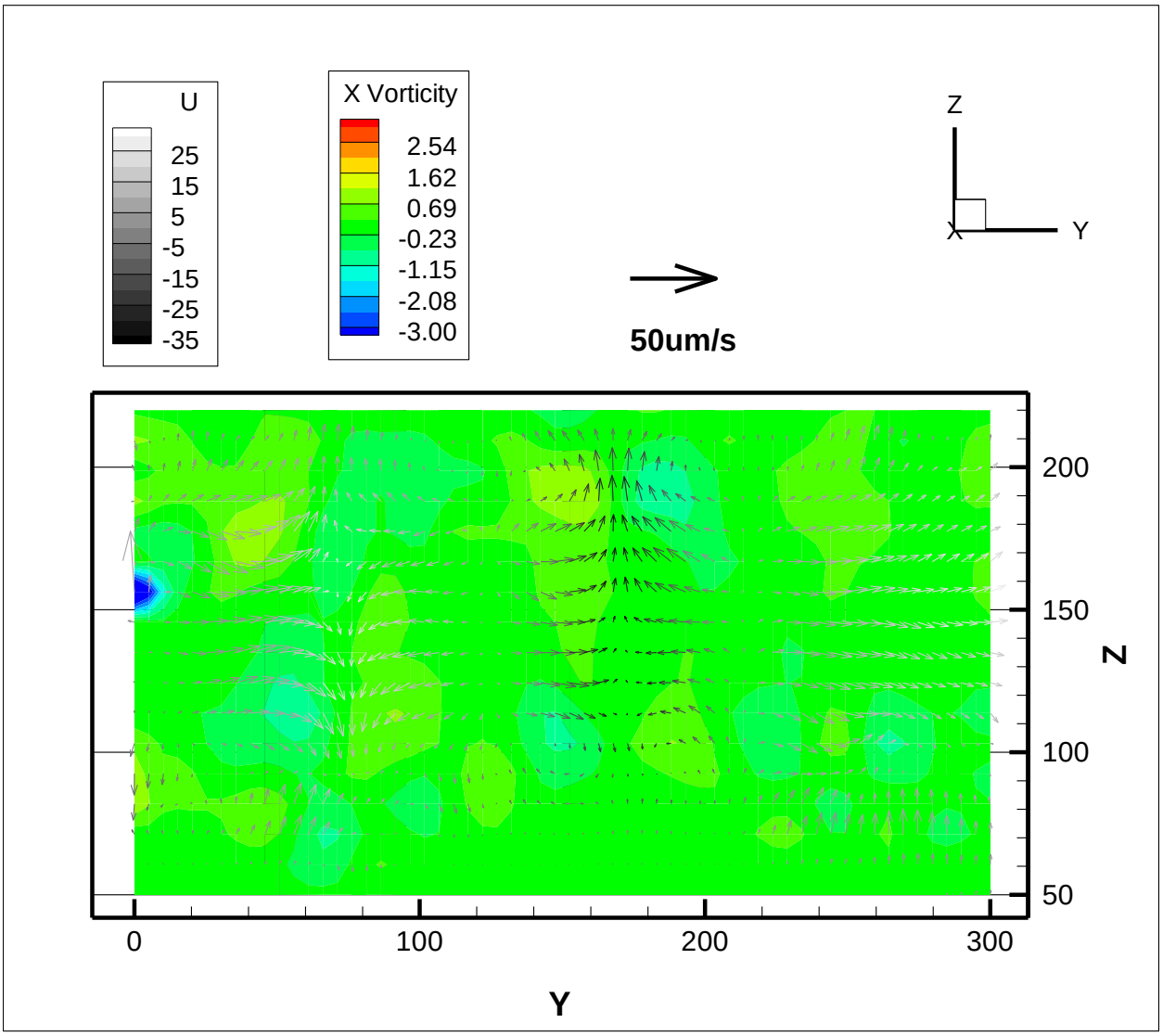

Figure 5-34 Partial Velocity Profile at Y-Z plane of the stagger array post configuration at X= 175. U component is shown by the gray scale and the X vorticity is shown by contour plot on the background

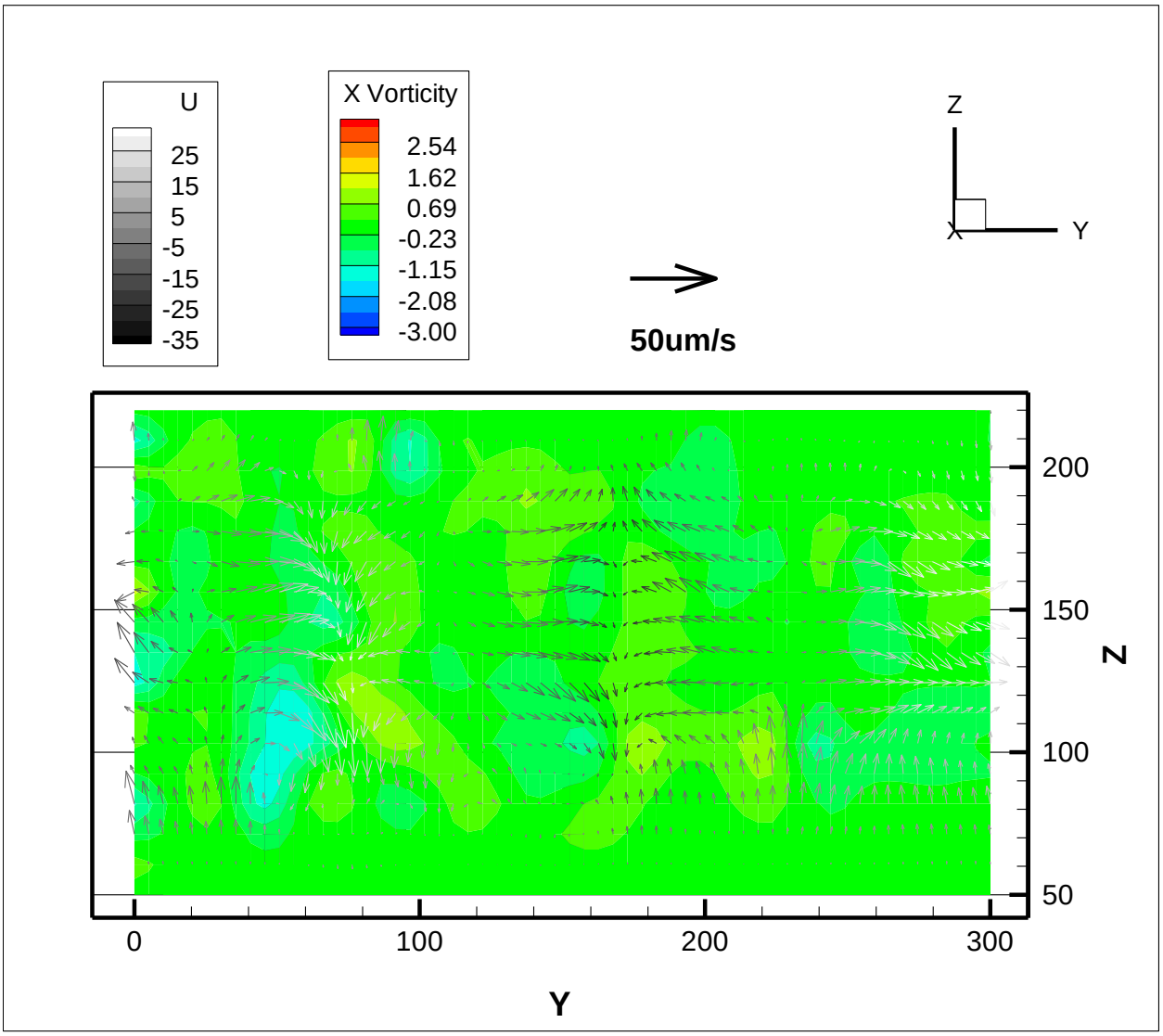

Figure 5-35 Partial Velocity Profile at Y-Z plane of the stagger array post configuration at X= 195. U component is shown by the gray scale and the X vorticity is shown by contour plot on the background

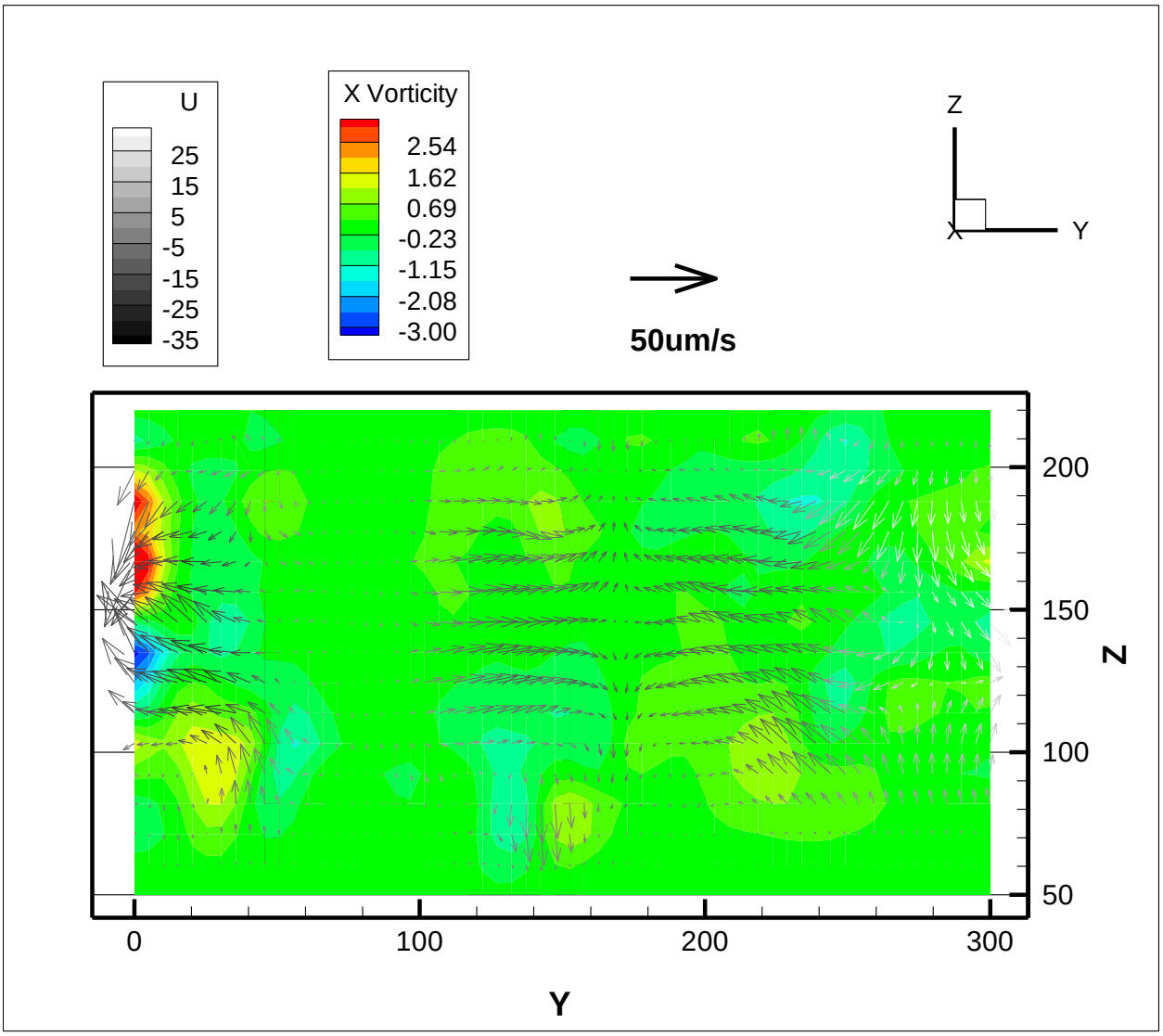

Figure 5-36 Partial Velocity Profile at Y-Z plane of the stagger array post configuration at X= 215. U component is shown by the gray scale and the X vorticity is shown by contour plot on the background

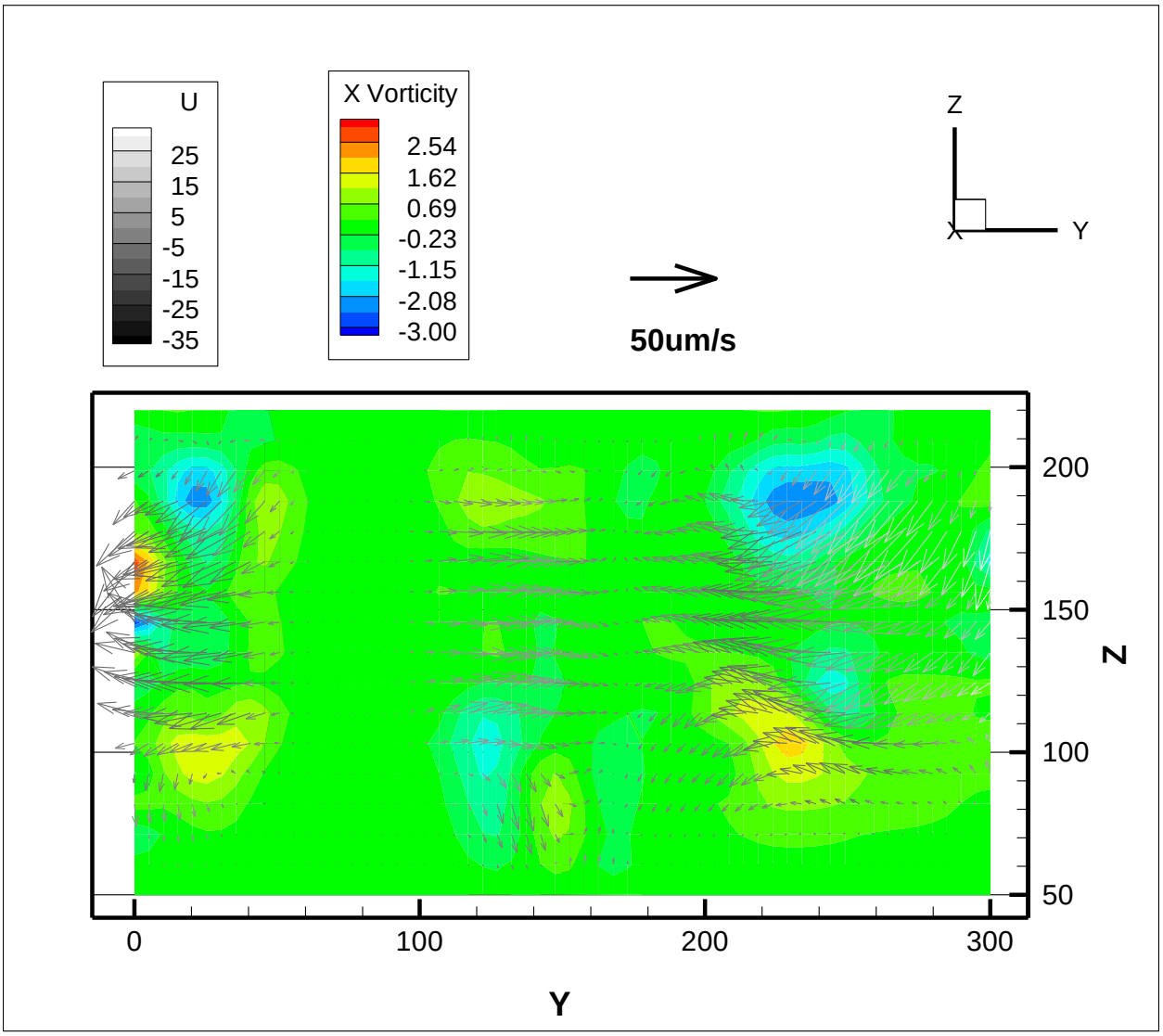

Figure 5-37 Partial Velocity Profile at Y-Z plane of the stagger array post configuration at X= 235. U component is shown by the gray scale and the X vorticity is shown by contour plot on the background

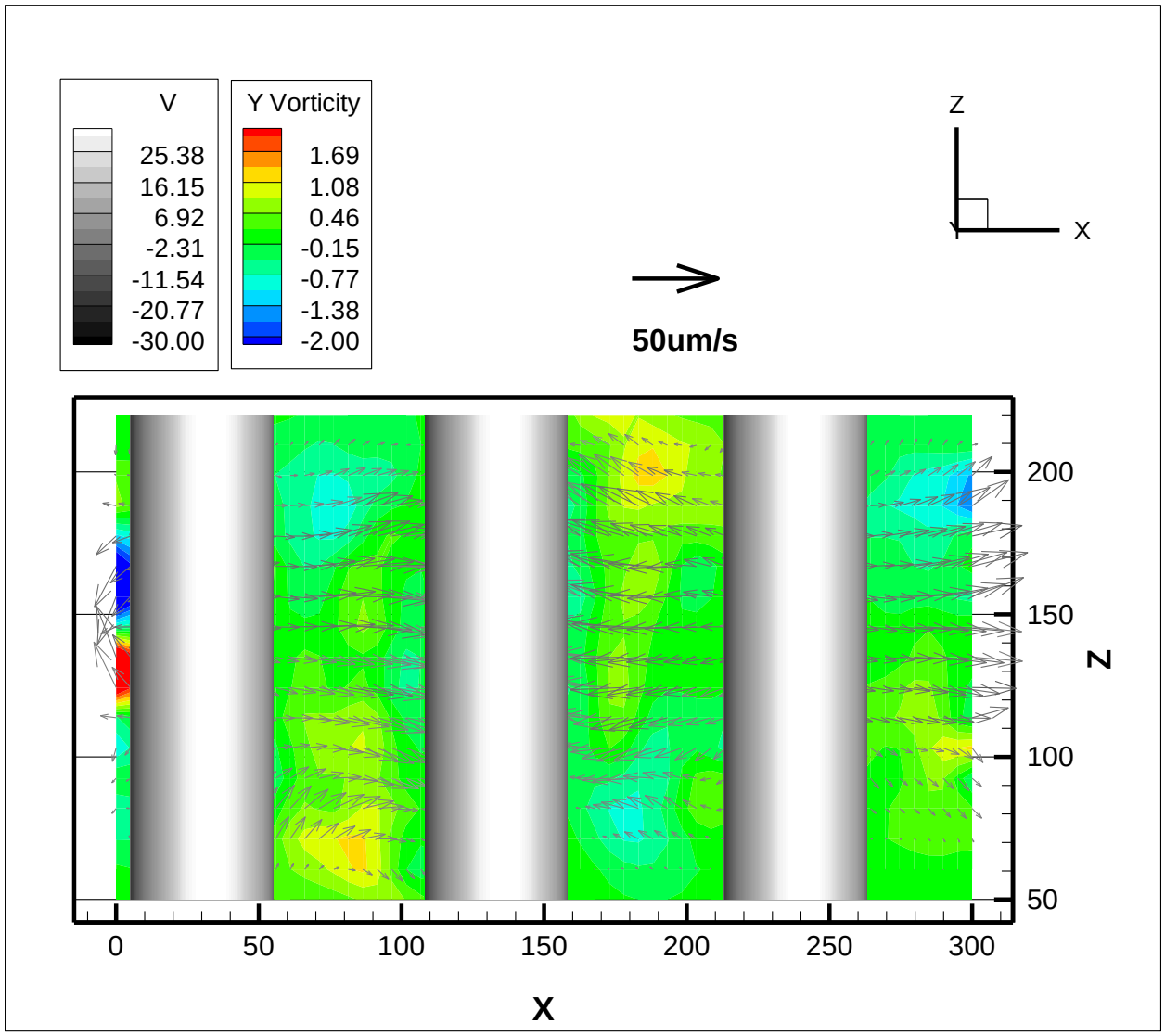

Figure 5-38 Partial Velocity Profile at X-Z plane of the stagger array post configuration at Y= 175. V component is shown by the gray scale and the Y vorticity is shown by contour plot on the background

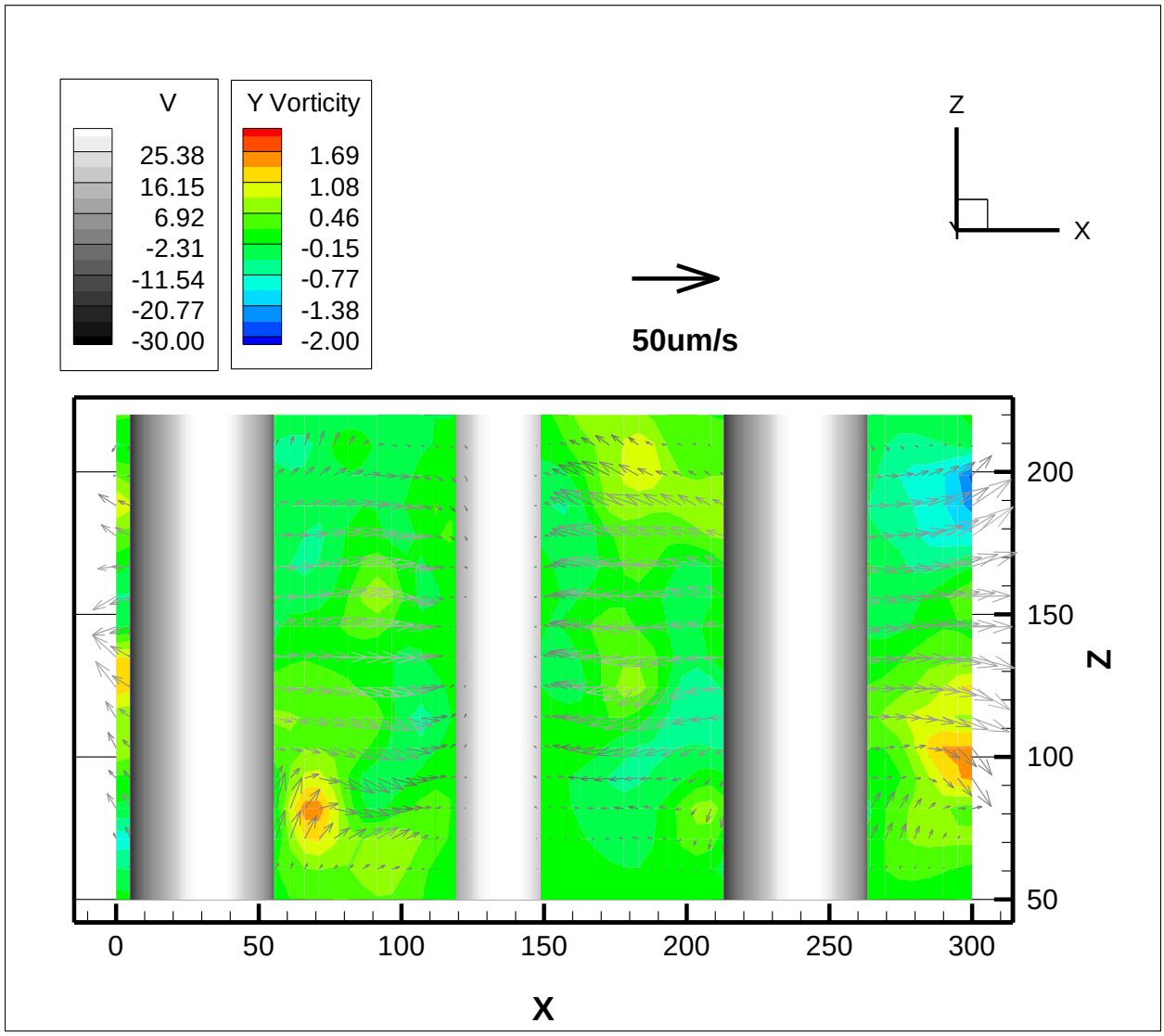

Figure 5-39 Partial Velocity Profile at X-Z plane of the stagger array post configuration at Y= 155. V component is shown by the gray scale and the Y vorticity is shown by contour plot on the background

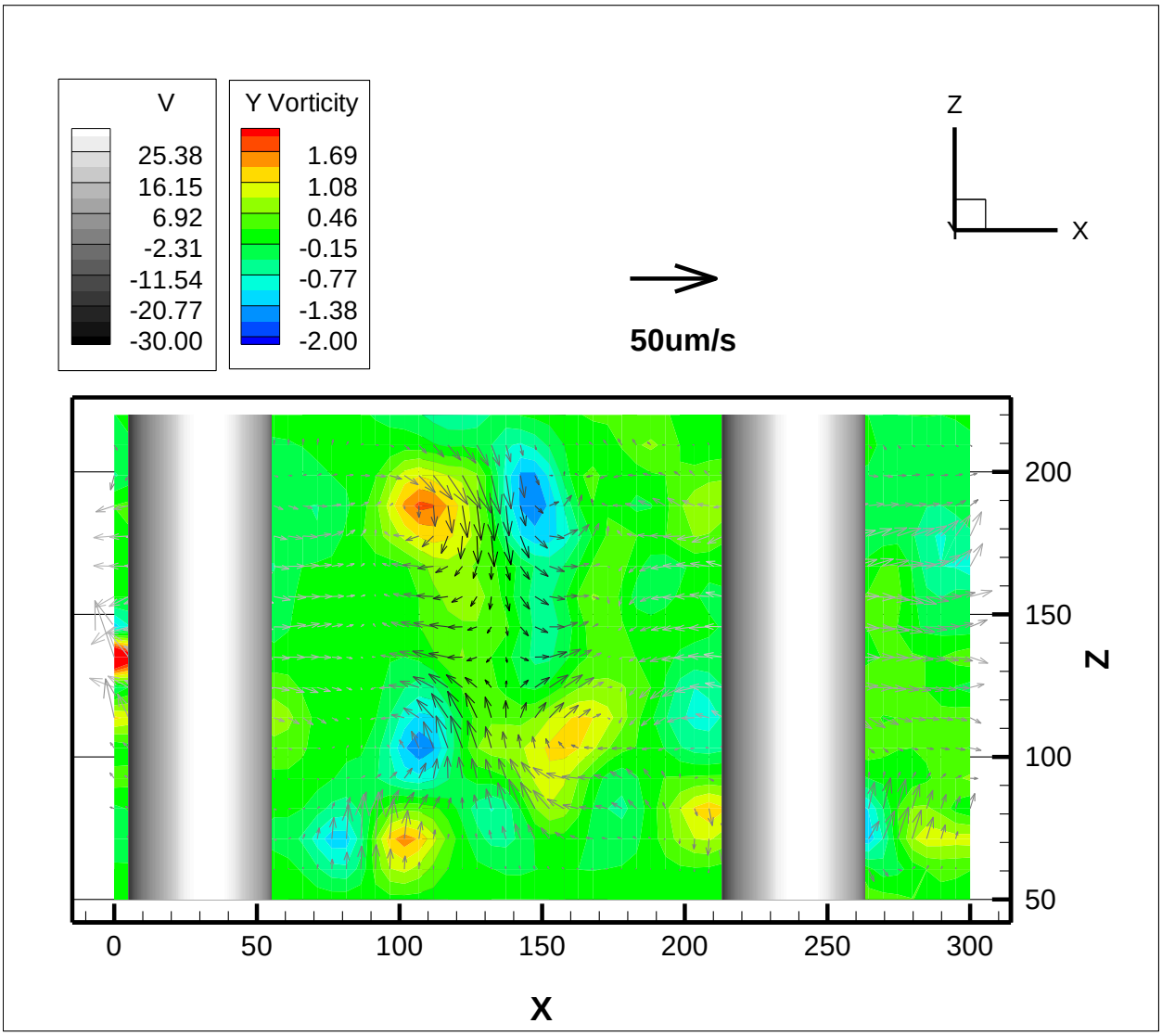

Figure 5-40 Partial Velocity Profile at X-Z plane of the stagger array post configuration at Y= 135. V component is shown by the gray scale and the Y vorticity is shown by contour plot on the background

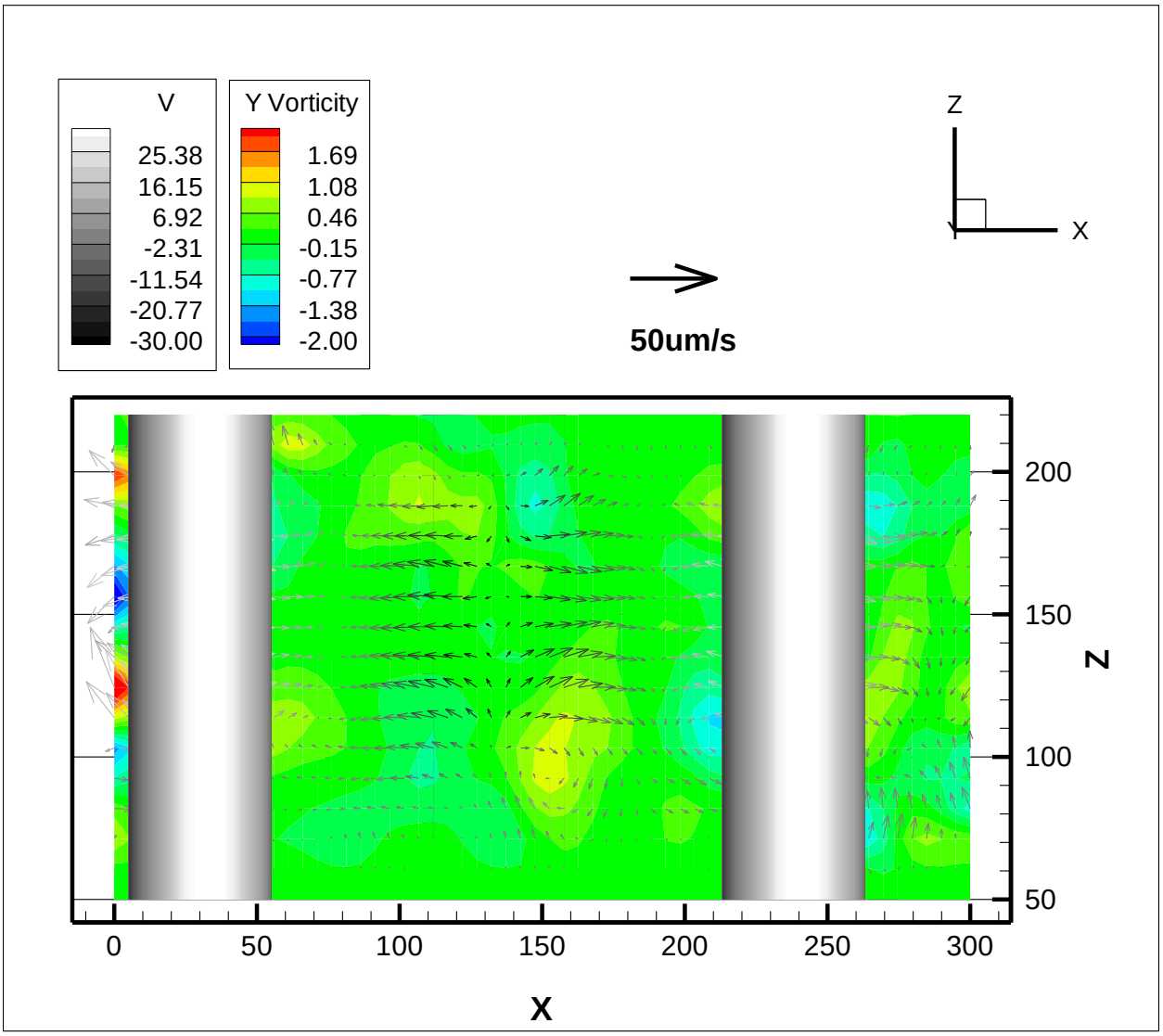

Figure 5-41 Partial Velocity Profile at X-Z plane of the stagger array post configuration at Y= 115. V component is shown by the gray scale and the Y vorticity is shown by contour plot on the background

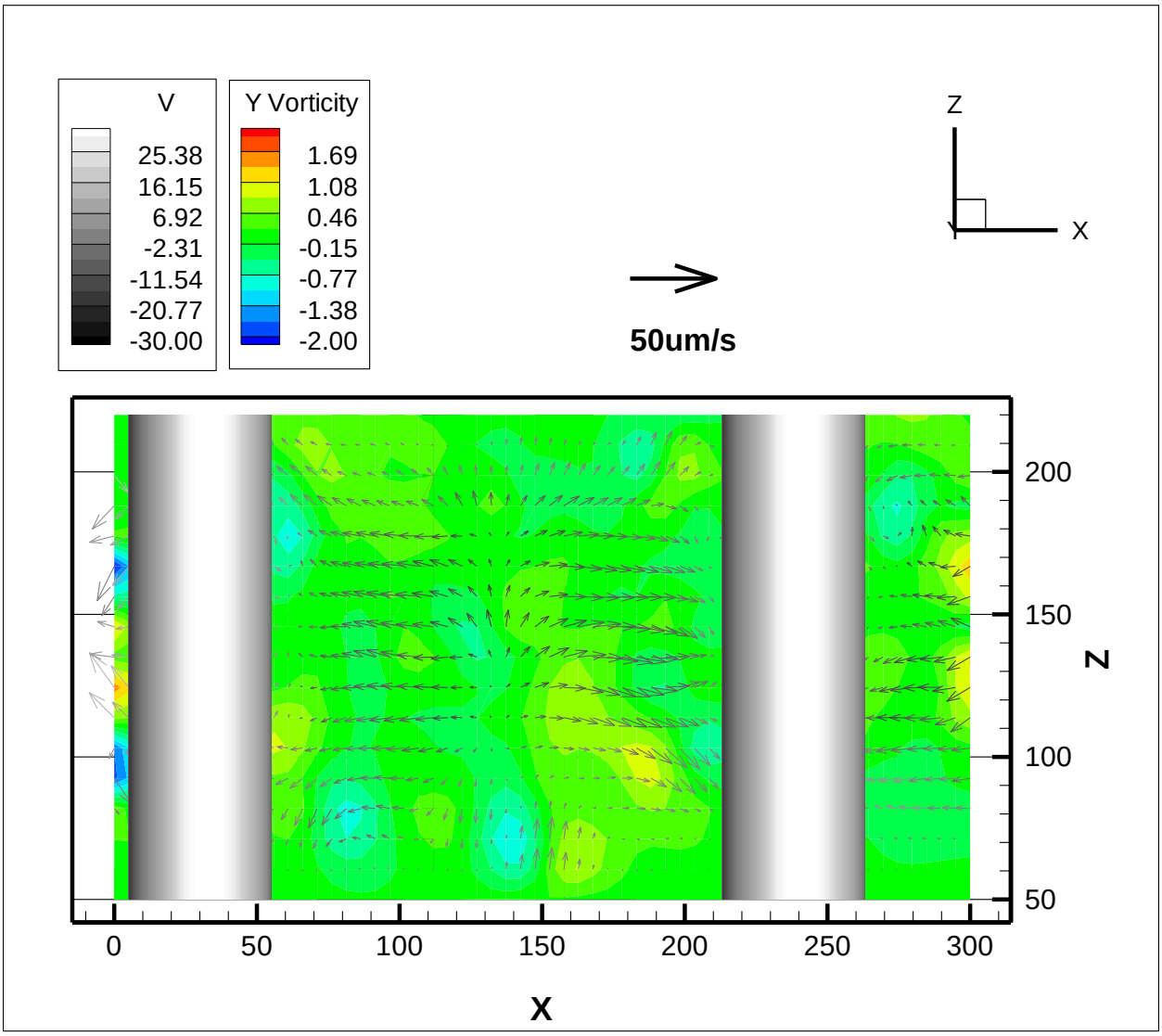

Figure 5-42 Partial Velocity Profile at X-Z plane of the stagger array post configuration at Y= 95. V component is shown by the gray scale and the Y vorticity is shown by contour plot on the background

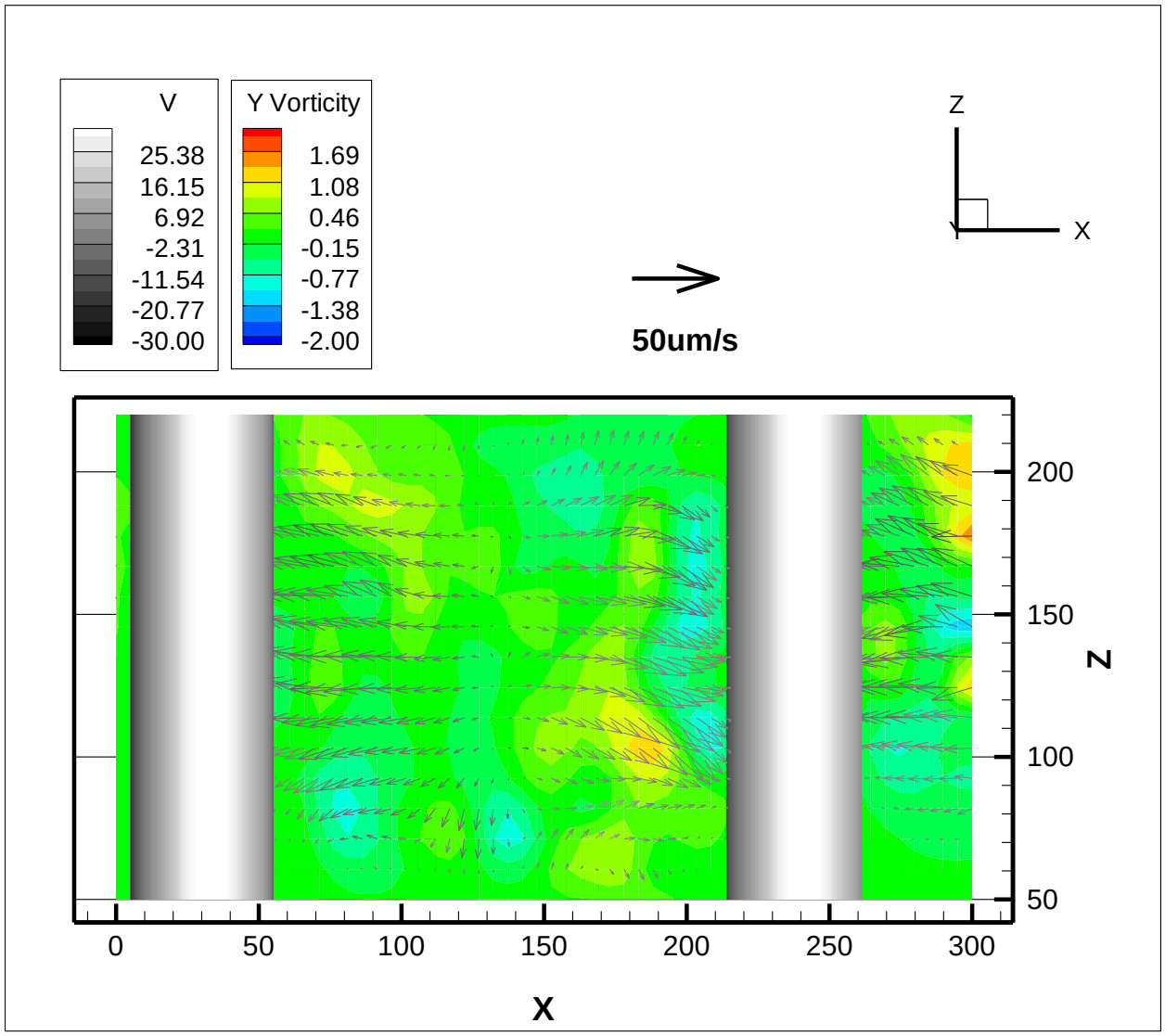

Figure 5-43 Partial Velocity Profile at X-Z plane of the stagger array post configuration at Y= 75. V component is shown by the gray scale and the Y vorticity is shown by contour plot on the background

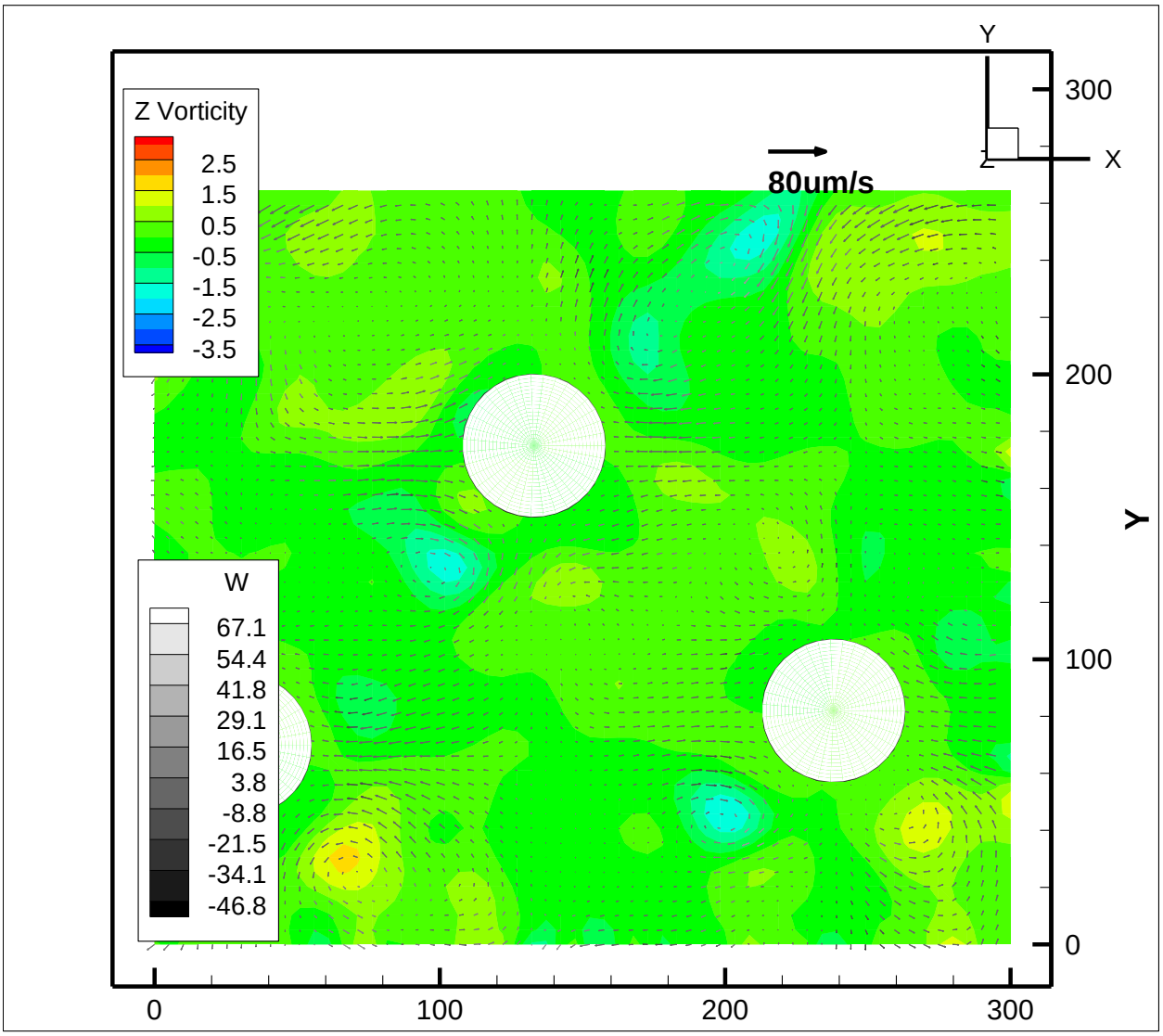

Figure 5-44 Velocity Profile at X-Y plane of the stagger array post configuration at Z= 92.5. The W component is shown in gray scale on the vector and the Z vorticity is shown as contour plot on the back ground.

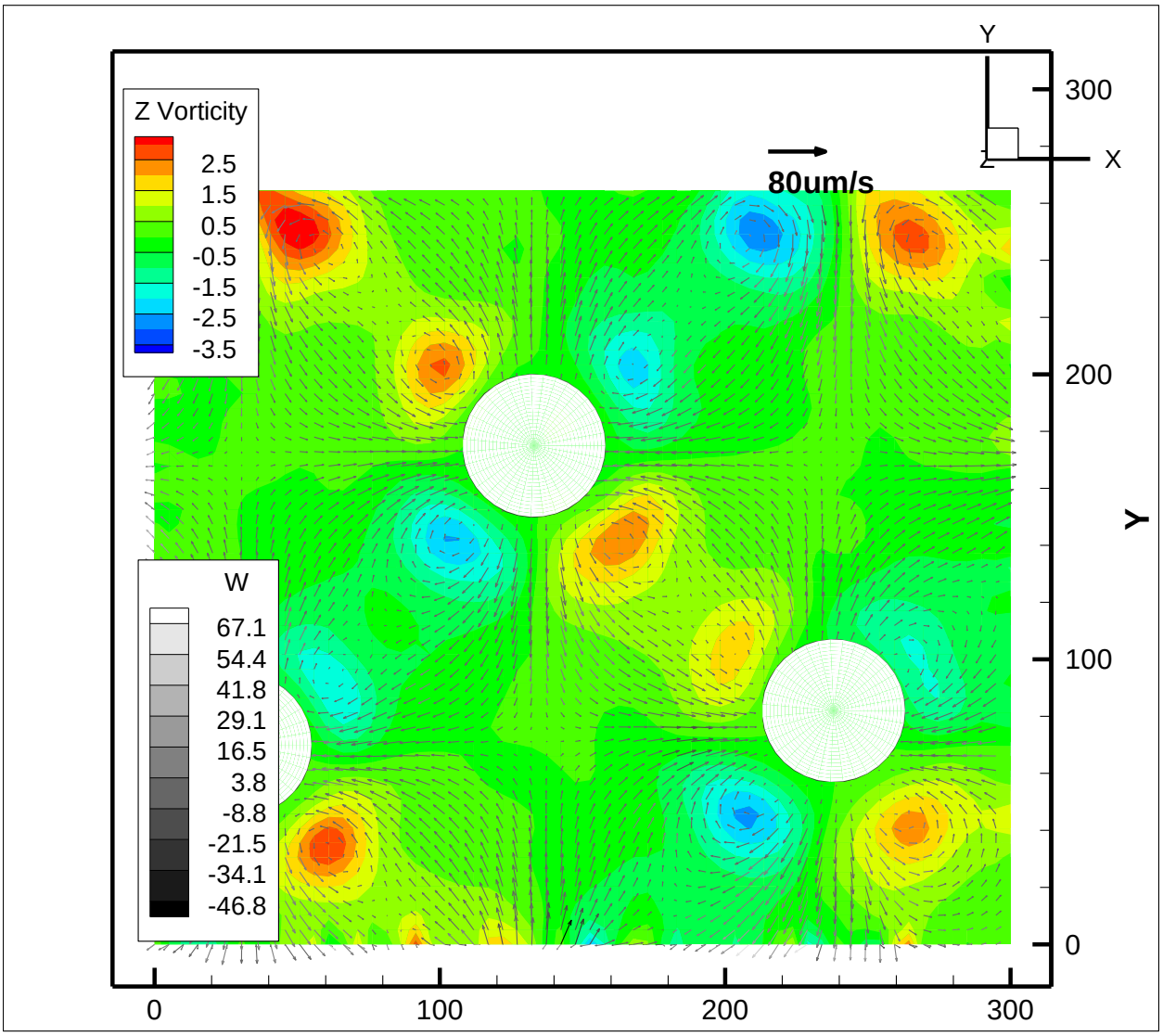

Figure 5-45 Velocity Profile at X-Y plane of the stagger array post configuration at Z= 135. The W component is shown in gray scale on the vector and the Z vorticity is shown as contour plot on the back ground.

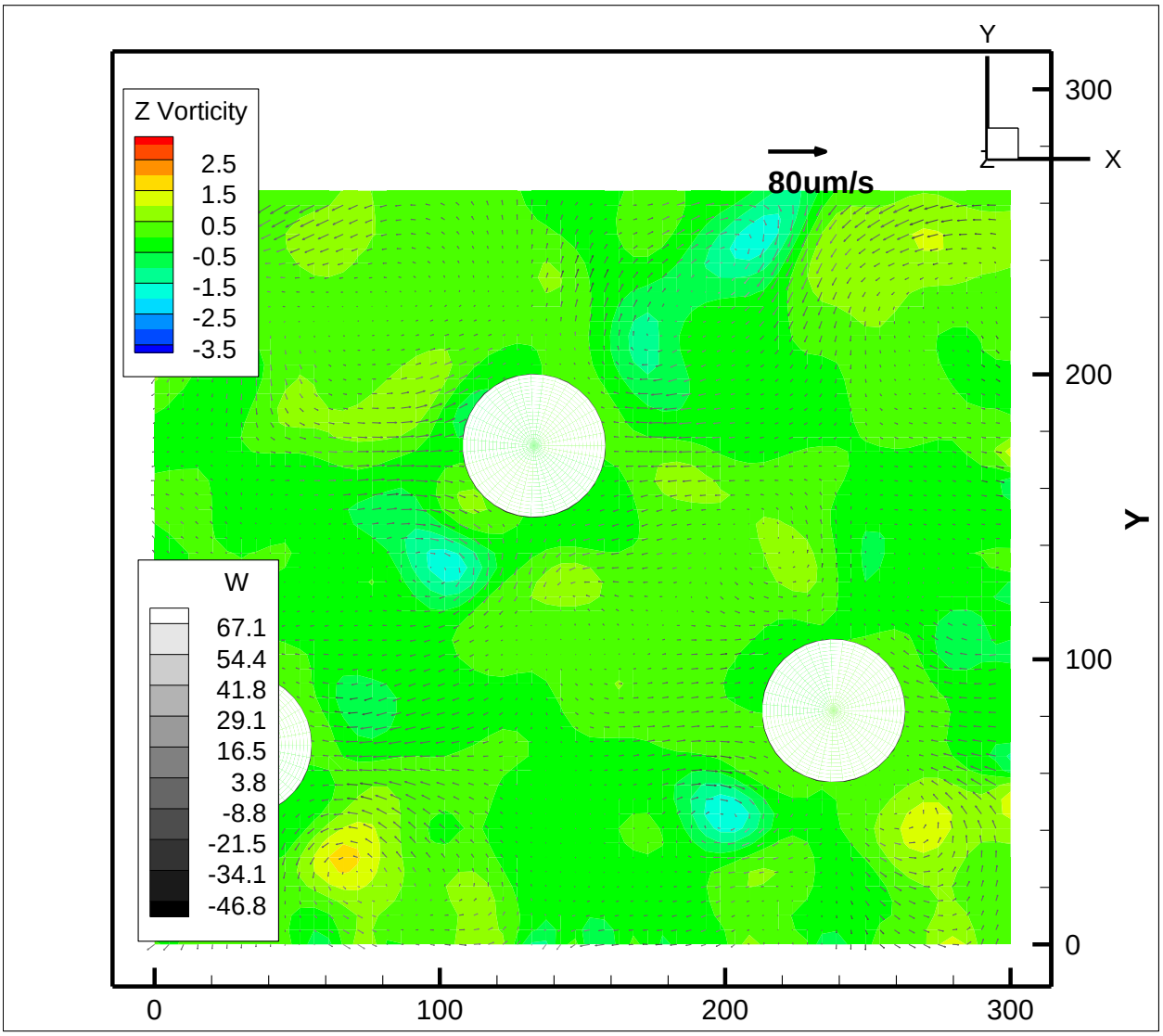

Figure 5-46 Velocity Profile at X-Y plane of the stagger array post configuration at Z= 177.5. The W component is shown in gray scale on the vector and the Z vorticity is shown as contour plot on the back ground.

5.3.5 **Discussion**

All three cylinder post configurations show three dimensional flow structures. Lutz *et al.* (2005) showed that steady streaming eddies formed by a cylinder post can be characterized by the DC boundary layer thickness δ_{DC}, as shown in Figure 5-8. When δ_{DC} is small or comparable to the cylinder radius, a counter-rotating induced eddy structure will present, as shown in Figure 5-8. 2-D analytical solution showed that the normalized eddy size δ_{DC}/a can be related to the normalized Stoke Layer thickness for the cylinder δ_{AC}/a, where a is the radius of the cylinder post, and $\delta_{AC} = \sqrt{\nu/\omega}$, where ν is the kinematic viscosity and ω is the oscillation frequency. The analytic curve is confirmed by their experimental results ((B. R. Lutz *et al.*, 2005), fig. 5). The current work is using water ($\nu = 0.0095 cm^2/s$) as the medium, with a frequency from 1260Hz to 3500Hz. The post size are 25 ~ 75μm in radius. The calculated δ_{AC}/a = 1.09 ~ 0.22. Both values are outside the right end of the figure, which means that $\delta_{DC} >> a$ and explains why in the results only the steady streaming eddies were present.

In the same study Lutz *et al.* (2005) also related the Stoke layer thickness δ_{AC}/h to the DC boundary layer thickness for junction streaming Δ_{DC}/h, which was defined as twice the distance of the center of the junction streaming eddy from channel wall. The junction streaming eddy is formed outside the 2-D steady streaming eddies, and limits the thickness of the 2-D eddies. They found that Δ_{DC}/h is roughly proportional to δ_{AC}/h. In the current work δ_{AC}/h = *0.22*, which is also outside the right end of the chart. This indicates that $\Delta_{DC} \sim h$ and the 2-D layer is negligible. This estimation is in agreement with the results shown in the previous section, which shows the flow fields are all three-dimensional.

The results of the single cylinder post channel provide the basic flow pattern in the current channel. The flow is symmetric in *X*, *Y* and *Z* directions, and the 4 eddies had the same

size and shape. The dividing stream plane formed by the adjacent eddies defined the flow regime of each eddy. There were no apparent boundaries to the eddies, the flow just decelerated and stopped at the outer region. This is probably due to the peak to peak voltage amplitude set for the experiment was not high enough, so the steady streaming velocity at the outer region reduced to the level that cannot be accurately measured by 3-D μPTV system.

The in-line array shows the cell-like flow structure, and the flow patterns were all symmetric in most cases. These eddies should extend longer but were interfered with the eddies caused by the adjacent posts, therefore formed the array structure. This is the most preferable design for the hydrodynamic tweezers application, since the flow pattern of this configuration is very symmetric, it can be expected that the trapping performance of each post should be very similar.

The 3-D flow structure of the stagger array configuration is the most complicated of all three cases. For each post the flow pattern was asymmetric in all *X, Y* and *Z* directions, and the eddies were highly coupled with the eddies from the adjacent post. Each diagonal eddy pairs shown in Figure 5-45 formed a stagnant zone in the middle of the eddy pair. Since these pairs of eddies have the same rotation direction, there is not a dividing stream plane in the middle, therefore the velocity in this area is at the lowest and about to change sign. This stagnation region may not be ideal for the hydrodynamic tweezers design, because the trapped particle/cell may escape through this region. It should also be noted that because the strength of the eddies are not even for those eddy pairs, the trapping force for each corner of a post will be uneven.

6 Conclusions and Future Works

6.1 Conclusion

1. A novel volumetric velocimetry technique was developed and verified with experiments. The use of color-coded pinhole concept was successfully implemented to a single lens microscope system to measure small scale flow field. A novel color separation algorithm and illumination method was also developed to improve the accuracy of the system
2. A modified particle identification algorithm was developed to solve the particle overlapping issue encountered in most high particle image density images. Synthetic image tests shows that the particle identification algorithm is able to resolve overlapped particle image up to 50% overlap under noisy conditions, while keeping the RMS peak location error under 0.07 pixels. The algorithm is also robust to the size changes up to a size ratio of 5.
3. A modified particle tracking algorithms were extended from 2-D to 3-D to improve the accuracy and efficiency of the technique. The tracking algorithm is verified with synthetic 3-D flow field shows that the current tracking algorithm is able to capture a rotational motion with high accuracy up to the displacement around 1.5% of the size of the measurement volume.
4. The accuracy of the 3-D µPTV system was verified with calibration experiments. The location uncertainties are less than 0.1 µm and 0.08 µm for the in-plane, and less than 0.82 µm for the out of plane components, respectively. The displacement uncertainties are 0.62 and 0.63 µm for the in-plane, and 0.77 µm for the out-of-plane components, respectively.

5. The 3-D μPTV system was successfully utilized to measure steady and unsteady backward-facing step micro channel flow. Roughly 400 vectors per image pair can be resolved with a two frame tracking method.
6. Using the 3-D μPTV system, three different configurations of microfluidic devices of hydrodynamic tweezers were tested. The 3-D flow structures were resolved and revealed.

6.2 **Future Works**

1. The illumination of the system can be improved to provide better illumination. High power light sources such as laser or high power LED modules. This would extend the capability of the 3-D μPTV system to measure high speed flows.
2. Calculate differential quantity directly with unstructured PTV data. PTV data is unstructured in nature. Right now the differential quantity such as vorticity can only be calculated from a structured grid. It is not clear if the differential quantities can be calculated directly from unstructured data and the results are more accurate.
3. Calculate wall shear stress. Wall shear stress has been important issue for different fields of study. The challenge of calculating wall shear stress is to mark the boundary and properly define the boundary location. With the 3-D μPTV system it is possible to get the accurate boundary point and calculate the wall shear stress.
4. For the hydrodynamic tweezers, the trapping force and other flow feature is closely related to the frequency of the oscillation source. It is therefore a natural extension of the current work to investigate the frequency dependency of the different post model designs.

Part II In-Vitro Study of Fluid Dynamics around Prosthetic Venous Valve

7 Introduction

7.1 Venous Valve and Chronic Venous Insufficiency (CVI)

Venous valves are bicuspid flap-like structure and made of elastic tissue. They are often found in the vein vessels in the lower extremities, they play an important role in circulating the blood from the lower extremities back to the heart. After the blood passing through capillaries from the arteries, the reduced pressure is not enough to push the blood back to the heart alone. In addition, the contraction of skeletal muscle in the leg and respiratory maneuvers cause the vein vessel to deform and squeeze the blood towards the heart. In this process, venous valves function as a check valve to prevent the blood flow to reverse due to gravity and transport the blood back to the heart more efficiently (Figure 7-1).

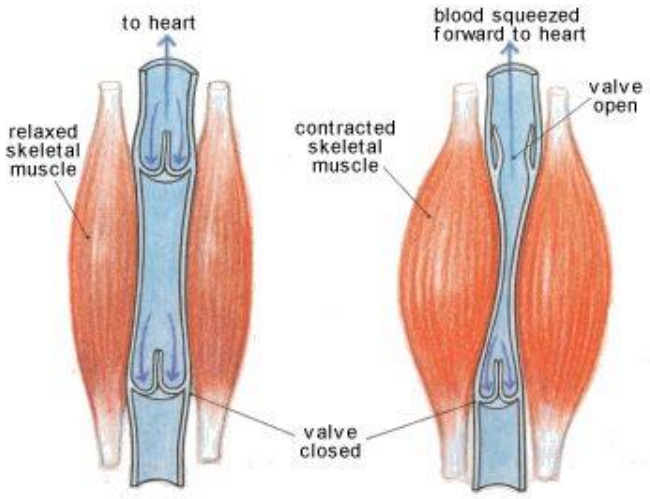

Figure 7-1 A normal functioning venous valve due to the effect of muscle pump. Contraction of skeletal muscles in the legs helps to pump blood toward the heart, but is prevented from pushing blood away from the heart by closure of the venous valves. Retrieved from http://www.nsbri.org/humanphysspace/focus2/page49.jpg

When the venous valves do not work normally, the blood flow is reversed and problems can happen to the lower extremities. Chronic venous insufficiency (CVI) of lower extremities is

a common medical problem, which costs 2% of total Western societies' health-care budgets. This disease affects 10% to 35% of adults in the United States, and it is the seventh most common chronic debilitating disease (Criqui *et al*., 2003). The main cause is that the venous valves of the patients become incompetent resulting in venous reflux and distal venous hypertension. The valve incompetence can be primary (idiopathic) or secondary (post-philebitic). Primary venous valve incompetence is usually the result of dilated vein vessel. The increase of vessel diameter causes the valve leaflets not to touch each other and unable to seal the vessel from reflux (Figure 7-2 (a)). The Secondary venous valve incompetence is mainly caused by deep vein thrombosis (DVT) or trauma (Bergan *et al*., 2006), and the valve leaflets are thickened or deformed (Figure 7-2 (b)).

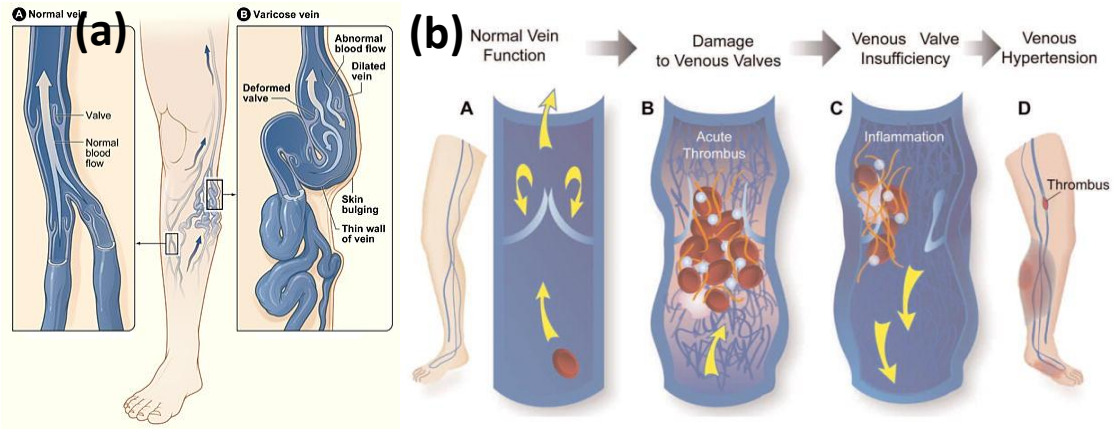

Figure 7-2 Venous Valve Incompetence: (a) Primary. The vessel is dilated and the valve closure is not complete. Retrieved from http://en.wikipedia.org/wiki/File:Varicose_veins.jpg. (b) Secondary. The valve leaflet is deformed or damaged by thrombus. From (Vazquez, Freeman, VanWoerkom, & Rondina, 2009)

7.2 **Prosthetic Valve**

Current treatments for deep vein valve incompetence, or chronic venous insufficiency (CVI), are limited to strategies that manage symptoms. Prosthetic valve implantation is one

proposed alternative for treating CVI. By replacing the incompetent venous valve with an artificial valve, all or part of the function of the native venous valve function is restored.

In the past few decades, prosthetic venous valves for the treatment of CVI have been a topic of interest. Most of the valves consist of three major parts: A valve frame, valve cusp(s) and a delivery system. A typical valve is shown in Figure 7-3 .The valve frame is usually made of nitinol or stainless steel that is self-expandable, to provide the support for the valve cusp(s) and prevent the vein vessel from over distension. The valve cusp(s) are usually made of biocompatible material to avoid immunological response and easier incorporation into the vessel wall. They are usually designed to mimic the native valve to provide the same function as the native ones. The delivery system is usually a catheter-based system, consisting of a guiding catheter wire that helps the valve to be deployed, as shown in Figure 7-4. Several valve designs had been tested with modest, yet still unfavorable durations of competency (de Borst & Moll, 2012; Zervides & Giannoukas, 2012; Pavcnik *et al*., 2008; Bergan, 2006). The primary failure modes of venous valves are thrombosis (blood clot forming inside the vessel) and fibrosis (excess fibrous tissue growing inside the vessel) surrounding the valve. They cause either loss of competency, patency or both. Hence, due the complex etiology of CVI, much remains to be optimized in order to develop a successful prosthetic venous valve.

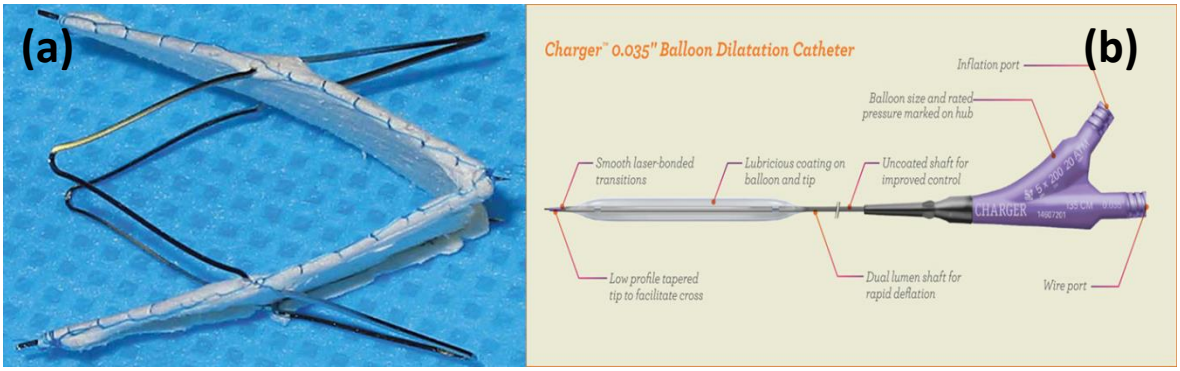

Figure 7-3 (a) A Prosthetic Valve frame and leaflet. From (Pavcnik *et al*., 2008)**. (b) A valve delivery system. Retrieved from http://www.bostonscientific.com/templatedata/imports/multimedia/PeripheralInterventions/charger/charger-schematic-1024x429.jpg**

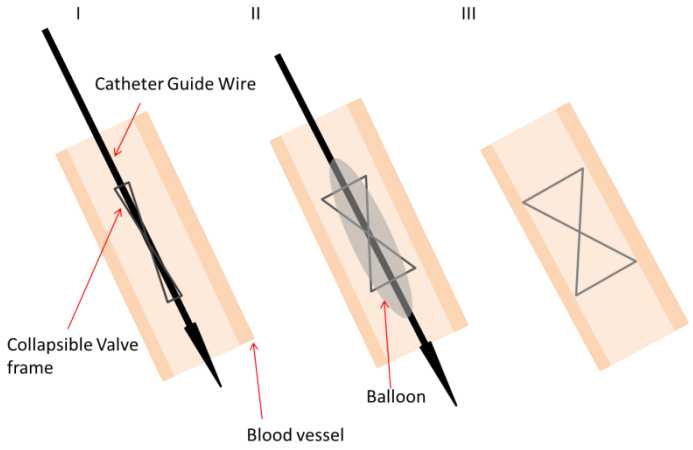

Figure 7-4 Implant of the prosthetic valve. At the first stage, the collapsible valve frame is compressed into the catheter guide wire and then the catheter is directed into the vessel for deployment. In the second stage the frame is expanded by the balloon and attached to the vessel wall. At the third stage, the catheter withdraws from the vessel, leaving only the valve in the vessel.

7.3 Fluid Dynamics of Venous Salves

7.3.1 Single Valve

Most of the previous studies of the prosthetic valves focused on the design of the self-expanding frame and the choice of biocompatible leaflets material (de Borst & Moll, 2012; Pavcnik *et al*., 2008; Zervides & Giannoukas, 2012). There are very few studies focusing on the fluid dynamics around the venous valve. Animal and human studies showed that the valve is not fully open during the opening phase (Karino & Motomiya, 1984 ; F. Lurie, Kistner, & Eklof, 2002), but forms a pocket region with the sinus wall to create a vortex structure behind the valve leaflets. Further study by Lurie *et al.* (F. Lurie, Kistner, Eklof, & Kessler, 2003) showed that four phases can be identified in a complete valve cycle. Complex fluid mechanics phenomenon such as flow separation and reattachment, and vertical flow in the sinus play important roles in the

operation of the valves. The valve is also a modulator of the venous flow in addition to preventing retrograde flow in the vein.

The native valve in the vein vessel is dilated at the sinus region. The role of the sinus pocket in the venous system is still not clear. In arterial system, the sinus pockets of the aortic valve are known to play a positive role in reducing the solid stress to the valve leaflet (Grande-Allen, Cochran, Reinhall, & Kunzelman, 2000; Beck, Thubrikar, & Robicsek, 2001; Katayama, Umetani, Sugiura, & Hisada, 2008) and prevent the leaflet from touching the vessel wall during systole (Fries *et al*., 2006). For venous valve, the function of the sinus is speculated to be preventing flow stagnation regions (flow stasis) by inducing a vertical flow behind the valve leaflet, and assisting valve closure by increasing the pressure inside the sinus pocket during the valve closing phase (F. Lurie *et al*., 2002; F. Lurie *et al*., 2003).

7.3.2 **Dual Valve**

While the functionality of a single venous valve has been studied in the past decade, less attention has focused on the coupling effect of multiple valves. Anatomy of the lower extremity veins shows that the distribution of the valves is not uniformly spaced in the venous system. For example, there are six valves in the great saphenous vein (GSV, a large, superficial vein of the leg and thigh), with more valves located below than above the knee; there are more valves in the tibial veins than popliteal veins (Bergan, 2006). Studies show that despite individual variability, at the junctions between the two major vein vessel (sapheno-femoral junction), multiple valves are present and the distance between two valves is 3-5 cm (Mühlberger, Morandini, & Brenner, 2009; Schweighofer, Mühlberger, & Brenner, 2010; Tasch & Brenner, 2012). These observations suggest that where and how the valves are spaced is important for the performance of the venous system.

Helical flow patterns have been studied extensively in the heart and arterial systems (Mohiaddin, Yang, & Kilner, 1994; Kilner, Yang, Mohiaddin, Firmin, & Longmore, 1993; Stonebridge & Brophy, 1991), and it was found that the helical flow limits flow instability (Caro *et al*., 1996; Morbiducci *et al*., 2009) and increases the efficiency of the flow system (Morbiducci *et al*., 2011). Since the anatomy in the venous system shows the multiple valve configurations is often present in the veins, similar effect could be created from the coupling of the valves with a misaligned angle. Lurie and Kistner (F. Lurie & Kistner, 2012) studied 15 healthy volunteers and 13 unaffected limbs of patients with primary chronic venous disease (CVD). The distance and relative position between the two most proximal valves of the GSV and femoral vein (FV, major vein near the thigh bone) were identified. The mean distance was found to be 3.8 - 4.6 cm and the mean angle between the valve orientation was 84.3 ~ 88.3 degrees. They hypothesized that this valve configuration increases the efficiency of venous return by creating a helical flow pattern. This was confirmed by a more recent study (F. Lurie & Kistner, 2013) using color and spectral Doppler imaging to calculate the velocity vectors at 5 cross-sectional planes of femoral and common femoral veins. Helical flow was present in close proximity and downstream from a valve and valve junction, and was more prevalent when the calf muscle pump was active. When valve was incompetent, the helical flow pattern disappeared and was replaced by disorganized flow. These findings suggest that in a venous system the valves may improve the efficiency and stabilize the blood flow by creating a helical flow pattern. These previous studies were done in-vivo and provided qualitative observations to the flow patterns around the two valves. Due to the technological limitations, however, all of the valve pairs observed in the previous in-vivo studies were misaligned by at least 60 degree angle; no control group (0 degree alignment) was investigated in-vivo to study the coupling effect between the valves.

Particle Image Velocimetry (PIV) has been a popular technique for cardiovascular studies because it can provide two-dimensional flow fields with higher spatial resolution. Several groups have applied this technique to measure flow fields around mechanical, prosthetic or native aortic valves in-vitro (Lim, Chew, Chew, & Low, 2001; Li, Lo, & Lu, 2010; Saikrishnan, Yap, Milligan, Vasilyev, & Yoganathan, 2012). Since the aortic flow is usually turbulent, the results in these studies are not applicable to venous flow. Nam *et al.* (Nam, Yeom, Ha, & Lee, 2012) applied the velocimetry technique to veins with a high-frequency ultrasound (HFUS) image system to image the flow around the valve area in a human superficial vein. Using echo speckles of red blood cells (RBCs) as flow tracers, the motions of valve cusps were simultaneously visualized and large-scale vortices were observed behind the sinus pocket while the main bloodstream was directed proximally. Due to the limited frame rate (30Hz), the HFUS system could only resolve blood flow speed to 4.2 mm/s, which is much lower than the peak velocity (18.2 cm/s) reported by Lurie *et al.* (F. Lurie *et al*., 2003) in patients.

In summary, fluid dynamics around venous valves are important to the efficiency and functionality of the valves, therefore very important to the design of a successful prosthetic valve. Pioneering in-vivo works using ultrasound techniques show some interesting results related to the functionality of sinus pocket and the coupling effect of multiple valves. Due to the limitation of technological advances, the resolution of the in-vivo studies is limited, and quantitative analysis of the flow field was limited to the bulk velocity, and the detail velocity distribution was unattainable. Only a few qualitative experimental work has been done regarding to the flow dynamics. A study on an in-vitro environment with high resolution velocimetry technique like PIV will provide valuable data to our understanding to the valve function and provide insight to improve the prosthetic valve design.

7.4 **Goals**

The main goals of the current work are:

A. To characterize the fluid dynamics of a bioprosthetic bicuspid venous valve using an in-vitro bench-top system.
B. To investigate the role of sinus to the valve function from the fluid dynamics point of view.
C. To study the flow around a pair of prosthetic venous valves in an in-vitro experimental setup.

To achieve these goals, a bench-top in-vitro flow system to approximate the venous physiological conditions was set up. Prototype prosthetic valves that mimic the native venous valve were tested in the flow system. The valve motion and flow field was captured and measured using Particle Image Velocimetry (PIV). The detailed flow field together with pressure and bulk flow rate data was analyzed. The effect of sinus and valve coupling effect were investigated, and suggestions to improve the prosthetic valve design based on the experimental data were made to help the design of the next generation of prosthetic valves.

8 Experimental Setup

8.1 Pulse Duplicator (PD) Flow Loop

A flow facility was developed to produce the physiological conditions of the blood flow through a venous valve. The flow facility shown in Figure 2-1 (Pulse Duplicator PD-1100, BDC Laboratories, Wheat Ridge, CO) consisted of three sub-systems: the pulsatile diaphragm pump, the flow regulating and system and the test section. The functionality of each of the component is described below.

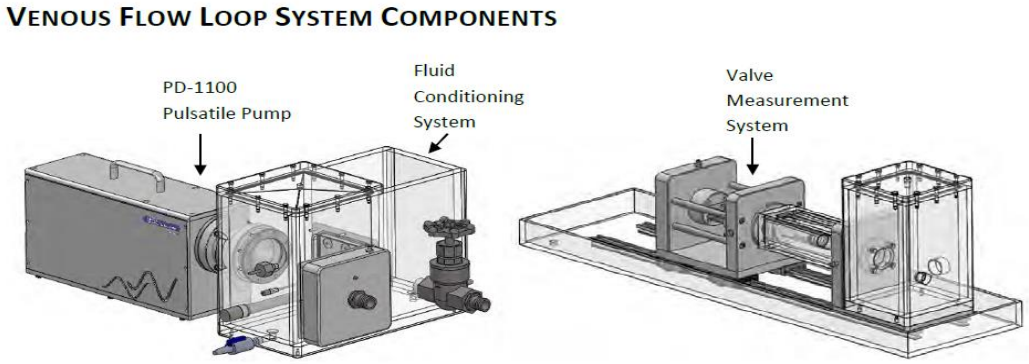

Figure 8-1 The Pulse Duplicator apparatus and system: the pulsatile pump, the flow conditioning system and the valve measurement system.

The computer controlled and servo motor driven pump (PD-1100, BDC Laboratories, Wheat Ridge, CO) provided control over the waveform and frequency of the resulting fluid flow. A flexible silicone diaphragm isolated the pump head from the main test flow loop. During systole phase which simulates the contraction phase of the heart, the diaphragm displaced the fluid due to movement of the pistons, and outward flow was created towards the test section. During the diastole phase which simulates the dilation phase of the heart, the diaphragm

collapsed and drew fluid from the reservoir tank. In this study the pulsatile flow waveform is simplified to a sinusoidal pressure waveform to provide the pulsatile flow condition.

The flow conditioning system provided flow directional control and mean pressure control. The pressure difference created by the pulsatile pump during valve closure was controlled by the Pressure Differential Control Valve (PDCV). Mean pressure of the system was controlled by a needle valve distal to the valve testing chamber that allowed for regulation of resistance.

The test section consisted of a square container made of Plexiglas and a round glass tube to mimic the geometry of the vessel. The whole test section was then mounted to the system for the valve testing. Two pressure transducers are used to measure the upstream and downstream pressure of the test section to evaluate the valve performance. An ultrasound flow probe (ME13PXN, Transonic system) was mounted upstream to provide flow rate measurement of the system. For experiments in the present study, the mean flow rate was set at 0.35L/min at 15 BPM (beats per minute) rate, and the peak pressure difference under diastole phase was adjusted to 2 mmHg. The pressure and flow rate data was recorded at 5 kHz data rate for 15 sec and the data is phase-averaged after processing. A MATLAB code was written to process the data log output of the PD system. The code identified the individual valve cycle and marked the four major valve events:

FFStart – Start of the forward flow, when the flow rate is larger than zero in the valve cycle.

FFEnd – End of the forward flow, when the flow rate drops down from positive to zero in a valve cycle.

EQEnd – End of equilibrium, when the flow rate reaches the maximum in a valve cycle.

CVEnd – End of closing volume, when the flow rate reaches the negative peak.

8.2 **Working Fluid**

To mimic the viscosity of the blood and also reduce the image distortion due to refraction, the working fluid was a solution of glycerol and water at a volume ratio of 2:3 with a resultant viscosity of 3.66 centipoise (*cP*) (25℃) with a 1.41 refraction index.

The dimensionless numbers used to characterize the pulsatile blood flow are Reynolds number and Wormersley number. The Reynolds number is defined as

$$Re = \frac{Vd}{\nu}, \tag{8-1}$$

where *V* is the flow velocity, d is the vessel diameter and *v* is the kinematic viscosity of the fluid. The Wormersley number is defined as

$$\alpha = \frac{D}{2}\sqrt{\frac{\omega}{\nu}}, \tag{8-2}$$

where ω is the angular frequency of the oscillation, d is the vessel diameter and *v* is the kinematic viscosity of the fluid. At the current testing condition, the Reynolds and Womersley numbers were 358 and 4.5, respectively.

8.3 **Particle Image Velocimetry (PIV) Setup**

Particle Image Velocimetry (PIV) setup was in conjunction with the PD flow loop platform to perform the velocity measurements. The PIV experimental set up is shown in Figure 8-2. A double-pulsed Nd:YAG Laser (Solo 120XT, New Wave Research) was used to illuminate the flow tracers. The PD flow loop was seeded with 10 µm polystyrene fluorescent particles (SPHERO™, 10~14µm, Nile Red), which has an excitation maximum of approximately 525 nm

with a subsequent emission maximum of approximately 560 nm. The fluorescent lights emitted from the particles were excited by the 532nm wavelength illuminating laser light. A band-pass filter is used to filter out the reflections from the laser wavelength, only allowed the fluorescent light emitted from the tracer particles to be recorded on the CCD camera. The Lens optics was used to shape the laser beam into a thin laser sheet (~1mm) to illuminate the area of interest. A 10-bit monochrome CCD camera (Uniquvision, UP-1830 -10) was used to capture tracer motions within this area. The resolution of the camera was 1024 x 1030 pixels to provide a 15.4µm/pixel spatial resolution, corresponding to an imaging area of 15.77mm x 15.86mm.

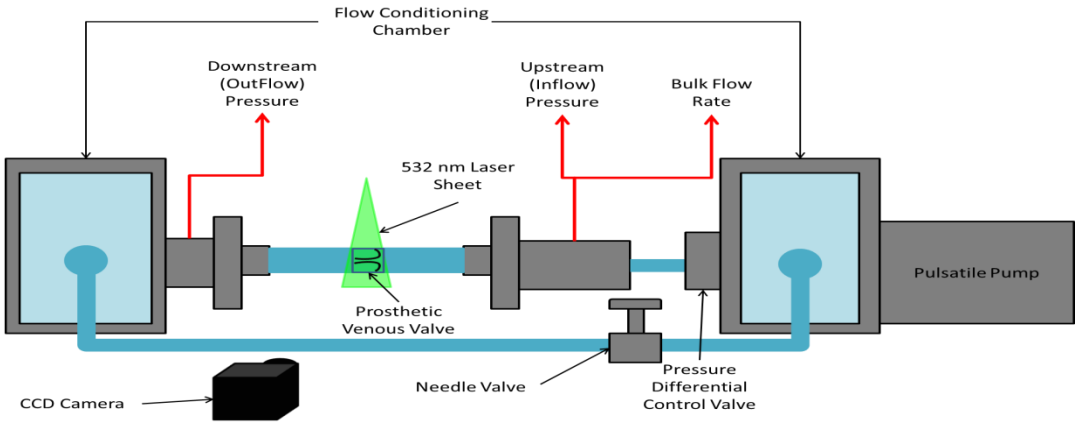

Figure 8-2 Schematics of the PIV experimental setup.

The PIV images were first pre-processed to remove the valve area and reflections from the glass wall. The pre-processed images were then processed using standard cross-correlation PIV algorithms. The interrogation window was set with a 50% overlap, and iteratively refined to 48 by 48 pixels with the window deformation technique (Raffel *et al.*, 2007). Outliers where then identified and replaced using universal outlier detection method (Westerweel & Scarano, 2005) described in section 3.2 of part I.

8.4 **Prosthetic Valve**

The bioprosthetic valve used for the present study was provided by Cook Biotech Inc (West Lafayette, IN). The valve was a third generation bioprosthetic venous valve (BVV3) frame with a 12 mm nominal diameter. Detailed information of the valve can be found in Pavcnik *et al*. (2008). During the experiment, the valve was placed into the round glass tube (12 mm I. D.) in the test section of the PD flow loop. The proximal side and distal side are referring to the leaflet surfaces that are facing the venous flow proximal or distal to the heart. Three different valve leaflet designs are tested in the current study. Figure 8-3 shows the side view of the full-height/half-height/quarter-height valve design. For the full height valve, the leaflet was sutured all the way to the start of the frame, while for the half height and quarter height valves the leaflet edges were shortened to be roughly half of the valve frame.

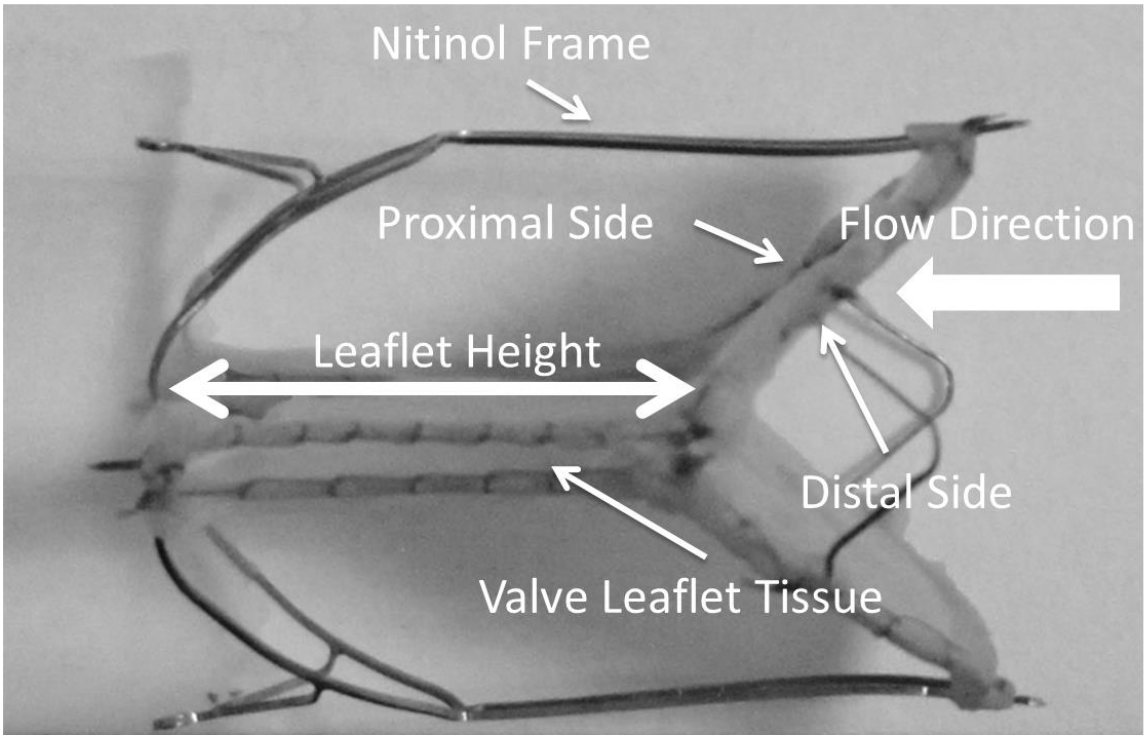

Figure 8-3 Side view of the bioprosthetic valve

8.5 **Valve Pairing Configuration**

Figure 8-4 shows the coordinate system used to in the valve pairing experiments, and the PIV measurement locations. The valve orientation was defined as the angle Θ to the horizontal plane (*X*-*Z* plane) in Figure 8-4. The angle between the two valves, $\Theta 2$-$\Theta 1$, was set to 0 degree and 90 degree. To investigate the coupling effect of the two valves, three different separation distances D = 3cm, 4cm and 5 cm were tested. These distances correspond to normalized separation distances of 2.5d, 3.3d and 4.2d, where d is nominal vessel diameter. There were a total of 6 different valve pairing configurations tested and the details are listed in Table 8-1.

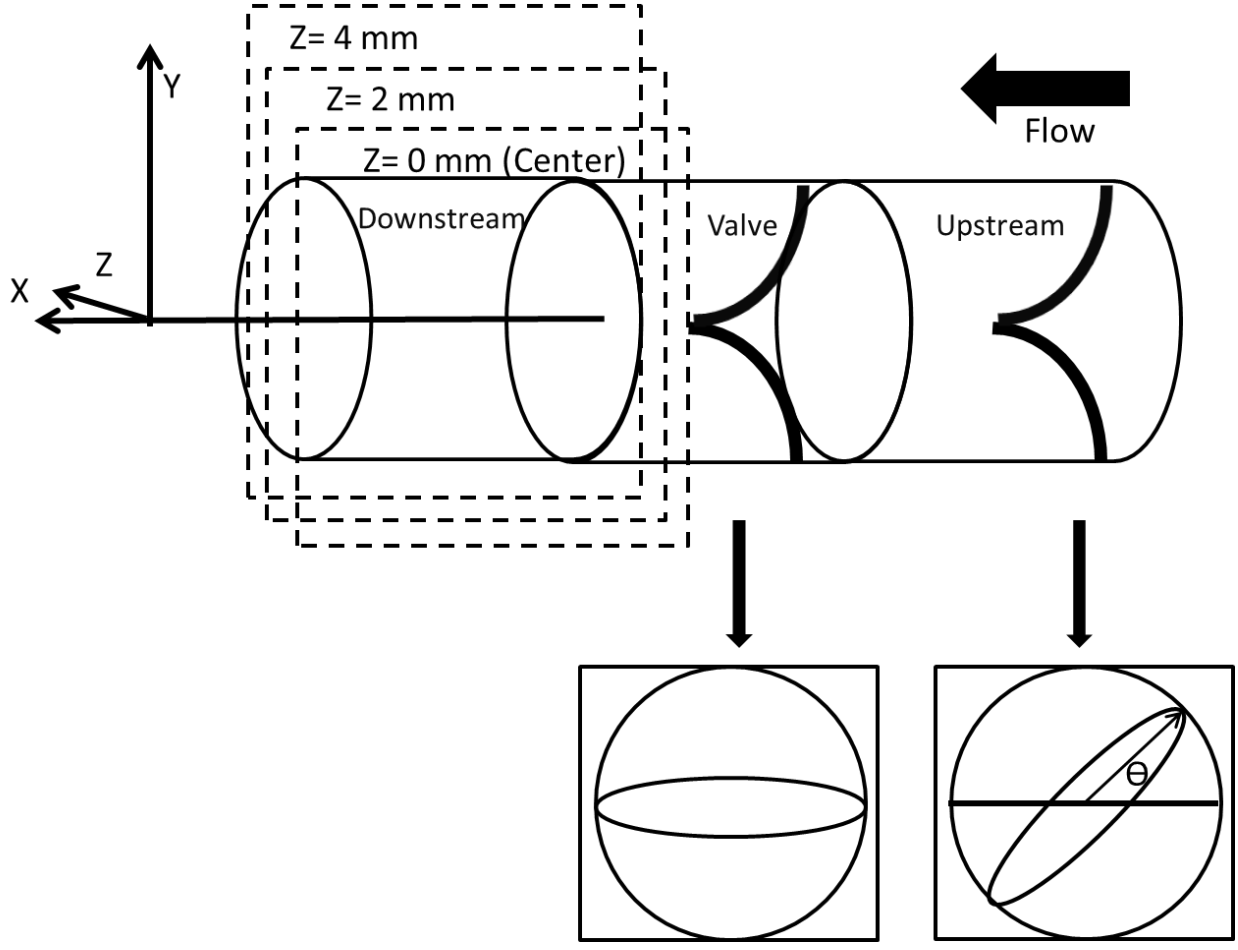

Figure 8-4 Coordinate system used in valve pairing experiments and the measurement locations

Valve Pairing Configuration	Separating Distance *D*	Θ_2-Θ_1
1	4cm	0°
2	4cm	90°
3	5cm	0°
4	5cm	90°
5	3cm	0°
6	3cm	90°

Table 8-1 The valve pairing configurations

8.6 **Valve Testing Configuration**

To investigate the effect of the sinus pocket, glass tubes of 12mm I.D. were used as the vessel in the test section and they were made with and without the sinus pocket, respectively. The sinus pocket dimension is shown in Figure 8-5. In order to investigate the effect of the sinus pocket to the prosthetic valve performance, two different valve designs were tested: the full-height design and the half-height design. The height is referring to the leaflet length in terms of the nominal radius of the valve frame.

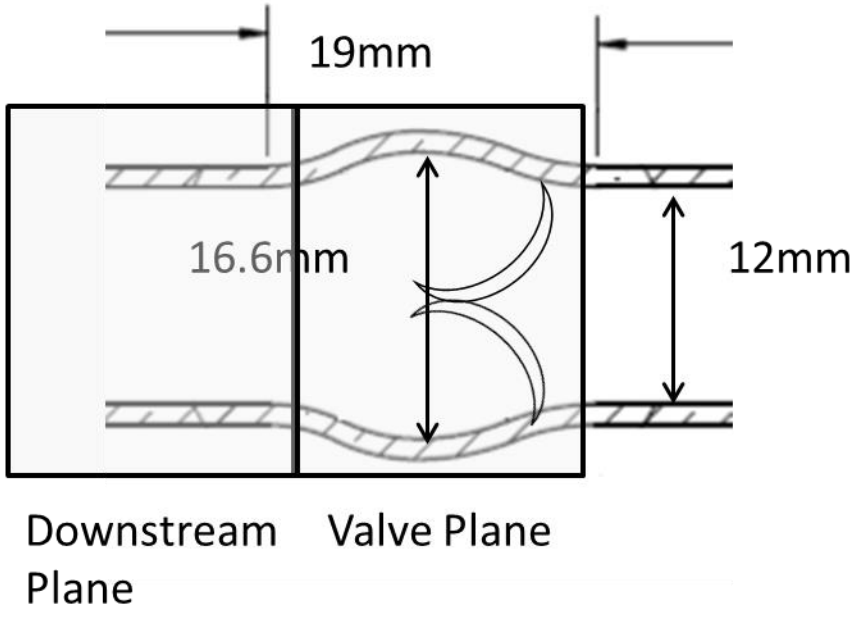

Figure 8-5 Dimensions of the tube with sinus pocket in the current study

9 Results and Discussions

9.1 Valve Cycle

Because of the pulsatile nature of the blood flow, it is helpful to understand the time variations of bulk flow properties such as pressure and flow rates before investigating the flow details. The bulk flow measurements from the pulse duplicator flow loop are presented in this section to describe the cyclic valve motions. The flow and pressure data of a single half-height valve are shown in Figure 9-1. The red line is the valve inflow pressure, the blue line is the outflow pressure, the green line indicates the flow rate and the black line represents the pressure difference between the inflow and outflow pressure. FFStart and FFEnd are marked by upward and downward-pointing green triangles. EQEnd is marked by the magenta diamond, and CVEnd is marked by a yellow triangle. From Figure 9-1, the four phases of the valve cycle defined by Lurie *et al.* (2003) can be identified and described as following. The bulk flow rate increases until it reaches a peak value (from FFStart to EQEnd), and the rate of increasing can be identified with two different slopes. This period is the opening phase and the equilibrium phase, separated by the change of the slope of the flow rate. The flow rate then decreases to a negative peak value and the pressure difference increases (from EQEnd to CVEnd). This period is the valve closing phase, since the flow rate is reducing. The flow rate then stabilizes around zero until the end of the cycle, and the pressure difference start to build up after the flow rate reaches the minimum magnitude (from CVEnd to FFStart). This period is the valve closed phase, since the valve is now closed and flow is stopped by the valve, hence the increasing pressure difference at the start of this phase. Later in the phase due to the sinusoidal pressure waveform from the pulse duplicator, the upstream pressure reduced and the pressure difference is then decreased again until the valve opens again.

Using these four valve events together with the pressure and bulk flow rate curve, several performance indices can be computed to compare the performance of the valve. A list of these performance indices and how they are calculated is listed in appendix A.

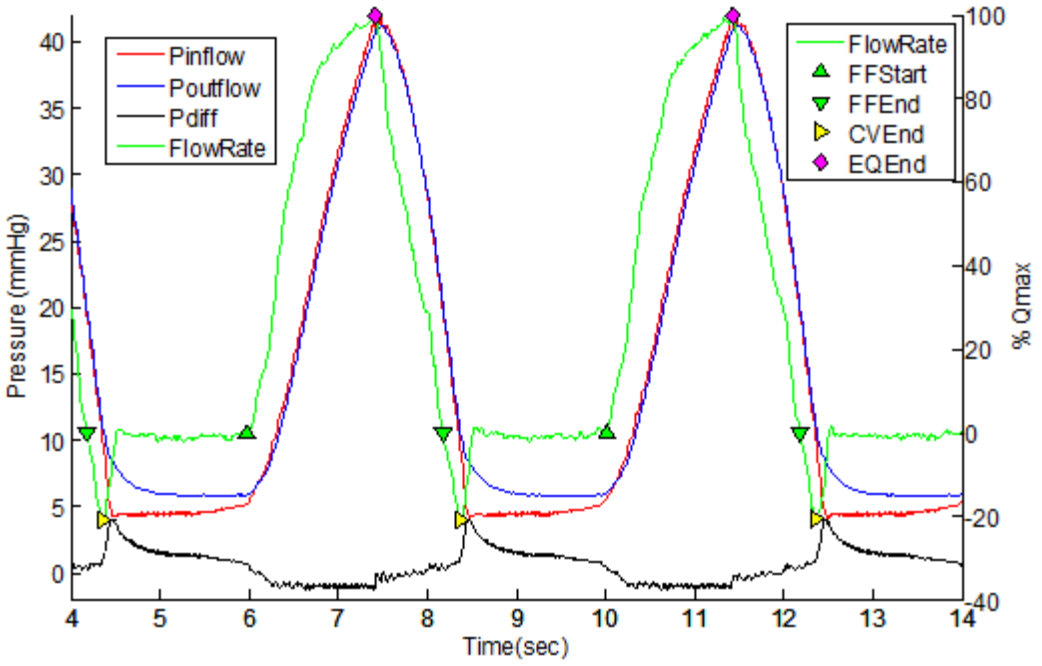

Figure 9-1 Valve log of the PIV experiment processed by MATLAB routine. The red line is the valve inflow pressure, the blue line is the outflow pressure, the green line indicates the flow rate and the black line represents the pressure difference between the inflow and outflow pressure. Start of forward flow (FFStart) and end of forward flow (FFEnd) are marked by upward and downward-pointing green triangles, respectively. End of equilibrium (EQEnd) is marked by the magenta diamond, and end of closing volume (CVEnd) is marked by a yellow triangle.

9.2 **Effect of Sinus**

In this section, in-vitro experiments of the single valve in a vessel with and without the sinus pocket are described. Effect of the sinus pocket is discussed in detail based on the experiment results.

9.2.1 **Hemodynamics**

Table 9-1 shows the performance indices calculated from the pressure and flow data calculated as described in section 9.1. The leakage for the cases with sinus was significantly larger than those without sinus, and the half height valve has the lowest total regurgitate volume. The closing time shows that the half-height valve without sinus has the fastest response, and valves without sinus were responding faster than the valve with sinus. The pressure difference data were comparable for all the valves and is less than 1.5 mmHg on average. The effective orifice area was also comparable, but the half-height valve without sinus had the largest value.

	Half-Height with Sinus	Half-Height w/o Sinus	Full-Height with Sinus	Full-Height w/o Sinus
CLOSING VOLUME(mL)	-2.3	-0.31	-0.82	-0.58
LEAKAGE VOLUME(mL)	-3.9	-0.31	-2.7	-1.4
TOTAL REGURGITATE VOLUME(mL/min)	94	9.2	52	30
STROKE VOLUME(mL)	18	24	20	22
MEAN REGURITATE FLOW(mL/s)	-4.9	-0.46	-2.4	-1.4
REGURGITATE VELOCITY	-25	-2	-11	-6.3
PERCENT CLOSING VOLUME TIME(%)	15	5.4	9.2	7.5
CLOSING TIME FOR VALVE(sec)	0.62	0.2	0.37	0.30
PERCENT LEAKAGE VOLUME TIME(sec)	32	33	36	37
REGURGITATION FRACTION VOLUME(%)	-34	-2.6	-17	-9.1
PERCENT STROKE VOLUME TIME(%)	52	62	55	56
SYSTOLIC DURATION(%)	68	67	64	63
PEAK POSITIVE PRESSURE DIFFERENCE(mmHg)	-0.9	0.72	-0.76	-0.46
MEAN POSITIVE PRESSURE DIFFERENCE(mmHg)	-1.3	-1.1	-1.2	-1.3
RMS FORWARD FLOW(mL/s)	11	12	11	12
MEAN FORWARD FLOW(mL/s)	8.8	9.3	9.2	9.8
EFFECTIVE ORIFICE AREA(cm2)	0.20	0.23	0.22	0.22
CARDIAC OUTPUT(mL/min)	370	354	355	358

Table 9-1 Hemodynamic performance indices of the 4 valve testing configurations.

9.2.2 **PIV Measurements**

Figure 9-2 shows the velocity fields measured by PIV overlaid with the calculated vorticity map at center plane of the valve region of the full-height valves, where the flow direction was from right to left. The velocity fields at four valve phases of the valve cycle are shown. At the opening phase, the valve leaflet expanded and created forward flow in the sinus region. In this phase, the jet flow coming out from the valve was not stronger than the ambient flow created by the valve motion. In the case with sinus, the forward flow was observed about 3mm away from the valve exit, and regions inside the sinus region were almost stagnant. In the case without sinus strong forward flow was present in the back of the leaflet, which is the region equivalent to the sinus pocket in the case with sinus region. In the equilibrium phase the valve opened fully, and there was less forward flow in the sinus / back of the leaflet region. Strong jet flows were formed at the valve exit plane for both cases, therefore strong vorticity were observed at the exit of the valve due to the shear flow. In the case with sinus, flow was formed due to the converging region formed by the full-height leaflet and the vessel wall. This is very different than the case without sinus, in which the leaflets and the vessel wall formed a diverging geometry near the tip of the leaflet, and the flow was observed to be much slower. In the closing phase, the jet diminished and reversed flow was observed at the sinus region for the case with sinus. For the case without sinus, the diminishing jet flow formed a narrower jet and the flow was inverted and moved towards the vessel wall. In closure phase, reversed flows were observed for both cases. Stronger reversed flow was found in the sinus region for the case with sinus especially, near the back of the leaflets.

Figure 9-3 shows the velocity fields measured by PIV overlaid with the calculated vorticity map at center plane of the valve region of the half-height valves. During opening and

equilibrium phases, higher vorticity was observed in both of the cases with sinus and without sinus, compared to the full-height valve cases. This observation suggests strong shear flow around the exit of the valve. Vorticity inside the sinus pocket was low during the valve closure phase, but vortical flow patterns were observed in both the cases with and without sinus.

Figure 9-4 and Figure 9-5 show the downstream velocity fields overlaid with the vorticity map of the all the testing configurations. The general flow feature was a starting vortex pair formed when the valve opens which transported downstream, as observed from the opening phase. In the equilibrium phase the exiting jet flow maintained a shear flow structure. During the closing phase the shear flow was diminishing but still maintained the pattern. At the valve closure phase, the flow was reversed for the cases with sinus but more random for the cases without sinus.

The axial velocity profiles of all valve configurations at the exit plane of the valve are shown in Figure 9-6 (a). For better comparison, the velocity profiles were roughly aligned so that the velocity peak locations are at the center of the figure. The jets of the cases with sinus were narrower than those without sinus. The peak velocities for the case with sinus were also lower than those without sinus. At the wall region, valves without sinus had velocity profiles that had local minimum, while the valves with sinus with profiles that had local maximum.

The axial velocity profiles of all valve configurations at downstream positions of the valve are shown in Figure 9-7. The measurement locations were normalized by the vessel diameter. In all cases, the jet flow profiles were shifted off-center, likely due to the slight asymmetry of the valve leaflet. The jet profiles were maintained in these locations, except the half-height valve without sinus case, where the jet flow profile shifted as the flow moved

downstream. Reversed flows at the wall region were found in all cases and all locations, corresponding to the shear flow structure observed in Figure 9-4 and Figure 9-5.

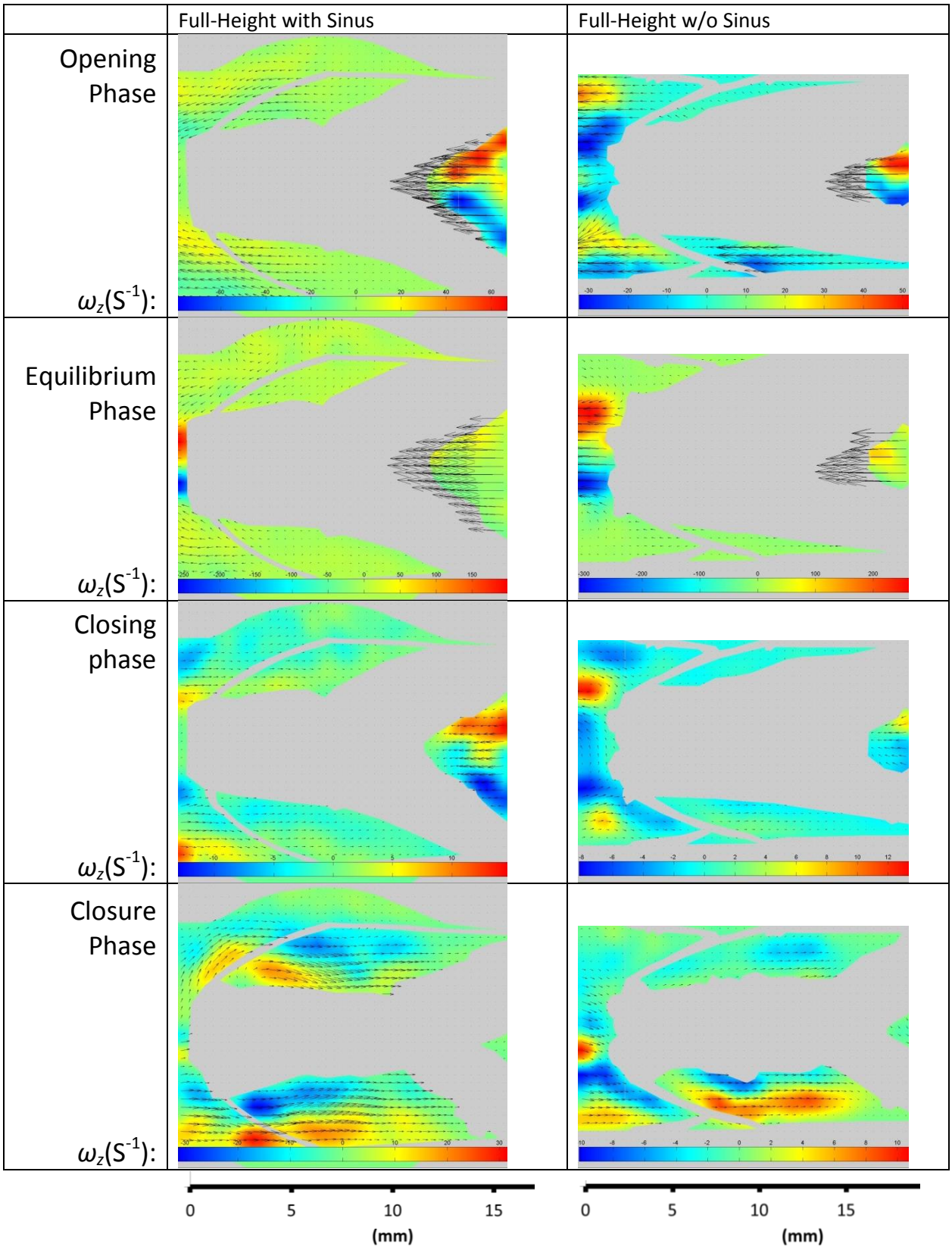

Figure 9-2 PIV measurement results of the full-height valves with and without sinus at the valve region for the 4 phases of valve motion. Color bar shows the vorticity colormap.

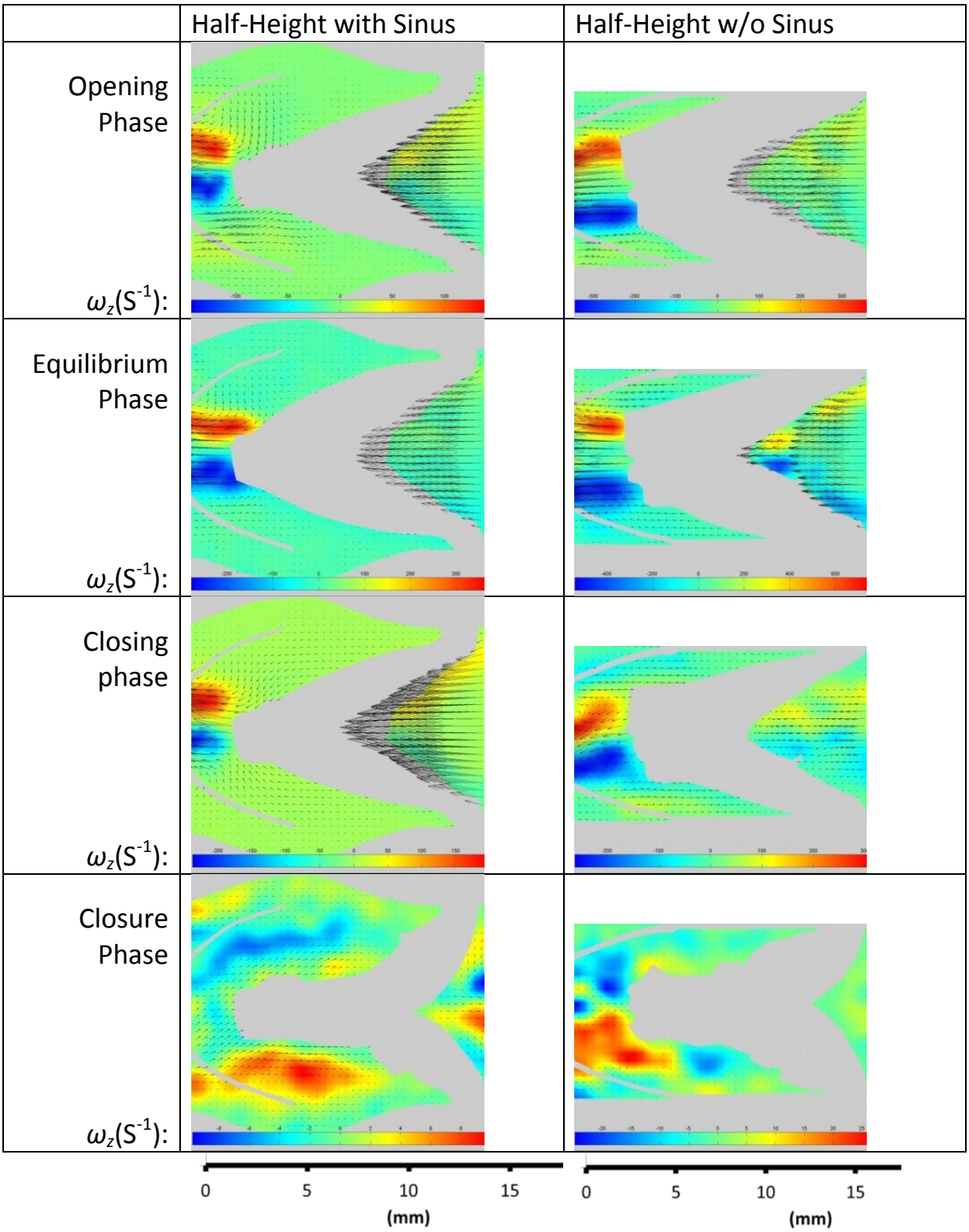

Figure 9-3 PIV measurement results of the half-height valves with and without sinus at the valve region for the 4 phases of valve motion. Color bar shows the vorticity colormap.

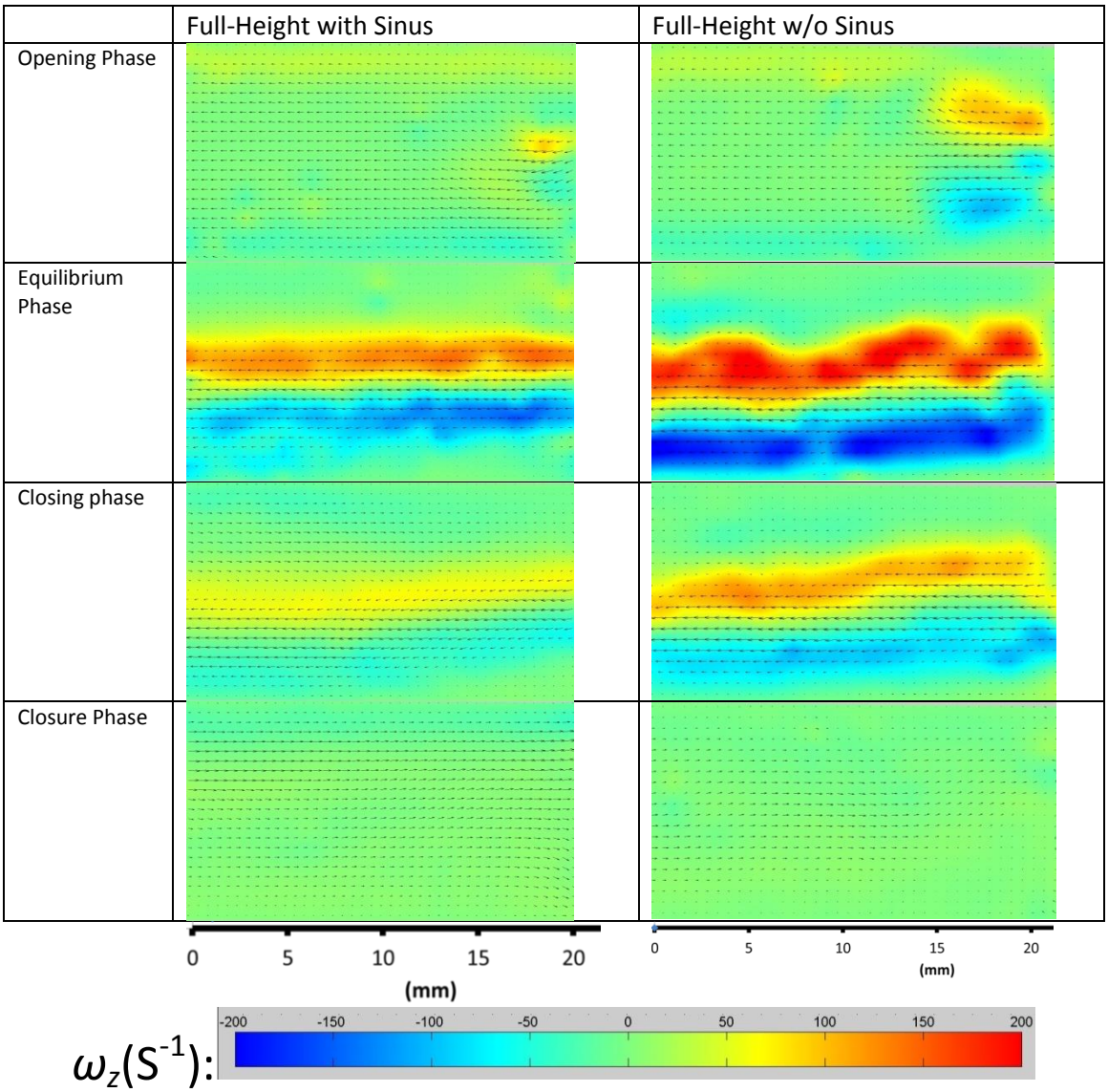

Figure 9-4 PIV measurement results of the full-height valves with and without sinus at the downstream region for the 4 phases of valve motion. Color bar of vorticity is shown on the bottom of the image.

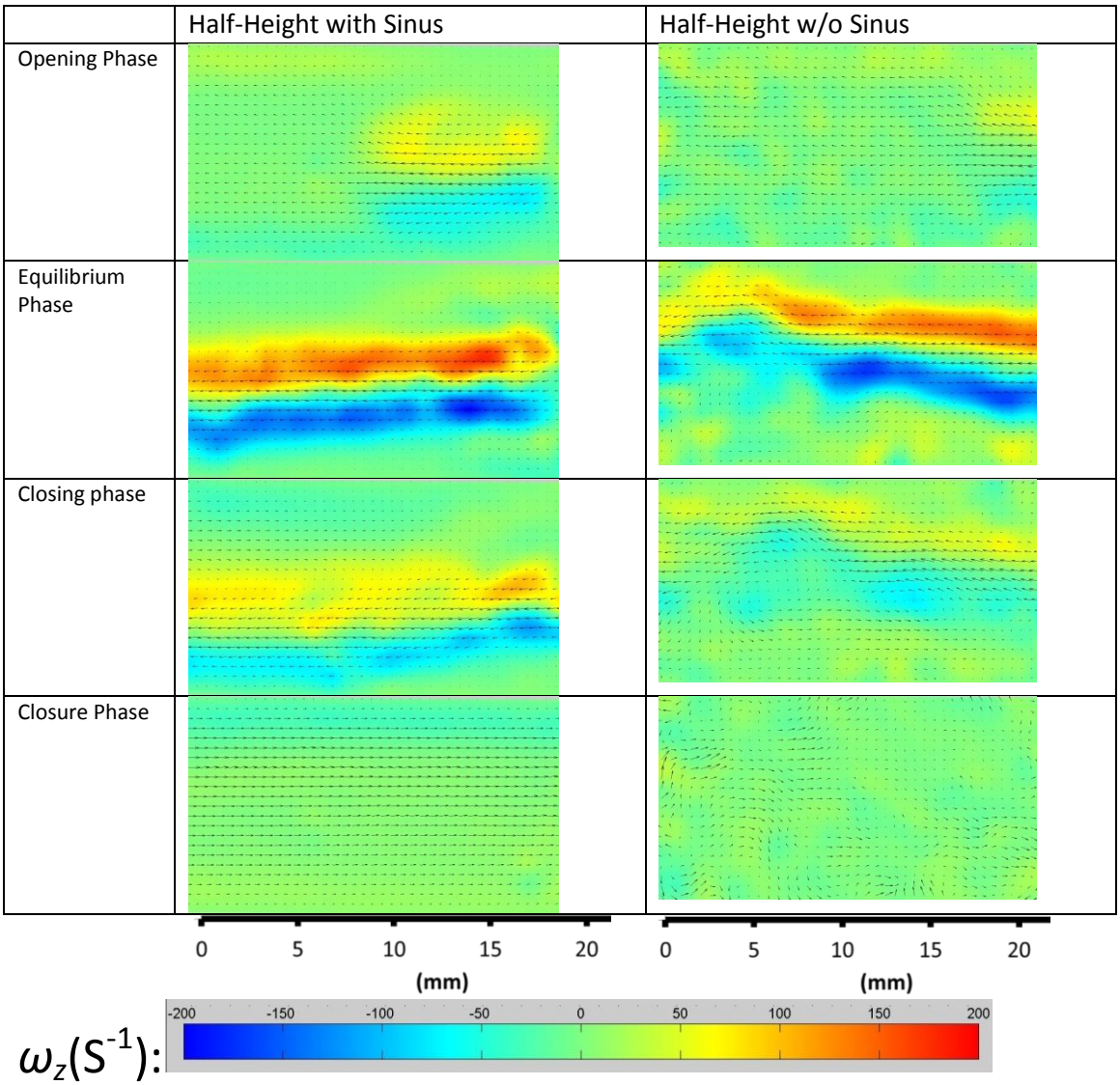

Figure 9-5 PIV measurement results of the half-height valves with and without sinus at the downstream region for the 4 phases of valve motion. Color bar of vorticity is shown on the bottom of the image.

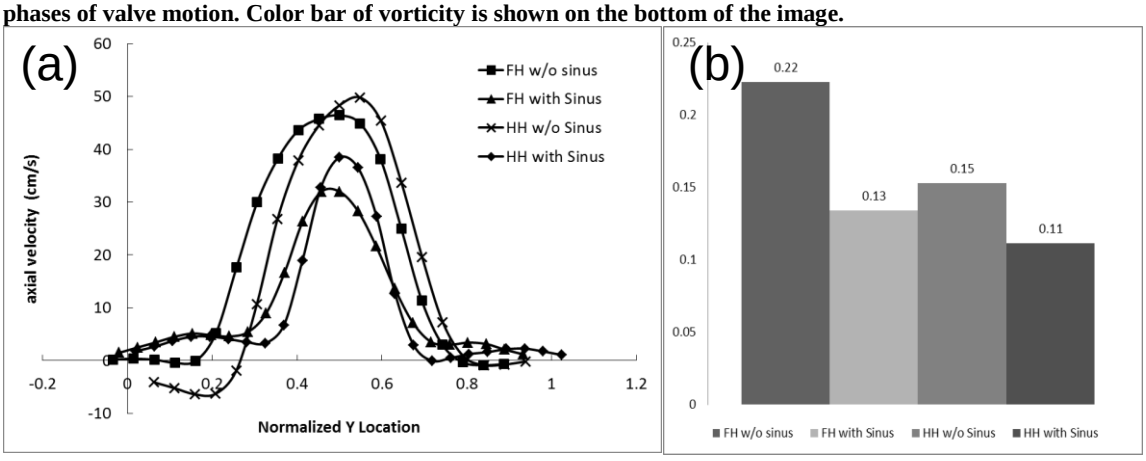

Figure 9-6 (a) Velocity profiles of the equilibrium phase at the exit of the 4 valve test configurations. The profiles are shifted to align to the center, and the locations are normalized. (b)Jet half width of the 4 valve test configurations normalized by the valve diameter calculated from Figure 9-6 (a).

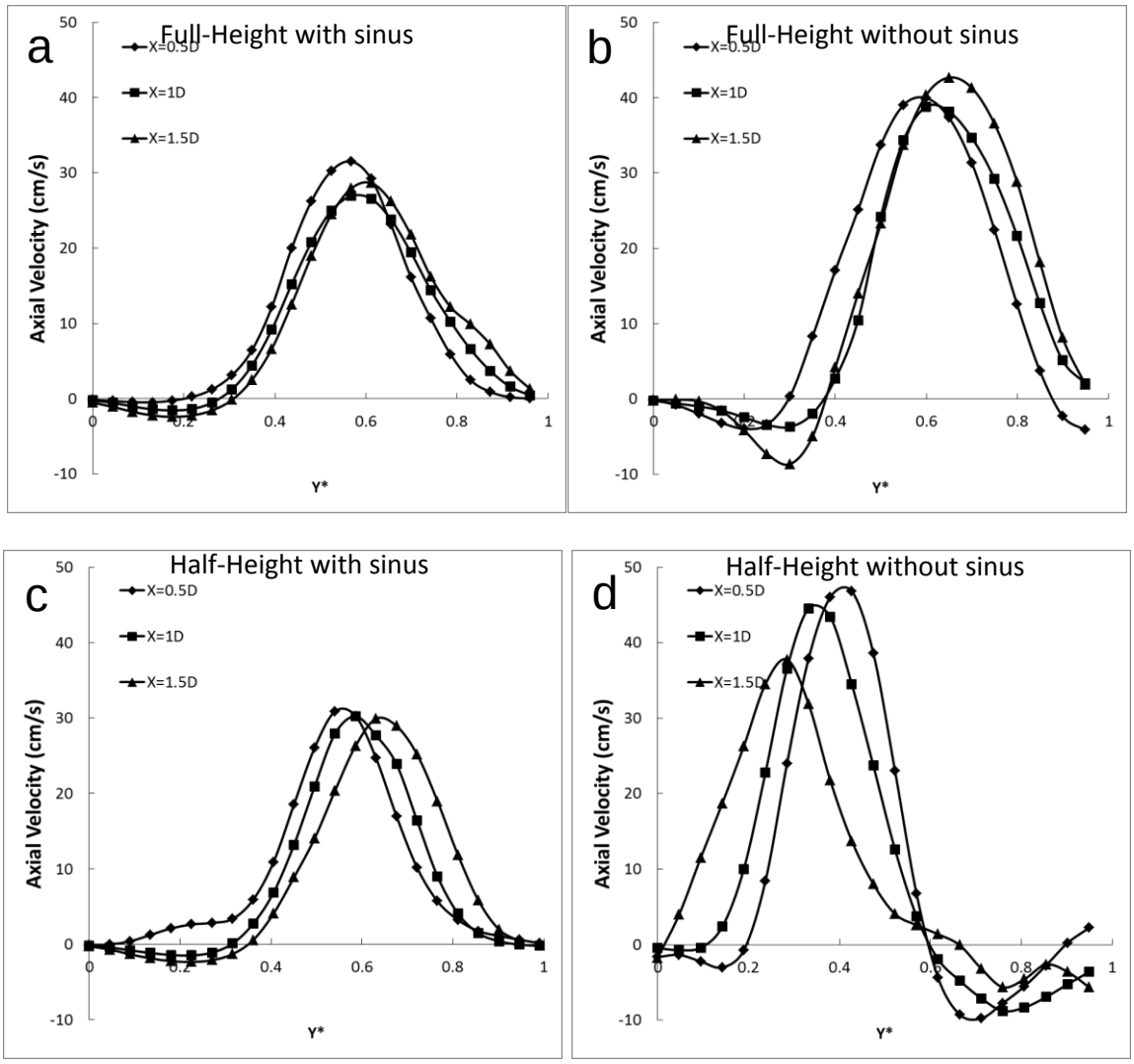

Figure 9-7 Velocity profiles of the equilibrium phase at different downstream locations for the 4 valve test configurations. The x locations are normalized by the diameter of the vessel. Y* are the normalized by the diameter of the vessel.

9.2.3 **Discussion**

The hemodynamic results show that the valve with sinus created more leakage than that without sinus in the current prosthetic valve. For both valve designs, the leakage from the valve with sinus was significantly larger than that without sinus. The main reason is that the valve frame is designed for the vessel without the sinus. The suturing points of the valve leaflet to the frame do not extend to the sinus region. This results in leakage from the side of the valve when

the valve is fully closed. The valve with sinus did respond slower where the closing time was 3 times slower for the half-height valve and 23% slower for the full-height valve. The effective orifice area (EOA) which is a measure of the valve performance and flow resistance was found to be at the same level for all valve configurations. This suggests that although the flow inside the sinus pocket created a slightly more resistance to the valve motion, it provides similar flow resistance to the flow system.

The leaflet length has an influence on the hemodynamic performance. The valve with half-height length responded faster (lower valve closing time), and had smaller regurgitation. This is because the short leaflet has less inertia to move, and reducing the number of suturing points due to shorter leaflet length also ensures better valve quality and symmetry of the leaflets.

The sinus pocket works as regulator of flow around the valve. The PIV results showed the vorticity was, in general, lower for the case with sinus than without at the shear layer region. This can be observed from the comparison of PIV measurements at the valve regions (Figure 9-2 and Figure 9-3). This also helps maintain the vortical flow structure during valve closing phase to prevent flow stasis between the leaflet and the vessel wall. The sinus pocket allows the flow to turn and form a vortex structure smoothly. Without the sinus, the space between the leaflet and the vessel wall was limited which can result in more sharp turns that may create local stagnation regions.

The sinus also creates a forward flow at the near wall region during valve opening and equilibrium phase, as seen in the velocity profile at the exit planes in Figure 9-6. This is because the fluid inside the sinus pocket is pushed out by the motion of the leaflet during valve opening to create the pressure gradient on the proximal side of the leaflets. This positive pressure gradient created the forward flow at the wall region near the exit of the valve and resulted in a weaker

shear layer. This can be seen in Figure 9-7, where the velocity profiles for the valve with sinus at the near wall region are smoother than those without the sinus. The positive pressure gradient formed by the sinus also causes normal stress on the leaflets to limit their opening. This effect can be seen by comparing the valve openings at equilibrium phase in Figure 9-2 and Figure 9-3. The half jet width, defined as the distance measure from the centerline of the jet where the velocity is equal to half of the centerline velocity, is shown in Figure 9-6(b). The jet width of the full-height valve with sinus was 59% of the one without sinus, and for half-height valve the ratio was 73%. These results show that the flow structure of half-height valve without sinus was closer to the one with sinus than the full-height valves. The PIV measurement in half-height valves (Figure 9-3) show that a vortical flow structure was present near the tip of the leaflet. It is located inside the sinus pocket for the half-height valve but not the case for the full-height valve. As a result, the full-height valve lost most of the benefit from the sinus pocket. For the half-height valve, the gap between the leaflet and the vessel wall was larger and the vortex structure was formed and maintained.

A decrease in leaflet length can provide similar effect as the sinus pocket for maintaining the vortical flow pattern near the leaflet tip. A comparison of the PIV results of the valves without sinus (Figure 9-2 and Figure 9-3) shows that the vortex structure was formed for the half-height valve during valve closure phase. For the full-height case, there was only entrained flow due to the closing motion of the leaflets. The vorticity was lower for the full-height valve than the half-height valve. This result implies that the vortical flow can exist without the sinus, but the leaflet lengths have to be shorter. The vortical structure only occurred at the tip of the leaflets but hard to reach the root of the leaflet when the leaflet was longer. Karino and Motomiya (1984) showed that although the vortex structure near the tip of the leaflet can induce

a counter-rotating vortex inside the pocket region, the flow velocity was extremely low. Flow can still be stagnant at the root of the leaflet and become a source of thrombosis. Hence shorter leaflets reduce the size of this stagnant region and likely reduce the chance of thrombosis.

One of the advantages of the sinus may be to reduce the solid stress on the leaflet. In a finite element analysis, Grande-Allen *at al.* (2000) showed that the leaflet stress was increased without the sinus on the aortic valve after Valve Sparing Root Replacement procedure. Katayama *et al.* (Katayama *et al*., 2008) showed that the sinus of valsalva results in a lower solid stress to the aortic valve leaflet and facilitates the gradual but smooth closure of the valve. In their simulations, deformations of the leaflet were reduced by the sinus. This is because the sinus pocket accommodates the retrograde flow and prevents the retrograde flow impinging the tip of the leaflets to form a torque to bend the leaflet tip. For the prosthetic valves, the effect of the solid stress may be less important than native venous valves, because the valve is connected to the rigid valve frame. For the fluid stress, the effect can be reduced by decrease of the leaflet length so the retrograde flow does not split up to form the bending torque.

In practice, all of the current valve designs are aimed for implanting the prosthetic valves to the straight vessel section. The proper position of competent valves in the lower extremity still requires more study (de Borst & Moll, 2012). Therefore, it is more desirable to design a valve that can function with the straight vessel wall but still have the benefit provided by the sinus.

The main limitation of this study is the vessel is rigid and has no compliance. This is likely the cause of the higher leakage for the valves with sinus because the rigid valve frame and the rigid vessel cannot provide good seal from the side of the valve.

9.3 **Effect of Valve Pairing**

In this section, in-vitro study of the coupling effect of a pair of bioprosthetic valves is described. Effect of valve pairing is discussed in detail based on the experiment results.

9.3.1 **Hemodynamics**

Data of a single cycle of the pressure, flow and the difference between the upstream and downstream pressure are shown in Figures 2b and 2c for all valve pairing configurations and the single valve data are listed as a base for comparison. The pressure and flow data is very similar for all the cases. The main difference to the single valve case is the pressure difference. All the valve pairing configurations had a larger pressure difference during valve opening phases. This is as expected because the pressure drop is larger from the two valves than the single valve. Table 2 shows the performance indices calculated from the pressure and flow data. Most of the indices are similar for all 6 configurations, with the exception of total regurgitation volume shown in Figure 2d. All valve pairing configurations has a smaller regurgitation volume compared to the single valve case. In all 6 cases, pairing configuration 4 (0 degree $D = 3.3d$) has the lowest regurgitation volume and the 90 degree configuration is larger than the 0 degree configuration at the same separation distance. For the 0 degree configurations, the total regurgitation volume increases with decreasing valve separation distance. For the 90 degree configurations, the total regurgitation volume is smallest at $D = 4$cm, and is largest for the $D = 2.5d$ case.

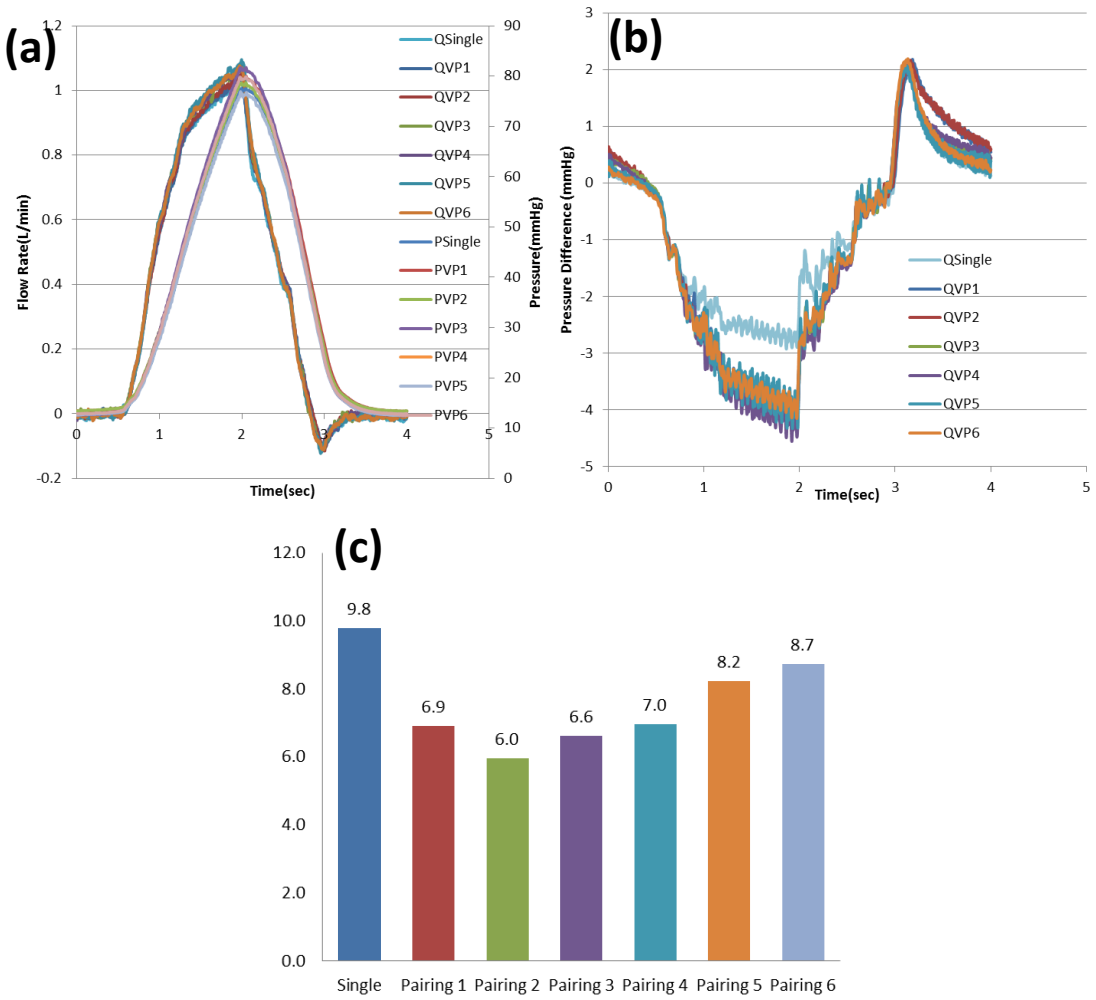

Figure 9-8 Hemodynamic Results of different valve pairing configurations

(a) Pressure and Flow rate data of a valve cycle of all the testing configurations in the present study

(b) Pressure difference of a valve cycle of all he testing valve pairing configurations

(c) The total regurgitation volume of all the valve pairing configurations tested in the current study.

	Single	Pairing 1	Pairing 2	Pairing 3	Pairing 4	Pairing 5	Pairing 6
CLOSING VOLUME(mL)	-0.17	-0.15	-0.15	-0.13	-0.14	-0.15	-0.17
LEAKAGE VOLUME(mL)	-0.48	-0.33	-0.25	-0.31	-0.33	-0.40	-0.41
TOTAL REGURGITATE VOLUME(mL/min)	9.8	7.2	6.0	6.6	7.0	8.2	8.7
STROKE VOLUME(mL)	24	24	24	24	24	24	24

MEAN REGURITATE FLOW(mL/s)	-0.43	-0.30	-0.25	-0.28	-0.29	-0.34	-0.37
REGURGITATE VELOCITY	-2.4	-2.0	-1.7	-1.9	-1.9	-2.2	-2.4
PERCENT CLOSING VOLUME TIME (%)	3.6	3.6	3.6	3.5	3.1	3.3	3.7
CLOSING TIME FOR VALVE(sec)	0.14	0.14	0.14	0.14	0.12	0.13	0.15
PERCENT LEAKAGE VOLUME TIME(sec)	38	40	39	39	40	40	39
REGURGITATION FRACTION VOLUME (%)	-2.7	-2.0	-1.7	-1.8	-1.9	-2.2	-2.4
PERCENT STROKE VOLUME TIME (%)	58	57	57	57	57	57	57
SYSTOLIC DURATION (%)	62	60	61	61	60	60	61
PEAK POSITIVE PRESSURE DIFFERENCE(mmHg)	-0.28	-0.57	-0.53	-0.28	-0.52	-0.30	-0.49
MEAN POSITIVE PRESSURE DIFFERENCE(mmHg)	-2.2	-3	-3.1	-3.1	-3	-2.9	-3
RMS FORWARD FLOW(mL/s)	13	13	13	13	13	13	13
MEAN FORWARD FLOW(mL/s)	10	10	10	11	11	11	11
EFFECTIVE ORIFICE AREA(cm2)	0.18	0.15	0.15	0.15	0.15	0.16	0.15
CARDIAC OUTPUT(mL/min)	370	360	364	371	369	371	372

Table 9-2 Hemodynamic performance indices of all the valve pairing configurations

9.3.2 **PIV Measurements**

9.3.2.1 Effect of Valve Configuration

Figure 9-9 shows the velocity fields measured by PIV overlaid with the calculated vorticity map at the Z=0, valve region of the valve pairing configuration 1, 2 and the single valve. The four phases of the valve cycle are shown. During the equilibrium phase a jet flow was formed at the exit the valve, where the flow coming out of the valve reached maximum speed and the entrainment from the side is also at maximum. In the single valve configuration, the flow was steady and the shear flow regions that have high vorticity on the jet boundaries were stable. This was not the case for both valve pairing configurations. In both cases, the flow became unstable and the shear layer broke into vortex sheets. This is suggested by the regions of concentrated vorticity shown in the comparison of phase 2 in

Figure 9-9. The flow of the 90 degree pairing configuration (Valve pairing configuration 2) was making a turn towards the upper wall at 0.3d downstream of the valve exit. In the other two cases the jet flow were straight without turning.

The influence of the valve pairing configuration extends to further downstream of the flow. Figure 9-10 shows the downstream velocity fields overlaid with the velocity magnitude map of the two valve pairing configurations at the equilibrium phase, and compared with the single valve results. In the single valve case, the jet stream was strong and extended across the measurement plane. Other part of the flow was kept unchanged. In the valve pairing configuration 1 case, the jet only maintained a relatively short distance (~0.6d) and then expanded to the entire measurement plane. In the valve pairing configuration 2 the jet flow was also mixed with the ambient fluid and expanded out similar to that in the valve pairing configuration1. The jet stream was also shifted off-center, and a strong vortex structure was

formed at the center region. The vortex structure blocked the way and caused the jet stream to turn to the edge region of the vessel.

The flow in between the two valves was altered the most due to the different configuration. Figure 9-11 shows the comparison of the flow patterns in between the valves of the three valve configurations at equilibrium phase. The flow at $Z = 0d$ (0mm), $Z = 0.17d$ (2mm) and $Z = 0.35d$ (4mm) were measured to investigate the variation at Z locations. The flow patterns were significantly different between the valve configurations. The flow in valve configuration 1 shows the jet structure was shifted off-center, which was similar to the case shown in single valve downstream in Figure 9-10. The jet flow structure coming out of the first valve remained unchanged until the inlet region of the second valve, and then turned to the center region of the vessel near the rear of the second valve. The jet flow region spread out as Z increased, because the momentum is transported to the low speed region. At the lower half of the vessel, the flow was mostly stagnant with small reverse flow region due to the shear flow at the edge of the jet stream. In valve configuration 2, the jet flow was uniform across the measurement plane (X-Y plane) as seen from a top view of the valve. The flow is also off-center so the velocity is higher at $Z = 0.17d$ plane. The jet structure was not significantly altered either until the inlet region of the second valve. At $Z = 0.35d$, the velocity at the inner region was slower than the outer region.

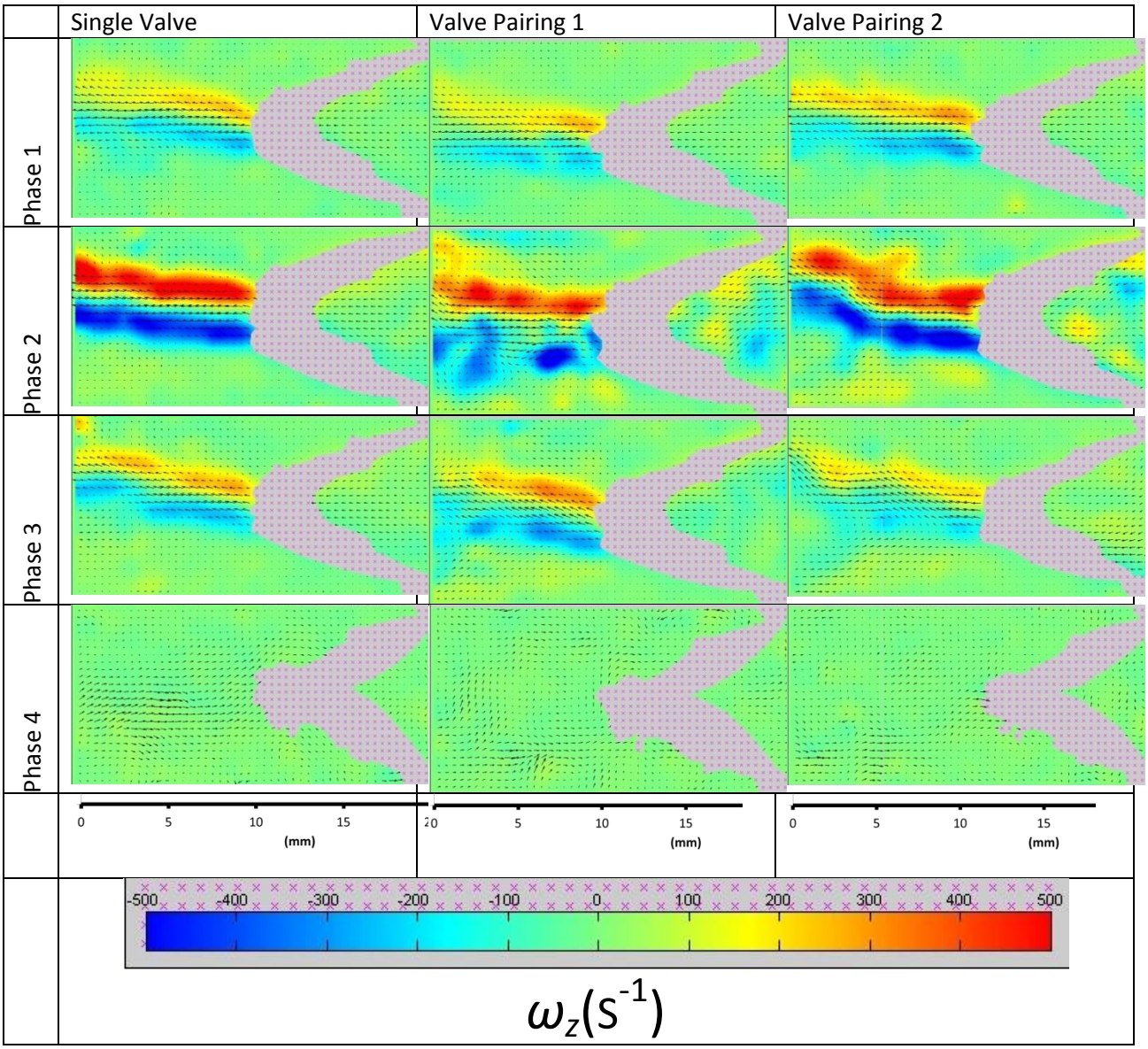

Figure 9-9 PIV Velocity vector fields and vorticity map of the four phases of the valve cycle for the single valve, valve pairing configuration 1 and 2 at the center plane of the valve region.

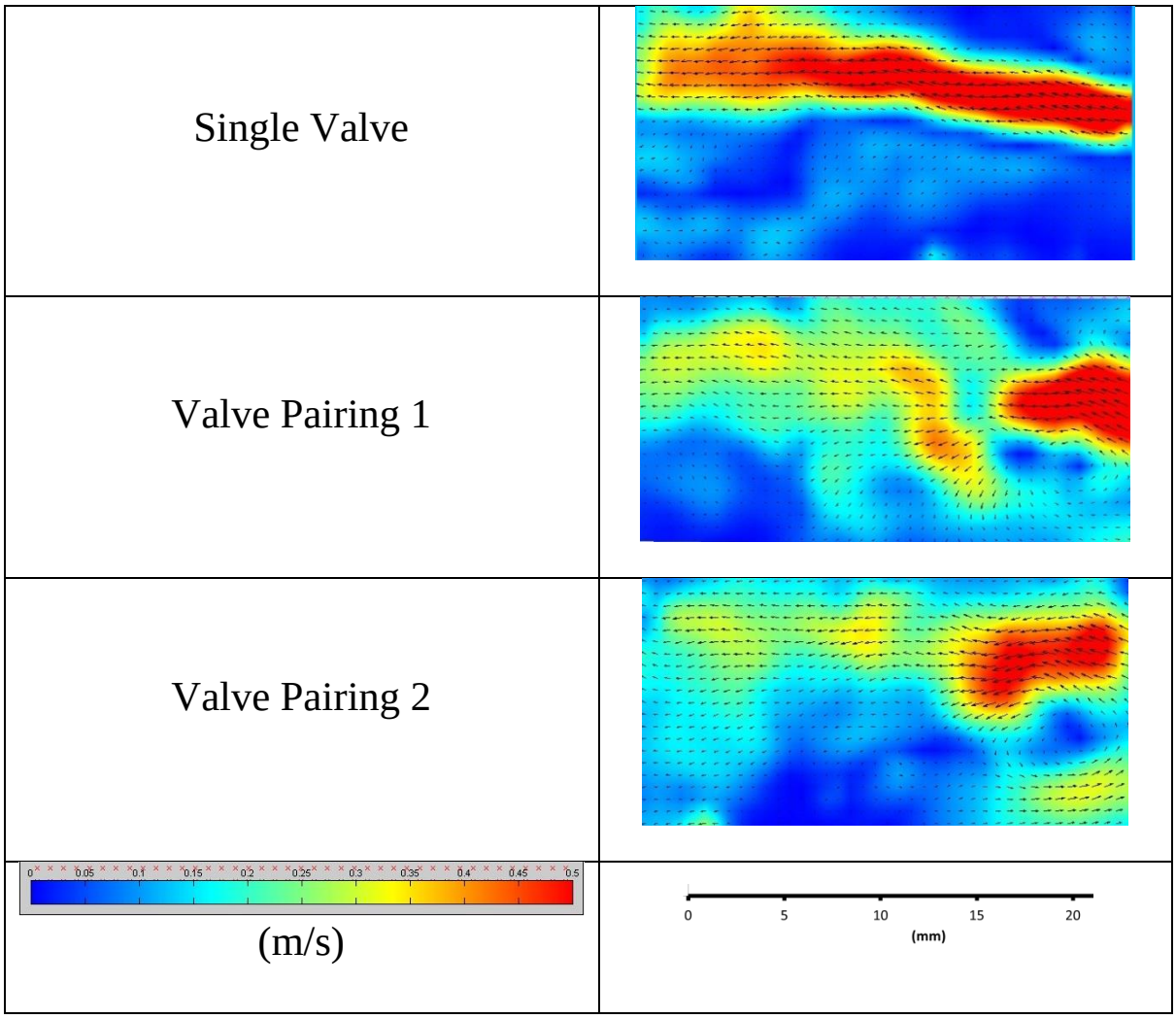

Figure 9-10 Velocity vector fields and the maps the velocity magnitude of the equilibrium phase of the valve cycle for the single valve, valve pairing configuration 1 and 2 at the center plane of the downstream region. The right edge of the image is at 0.8d downstream of the valve exit.

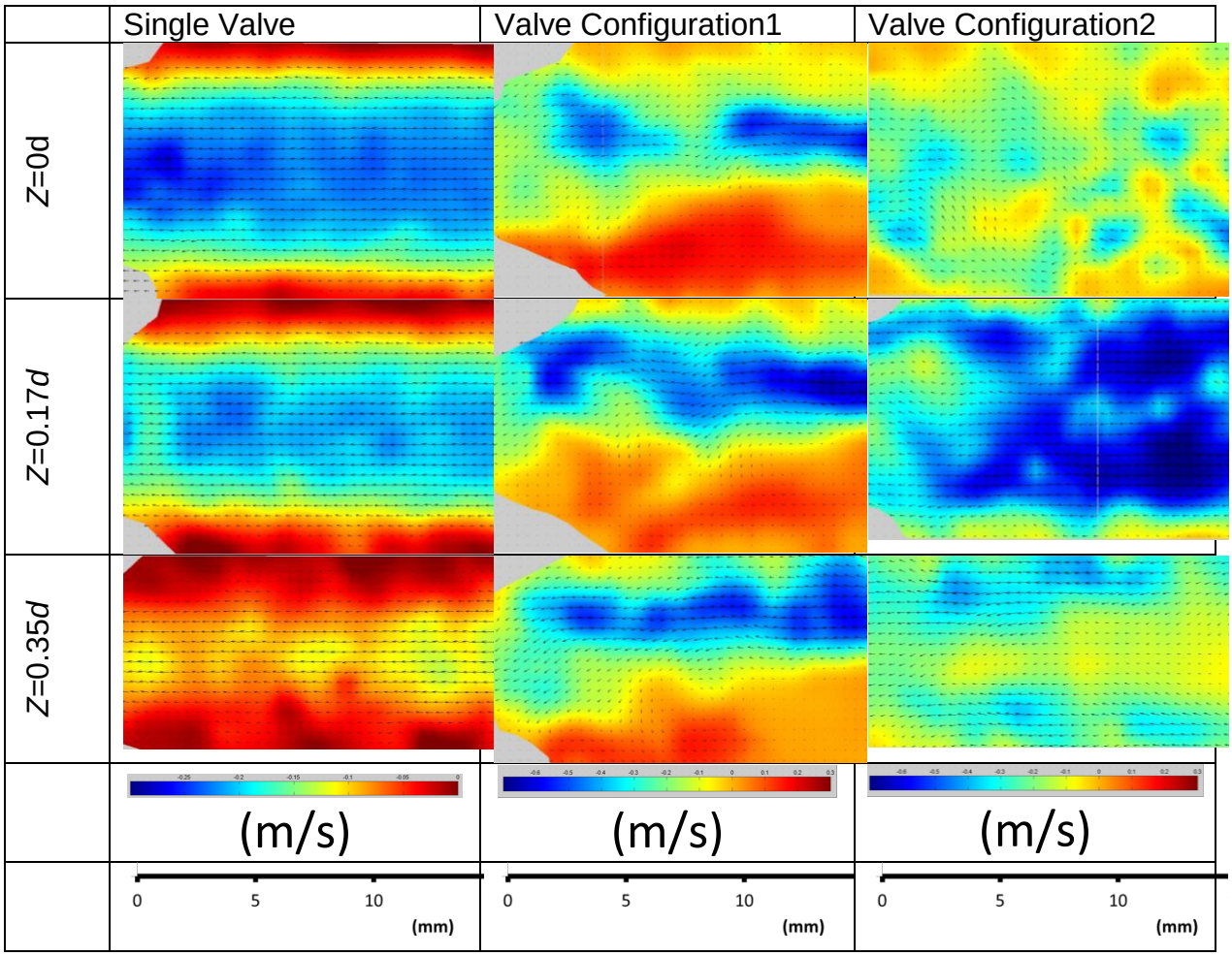

Figure 9-11 Velocity vector fields and the maps the u component of the velocity of the equilibrium phase of the valve cycle for the single valve, valve pairing configuration 1 and 2 at all measurement planes in the upstream (in between valves) region. The first valve (located upstream/distal side) is on the left side of the images, while the second valve (located downstream/ proximal side) is located right after the left edge of the images.

9.3.2.2 Effect of Valve Separating Distance

Figure 9-12 shows the velocity vectors overlaid with vorticity map during the equilibrium phase at the center plane for valve configuration 1~6 to show the effect of the separation distance between the two valves. In all 6 cases Jet flows exited the valves inclined to the vessel wall. The flow pattern is the most complex in the D=2.5d case, and several vortex concentrated regions were formed at the shear layer. In the D=3.3d cases, the shear layer were more continuous and uniform. The 90 degree configuration (Valve pairing configuration 2) had the most uniform vorticity distribution of the 6 cases. The vorticity patterns became more similar to each other for both D=4.2d cases.

Figure 9-13 shows the velocity fields overlaid with the fluid shear calculated from the velocity data for the 6 valve pairing configurations at different Z locations around the valve region. The fluid shear distributions were similar to the vorticity distributions. At Z = 0.17d planes, the strength of fluid shear was weaker than the center (Z = 0d) plane, but trends of the flow structure were similar to the vorticity data presented in the previous section. For the Z = 0.35d plane, the fluid shear was significantly weaker and resulted in a smaller region of strong fluid shear. For the 0 degree configuration, the jet stream direction was similar at all different Z locations, with the difference in the strength and the width of the jet stream decreased with increase in Z. For the 90 degree configuration, however, the jet stream had a larger turning angle towards the vessel wall. The fluid shear was weaker and the jet stream region shrank in width. This suggests a more three-dimensional flow pattern for the 90 degree configuration as compared to the 0 degree configuration. The fluid shear was lower at Z = 0.35d cases, similar to the single valve case.

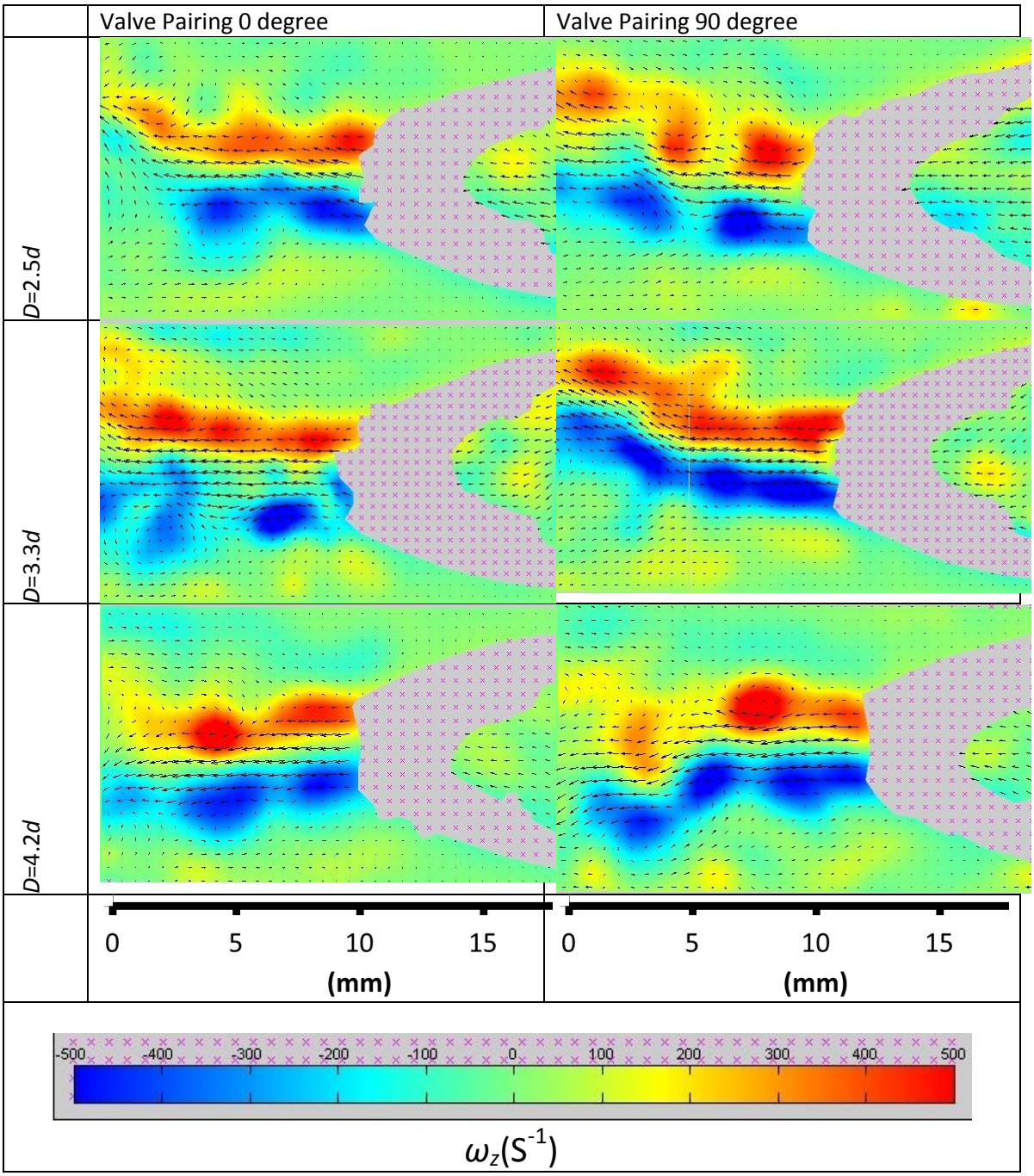

Figure 9-12 Velocity vector fields and the maps the vorticity of the equilibrium phase of the valve cycle for the valve pairing configuration 1 and 2 at different separating distances in the valve region

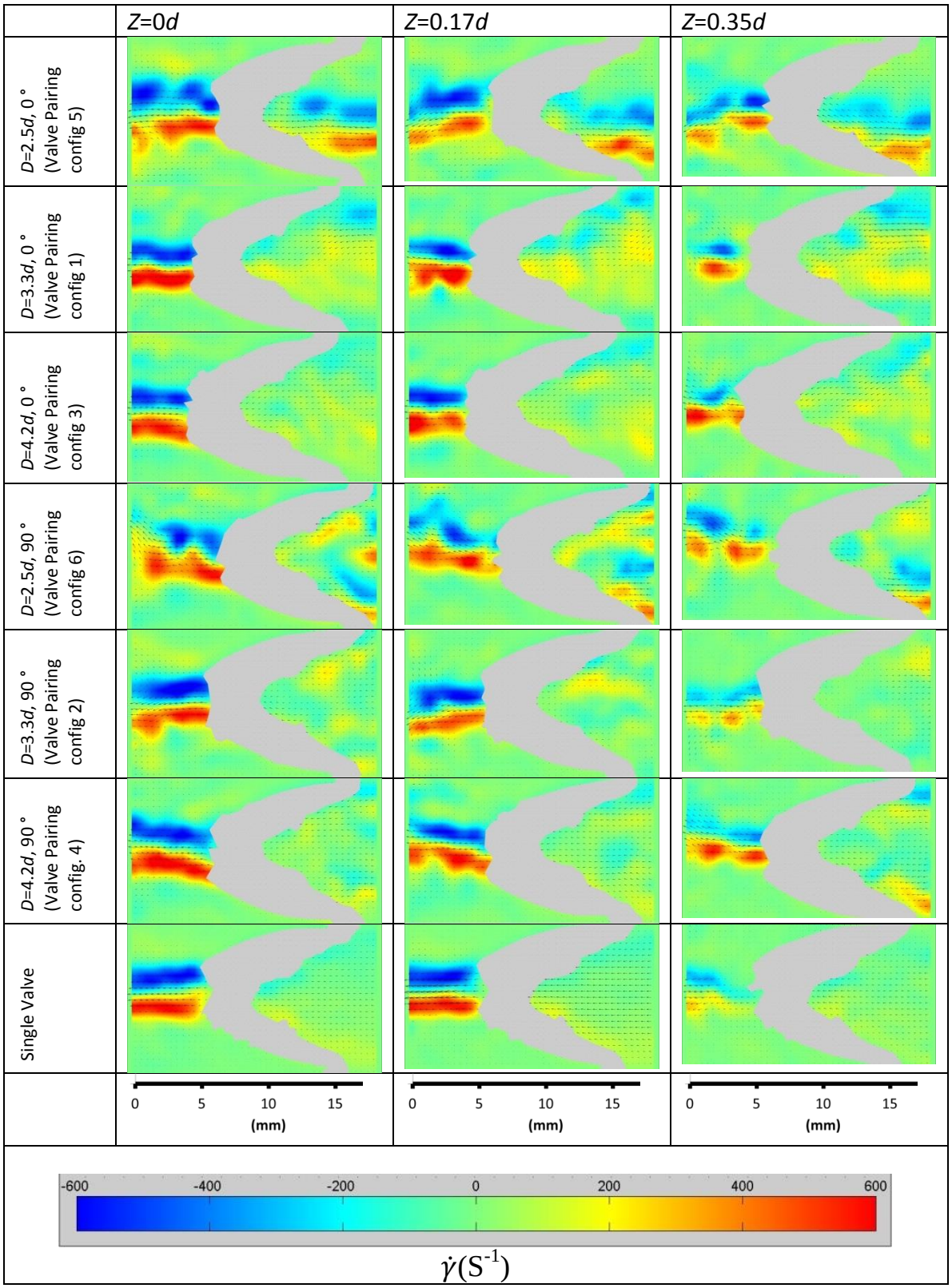

Figure 9-13 Velocity vector fields and the maps the fluid shear of the equilibrium phase of the valve cycle for all the valve pairing configurations at different separating distances in the valve region. The results of a single valve configuration are listed at the end for comparison.

9.3.3 **Discussion**

9.3.3.1 Effect of Valve Configuration

The pairing configuration significantly altered the flow structure between the valves. In the 0 degree pairing configuration (configuration 1, Figure 9-11), the flow pattern is similar to the downstream flow of a single valve (Figure 9-10) up to 0.25*d* before the second valve, where the jet flow turned to the center region of the vessel. This is because the jet flow from the first valve was off-center and had to turn to the inlet of the second valve. The flow patterns were similar for different *Z* planes. The turning of the flow also created a reversed flow region at the bottom half of the vessel. The reversed flow region is known to be a high risk factor for thrombosis. The flows of the 90 degree configuration (configuration 2, Figure 9-11) were different between *Z* planes, and asymmetry can be observed as the highest flow velocities were at $Z = 0.17d$ plane. At the center plane $Z = 0d$, no jet flow can be observed and non-uniform flow patterns were observed. At the edge ($Z = 0.35d$), higher flow velocities were observed at the outer region of the vessel and the center region of the vessel had very low velocities. No reversed flow region like valve pairing configuration 1 was observed for this case. All these observations suggest a complicated three-dimensional flow structure was formed in between the two valves for this valve configuration.

Compare the flow patterns of phase 2 in Figure 9-9, it can be observed that the valve pairing break the stable shear flow structure seen in the single valve case. In valve pairing configuration 1, the shear layer broke up into unstable rollers. The slight phase lag between the two valves that creates an unsteady flow is likely the cause of this unsteady flow structure. In valve configuration 2, the shear layer was more continuous but an abrupt turn could be observed

towards the vessel wall. This strongly suggests a complicated three-dimensional structure was present for valve pairing configuration 2.

The valve pairing enhanced the jet mixing to the ambient flow. Downstream flow in Figure 9-10 shows that the jet flow spread out for both valve pairing configurations around 1.2 to 1.5*d*, but in the single valve case the jet flow maintained at least 2.8*d* downstream of the valve exit. This suggests a better mixing due to the three-dimensional flow structure for the valve pairing configuration.

From the above observations, the orthogonal valve pairing configuration (valve pairing configuration 2) can create a more stable three-dimensional flow structure and cause better mixing of the flow. It also prevents reversed flow region in between the valves. Lurie and Kistner (2013) suggested that the orthogonal valve pairing configuration is preferred in nature, because it creates the helical flow pattern that increases the efficiency of the venous return flow. The current work is agreement with their findings.

9.3.3.2 Effect of Valve Separating Distance

The coupling effect of the valve pairing can last longer in the vessel, but the effect fades with longer separation distance. In the range tested in this work (D=2.5~4.2d) the flow around the downstream valves were all altered by the upstream valves, suggesting that the coupling effect extends beyond 4 times the vessel diameter. The flow features observed in the previous section for each valve pairing configuration were also observed at all different separation distances. With shorter separation distance, the coupling effect was stronger and the flow patterns of the two pairing orientations were more distinct. For D= 4.2d in Figure 9-12, the flow patterns were more similar at the center region. The mixing of the jet stream from the upstream

valve damped out the effect of the valve configurations as the distance increased which provides a more uniform upstream flow to the downstream valve. This trend was consistent with the findings by Lurie and Kistner (2012) that the distance between the two venous valves is about 4 cm. If the distance is longer, the effect of valve pairing is reduced and does not contribute to forming of the helical flow.

The measurements taken at different *Z* locations in Figure 9-13 shows that the flow was slower, and the jet stream width was also smaller than that at the center region. This is as expected since the opening of the valve decreases at the edge. For the orthogonal valve pairing configurations (configuration 2, 4 and 6), the flows were altered more at the edge. The jet stream turning angle was larger and started earlier than the center region. This variation in *Z* location also implies likely the flow has a three-dimensional structure. The rotational flow structure at the edge is likely beneficial to the venous flow, because it decrease the stagnant region around the vessel wall which may decrease the risk of thrombosis.

10 Conclusions and Future Work

10.1 Conclusion

1. An in-vitro bench-top flow system to simulate the physiological conditions of venous system was successfully setup for the study of the flow around venous valves. 2-D PIV measurements at multiple planes were successfully performed to resolve the unsteady pulsatile flow around the valves.
2. The sinus functions as a flow regulator to smooth the entrainment velocity profile and reduce the jet width. It also helps to maintain the vortex structure near the valve jet exit plane.
3. For the current prosthetic valve design, it is better to have a valve with shorter leaflet. The main advantage of the shorter leaflet is to reduce the region of flow stasis, and it has a similar performance to the valve with sinus. It also reduces the energy loss of the valve, making the valve a more efficient flow device.
4. Helical flow patterns can be created with either two valves pairing in different orientations or by combining a venous junction and a valve. The orthogonal valve pairing configuration has the benefit to create the helical flow pattern that increase the mixing of the blood flow and prevent reversed flow in between the valves.
5. The distance between the valves affects the degree of helical flow created by the two-valve pairing, and an optimized separation distance maintains the helical flow patterns created by the two valves.

10.2 **Future Works**

1. The main feature of vein vessels is that they are compliant and collapsible. In the current work the vessel wall is rigid, which may create different effect than the true venous vessel due to the interaction between the vessel wall and flow. To use a compliant material that can simulate the material properties of the venous vessel to replace the rigid tube should make the in-vitro system more close to the real conditions.
2. The influence of the pulse waveform to the flow pattern can be studied using a more realistic pressure waveform. A sinusoidal pulse waveform was used in the study to simulate the pulsatile blood flow. While this is good to provide a unified flow initial condition for comparison between valves, it should be noted that in real venous system the pulse wave form is very complicated. It is a combination effect of the pumping of the heart, the internal pressure change due to respiration and the movement of the leg (the muscle pump). More study is needed to understand the influence of different waveform and the interaction to the flow.
3. Lurie and Kistner (2013) showed that helical flow is not present at the SFJ (sapheno femoral junction) with an incompetent valve. From the results of a single valve configuration, it is shown that merely a valve itself does not create helical flow pattern. Since a junction of two vessels is often observed in between the valves, more study should be focus on the interaction between the junction and the valves and the resulting three-dimensional flow patterns,
4. Due to the 3-D nature of the flow, a three-dimensional method, such as the 3D-PTV technique described in part I, should be applied to help the understanding of the complicated 3-D flow structure.

Appendix Calculation of Valve Performance Indices

The valve performance indices are calculated from the pulse duplicator data log. The four events mark the time points that are important in the valve cycle, and therefore used during calculation. These indices are defined and calculated as below.

Inputs parameters (from data log or fluid properties):

FFStart – Time point marks the start of the forward flow, when the flow rate is larger than zero in the valve cycle.

FFEnd – Time point marks the end of the forward flow, when the flow rate drops down from positive to zero in a valve cycle.

EQEnd – Time point marks the end of equilibrium, when the flow rate reaches the maximum in a valve cycle.

CVEnd – Time point marks the end of closing volume, when the flow rate reaches the negative peak.

Cycle Start – Time point marks the start of a valve cycle

Cycle End – Time point marks the end of a valve cycle

PPD – Positive Pressure Difference, marks the end of Inflow Pressure > Inflow Outflow.

Q (ml/sec) – bulk flow rate measured by the flowmeter

P_{in} *(mmHg)* – inflow pressure measured upstream of the test section

P_{out} *(mmHg)* – outflow pressure measured downstream of the test section

ρ (g/cm^3) – blood mimicking fluid density.

T_{pulse} – period of the valve cycle

Valve Indices calculated:

CLOSING VOLUME (ml) – Volume of fluid passing during valve closure. Volume between the end of forward flow (*FFEnd*) and the end of closing flow (*CVEnd*)

$$V_C = \int_{FFend}^{CVend} Q(t)dt \tag{A-1}$$

LEAKAGE VOLUME (ml) – Volume of fluid passing through the valve while closed, defined as: the volume between the start of the test cycle and the start of forward flow (*FFStart*) plus the volume between the end of closing flow and (*CVEnd*) and the finish of the test cycle.

$$V_L = \int_{CycleStart}^{FFStart} Q(t)dt + \int_{CVEnd}^{CycleEnd} Q(t)dt \tag{A-2}$$

T.REG VOLUME (ml) – Total Regurgitate flow through the valve, defined as the closing volume plus the leakage volume.

$$V_{TReg} = V_C + V_L \tag{A-3}$$

STROKE VOLUME (ml) – Stroke volume through the valve, defined as the volume between the start of forward flow (*FFStart*) and the end of forward flow (*FFEnd*)

$$V_S = \int_{FFStart}^{FFEnd} Q(t)dt \tag{A-4}$$

MEAN REG FLOW (ml /sec) – Mean regurgitate flow through the valve during valve closure, defined as the total regurgitate volume divided by the total closure time.

$$\overline{Q_{Reg}} = \frac{V_{TReg}}{FFStart - Cycle\ Start + Cycle\ End - CVEnd} \tag{A-5}$$

REG VEL (cm/sec) – Mean regurgitate velocity through the test valve, defined as the mean regurgitate flow rate (ml/sec or cm^3/sec) divided by the valve effective orifice area (AOE, cm^2)

$$v_{reg} = \frac{V_{TReg}}{AOE} \tag{A-6}$$

***CV** (%PULSE)* – Closing volume time (*CVEnd – FFEnd*) as a percent of the total pulse

$$CV = \frac{CVEnd - FFEnd}{T_{pulse}} \times 100 \tag{A-7}$$

CT (sec) – Valve closing time

$$CT = CVEnd - FFEnd \tag{A-8}$$

LV (%PULSE) – Leakage volume time ([*FFStart* – Cycle Start] + [Cycle End – *CVEnd*]) as a percent of the total pulse

$$LV = \frac{[FFStart - CycleStart + CycleEnd - CVEnd]}{T_{Pulse}} \times 100 \tag{A-9}$$

***RF** (%PULSE)* – Regurgitate fraction volume as a percent of the total stroke volume

$$RF = \frac{V_{TReg}}{V_S} \times 100 \tag{A-10}$$

***SV** (%PULSE)* – Stroke volume time *(FFEnd – FFStart*) as a percent of the total pulse

$$SV = \frac{FFEnd - FFStart}{T_{pulse}} \times 100 \tag{A-11}$$

***SD** (%PULSE)* – Systolic Duration, defined as the closing volume time as a percentage of the total pulse plus the stroke volume as a percentage of the total pulse

$$SD = CV + SV \tag{A-12}$$

PPD MAX (mmHg) – Peak value of the positive pressure difference ($P_{in} - P_{out}$) over the time period ranging from the start of forward flow to the end of $P_{in} > P_{out}$.

$$PPD_M = \max[P_{in} - P_{out}]|_{FFStart}^{PPD} \tag{A-13}$$

PPD MEAN (mmHg) – Mean positive pressure difference ($P_{in} - P_{out}$) over the time period ranging from the start of forward flow to the end of $P_{in} > P_{out}$.

$$\overline{PPD} = \frac{\int_{FFStart}^{PPD}[P_{in}(t) - P_{out}(t)]dt}{PPD - FFStart} \quad \text{(A-14)}$$

RMS F. FLOW (ml/sec) – RMS (Root Mean Square) flow over the time period ranging from the start of forward flow start to forward flow end.

$$Q_{RMSFF} = \sqrt{\frac{\int_{FFStart}^{PPD} Q(t)^2 dt}{PPD - FFStart}} \quad \text{(A-15)}$$

MEAN F. MEAN (mmHg) – Mean flow over the time period ranging from the start of forward flow to the end of forward flow

$$\overline{Q_{FF}} = \frac{\int_{FFStart}^{FFEnd} Q(t)dt}{FFEnd - FFStart} \quad \text{(A-16)}$$

AEO (cm^2) – Effective Orifice Area or EOA is a metric used when evaluating the performance of prosthetic valves. The calculation is based off the ISO 5840 standard (Cardiovascular implants - Cardiac valve prostheses) and allows for real-time feedback of valve performance. The following equations are used in the calculation:

$$AEO = \frac{Q_{RMSFF}(ml/sec)}{51.6 \times \sqrt{\frac{\overline{PPD}(mmHg)}{\rho}}} \quad \text{(A-17)}$$

The Effective Orifice Area equation is derived from the Bernoulli Equation. The constant (51.6) is not dimensionless, thus, this equation is only valid with the units shown.

C.O. (l/min) – Cardiac Output defined as the stroke flow less all regurgitate flow

$$CO = \frac{V_S - V_{TReg}}{T_{pulse}} \quad \text{(A-18)}$$

References

Adrian, R. J., & Westerweel, J. (2011). *Particle image velocimetry*. Cambridge; New York: Cambridge University Press.

Adrian, R. J., & Yao, C. S. (1985). Pulsed laser technique application to liquid and gaseous flows and the scattering power of seed materials. *Applied Optics, 24*(1), 44-52.

Agüí, J. C., & Jimenez, J. (1987). On the performance of particle tracking. *Journal of Fluid Mechanics, 185*(1), 447-468.

Anderson, J. R., Chiu, D. T., Wu, H., Schueller, O. J., & Whitesides, G. M. (2000). Fabrication of microfluidic systems in poly (dimethylsiloxane). *Electrophoresis, 21*, 27-40.

Angarita-Jaimes, N., McGhee, E., Chennaoui, M., Campbell, H. I., Zhang, S., Towers, C. E., . . . Towers, D. P. (2006). Wavefront sensing for single view three-component three-dimensional flow velocimetry. *Experiments in Fluids, 41*(6), 881-891. doi:10.1007/s00348-006-0204-z

Angarita-Jaimes, N. C., Roca M, A. G., Towers, C. E., Read, N. D., & Towers, D. P. (2009). Algorithms for the automated analysis of cellular dynamics within living fungal colonies. *Cytometry Part a, 75A*(9), 768-780. doi:10.1002/cyto.a.20750

Baek, S., & Lee, S. (1996). A new two-frame particle tracking algorithm using match probability. *Experiments in Fluids, 22*(1), 23-32.

Beck, A., Thubrikar, M. J., & Robicsek, F. (2001). Stress analysis of the aortic valve with and without the sinuses of valsalva. *The Journal of Heart Valve Disease, 10*(1), 1-11.

Bergan, J. J. (2006). *The vein book* Academic Press.

Bergan, J. J., Schmid-Schönbein, G. W., Smith, P. D. C., Nicolaides, A. N., Boisseau, M. R., & Eklof, B. (2006). Chronic venous disease. *New England Journal of Medicine, 355*(5), 488-498.

Bohren, C. F., & Huffman, D. R.,. (1983). *Absorption and scattering of light by small particles*. New York: Wiley.

Born, M., & Wolf, E. (1999). *Principles of optics: Electromagnetic theory of propagation, interference and diffraction of light* CUP Archive.

Bown, M. R., MacInnes, J. M., Allen, R. W. K., & Zimmerman, W. B. J. (2006). Three-dimensional, three-component velocity measurements using stereoscopic micro-PIV and PTV. *Measurement Science & Technology, 17*(8), 2175-2185. doi:10.1088/0957-0233/17/8/017

Brady, M. R., Raben, S. G., & Vlachos, P. P. (2009). Methods for digital particle image sizing (DPIS): Comparisons and improvements. *Flow Measurement and Instrumentation, 20*(6), 207-219.

Brevis, W., Niño, Y., & Jirka, G. H. (2011). Integrating cross-correlation and relaxation algorithms for particle tracking velocimetry. *Experiments in Fluids, 50*(1), 135-147.

Caro, C. G., Doorly, D. J., Tarnawski, M., Scott, K. T., Long, Q., & Dumoulin, C. L. (1996). Non-planar curvature and branching of arteries and non-planar-type flow. *Proceedings of the Royal Society of London.Series A: Mathematical, Physical and Engineering Sciences, 452*(1944), 185-197.

Chen, S., Angarita-Jaimes, N., Angarita-Jaimes, D., Pelc, B., Greenaway, A. H., Towers, C. E., . . . Towers, D. P. (2009). Wavefront sensing for three-component three-dimensional flow velocimetry in microfluidics. *Experiments in Fluids, 47*(4-5), 849-863. doi:10.1007/s00348-009-0737-z

Choi, Y., & Lee, S. (2009). Three-dimensional volumetric measurement of red blood cell motion using digital holographic microscopy. *Applied Optics, 48*(16), 2983-2990.

Cierpka, C., Rossi, M., Segura, R., & Kaehler, C. J. (2011). On the calibration of astigmatism particle tracking velocimetry for microflows. *Measurement Science & Technology, 22*(1), 015401. doi:10.1088/0957-0233/22/1/015401

Cierpka, C., Segura, R., Hain, R., & Kaehler, C. J. (2010). A simple single camera 3C3D velocity measurement technique without errors due to depth of correlation and spatial averaging for microfluidics. *Measurement Science & Technology, 21*(4), 045401. doi:10.1088/0957-0233/21/4/045401

Cowen, E., & Monismith, S. (1997). A hybrid digital particle tracking velocimetry technique. *Experiments in Fluids, 22*(3), 199-211.

Criqui, M. H., Jamosmos, M., Fronek, A., Denenberg, J. O., Langer, R. D., Bergan, J., & Golomb, B. A. (2003). Chronic venous disease in an ethnically diverse population the san diego population study. *American Journal of Epidemiology, 158*(5), 448-456.

de Borst, G. J., & Moll, F. L. (2012). Percutaneous venous valve designs for treatment of deep venous insufficiency. *Journal of Endovascular Therapy, 19*(2), 291-302.

Duffy, D. C., McDonald, J. C., Schueller, O. J., & Whitesides, G. M. (1998). Rapid prototyping of microfluidic systems in poly (dimethylsiloxane). *Analytical Chemistry, 70*(23), 4974-4984.

Duncan, J., Dabiri, D., Hove, J., & Gharib, M. (2010). Universal outlier detection for particle image velocimetry (PIV) and particle tracking velocimetry (PTV) data. *Measurement Science & Technology, 21*(5), 057002. doi:10.1088/0957-0233/21/5/057002

Estevadeordal, J., & Goss, L. (2005). PIV with LED: Particle shadow velocimetry (PSV). Paper presented at the *43rd AIAA Aerospace Sciences Meeting and Exhibit, Meeting Papers,* 12355-12364.

Fries, R., Graeter, T., Aicher, D., Reul, H., Schmitz, C., Böhm, M., & Schäfers, H. (2006). In vitro comparison of aortic valve movement after valve-preserving aortic replacement. *The Journal of Thoracic and Cardiovascular Surgery, 132*(1), 32-37.

Gharib, M., Kremers, D., Koochesfahani, M., & Kemp, M. (2002). Leonardo's vision of flow visualization. *Experiments in Fluids, 33*(1), 219-223.

Gibson, S. F., & Lanni, F. (1991). Experimental test of an analytical model of aberration in an oil-immersion objective lens used in 3-dimensional light-microscopy. *Journal of the Optical Society of America A-Optics Image Science and Vision, 8*(10), 1601-1613.

Grande-Allen, K. J., Cochran, R. P., Reinhall, P. G., & Kunzelman, K. S. (2000). Re-creation of sinuses is important for sparing the aortic valve: A finite element study. *The Journal of Thoracic and Cardiovascular Surgery, 119*(4), 753-763.

Grothe, R., & Dabiri, D. (2008). An improved three-dimensional characterization of defocusing digital particle image velocimetry (DDPIV) based on a new imaging volume definition. *Measurement Science and Technology, 19*(6), 065402.

Guerrero J A, Mendoza-Santoyo F, Moreno D, Funes-Gallanzi M and Fernandez,S. (2000). Particle positioning from CCD images: Experiments and comparison to the generalized lorenz-mie theory [Abstract]. *Meas.Sci.Technol., 11*(5) 568. Retrieved from http://stacks.iop.org/0957-0233/11/i=5/a=318

Gunes, H., Sirisup, S., & Karniadakis, G. E. (2006). Gappy data: To krig or not to krig? *Journal of Computational Physics, 212*(1), 358-382.

Kajitani, L., & Dabiri, D. (2005). A full three-dimensional characterization of defocusing digital particle image velocimetry. *Measurement Science & Technology, 16*(3), 790-804. doi:10.1088/0957-0233/16/3/022

Karino, T., & Motomiya, M. (1984). Flow through a venous valve and its implication for thrombus formation. *Thrombosis Research, 36*(3), 245-257.

Katayama, S., Umetani, N., Sugiura, S., & Hisada, T. (2008). The sinus of valsalva relieves abnormal stress on aortic valve leaflets by facilitating smooth closure. *The Journal of Thoracic and Cardiovascular Surgery, 136*(6), 1528-1535. e1.

Keane, R., Adrian, R., & Zhang, Y. (1995). Super-resolution particle imaging velocimetry. *Measurement Science and Technology, 6*(6), 754.

Kilner, P. J., Yang, G., Mohiaddin, R., Firmin, D., & Longmore, D. (1993). Helical and retrograde secondary flow patterns in the aortic arch studied by three-directional magnetic resonance velocity mapping. *Circulation, 88*(5), 2235-2247.

Kim, H., & Lee, S. (2002). Performance improvement of two-frame particle tracking velocimetry using a hybrid adaptive scheme. *Measurement Science and Technology, 13*(4), 573.

Klein, S., Moran, J., Frakes, D., & Posner, J. (2012). Three-dimensional three-component particle velocimetry for microscale flows using volumetric scanning. *Measurement Science and Technology, 23*(8), 085304.

Kumar, A., Cierpka, C., Williams, S. J., Kaehler, C. J., & Wereley, S. T. (2011). 3D3C velocimetry measurements of an electrothermal microvortex using wavefront deformation PTV and a single camera. *Microfluidics and Nanofluidics, 10*(2), 355-365. doi:10.1007/s10404-010-0674-4

Lee, S. J., & Kim, S. (2009). Advanced particle-based velocimetry techniques for microscale flows. *Microfluidics and Nanofluidics, 6*(5), 577-588. doi:10.1007/s10404-009-0409-6

Lei, Y., Tien, W., Duncan, J., Paul, M., Ponchaut, N., Mouton, C., . . . Hove, J. (2012). A vision-based hybrid particle tracking velocimetry (PTV) technique using a modified cascade correlation peak-finding method. *Experiments in Fluids, 53*(5), 1251-1268.

Li, C., Lo, C., & Lu, P. (2010). Estimation of viscous dissipative stresses induced by a mechanical heart valve using PIV data. *Annals of Biomedical Engineering, 38*(3), 903-916.

Liao, Q., & Cowen, E. A. (2005). An efficient anti-aliasing spectral continuous window shifting technique for PIV. *Experiments in Fluids, 38*(2), 197-208.

Lieu, V. H., House, T. A., Crawford, J. T., & Schwartz, D. T. (2011). Microeddy design and application for single cell trapping and monitoring. Paper presented at the *Solid-State Sensors, Actuators and Microsystems Conference (TRANSDUCERS), 2011 16th International,* 286-289.

Lim, W., Chew, Y., Chew, T., & Low, H. (2001). Pulsatile flow studies of a porcine bioprosthetic aortic valve in vitro: PIV measurements and shear-induced blood damage. *Journal of Biomechanics, 34*(11), 1417-1427.

Lin, D., Angarita-Jaimes, N. C., Chen, S., Greenaway, A. H., Towers, C. E., & Towers, D. P. (2008). Three-dimensional particle imaging by defocusing method with an annular aperture. *Optics Letters, 33*(9), 905-907. doi:10.1364/OL.33.000905

Lindken, R., Rossi, M., Grosse, S., & Westerweel, J. (2009). Micro-particle image velocimetry (mu PIV): Recent developments, applications, and guidelines. *Lab on a Chip, 9*(17), 2551-2567. doi:10.1039/b906558j

Lindken, R., Westerweel, J., & Wieneke, B. (2006). Stereoscopic micro particle image velocimetry. *Experiments in Fluids, 41*(2), 161-171. doi:10.1007/s00348-006-0154-5

Lu, J., Gharib, M., Gharib, M., & California Institute of Technology. Division of Engineering and Applied Science. (2008). *Quantitative three-dimensional imaging of droplet convection and cardiac cell motions based on micro DDPIV.* California Institute of Technology).

Lu, J., Pereira, F., Fraser, S. E., & Gharib, M. (2008). Three-dimensional real-time imaging of cardiac cell motions in living embryos. *Journal of Biomedical Optics, 13*(1), 014006. doi:10.1117/1.2830824

Luo, B., & Hancock, E. R. (2002). Iterative procrustes alignment with the EM algorithm. *Image and Vision Computing, 20*(5-6), 377-396. doi:10.1016/S0262-8856(02)00010-0

Luo, R., Yang, X. Y., Peng, X. F., & Sun, Y. F. (2006). Three-dimensional tracking of fluorescent particles applied to micro-fluidic measurements. *Journal of Micromechanics and Microengineering, 16*(8), 1689-1699. doi:10.1088/0960-1317/16/8/034

Luo, R., & Sun, Y. (2011). Pattern matching for three-dimensional tracking of sub-micron fluorescent particles. *Measurement Science & Technology, 22*(4), 045402. doi:10.1088/0957-0233/22/4/045402

Lurie, F., & Kistner, R. (2012). The relative position of paired valves at venous junctions suggests their role in modulating three-dimensional flow pattern in veins. *European Journal of Vascular and Endovascular Surgery,*

Lurie, F., & Kistner, R. L. (2013). On the existence of helical flow in veins of the lower extremities. *Journal of Vascular Surgery: Venous and Lymphatic Disorders,*

Lurie, F., Kistner, R. L., & Eklof, B. (2002). The mechanism of venous valve closure in normal physiologic conditions. *Journal of Vascular Surgery, 35*(4), 713-717.

Lurie, F., Kistner, R. L., Eklof, B., & Kessler, D. (2003). Mechanism of venous valve closure and role of the valve in circulation: A new concept. *Journal of Vascular Surgery, 38*(5), 955-961.

Lutz, B. R., Chen, J., & Schwartz, D. T. (2005). Microscopic steady streaming eddies created around short cylinders in a channel: Flow visualization and stokes layer scaling. *Physics of Fluids, 17*(2), 023601. doi:10.1063/1.1824137

Lutz, B. R., Chen, J., & Schwartz, D. T. (2006). Hydrodynamic tweezers: 1. noncontact trapping of single cells using steady streaming microeddies. *Analytical Chemistry, 78*(15), 5429-5435. doi:10.1021/ac060555y

Maas, H. G., Gruen, A., & Papantoniou, D. (1993). Particle tracking velocimetry in 3-dimensional flows .1. photogrammetric determination of particle coordinates. *Experiments in Fluids, 15*(2), 133-146.

Marxen, M., Sullivan, P. E., Loewen, M. R., & Jahne, B. (2000). Comparison of gaussian particle center estimators and the achievable measurement density for particle tracking velocimetry. *Experiments in Fluids, 29*(2), 145-153. doi:10.1007/s003489900085

Meinhart, C. D., & Wereley, S. T. (2003). The theory of diffraction-limited resolution in microparticle image velocimetry. *Measurement Science & Technology, 14*(7), 1047-1053. doi:10.1088/0957-0233/14/7/320

Meinhart, C., Wereley, S., & Gray, M. (2000). Volume illumination for two-dimensional particle image velocimetry. *Measurement Science & Technology, 11*(6), 809-814. doi:10.1088/0957-0233/11/6/326

Meinhart, C., Wereley, S., & Santiago, J. (1999). PIV measurements of a microchannel flow. *Experiments in Fluids, 27*(5), 414-419. doi:10.1007/s003480050366

Mikheev, A., & Zubtsov, V. (2008). Enhanced particle-tracking velocimetry (EPTV) with a combined two-component pair-matching algorithm. *Measurement Science and Technology, 19*(8), 085401.

Mohiaddin, R. H., Yang, G. Z., & Kilner, P. J. (1994). Visualization of flow by vector analysis of multidirectional cine MR velocity mapping. *Journal of Computer Assisted Tomography, 18*(3), 383-392.

Morbiducci, U., Ponzini, R., Rizzo, G., Cadioli, M., Esposito, A., De Cobelli, F., . . . Redaelli, A. (2009). In vivo quantification of helical blood flow in human aorta by time-resolved three-dimensional cine phase contrast magnetic resonance imaging. *Annals of Biomedical Engineering, 37*(3), 516-531.

Morbiducci, U., Ponzini, R., Rizzo, G., Cadioli, M., Esposito, A., Montevecchi, F. M., & Redaelli, A. (2011). Mechanistic insight into the physiological relevance of helical blood flow in the human aorta: An in vivo study. *Biomechanics and Modeling in Mechanobiology, 10*(3), 339-355.

Moreno, D., Santoyo, F. M., Guerrero, J. A., & Funes-Gallanzi, M. (2000). Particle positioning from charge-coupled device images by the generalized lorenz-mie theory and comparison with experiment. *Applied Optics, 39*(28), 5117-5124. doi:10.1364/AO.39.005117

Mühlberger, D., Morandini, L., & Brenner, E. (2009). Venous valves and major superficial tributary veins near the saphenofemoral junction. *Journal of Vascular Surgery, 49*(6), 1562-1569.

Nam, K., Yeom, E., Ha, H., & Lee, S. (2012). Velocity field measurements of valvular blood flow in a human superficial vein using high-frequency ultrasound speckle image velocimetry. *The International Journal of Cardiovascular Imaging, 28*(1), 69-77.

Nogueira, J., Lecuona, A., & Rodriguez, P. (2001). Identification of a new source of peak locking, analysis and its removal in conventional and super-resolution PIV techniques. *Experiments in Fluids, 30*(3), 309-316.

Nogueira, J., Lecuona, A., & Rodriguez, P. (2005). Limits on the resolution of correlation PIV iterative methods. fundamentals. *Experiments in Fluids, 39*(2), 305-313.

Nogueira, J., Lecuona, A., & Rodriguez, P. A. (2001). Local field correction PIV, implemented by means of simple algorithms, and multigrid versions. *Measurement Science & Technology, 12*(11), 1911-1921. doi:10.1088/0957-0233/12/11/321

Ohmi, K., & Li, H. (2000). Particle-tracking velocimetry with new algorithms. *Measurement Science and Technology, 11*(6), 603.

Olsen, M., & Adrian, R. (2000). Out-of-focus effects on particle image visibility and correlation in microscopic particle image velocimetry. *Experiments in Fluids, 29*(1), S166-S174.

Ooms, T. A., Lindken, R., & Westerweel, J. (2009). Digital holographic microscopy applied to measurement of a flow in a T-shaped micromixer. *Experiments in Fluids, 47*(6), 941-955. doi:10.1007/s00348-009-0683-9

OTSU, N. (1979). Threshold selection method from gray-level histograms. *Ieee Transactions on Systems Man and Cybernetics, 9*(1), 62-66.

Ovryn, B. (2000). Three-dimensional forward scattering particle image velocimetry applied to a microscopic field-of-view. *Experiments in Fluids, 29,* S175-S184. doi:10.1007/s003480070019

Panday, S. P., Ohmi, K., & Nose, K. (2011). An ant colony optimization based stereoscopic particle pairing algorithm for three-dimensional particle tracking velocimetry. *Flow Measurement and Instrumentation, 22*(1), 86-95.

Park, J. S., Choi, C. K., & Kihm, K. D. (2004). Optically sliced micro-PIV using confocal laser scanning microscopy (CLSM). *Experiments in Fluids, 37*(1), 105-119.

Park, J. S., & Kihm, K. D. (2006a). Three-dimensional micro-PTV using deconvolution microscopy. *Experiments in Fluids, 40*(3), 491-499. doi:10.1007/s00348-005-0090-9

Park, J. S., & Kihm, K. D. (2006b). Use of confocal laser scanning microscopy (CLSM) for depthwise resolved microscale-particle image velocimetry (mu-PIV). *Optics and Lasers in Engineering, 44*(3-4), 208-223. doi:10.1016/j.optlaseng.2005.04.005

Pavcnik, D., Uchida, B., Kaufman, J., Hinds, M., Keller, F. S., & Rösch, J. (2008). Percutaneous management of chronic deep venous reflux: Review of experimental work and early clinical experience with bioprosthetic valve. *Vascular Medicine, 13*(1), 75-84.

Pereira, F., & Gharib, M. (2002). Defocusing digital particle image velocimetry and the three-dimensional characterization of two-phase flows. *Measurement Science & Technology, 13*(5), 683-694. doi:10.1088/0957-0233/13/5/305

Pereira, F., Gharib, M., Dabiri, D., & Modarress, D. (2000). Defocusing digital particle image velocimetry: A 3-component 3-dimensional DPIV measurement technique. application to bubbly flows. *Experiments in Fluids, 29*, S78-S84. doi:10.1007/s003480070010

Pereira, F., Lu, J., Castano-Graff, E., & Gharib, M. (2007). Microscale 3D flow mapping with mu DDPIV. *Experiments in Fluids, 42*(4), 589-599. doi:10.1007/s00348-007-0267-5

Peterson, S. D., Chuang, H., & Wereley, S. T. (2008). Three-dimensional particle tracking using micro-particle image velocimetry hardware. *Measurement Science & Technology, 19*(11), 115406. doi:10.1088/0957-0233/19/11/115406

Pilu, M. (1997). A direct method for stereo correspondence based on singular value decomposition. *Proceedings /, ,* 261.

Ponchaut, N. F., Hornung, H. G., & California Institute of Technology. Division of Engineering and Applied Science. (2005). *Part I. 3DPTV : Advances and error analysis. part II. extension of guderley's solution for converging shock waves.* California Institute of Technology).

Pratt, W. K. (1991). *Digital image processing*. New York: Wiley.

Raffel, M., Willert, C. E., Wereley, S. T., & Kompenhans, J. (2007). *Particle image velocimetry: A practical guide* Springer.

Richards, J. A., & Jia, X. (1999). *Remote sensing digital image analysis : An introduction*. Berlin; New York: Springer.

Ruhnau, P., Guetter, C., Putze, T., & Schnörr, C. (2005). A variational approach for particle tracking velocimetry. *Measurement Science and Technology, 16*(7), 1449.

Saga, T., Kobayashi, T., Segawa, S., & Hu, H. (2001). Development and evaluation of an improved correlation based PTV method. *Journal of Visualization, 4*(1), 29-37.

Saikrishnan, N., Yap, C., Milligan, N. C., Vasilyev, N. V., & Yoganathan, A. P. (2012). In vitro characterization of bicuspid aortic valve hemodynamics using particle image velocimetry. *Annals of Biomedical Engineering, 40*(8), 1760-1775.

Santiago, J., Wereley, S., Meinhart, C., Beebe, D., & Adrian, R. (1998). A particle image velocimetry system for microfluidics. *Experiments in Fluids, 25*(4), 316-319. doi:10.1007/s003480050235

Satake, S., Kunugi, T., Sato, K., Ito, T., Kanamori, H., & Taniguchi, J. (2006). Measurements of 3D flow in a micro-pipe via micro digital holographic particle tracking velocimetry. *Measurement Science & Technology, 17*(7), 1647-1651. doi:10.1088/0957-0233/17/7/002

Satake, S., Kunugi, T., Sato, K., Ito, T., & Taniguchi, J. (2005). Three-dimensional flow tracking in a micro channel with high time resolution using micro digital-holographic particle-tracking velocimetry. *Optical Review, 12*(6), 442-444. doi:10.1007/s10043-005-0442-y

Scarano, F. (2003). Theory of non-isotropic spatial resolution in PIV. *Experiments in Fluids, 35*(3), 268-277.

Schönemann, P. H. (1966). A generalized solution of the orthogonal procrustes problem. *Psychometrika Psychometrika, 31*(1), 1-10.

Schweighofer, G., Mühlberger, D., & Brenner, E. (2010). The anatomy of the small saphenous vein: Fascial and neural relations, saphenofemoral junction, and valves. *Journal of Vascular Surgery, 51*(4), 982-989.

Scott, G. L., & Longuethiggins, H. C. (1991). An algorithm for associating the features of 2 images. *Proceedings of the Royal Society of London Series B-Biological Sciences, 244*(1309), 21-26. doi:10.1098/rspb.1991.0045

Sheng, J., Malkiel, E., & Katz, J. (2006). Digital holographic microscope for measuring three-dimensional particle distributions and motions. *Applied Optics, 45*(16), 3893-3901. doi:10.1364/AO.45.003893

Shindler, L., Moroni, M., & Cenedese, A. (2010). Spatial–temporal improvements of a two-frame particle-tracking algorithm. *Measurement Science and Technology, 21*(11), 115401.

Shinneeb, A., Bugg, J., & Balachandar, R. (2004). Variable threshold outlier identification in PIV data. *Measurement Science & Technology, 15*(9), 1722-1732. doi:10.1088/0957-0233/15/9/008

Song, X., Yamamoto, F., Iguchi, M., & Murai, Y. (1999). A new tracking algorithm of PIV and removal of spurious vectors using delaunay tessellation. *Experiments in Fluids, 26*(4), 371-380.

Speidel, M., Jonas, A., & Florin, E. L. (2003). Three-dimensional tracking of fluorescent nanoparticles with subnanometer precision by use of off-focus imaging. *Optics Letters, 28*(2), 69-71. doi:10.1364/OL.28.000069

Stellmacher, M., & Obermayer, K. (2000). A new particle tracking algorithm based on deterministic annealing and alternative distance measures. *Experiments in Fluids, 28*(6), 506-518.

Stonebridge, P., & Brophy, C. (1991). Spiral laminar flow in arteries? *The Lancet, 338*(8779), 1360-1361.

Stoyan, D. (1994). A. OKABE, B. BOOTS and K. SUGIHARA: Spatial tessellations. concepts and applications of voronoi diagrams. J. wiley and sons, chichester, new york, brisbane, toronto and singapore 1992, pp. 532, £49.95. *Biom.J.Biometrical Journal, 36*(2), 146-146.

Takehara, K., Adrian, R., Etoh, G., & Christensen, K. (2000). A kalman tracker for super-resolution PIV. *Experiments in Fluids, 29*(1), S034-S041.

Takehara, K., & Etoh, T. (1999). A study on particle identification in PTV particle mask correlation method. *J Vis Journal of Visualization, 1*(3), 313-323.

Tasch, C., & Brenner, E. (2012). The ostial valve of the great saphenous vein. *Phlebology, 27*(4), 179-183.

Towers, C. E., Towers, D. P., Campbell, H. I., Zhang, S. J., & Greenaway, A. H. (2006). Three-dimensional particle imaging by wavefront sensing. *Optics Letters, 31*(9), 1220-1222. doi:10.1364/OL.31.001220

Uemura, T., Yamamoto, F., & Ohmi, K. (1989). A high speed algorithm of image analysis for real time measurement of two-dimensional velocity distribution. *Flow Visualization, ,* 129-133.

Ullman, S. (1979). *The interpretation of visual motion*. Cambridge, Mass.: MIT Press.

Vazquez, S. R., Freeman, A., VanWoerkom, R. C., & Rondina, M. T. (2009). Contemporary issues in the prevention and management of postthrombotic syndrome. *The Annals of Pharmacotherapy, 43*(11), 1824-1835.

Westerweel, J., & Scarano, F. (2005). Universal outlier detection for PIV data. *Experiments in Fluids, 39*(6), 1096-1100. doi:10.1007/s00348-005-0016-6

Willert C E and Gharib,M. (1992). Three-dimensional particle imaging with a single camera [Abstract]. *Exp.Fluids, 12*(6) 353. Retrieved from http://dx.doi.org/10.1007/BF00193880

WILLERT, C., & GHARIB, M. (1991). Digital particle image velocimetry. *Experiments in Fluids, 10*(4), 181-193.

Williams, S. J., Park, C., & Wereley, S. T. (2010). Advances and applications on microfluidic velocimetry techniques. *Microfluidics and Nanofluidics, 8*(6), 709-726. doi:10.1007/s10404-010-0588-1

Wu, M. M., Roberts, J. W., & Buckley, M. (2005). Three-dimensional fluorescent particle tracking at micron-scale using a single camera. *Experiments in Fluids, 38*(4), 461-465. doi:10.1007/s00348-004-0925-9

Yoon, S. Y., & Kim, K. C. (2006). 3D particle position and 3D velocity field measurement in a microvolume via the defocusing concept. *Measurement Science & Technology, 17*(11), 2897-2905. doi:10.1088/0957-0233/17/11/006

Young, C., Johnson, D., & Weckman, E. (2004). A model-based validation framework for PIV and PTV. *Experiments in Fluids, 36*(1), 23-35. doi:10.1007/s00348-003-0602-4

Yu, C., Yoon, J., & Kim, H. (2009). Development and validation of stereoscopic micro-PTV using match probability. *Journal of Mechanical Science and Technology, 23*(3), 845-855. doi:10.1007/s12206-008-1209-8

Zervides, C., & Giannoukas, A. D. (2012). Historical overview of venous valve prostheses for the treatment of deep venous valve insufficiency. *Journal of Endovascular Therapy, 19*(2), 281-290.

Zhang, Z., & Menq, C. (2008). Three-dimensional particle tracking with subnanometer resolution using off-focus images. *Applied Optics, 47*(13), 2361-2370. doi:10.1364/AO.47.002361